

Stabilization of Mercury in River Water and Sediment Using Biochars

by

Peng Liu

A thesis

presented to the University of Waterloo

in fulfillment of the

thesis requirement for the degree of

Doctor of Philosophy

in

Earth and Environmental Sciences

Waterloo, Ontario, Canada, 2016

© Peng Liu 2016

Author's Declaration

I hereby declare that I am the sole author of this thesis. This is a true copy of the thesis, including any required final revisions, as accepted by my examiners.

I understand that my thesis may be made electronically available to the public.

Abstract

Mercury (Hg) is a common contaminant in air, oceans, lakes, rivers, soils, and sediments as elemental, inorganic and organic forms. Organic Hg (*e.g.*, methylmercury (MeHg)), which is much more toxic than other forms and can cause central nervous system defects, and can be converted from inorganic or elemental forms by microbes. Efforts have been made to decrease the production of MeHg by dredging Hg-contaminated sediment, *in situ* capping, or by converting Hg to stable forms using reactive media to decrease its bioavailability. However, current remediation techniques are commonly burdened by high capital costs or by secondary contamination. The application of biochar, which is an alternative to activated carbon and can promote Hg stabilization, may be a cost-effective reactive material for managing Hg-contaminated sites. This thesis describes laboratory batch and anaerobic microcosm experiments for evaluating the addition of biochar for Hg stabilization in water and sediment.

Laboratory batch experiments were conducted to evaluate the treatment of Hg in aqueous solution at environmental concentrations using 36 biochar samples. The biochars were prepared from various feedstocks (wood, agricultural residue, and manure) pyrolyzed at different temperatures (300, 600, and 700°C). The results indicate >90% removal of total Hg (THg) aqueous concentrations was achieved in systems containing biochars produced at 600°C and 700°C (high T) and 40-90% removal for biochars produced at 300°C (low T). Sulfur (S) X-ray absorption near edge structure (XANES) spectra obtained from biochars with adsorbed Hg were similar to those of washed biochars. Micro-X-ray fluorescence (μ -XRF) mapping results indicate that Hg was heterogeneously distributed across biochar particles. Extended X-ray absorption fine

structure (EXAFS) modeling indicates Hg was bound to S in biochars with high S contents and bound to O and Cl in biochars with low S contents. These experiments provide information on the effectiveness and mechanisms of Hg removal in aqueous solutions.

Components released from the biochars during these batch experiments include anions, cations, alkalinity, organic acids (OAs), dissolved organic carbon (DOC), and nutrients. These components may influence the speciation of Hg (*e.g.*, complexation with Hg), facilitate the transport of Hg, promote the growth of organisms, and stimulate the methylation of Hg. The analyses show elevated concentrations of anions (*e.g.*, for SO_4^{2-} up to 1000 mg L^{-1} from manure-based biochars) and nutrients (NO_3^- , $\text{PO}_4\text{-P}$, $\text{NH}_3\text{-N}$, and K) were observed in the majority of aqueous solutions reacted with the biochars. The release of alkalinity OAs and DOC was highly variable and dependent on the feedstock and pyrolysis temperature. Alkalinity released from wood-based biochar was significantly lower than from others. Concentrations of OAs and DOC released from low-T biochars were higher than from high-T biochars. The carbon (C) in the OAs represented 1-60% of the DOC released, indicating the presence of other DOC forms. The C released as DOC represented up to 3% (majority $<0.1\%$) of the total C in the biochar. The modeling analyses of Hg-dissolved organic matter (DOM) complexes suggest that the majority of Hg was likely complexed with thiol groups.

Long-term microcosm experiments were carried out by co-blending Hg-contaminated sediment, biochar, and river water under anaerobic conditions, followed by monitoring for more than 500 days. Factors that may control the evolution of THg and

MeHg in aqueous solution were evaluated. Furthermore, the Hg spatial distribution and speciation associated with biochar particles were investigated.

The results indicate aqueous concentrations of 0.2- μm THg for co-blended systems were less than for sediment controls during the experimental period; 0.45- μm THg concentrations of co-blended systems decreased by 20-92% compared with the controls. Two peaks in MeHg concentrations were observed at early (~40 days) and late (~400 days) times. These peaks corresponded to the onset of iron and sulfate reducing conditions (early peak) and methanogenic conditions (late peak). The MeHg concentrations in the amended systems were less than those observed in the controls, except for late peaks in the microcosms containing a high-T oak wood biochar and switchgrass (600°C) biochars. Pyrosequencing analyses showed shifts in percentages of microbial sequences associated with fermenters, iron-reducing bacteria (FeRB), sulfate-reducing bacteria (SRB), and methanogens that were correlated to changes in C sources (DOC, OAs, and alkalinity) and electron acceptors (NO_3^- , Fe, and SO_4^{2-}). Twelve mercury methylators grouped into SRB, FeRB, methanogens, and fermenters based on the pyrosequencing results were detected in the systems.

The fate of the removed Hg was studied using X-ray absorption spectroscopy. Hg was observed to co-occur with S, Cu, Fe, Mn, and Zn on the surface and inside the biochar particles as indicated by μ -XRF mapping. EXAFS modeling showed that Hg was present in an oxide form on the surface of an iron (hydro)oxide particle from fresh sediment and in Hg-sulfide forms for the Hg-rich areas of biochar particles after co-blending with sediment. Sulfur XANES showed the presence of sulfide in these biochar particles. After the addition of biochars, a fraction of the Hg in unstable forms (*e.g.*,

dissolvable, HgO, colloidal, nano) in the sediment was likely converted to Hg-sulfide forms. These more stable forms bound on and within the biochar particles are anticipated to have decreased mobility and decreased bioavailability relative to the Hg in the unamended sediment.

The detected fluorescence intensity in conventional XRF mapping represents the sum of information along the path of microbeam penetration into the sample, usually limited by the thickness of thin sections. To overcome this limitation, confocal X-ray micro-fluorescence imaging (CXMFI) was applied to delineate the three-dimensional spatial distribution of elements accumulated within switchgrass biochar particles. The maps indicate that Hg, Fe, Ti, Cr, Mn, Co, Ni, Cu, Zn, and As were distributed within the structural material of low-T switchgrass biochar, whereas these elements were preferentially observed on the surfaces of high-T switchgrass biochar. These observations suggest that the accumulations of Hg and other elements in biochars may be through an early-stage diagenetic process, rather than a simple surface adsorption reaction.

Hard-wood biochar was sulfurized using CaS_x (CPS-CL2) and a dimercapto-related (DMC-CL2) compound to further promote Hg removal. With an initial THg concentration of $17,800 \text{ ng L}^{-1}$, final THg concentrations were 40 and 7.0 ng L^{-1} using CPS-CL2 and DMC-CL2, and 370 ng L^{-1} using unmodified hard-wood biochar; for an initial THg concentration of $245,000 \text{ ng L}^{-1}$, final concentrations were 74 and 110 ng L^{-1} using CPS-CL2 and DMC-CL2, and $5,700 \text{ ng L}^{-1}$ using the unmodified form; for an initial concentration of $4,960 \text{ } \mu\text{g L}^{-1}$, final concentrations were 10 and $29 \text{ } \mu\text{g L}^{-1}$ using CPS-CL2 and DMC-CL2, and $170 \text{ } \mu\text{g L}^{-1}$ using the unmodified biochar. The THg removal percentages were $>99.5\%$ using the modified biochars for these three initial

concentrations. A suite of synchrotron-based techniques was applied to characterize biochars loaded with Hg. S XANES analyses indicates polysulfur- and thiol-like structures were present in the modified biochars. The accumulated Hg was distributed primarily on the edges of the modified biochar particles as indicated by μ -XRF mapping and CXMFI techniques. Hg EXAFS analysis shows Hg was bound to S in sulfurized biochars.

This study demonstrates that biochars may be effective reactive media for Hg removal from aqueous solution and for Hg stabilization in amended sediment. The extent of Hg removal was further enhanced after sulfurization of the biochar. The results also suggest that the Hg stabilization process may be effective for years or longer through strong binding with biochar particles.

Acknowledgment

First and foremost, I wish to express my sincerest gratitude to my co-supervisors and mentors, Dr. Carol Ptacek and Dr. David Blowes, who were abundantly helpful and offered invaluable guidance and support throughout the course of my degree. They also gave me extraordinary experiences throughout the research period. I am inspired by their passion for research and indebted to them for the opportunities they have provided to me. I am heartily thankful to them.

I thank my committee members Dr. Doug Gould and Dr. David Rudolph for their valuable advices and insightful discussions of science. Thank you to Dr. Doug Gould for inspiring my interest in geomicrobiology. I also thank my internal-external examiner Dr. Laura Hug and external examiner Dr. Derek Peak for their thorough and insightful comments of this thesis. I also thank Dr. Raoul-Marie Couture, who was a committee member for the first two years of my thesis and gave me a different perspective of my research during my comprehensive examination.

Funding for this research was provided by E. I. du Pont de Nemours and Company, Natural Sciences and Engineering Research Council of Canada (NSERC), a Collaborative Research and Development Grants awarded to C. Ptacek and D. Blowes, a Discovery Grant awarded to C. Ptacek, an Ontario Research Fund-Research Excellence Grant awarded to D. Blowes and C. Ptacek, and a Canada Research Chair held by D. Blowes.

I would like to thank Richard Landis, Jim Dyer, Nancy Grosso, William Berti, Erin Mack, Ralph Stahl and Michael Liberati of DuPont; Scott Brooks of Oak Ridge

National Laboratories, U.S. Department of Energy; and members of the South River Science Team for their advice and ongoing support.

Thank you to all of the graduate students, laboratory technicians, research assistants, postdocs, and coop students for assistance with laboratory experiments and related analyses and discussion. This includes Alana Ou Wang, Krista Paulson, Jing Ma, Laura Groza, Joy Hu, Syed Ismail Hussain, Shannon Daugherty, Blair Gibson, Krista Desrochers, Matt Lindsay, Julia Jamieson-Hanes, Sara Fellin, Matt Corriveau, James Tordiff, and Andrew O'Malley. I also want to thank Ms. Gillian Binsted (BSc, MAsc, Member of the Editor's Association of Canada) for providing English editorial and technical comments in Chapters 2, 3, 4, and 7.

Synchrotron-based techniques were performed at Sector 13 GSECARS and Sector 20 PNC/XSD of Advanced Photon Source (APS) and SXRMB of Canadian Light Source (CLS). GSECARS is supported by the National Science Foundation-Earth Sciences (EAR-1128799) and Department of Energy-GeoSciences (DE-FG02-94ER14466). PNC/XSD is supported by the US Department of Energy - Basic Energy Sciences, the CLS and its funding partners, the University of Washington, and the Advanced Photon Source. This research used resources of the APS, a U.S. Department of Energy (DOE) Office of Science User Facility operated for the DOE Office of Science by Argonne National Laboratory. CLS is supported by the Canada Foundation for Innovation, NSERC, the University of Saskatchewan, the Government of Saskatchewan, Western Economic Diversification Canada, the National Research Council Canada, and the Canadian Institutes of Health Research. I received support from the CLS Graduate Student Travel Support Program.

I want to give special thanks to the beamline scientist for their help with the experimental setups and data collection at the beamlines and their insightful data interpretation. The beamline scientists who supported my work include Dr. Matt Newville, Dr. Tony Lanzirotti, Dr. Yongfeng Hu, Dr. Zou Finfrock, Dr. Robert Gordon, and Dr. Qunfeng Xiao. I extend my sincere thanks to my parents, parents-in-law, and everyone else who supported and encouraged me throughout this endeavor.

Finally, I am sincerely grateful to my wife, YingYing Liu, for her loving support, encouragement, patience and understanding over the years. You always believed in me and I would not have made it without you. I also want to thank our lovely daughter, Christina, who makes our lives more colorful.

Dedication

To YingYing Liu and Christina Yuan Liu.

Table of Contents

Author's Declaration	ii
Abstract.....	iii
Acknowledgment.....	viii
Dedication	xi
Table of Contents	xii
List of Tables.....	xvi
List of Figures.....	xvii
List of Abbreviations.....	xxii
Chapter 1: <i>Introduction</i>	1
1.1 Background	2
1.1.1 Challenges of Mercury-Contaminated Site Remediation.....	2
1.1.2 Remediation Options	3
1.1.3 Biochar	4
1.1.4 South River Hg-Contaminated Sites	6
1.1.5 X-ray Absorption Spectroscopy	9
1.2 Research Objectives	13
1.3 Thesis Organization	14
Chapter 2: <i>Aqueous Leaching of Organic Acids and Dissolved Organic Carbon from Various Biochars Prepared at Different Temperatures</i>	24
2.1 Executive Summary	25
2.2 Introduction	25
2.3 Materials and Methods.....	28
2.3.1 Preparation of Biochar Source Materials	28
2.3.2 Characterization of Solid-Phase Biochar.....	29
2.3.3 Release of Alkalinity, OAs and DOC from Biochar to Aqueous Solutions.....	30
2.3.4 Statistical Analysis	33
2.4 Results and Discussion.....	33
2.4.1 Total C Contents in Biochar	33
2.4.2 One-Time Release of Short-Chain OAs and DOC.....	34
2.4.3 pH and Alkalinity in One-Time Release Experiments	37
2.4.4 Continuous Release of OAs and DOC	39
2.4.5 SEM/EDX	42
2.4.6 FT-IR	43
2.4.7 Environmental Relevance.....	45
2.5 Conclusions.....	46
Chapter 3: <i>Mechanisms of Mercury Removal by Biochars Produced from Different Feedstocks Determined using X-ray Absorption Spectroscopy</i>	55
3.1 Executive Summary	56
3.2 Introduction	56
3.3 Materials and Methods.....	59
3.3.1 Biochars Employed	59
3.3.2 Batch Experiments for Hg Removal	59
3.3.3 Water Analyses.....	60

3.3.4 S Content	60
3.3.5 X-ray Absorption Spectroscopy (XAS)	60
3.3.6 Statistical Analysis	64
3.4 Results and Discussion.....	64
3.4.1 Removal of Hg	64
3.4.2 SO ₄ ²⁻	65
3.4.3 S Content	66
3.4.4 S XANES Analyses.....	67
3.4.5 μ-XRF Mapping	69
3.4.6 Hg XANES Analysis and EXAFS Modelling.....	70
3.5 Conclusions.....	72
Chapter 4: <i>Evaluation of Mercury Stabilization in Sediment by Biochars under Reducing Conditions</i>.....	83
4.1 Executive Summary	84
4.2 Introduction.....	84
4.3 Materials and Methods.....	86
4.3.1 Materials.....	86
4.3.2 Microcosm Experiment	87
4.3.3 Chemical Analyses	87
4.3.4 Pyrosequencing analysis.....	89
4.3.5 X-Ray Absorption Spectroscopy.....	89
4.3.6 Correction Method for X-Ray Fluorescence Attenuation	90
4.4 Results and Discussion.....	91
4.4.1 Overview of Sediment, River Water, and Biochar.....	91
4.4.2 pH, Redox Potential and Alkalinity	91
4.4.3 Aqueous THg and MeHg	92
4.4.4 Aqueous Fe and SO ₄ ²⁻	93
4.4.5 Solid-Phase MeHg.....	94
4.4.6 Aqueous Carbon Source.....	94
4.4.7 Potential Methylators	95
4.4.8 μ-XRF and EXAFS	96
4.4.9 Confocal X-Ray Micro-Fluorescence Imaging	97
4.5 Conclusions.....	99
Chapter 5: <i>Control of Mercury and Methylmercury in Contaminated Sediments Using Biochars</i>.....	107
5.1 Executive Summary	108
5.2 Introduction.....	108
5.3 Materials and Methods.....	111
5.3.1 Materials.....	111
5.3.2 Anaerobic Microcosm Experiments	112
5.3.3 Water Analyses.....	113
5.3.4 Solid Phase Analysis	114
5.3.5 Statistical Analysis	115
5.4 Results and Discussion.....	115
5.4.1 Overview of Sediment, River Water, and Biochar Samples	115
5.4.2 Aqueous Chemistry	115

5.4.3 THg in Aqueous Phase	116
5.4.4 MeHg	118
5.4.5 Carbon Sources for Microbes	120
5.4.6 Electron Acceptors for Microbes	122
5.4.7 Pyrosequencing	124
5.5 Implications for Remediation of Hg-contaminated Sites	127
Chapter 6: <i>Mercury Stabilization Mechanisms in Contaminated Sediment Amended with Biochars Determined using X-ray Absorption Spectroscopy</i>	135
6.1 Executive Summary	136
6.2 Introduction	137
6.3 Materials and Methods	138
6.3.1 Samples for Synchrotron Analysis	138
6.3.2 X-ray Absorption Spectroscopy	139
6.4 Results and Discussion	141
6.4.1 XAS Analysis for Fresh Sediment and Sediment Control	141
6.4.2 Micro-XRF Maps of Biochar Particles from Amended Systems	143
6.4.3 Hg and Cu EXAFS	144
6.4.4 S XANES	146
6.5 Environmental Applications	147
Chapter 7: <i>Mechanisms of Mercury Stabilization by Sulfurized Biochars Determined using X-ray Absorption Spectroscopy</i>	154
7.1 Executive Summary	155
7.2 Introduction	155
7.3 Materials and Methods	158
7.3.1 Biochar Sulfurization	158
7.3.2 Batch Experiments	159
7.3.3 Solid Samples for X-Ray Absorption Spectroscopy	160
7.3.4 S X-Ray Absorption Near-Edge Structure Spectra	160
7.3.5 Micro-X-Ray Fluorescence Mapping	161
7.3.6 Hg Extended X-Ray Absorption Fine Structure Spectra	161
7.3.7 Confocal X-Ray Micro-Fluorescence Imaging	161
7.4 Results and Discussion	162
7.4.1 Aqueous Chemistry	162
7.4.2 Hg Removal	162
7.4.3 S XANES	164
7.4.4 Hg μ -XRF Maps	166
7.4.5 Confocal X-Ray Micro-Fluorescence Imaging	166
7.4.6 Hg EXAFS	167
7.5 Environmental Applications	169
Chapter 8: <i>Conclusions</i>	177
8.1 Summary of Findings	178
8.2 Scientific Contributions	184
8.3 Implications of Research Results	185
8.4 Future Research	186
References	192
Appendix A: <i>Summary of Data Presented in Chapter 2</i>	222

Appendix B: Summary of Data Presented in Chapter 3	230
Appendix C: Supplementary Information in Chapter 4	233
Appendix D: Supplementary Information in Chapter 5	252
Appendix E: Summary of Data and Supplementary Information Presented in Chapter 6	301
Appendix F: Supplementary Information in Chapter 7	323
Appendix G: Release of Nutrients and Trace Elements from Various Biochars and Implications for Mercury Remediation	330
G.1 Executive Summary	331
G.2 Introduction	331
G.3 Materials and Methods	333
G.3.1 Biochar Samples	333
G.3.2 Batch-Experiment Set-up	334
G.3.3 Water Sample Analysis	335
G.3.4 Specific Surface Area	335
G.3.5 Speciation Modeling.....	335
G.3.6 Statistical Analysis	336
G.4 Results and Discussion.....	336
G.4.1 Summary of Hg Removal and Release of SO ₄ ²⁻ , OAs, and DOC	336
G.4.2 Specific Surface Area	337
G.4.3 Anions.....	338
G.4.4 Major Cations	339
G.4.5 Trace Elements	340
G.4.6 Nutrients	341
G.4.7 Hg-DOM Complexes Modelled by PHREEQC	342
G.5 Conclusion.....	344

List of Tables

Table 2.1 Chemical composition of river water from South River near Waynesboro, VA, USA (Unit mg L ⁻¹ , except ionic strength as mol L ⁻¹).....	47
Table 2.2 C contents of all biochars as a function of biochar feedstocks and pyrolysis temperatures.	48
Table 2.3 Calculated first-order rate constants for the release of OAs and DOC as a function of number of washing steps and percentages of DOC in total C of biochars ^a	49
Table 3.1 Abbreviations, sources of feedstock, and pyrolysis temperatures for biochar samples.....	74
Table 3.2 S content of biochars as a function of pyrolysis temperature.	75
Table 3.3 Percentage (%) of different S forms calculated by LCF	76
Table 3.4 Hg EXAFS fitting results ^a	77
Table 6.1 EXAFS fitting results of bulk and Hg-enriched area of μ -XRF maps of sediment control (SRD) and biochar amended systems.....	149
Table 7.1 Hg EXAFS fitting results for bulk and thin-sections (micro) of unmodified and CPS and DMC modified biochars ^a	171

List of Figures

Figure 1.1 Schematic illustration of the structural transformations in biochar production during pyrolysis. The transformations involve char forming, devolatilization, secondary cracking, condensation, and soot deposition. Modified from Bandosz (2006).....	17
Figure 1.2 Biochar stability with regard to pyrolysis temperature, carbon content, fused aromatic rings, and mineral content (after Singh et al. (2012))	18
Figure 1.3 Conceptual diagram of biochar application in river/pond and floodplain soil. The bottom part indicates a proposed Hg stabilization process.	19
Figure 1.4 Total Hg contents of 34 samples along the South River, Virginia including river sediment, floodplain soil, and pond sediment. RRM represents relative river mile; numbers after RRM represents miles from the historical point of Hg release (star). Multi samples were collected for transactions of RRM0.1, RRM0.15, RRM2.4, RRM3.4, and RRM3.5.	20
Figure 1.5 Principle of X-ray absorption near edge structure (XANES) and extended X-ray absorption fine structure (EXAFS) spectroscopy indicated by Hg L _{III} -edge of metacinnabar	21
Figure 1.6 Lines for electron binding energy, X-ray emission lines, and electron configuration of elements. Bold K, L, and M are electron shell notation. The letter and number on the left side (<i>e.g.</i> K, L ₁ , L ₂) are lines for electron binding energies. The letter, Greek symbol, and number with arrows are X-ray emission lines. The numbers, letters, and fractions are electron configuration.	22
Figure 1.7 Setup of confocal X-ray micro-fluorescence imaging and schematic illustration of the optics using collimating channels. The channels are formed from a set of staggered, absorbing pillars. The inset on the left side illustrates that the pillars absorb photons by tapering away its edges from the axis of each channel. The α (35°) represents the angle between the sample holder and incident beam. The dashed lines with arrow at both ends represents the stage moving direction. Modified from Woll et al. (2014)	23
Figure 2.1 Concentration of organic acids and DOC in aqueous solution leached from each biochar sample (a, b), and the percentage of total dissolved C composed of five components (c, d). The other C was the difference between DOC and organic acids. * after biochar name indicates no data was available for high-T biochar; ** after biochar name indicates no data was available for low-T biochar.....	50
Figure 2.2 pH and alkalinity values of aqueous solutions mixed with low-T and high-T biochars. * after biochar name indicates no data was available for high-T biochar; ** after biochar name indicates no data was available for low-T biochar.....	51

Figure 2.3	Concentrations of acetate, formate and DOC released by activated carbon, wood, switchgrass, poultry manure, and mushroom soil biochars during sequential leaching. The dashed vertical line indicates the solid phase was left on the filter for 10 hours prior to the 5 th washing step. The dashed blue lines represent the regression curves of the C release using $C = C_0 \exp(-k t)$ for the orange circle data points by excluding the 5 th step. The calculated regression coefficients are provided in Table 2.3. ...	52
Figure 2.4	SEM/EDX images of representative biochar samples.....	53
Figure 2.5	FTIR spectra of representative biochar and activated carbon samples. Dashed lines represent the following functional groups: v1, hydroxyl (-OH, 3449 cm ⁻¹); v2, aliphatic (-CH, -CH ₂ , or -CH ₃ , 2920 and 2847 cm ⁻¹); v3, thiol (2511 cm ⁻¹); v4, quinone (-(CO)-, 1630 cm ⁻¹); v5 v9, sulfate (1114, 615 cm ⁻¹); v6, Phosphorus-containing (1039 cm ⁻¹); v7, carbonate (870 cm ⁻¹); v8, C-S (713 cm ⁻¹).	54
Figure 3.1	THg concentrations and % Hg removal from aqueous solution in batch tests containing biochar and river water spiked with Hg. C represents the control containing Hg-spiked river water with no biochar added.....	78
Figure 3.2	Concentrations of SO ₄ ²⁻ in river water (control C) versus concentrations in batch mixtures containing river water and biochar.....	79
Figure 3.3	^{a b} S XANES spectra for 17 S standards. ^{c d} S XANES spectra for unwashed and washed biochars; the number after the sample name indicates the number of times that the sample was washed. The dashed blue line indicates the fitted curves for samples using LCF. Spectra identifications displayed on the left side of subplots b, c, and d indicate samples where the spectra were reduced by half for ease of display. ^e S XANES spectra for activated carbon and biochars with adsorbed Hg(II).	80
Figure 3.4	Microscope photos under reflection mode (left) and Hg L _α line μ-XRF maps (right) in thin sections. The white bars represent 100 μm. The EXAFS spectra for modeling were collected at the locations indicated by white arrows. Note: For AC-Coarse and CL2-Coarse, a high resolution mapping area is displayed directly below each map. The XRF spectra displayed on the right side were collected over the areas identified by white squares in the maps directly to the left of the XRF spectra.	81
Figure 3.5	^a Normalized Hg XANES spectra. ^b First-derivative spectra, where IPD is the inflection point difference. ^c k ³ -weighted chi spectra (black line) and best fit (light blue-dash line). ^d Fourier-transformed magnitude spectra. ^e Fourier-transformed real part.	82
Figure 4.1	Concentrations of 0.2- and 0.45-μm filtered THg, MeHg, Fe, and SO ₄ ²⁻ in aqueous solutions of controls and amended systems vs. time. The blue bars indicate two stages of MeHg production: a combined iron and sulfate reduction period (first) and a methanogenic period (second).....	101

Figure 4.2 MeHg content in sediment control and amended systems (low-T and high-T switchgrass biochars) at day 0, 65, 100, 154, 235, and 387.	102
Figure 4.3 Carbon sources (dissolved organic carbon (DOC), acetate, and alkalinity) of controls and amended systems against time. The blue bars indicate two stages of MeHg production: a combined iron and sulfate reduction period (first) and a methanogenic period (second).	103
Figure 4.4 Percentages of species identified as known Hg methylators, including sulfate reducing bacteria, iron-reducing bacteria, and fermentative bacteria in sediment control and amended systems. For each sample, columns from left to right represent samples from day 0, 65, 100, 154, 235, and 387, respectively.	104
Figure 4.5 Micro-XRF maps (Hg, Cu, Fe, and S) of thin-sections of low-T (top) and high-T (intermediate) biochar particles from amended systems at days 235 and 387, respectively. The first column shows microscopic images and the last column XRF spectra were collected from the area indicated by the white arrow. The S map was collected at a different time and with a different beamline setup. The white scale represents 100 μm . ^a Edge-step normalized Hg L _{III} -edge XANES spectra were collected at the point indicated by the gray arrow. ^b k^3 -weighted chi spectra (black solid line) and the best fit data (light-blue dash line). ^c Fourier-transform magnitude spectra and the best fit data. ^d Fourier-transform real part and the best fit data.	105
Figure 4.6 Confocal X-ray micro-fluorescence imaging showing the distribution of K, Fe, and Hg in low-T (upper) and high-T (bottom) biochar particles (not physically sectioned) collected from the amended systems after 600 d. The low-T switchgrass biochar particle was analyzed perpendicular and the high-T biochar particle was analyzed parallel to the straw, which accounts for the differences in pore structure. The thick white arrow indicates the surface of the particle. The thin white arrow indicates the incident and emitted beam paths. Note: vertical exaggeration is ~ 7	106
Figure 5.1 Concentrations of 0.2 and 0.45 μm filtered THg and 0.45 μm filtered MeHg in aqueous solutions of controls and amended systems against time. The data of sediment control and low-T and high-T switchgrass biochar is from Chapter 4.	129
Figure 5.2 MeHg contents in sediment control and amended systems (activated carbon, OAK700, low-T and high-T switchgrass, and poultry manure) at day 0, 65, 100, 154, 235, and 387. The data of sediment control and low-T and high-T switchgrass biochar is from Chapter 4.	130
Figure 5.3 Concentration of carbon sources (DOC, acetate and alkalinity) in aqueous solutions of controls and amended systems against time. The data of sediment control and low-T and high-T switchgrass biochar is from Chapter 4.	131

Figure 5.4 Concentration of electron acceptor (NO_3^- , Mn, Fe, and SO_4^{2-} in redox sequence) in aqueous solutions of controls and amended systems against time. The Fe and SO_4^{2-} concentrations of sediment control and low-T and high-T switchgrass biochar are from Chapter 4.	132
Figure 5.5 Pyrosequencing results of percentages in genus level including fermenters, FeRB, SRB, and methanogens of sediment control and amended systems of activated carbon, OAK700 (duplicate amended systems), low-T and high-T switchgrass biochar, and poultry manure biochar (duplicate amended systems). For each sample, columns from left to right represent days 0, 65, 100, 154, 235, and 387.	133
Figure 5.6 Percentages of species identified as known Hg methylators including SRB, FeRB, methanogen, and fermentative bacteria at different days from sediment control and amended systems. For each sample, columns from left to right represents day 0, 65, 100, 154, 235, and 387. The data of sediment control and low-T and high-T switchgrass biochar is from Chapter 4.	134
Figure 6.1 Micro-XRF maps (Hg, Cu and Fe) of particles from fresh sediment and sediment control at day 235. The first column of first two rows is the microscopic pictures and the last column is the XRF spectra collected from the area indicated by the white arrow in Hg L_α maps. The white line represents 100 μm . The points indicated by the white arrow in Hg and Cu maps mean Hg and Cu EXAFS spectra were collected. The bottom row includes ^a Edge-step normalized Hg L_{III} -edge XANES spectra of the spots indicated in the micro-XRF maps and bulk fresh sediment. ^b k^3 -weighted chi spectra (black solid line) and the best fit data (light-blue dash line). ^c Fourier-transform magnitude spectra and the best fit data. Fourier transform data are corrected for phase shift. ^d Fourier-transform real part and the best fit data.	150
Figure 6.2 Micro XRF maps (Hg, Cu, Fe, and S) of activated carbon and biochar particles from the sediment amended systems at day 387. The first column is the microscopic pictures and the last column is the XRF spectra collected from the area indicated by the white arrow in Hg L_α maps. The white line represents 100 μm . The points indicated by the white arrow in Hg, Cu and S maps mean Hg and Cu EXAFS and S XANES spectra were collected. S XRF maps were collected at different time due to beamline setup, and S XRF maps were not well aligned with other maps	151
Figure 6.3 ^a Edge-step normalized Hg L_{III} -edge XANES spectra of the spots indicated in the μ -XRF maps. ^b k^3 -weighted chi spectra (black solid line) and the best fit data (light-blue dash line). ^c Fourier-transform magnitude spectra and the best fit data. Fourier transform data are corrected for phase shift. ^d Fourier-transform real part and the best fit data. M1 and bulk represent the spectra were collected from Hg-enriched area of μ -XRF maps and ground bulk biochars from amended systems.	152

Figure 6.4 S XANES spectra of activated carbon (AC) and CL2 particles from amended systems and control at day 387. <i>Bulk</i> represents results of bulk sample analysis. <i>MI</i> represents the spectra from spots on thin-sections. S forms indicated by lines 1-6 are assigned as inorganic-sulfide, elemental, thiol, thiophenic, sulfonate, and ester-sulfate sulfur, respectively, as assigned by Manceau and Nagy (2012) and Vairavamurthy (1998).....	153
Figure 7.1 THg concentrations from aqueous solution in batch tests containing unmodified biochar (CL2) and CPS- and DMC-modified (target S contents of 0.5, 2, and 5%) biochars at three different initial concentrations. Error bars represent standard error of the mean derived from duplicate experiments.....	172
Figure 7.2 S XANES spectra of a) six reference materials (one in b), CPS, and DMC, b) unmodified and sulfurized CL2 (with and without Hg), and c) sulfurized CL2 exposed to air for 10 and 60 d. Spectra of elemental S and CaSO ₄ were reduced by half for ease of display.	173
Figure 7.3 Microscope photos under reflection mode (R; 1 st column), transmission mode (T; 2 nd column), Hg L _α line μ-XRF maps (3 rd column), and the XRF spectra of the Hg-enriched area indicated by the white arrow of unmodified biochar (CL2) and CPS- and DMC-modified biochars in thin-sections. The white bar represents 100 μm. The EXAFS spectra for modeling were also collected at the locations indicated by the white arrows.....	174
Figure 7.4 Confocal X-ray micro-fluorescence imaging showing the distribution of Hg in unmodified and modified biochar particles (not physically sectioned) with adsorbed Hg. Photos in the bottom right corner show the orientation of the particles for analysis. The white bars on the particle indicate the imaging area (600×60 μm ²) with an imaging depth as 350 μm. The thick white arrow indicates the surface of the particle. The thin white arrow indicates the incident and emitted beam paths. Vertical exaggeration is ~8.	175
Figure 7.5 a) Normalized Hg XANES spectra collected from bulk samples and Hg-enriched areas (micro) in thin-sections of bulk unmodified (raw) and sulfurized (CPS and DMC) biochars. b) k ³ -weighted chi spectra (black line) and best fit (light blue-dash line). c) Fourier-transformed magnitude spectra. d) Fourier-transformed real part.	176
Figure 8.1 Rapid adsorption of Hg by biochar particles in the amended systems at the beginning of the experiment.....	189
Figure 8.2 The release of Hg during the dissolution of iron oxide at the iron reducing stage.	190
Figure 8.3 Production of MeHg during the methanogenic stage (adapted from Fig. 5.1).	191

List of Abbreviations

AC1	Activated carbon1
AC2	Activated carbon2
APS	Advanced Photon Source
CA1H	High-T cocoa husk (600°C)
CA1L	Low-T cocoa husk (300°C)
CC1H	High-T corn cob1
CC1L	Low-T corn cob1
CC2H	High-T corn cob2
CC2L	Low-T corn cob2
CL1	Commercial wood biochar1 (Wicked Good Charcoal Co.)
CL2	Commercial wood biochar2 (Cowboy Charcoal Co.)
CL5	Commercial wood biochar5 (Biochar Engineering Co.)
CLS	Canadian Light Source
CN	Coordination numbers
CS1H	High-T corn stovers1
CS1L	Low-T corn stovers1
CS2H	High-T corn stovers2
CS2L	Low-T corn stovers2
CT1H	High-T cotton seed husk
CT1L	Low-T cotton seed husk
CXMFI	Confocal X-ray micro-fluorescence imaging
CVAFS	Cold vapor atomic fluorescence spectrometry
DOC	Dissolved organic carbon
DOE	U.S. Department of Energy
DOM	Dissolved organic matter
EPA	U.S. Environmental Protection Agency
EXAFS	Extended X-ray absorption fine structure
FeRB	Iron-reducing bacteria
FT-IR	Fourier transform infrared spectroscopy
GR2H	High-T wheat shaft
GR2L	Low-T wheat shaft
GR3H	High-T spent hops
GR3L	Low-T spent hops
GR4H	High-T switchgrass
GR4L	Low-T switchgrass
GRASS300	Low-T switchgrass
GRASS600	High-T switchgrass
High T	High temperature
ICP-MS	Inductively couple plasma – mass spectrometry
ICP-OES	Inductively couple plasma – optical emission spectrometry
LCF	Linear combination fitting
Low T	Low temperature
MANURE300	Low-T chicken manure
MANURE600	High-T chicken manure
MB1H	High-T cow manure
MB1L	Low-T cow manure
MDL	Method detection limit
MeHg	Methylmercury

MP1H	High-T chicken manure
MP1L	Low-T chicken manure
MP2L	Low-T chicken manure
MP3H	High-T chicken manure
MU1H	High-T mushroom soil
MU1L	Low-T mushroom soil
MU2H	High-T mushroom soil
MU2L	Low-T mushroom soil
MU3H	High-T mushroom soil
OA	Organic acid
OAK700	Commercial wood biochar ² (Cowboy Charcoal Co.)
PCR	Polymerase chain reaction
QA/QC	Quality assurance/quality control
SEM/EDX	Scanning electron microscope/energy dispersive X-ray
SRB	Sulfate-reducing bacteria
SSA	Specific surface area
SW1H	High-T mulch
SW1L	Low-T mulch
SW2H	High-T pine bark
SW2L	Low-T pine bark
THg	Total Hg
TOC	Total organic carbon
UV	Ultraviolet
XANES	X-ray absorption near-edge structure
XAS	X-ray absorption spectroscopy
XRF	X-ray fluorescence

Chapter 1: *Introduction*

1.1 Background

1.1.1 Challenges of Mercury-Contaminated Site Remediation

Large quantities of heavy metals have been discharged to the environment as a result of the early stages of industrialization and these discharges are continuing (Hao, 2010). In particular, large quantities of mercury (Hg) were released into the environment owing to its widespread usage and important role in a variety of industries, including chlor-alkali production, Hg mining, Au mining, and fossil fuel combustion (Scoullou et al., 2001).

Although strict environmental regulations have been enacted in many parts of the world over the past several decades, approximately 10,000 tons of Hg are still released each year worldwide from both natural and anthropogenic sources according to the World Health Organization (Reuther & Wheeler, 1996). Consequently, Hg is widely distributed in rivers, soils, lakes, oceans, and sediments (Ebinghaus et al., 1999). Under certain environmental settings, inorganic Hg can be transformed to organic Hg, e.g. methylmercury (MeHg) and dimethylmercury (Jonsson et al., 2016). The organic Hg is considerably more toxic than inorganic Hg due to the high potential for bioaccumulation in fish and other organisms (Boening, 2000).

MeHg can be produced through abiotic or biotic processes, but biotic processes are considered to be the major pathway (Celo et al., 2006; Morel et al., 1998). Sulfate reducing bacteria, iron reducing bacteria, and methanogens are among potential Hg methylators (Acha et al., 2012; Fleming et al., 2006; Gilmour et al., 1992; Yu et al., 2013). A number of factors can affect MeHg formation, including pH, redox potential, alkalinity, temperature, the concentrations and form of inorganic Hg species, ionic strength, the type and activity of microorganisms, dissolved organic carbon (DOC), electron donors for microbes (*e.g.*, labile organic compounds), electron acceptors (*e.g.*,

O₂, NO₃⁻, Fe²⁺, SO₄²⁻, inorganic C), and S²⁻, Cl⁻, etc. (Ortiz et al., 2015; Ullrich et al., 2001). The extent to which these factors influence the rate of MeHg formation appears to vary, with contradictory results obtained in different studies (Graham et al., 2012; Ravichandran, 2004; Ullrich et al., 2001). Generally, the presence of labile organic matter, such as acetate, moderate concentrations of SO₄²⁻, low levels of salinity, low pH values, and an elevated supply of natural DOC appear to stimulate Hg methylation (Compeau & Bartha, 1987; Desrochers et al., 2015; Driscoll et al., 2007; Gilmour & Henry, 1991; King et al., 2000).

Concentrations of MeHg in natural waters are usually low (ng L⁻¹), but aquatic organisms can bioaccumulate MeHg to high concentrations. When organisms containing MeHg are consumed, MeHg further bioaccumulates to levels which can cause health effects in organisms higher in the food chain, including humans. Toxicology studies have shown that both Hg and MeHg are highly toxic to the human kidney and brain (Clarkson, 1997). Therefore, steps must be taken to either remove Hg from rivers, lakes, or sediments where it may be a threat to organisms, or methods must be developed to stabilize Hg *in situ* in a manner which limits its bioavailability.

1.1.2 Remediation Options

A range of methods is available for treating or stabilizing Hg in contaminated water, soil and sediment. The treatment methods include soil washing, thermal treatment of excavated soil, physical barriers to immobilize Hg, electro-kinetic methods, geohydrological isolation, solidification and stabilization by mixing with cement, activated carbon, or sulfur-containing chemicals (Bundschuh et al., 2015; Ebinghaus et al., 1999; Ghosh et al., 2011; Lu et al., 2012; Scullion, 2006; Virkutyte et al., 2002; Wang

et al., 2012). Commonly adopted methods include activated carbon adsorption, capping, dredging, natural attenuation, and various biological processes (Nirmal Kumar et al., 2010; Wang et al., 2012; Wang et al., 2004).

The use of activated carbon is costly and the production of activated carbon is energy intensive and requires chemicals to produce (Sud et al., 2008). Capping and dredging can alter the original ecosystem and pose potential ecological risks (Babut et al., 2006). Natural attenuation processes require long times and may not be effective. Natural attenuation was recommended as the remediation approach for Hg contamination in a number of large watersheds; however, MeHg concentrations were not observed to decrease as had been anticipated leading to the implementation of more active methods of control (Livingston, 2006). The use of biochar as an alternative treatment media has the potential to lower costs associated with remediation due to the widespread availability of this material (Lehmann & Joseph, 2009). Biochar can be conveniently produced on site from agriculture waste (crop residues, manure) and other carbonaceous materials, and can potentially be applied for large-scale remediation projects in a cost-effective manner.

1.1.3 Biochar

The use of biochars has attracted great interest in environmental remediation processes, and the application of biochar as a reactive media represents an alternative which has potential for mitigating Hg contamination. Biochar is the generic name for stable, carbon-rich charcoal produced by the thermal decomposition of various widely distributed and inexpensive feedstocks (crop residues, manures, wood chips, biosolids, etc.) under low/no O₂ conditions at relatively low temperatures (<700 °C) (Fig. 1.1) (Lehmann & Joseph, 2009).

Biochars prepared from readily available and inexpensive materials have been used for inorganic Hg removal in aqueous solution (Anoop Krishnan & Anirudhan, 2002; Kadirvelu et al., 2004; Namasivayam & Kadirvelu, 1999; Rao et al., 2009; Zabihi et al., 2010). Several studies have applied biochar as an amendment to promote Hg stabilization in sediment (Bundschuh et al., 2015; Gomez-Eyles et al., 2013). These studies focused on the bioavailability of Hg and sorption of Hg and MeHg after amending sediments with biochars. Despite the advantages associated with biochar production and the potential for Hg removal, uncertainties still exist. The uncertainties include its potential to release components which may provide electron donors and acceptors for microbial growth which may stimulate the methylation process, the longevity of Hg stabilization by biochar, and the potential for biochar to facilitate Hg transport. Extremely strong bonds can form between Hg and the reduced sulfur sites in dissolved organic matter (Ravichandran, 2004). Strong complexation to S- and C-moieties can facilitate the transport of Hg from polluted soils and sediments to rivers, lakes, and groundwater (Krabbenhoft & Babiarz, 1992; Riscassi & Scanlon, 2011; Santoro et al., 2012).

The aging of biochar may affect the longevity of the Hg stabilization process. The stability of biochar in soil is related to the pyrolysis temperature, feedstocks, carbon content, fused aromatic rings, and mineral nutrient content (Singh et al., 2012), as shown in Fig. 1.2. The aging of biochar can be caused by microbial (habitation, release of enzymes), chemical (redox oscillation, ion exchange), physical (pressure, thaw freeze cycle, erosion, other forces), and combined effects (Hale et al., 2012a). When biochar ages, its elemental composition, surface functional groups, surface charge, cation exchange capacity, surface area, acid neutralization, etc. also change (Cheng et al., 2008;

Cheng et al., 2006; Hale et al., 2012a; Harvey et al., 2012; Kwon & Pignatello, 2005; Mao et al., 2012). These changes may lead to a change in Hg bonding to the particles and/or changes to the dynamics of methylation reactions.

Biochar can be applied as a reactive media as layers at the sediment/water interface in water bodies and co-blended into soil for stabilizing Hg at contaminated sites, as illustrated in Fig. 1.3. Biochar can be distributed to form a reactive cap or layer, or can be mixed with the sediment (Gomez-Eyles et al., 2013; Hadnagy et al., 2014; Kupryianchyk et al., 2015; Patmont et al., 2015). Additionally, biochar can be used as reactive media for use in permeable reactive barriers for the remediation of heavy metal contaminated groundwater (Benner et al., 1999; Blowes et al., 1997), in containerized treatment systems (Hussain et al., 2014; Robertson et al., 2009), and in constructed wetlands (Easton et al., 2015; Hussain et al., 2015). Because the density of biochar is low, encasement of the biochar may be required, for example, through the use of geotextiles to maximize its stability (Shackley et al., 2016).

1.1.4 South River Hg-Contaminated Sites

This research focuses on providing an improved understanding of the effectiveness of biochar as an amendment at a Hg contaminated site. The site was an acetate rayon fiber facility located in Waynesboro, Virginia. This facility used mercuric sulfate as a catalyst for manufacturing from 1929 to 1950 (Carter, 1977), and allowed the release of Hg both on site and to an off-site discharge pipe. At the site, Hg is converted to MeHg which has a very strong potential for bioaccumulation (Mason et al., 1995).

The total Hg (THg) and MeHg concentrations in tissues of fish from the South River exceed the USEPA criteria up to 11 times for Hg (0.3 mg kg^{-1}) and up to ten times

for MeHg (0.3 mg kg^{-1}) (Virginia Department of Environmental Quality, 2008). Average concentrations of THg in the South River water increase rapidly from background concentrations to a maximum of around 13 ng L^{-1} at 19 km downstream of the manufacturing facility and MeHg increases to 1.7 ng L^{-1} at the same location (Flanders et al., 2010). The THg contents vary greatly and range from 0.6 to $280 \text{ } \mu\text{g g}^{-1}$ for 34 analyzed samples along the length of the river (Fig. 1.4). Even along the same transect, THg contents show pronounced differences (*e.g.* 1.1 - $187 \text{ } \mu\text{g g}^{-1}$ across transect RRM3.5 (relative river mile)). Monitoring of Hg and MeHg concentrations in river water, sediments, floodplain soils, and biota in the South River watershed has continued for 37 years since the mid-1970s. Compared to the Middle River and North River, which did not receive input from the former manufacturing facility, mercury concentrations are higher in surface water, sediment, biota and floodplain soils of the South River (Rhoades et al., 2009). Population level impacts have been observed in some biota within and downstream from the South River (Bolgiano, 1980; Jackson et al., 2011).

Approaches to minimize the future exposure of organisms to Hg are now being developed. The site specific requirements for remediation are to 1) manage and reduce the risk for exposure of aquatic life to Hg in the river; 2) stabilize the Hg in the floodplain and bank soils to decrease the Hg load to the river; 3) manipulate the methylation cycle of Hg; and 4) reclaim the South River (South River Science Team, 2015).

Several studies have been conducted to evaluate different reactive media and methods for the control of Hg and MeHg in the South River site. Desrochers (2013) and Paulson (2014) conducted column experiments to evaluate Hg and MeHg control in sediments collected from different locations along the South River. Reactive treatment

columns filled with a hardwood biochar were used to treat the effluents derived from the South River sediments, resulting in >98% Hg removal from the effluents. In these treatment columns, Hg removed from the effluent accumulated within the first 2-3 cm at contents up to $7.7 \mu\text{g g}^{-1}$. The Hg uptake capacity by the hardwood biochar was not achieved in the column experiments.

Desrochers et al. (2015) and Paulson et al. (2016) introduced organic carbon sources (electron acceptor for microbes) and SO_4^{2-} (electron acceptor) to columns filled with different sediments. They hypothesized that Hg can be converted to stable forms as Hg sulfide minerals to decrease its bioavailability, but the results indicate Hg methylators were stimulated and elevated MeHg concentrations were observed in the effluent of the columns. Hogberg (2015) conducted a series of treatment column experiments using Hg-spiked water as an input solution to evaluate the Hg removal capacity of the hardwood biochar. The results indicate the Hg accumulated in the biochar at a content of $97.4 \mu\text{g g}^{-1}$ in the first 1-2 cm of the column after 609 pore volumes of flow. Fellin (2016) co-blended sediment and different reactive materials to evaluate the stabilization of Hg through saturated columns. The results indicate the application of a sulfurized biochar resulted in 83% decrease of cumulative released Hg compared with a control column.

The studies in this thesis complement the previous studies, focusing on the evaluation of a broader range of biochars for Hg removal and evaluation of long-term removal of Hg by a subset of the biochars. The research findings in this study are anticipated to benefit the selection of remedial actions to protect the ecosystem at the South River site. The findings are also anticipated to benefit remediation efforts at other Hg-contaminated sites with similar environments to the South River site. Other Hg-

contaminated sites in North America include the English–Wabigoon River system in Ontario (Takaoka et al., 2013), the St. Lawrence River in Quebec (Avramescu et al., 2011; Rukavina et al., 1990), abandoned gold mine tailings of Goldenville in Nova Scotia (Wong et al., 1999), Canada, and surface freshwater systems in California (Donovan et al., 2016; Gill & Bruland, 1990; Lowry et al., 2004), the Carson River in Nevada (Henny et al., 2002), and the Oak Ridge in Tennessee (Han et al., 2006), USA. In addition, there are a large number of documented Hg contaminated sites in areas outside of North America which may require remediation, such as the Idrija River in Slovenia (Biester et al., 2000), gold mine impacted areas of Brazil (Malm, 1998; Veiga & Hinton, 2002) and Peru (Adler Miserendino et al., 2013; Gammons et al., 2006), and several sites in Sweden (Wiederhold et al., 2014).

1.1.5 X-ray Absorption Spectroscopy

X-ray absorption spectroscopy (XAS) has been widely used as a research tool in the fields of physics, material sciences and engineering, chemistry, earth sciences, and biology. XAS can be applied to delineate spatial distributions, oxidation states, and binding environments of elements through the interaction of incident beam and inner shell electrons of the elements. XAS-related techniques applied in this study include micro-X-ray fluorescence (μ -XRF) mapping, confocal X-ray micro-fluorescence imaging (CMXFI), X-ray absorption near-edge structure (XANES) and extended X-ray absorption fine structure (EXAFS) analyses (Fig. 1.5).

Micro-XRF mapping allows the examination of the distribution of elements of interest in a particle or a small area of a particle in the form of a thin section. Micro-XRF mapping can simultaneously illustrate the spatial distribution of several elements, which

can help to define the binding environment and enriched areas of elements of interest. The principle of XRF mapping involves the measurement of characteristic emission fluorescence lines of elements (Fig. 1.6). For example, S $K_{\alpha 1}$ lines (2.307 keV) is generated due to the fill of a vacancy of an electron (1s) in the K shell with the electron ($2p_{3/2}$) in L_{III} subshell; Hg $L_{\alpha 1}$ line (9.988 keV) is generated due to the filling of a vacancy of an electron ($2p_{3/2}$) in the L shell with an electron ($3d_{5/2}$) in the M_V shell. The detected fluorescence intensity in conventional XRF mapping represents the sum of information along the path where the microbeam penetrates the sample (Vincze et al., 2004). If fine structures exist along the beam path, these fine structures cannot be captured by conventional XRF mapping.

CXMFPI can overcome this limitation by delineating the spatial distribution of elements in three dimensions (Fig. 1.7). CXMFPI is a non-destructive technique, which provides compositional and structural information from precise locations on the surface of, and within, intact particles. CXMFPI utilizes two X-ray optics, one to focus the incident X-ray beam and the second to collect X-ray fluorescence data from a specific point within the particle, to provide spatially-resolved μ -XRF analyses (Vincze et al., 2004; Woll et al., 2012). CXMFPI provides three-dimensional information on structural and composition variations within samples, including layered materials, which cannot be distinguished by traditional μ -XRF methods. CXMFPI also has been used to characterize medieval stained glass (Choudhury et al., 2015a), Se accumulations in fish eye lens (Choudhury et al., 2015b), and particles embedded on the surface and in the subsurface of a mineralogical matrix (Cordes et al., 2015). These diverse applications illustrate the

potential to utilize this emerging technique to study a wide variety of complex natural and synthetic materials.

XANES spectra can help to define the oxidation state of an element and its primary binding environment, and can be used as a fingerprint to determine the portions of each species in a mixture by fitting the measured spectra with a linear combination fitting of XANES spectra of reference materials. The principle involves the different excitation energies (binding energy, absorption edge energy) that are required to excite the inner shell electron due to different electron configurations of the outer shell (Fig. 1.5). In general, the loss of electrons in the outer shell will cause an increase in binding energy of the core level electrons, because the nucleus is less-shielded and carries a higher effective charge.

EXAFS spectra can help to define the local structural information (binding elements, coordination number, bond length, etc.) of the atom of interest by modeling the following equation (Calvin, 2013).

$$\chi(k) = S_0^2 \sum_{i=1}^n N_i \frac{f_i(k)}{kD_i^2} e^{\frac{2D_i}{\lambda(k)}} e^{-2k^2\sigma_i^2} \sin(2kD_i + \delta_i(k))$$

where: $\chi(k)$ is the EXAFS contribution from all scattering paths,

S_0^2 is the amplitude reduction factor with a value between 0.7-1 which account for the relaxation of the remaining electrons in the absorbing atom due to the missing core electron,

Σ is the sum of n scattering paths,

N_i is the degeneracy (number of atoms of the same species at the same average distance),

k is wavenumber (cm^{-1}), as $k = \frac{1}{h} \sqrt{2m_e(E - E_0)}$,

E is the energy of the incident beam (eV),

E_0 is the edge energy, which is required to remove the photoelectron from the absorbing atom,

$f_i(k)$ is a proportionality constant for i^{th} scattering path that is proportional to the possibility that the photoelectrons scatter elastically off of the atom,

D_i is half of the path length (distance from the absorbing atom to the scattering atom),

$e^{\frac{2D_i}{\lambda(k)}}$ is applied to account for the suppression of EXAFS due to inelastic scattering of the photoelectron and decay of the core hole,

$\lambda(k)$ is the mean free path, representing how far the photoelectron can travel and still participate in the EXAFS,

$e^{-2k^2\sigma_i^2}$ is applied to account for the suppression of EXAFS due to absorbing element in more than one crystallographic environment, and static and thermal disorder of the absorbing atom,

σ_i is mean square radial displacement (the variance in the half path length (D_i)),

and

$\delta_i(k)$ is applied to account for the phase shift, which is element specific.

EXAFS data involves multiple path scattering of photoelectrons due to the different scattering atoms surrounding the absorption atom (central atom). A Fourier transform can be applied to isolate and identify the multiple scattering paths in the form of peaks at a distance equal to the half path length (D_i). D_i is the distance between the absorbing atom and the scattering atom, and is equivalent to the bond length between the

two atoms. Degeneracy (N_i) can also be obtained through the modeling process and is equal to the number of the same scattering atoms at the same average distance.

The application of XAS techniques can be used to delineate the mechanisms leading to Hg removal onto reactive media and stabilization mechanisms within amended sediments, both of which are important to evaluate the bioavailability and stability of Hg after removal by reactive materials. In Hg-related studies, XAS has been applied to characterize Hg removal mechanisms onto reactive media (Gibson et al., 2011); Hg speciation and spatial distribution in contaminated sediments (Gibson et al., 2015), Hg speciation on suspended particles (Gu et al., 2014) and soil organic matter (Skylberg et al., 2006), and formation of nanocolloidal Hg sulfide in sulfide-containing systems (Gerbig et al., 2011). XAS has also been applied to characterize S speciation which plays important roles in Hg speciation, *e.g.*, complexation of Hg with reduced S groups in soil organic matter (Skylberg et al., 2006; Skylberg et al., 2000) and Hg adsorption by S impregnated activated carbon fibers (Hsi et al., 2001).

1.2 Research Objectives

The primary objective of this research is to evaluate the effectiveness of biochar as a solid-phase amendment to promote Hg stabilization at a contaminated industrial site located in Waynesboro, Virginia. At this site, Hg is distributed in river sediment, bank, pond sediments and floodplain soils and poses a threat to ecosystem health. Management steps are required to mitigate the release of Hg. The overall goal is to limit Hg availability and to decrease MeHg production, and therefore the potential for MeHg bioaccumulation.

The research consists of a series of laboratory studies designed to contribute towards this goal, each addressing a knowledge gap surrounding Hg stabilization and MeHg reduction. Specific objectives of this research include:

- 1) Evaluation of the potential for release of organic acids, DOC, inorganic carbon, and nutrients from 36 biochars produced from various feedstocks and pyrolyzed at different temperatures.
- 2) Examination of the efficiency and mechanisms of Hg removal from aqueous solution by the 36 distinct biochar samples.
- 3) Investigation of Hg and MeHg uptake and Hg species distribution by confocal X-ray fluorescence imaging after amending sediment with low-T and high-T switchgrass biochars.
- 4) Investigation of geochemical and microbiological controls on THg and MeHg evolution after amending contaminated sediment with biochars.
- 5) Investigation of the final Hg speciation and distribution in biochar particles from microcosm experiments containing sediment amended with biochars.
- 6) Examination of the efficiency and mechanisms of Hg removal from aqueous solution using sulfurized biochar samples.

1.3 Thesis Organization

This thesis is presented as an introduction (Chapter 1), followed by a series of six research chapters (Chapters 2-7) to address the objectives outlined in the previous section, and a conclusion (Chapter 8). The first two research chapters describe batch-style experiments designed to evaluate the potential for biochar samples to remove Hg from aqueous solution. The first research paper, which is presented as Chapter 2, describes the release of organic acids, DOC, and inorganic carbon, from 36 biochars and

two sources of activated carbon, which may be utilized by microbes for carbon and energy sources for Hg methylation. Chapter 3 presents Hg removal efficiencies using the 38 reactive media, and removal mechanisms characterized by synchrotron-based techniques, including Hg and S XANES, Hg EXAFS modeling, and μ -XRF maps.

A subset of the 36 biochars were selected for detailed study to evaluate the long-term stabilization of Hg and formation of MeHg through the use of anaerobic microcosm experiments. The subset of biochars included activated carbon and four biochar samples identified in Chapters 2 and 3 for their effective removal of Hg and also because they were observed to release a wide range of concentrations of organic acids, DOC, and sulfate. The following three chapters (Chapters 4-6) focus on different aspects of these anaerobic microcosm experiments. Chapter 4 presents the control of Hg and MeHg aqueous concentrations and solid phase Hg distribution after amending the sediment with low-T and high-T switchgrass biochars only. The synchrotron-based techniques used in Chapter 4 include Hg XANES and EXAFS modeling, μ -XRF maps, and CXMFI. Chapter 5 presents the evolution of biogeochemical reactions and changes in aqueous THg and MeHg concentrations in response to the addition of a broader selection of biochars, including activated carbon, hardwood biochar, low-T and high-T switchgrass biochars, and high-T manure biochar. Chapter 6 presents results showing the detailed characterization of Hg speciation and distribution in the biochar particles described in Chapter 5. In Chapter 6, the suite of XAS techniques described in Chapter 3 was applied to characterize the mechanisms controlling Hg binding to the biochar particles.

Chapter 7 presents the results of Hg removal using these sulfurized biochars and mechanisms of removal were evaluated using synchrotron-based techniques, including Hg and S XANES, Hg EXAFS modeling, μ -XRF maps, and CXMFI. Chapter 8 summarizes the results of the research chapters and provides recommendations for field applications and future research. Finally, the release of nutrients and other elements from biochars and implications of these constituents on applications for Hg removal are discussed in Appendix G.

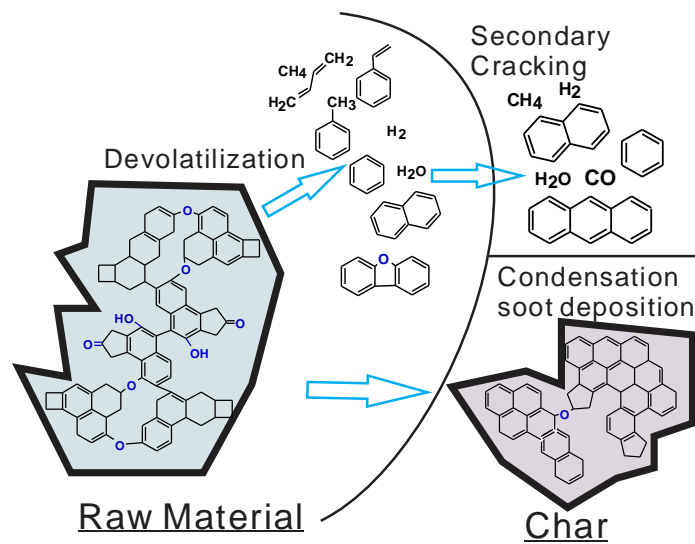


Figure 1.1 Schematic illustration of the structural transformations in biochar production during pyrolysis. The transformations involve char forming, devolatilization, secondary cracking, condensation, and soot deposition. Modified from Bandosz (2006)

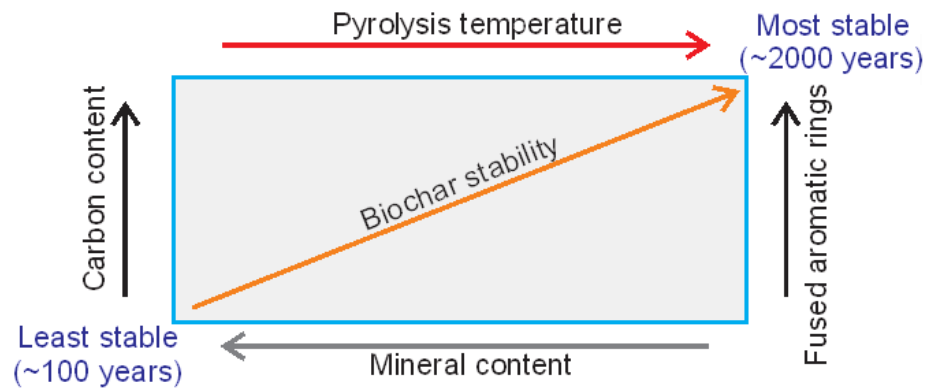


Figure 1.2 Biochar stability with regard to pyrolysis temperature, carbon content, fused aromatic rings, and mineral content (after Singh et al. (2012))

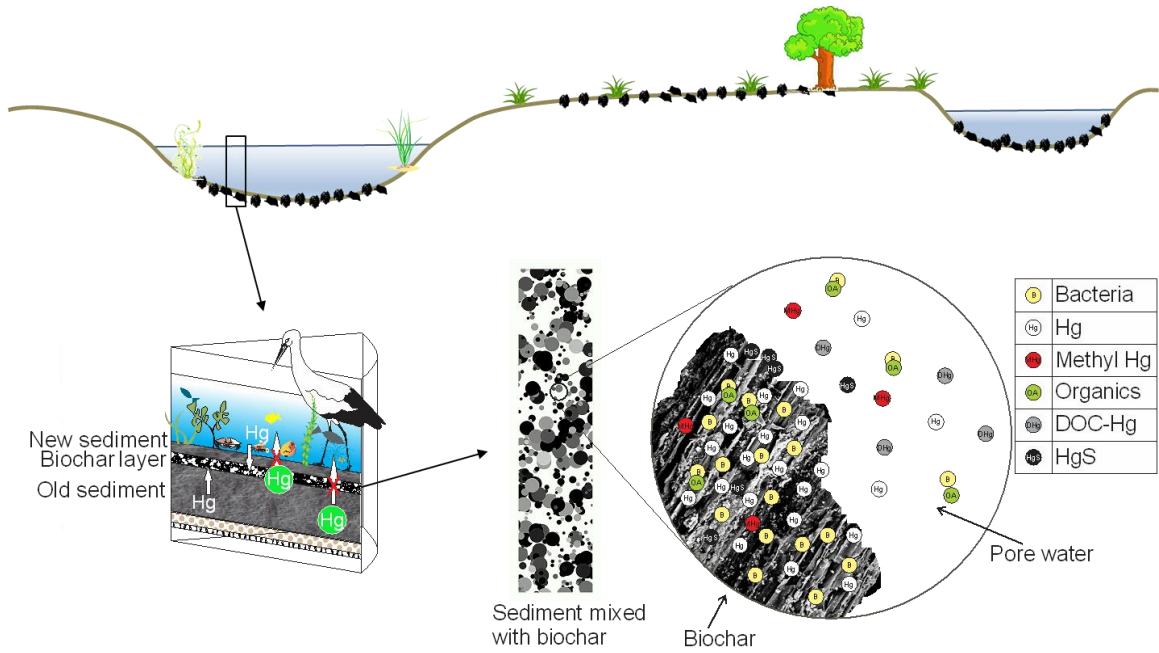


Figure 1.3 Conceptual diagram of biochar application in river/pond and floodplain soil. The bottom part indicates a proposed Hg stabilization process.

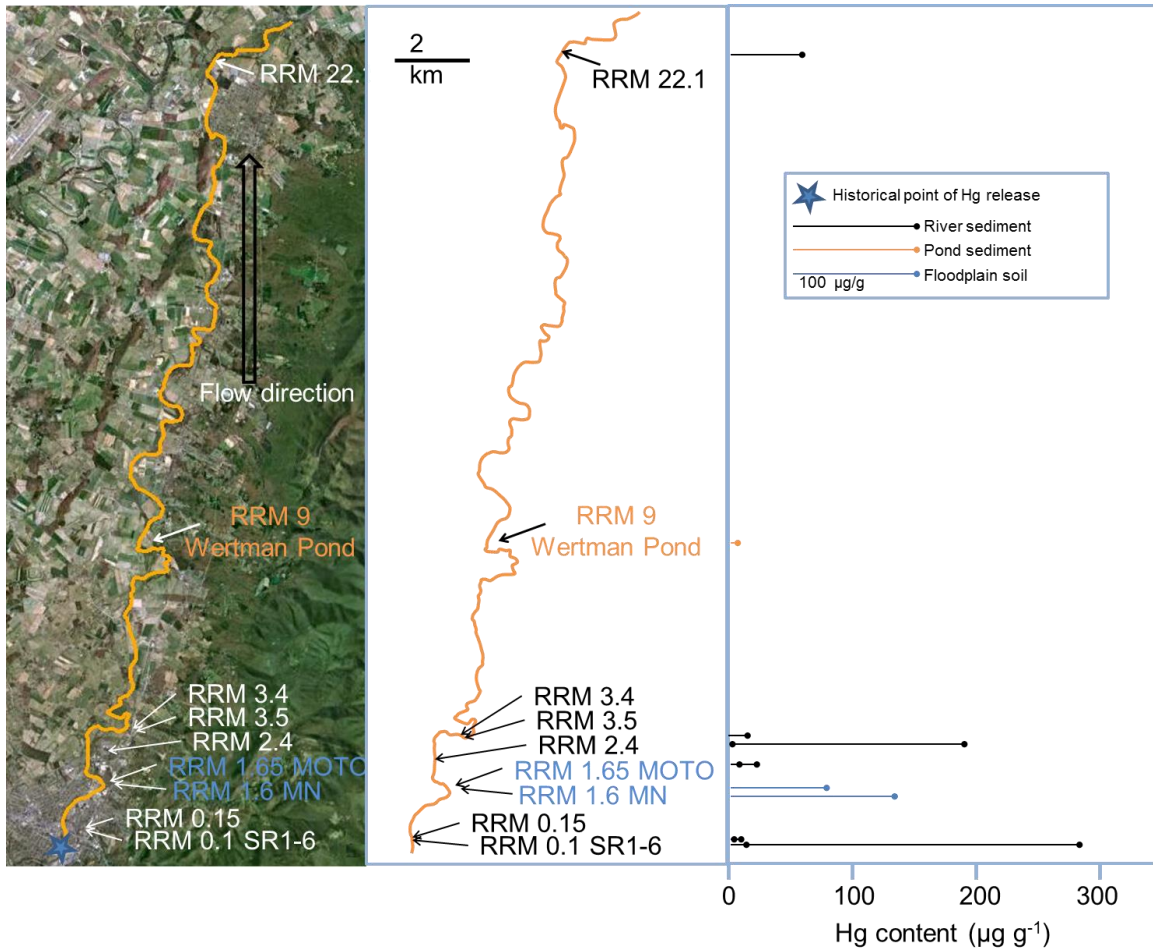


Figure 1.4 Total Hg contents of 34 samples along the South River, Virginia including river sediment, floodplain soil, and pond sediment. RRM represents relative river mile; numbers after RRM represents miles from the historical point of Hg release (star). Multi samples were collected for transactions of RRM0.1, RRM0.15, RRM2.4, RRM3.4, and RRM3.5.

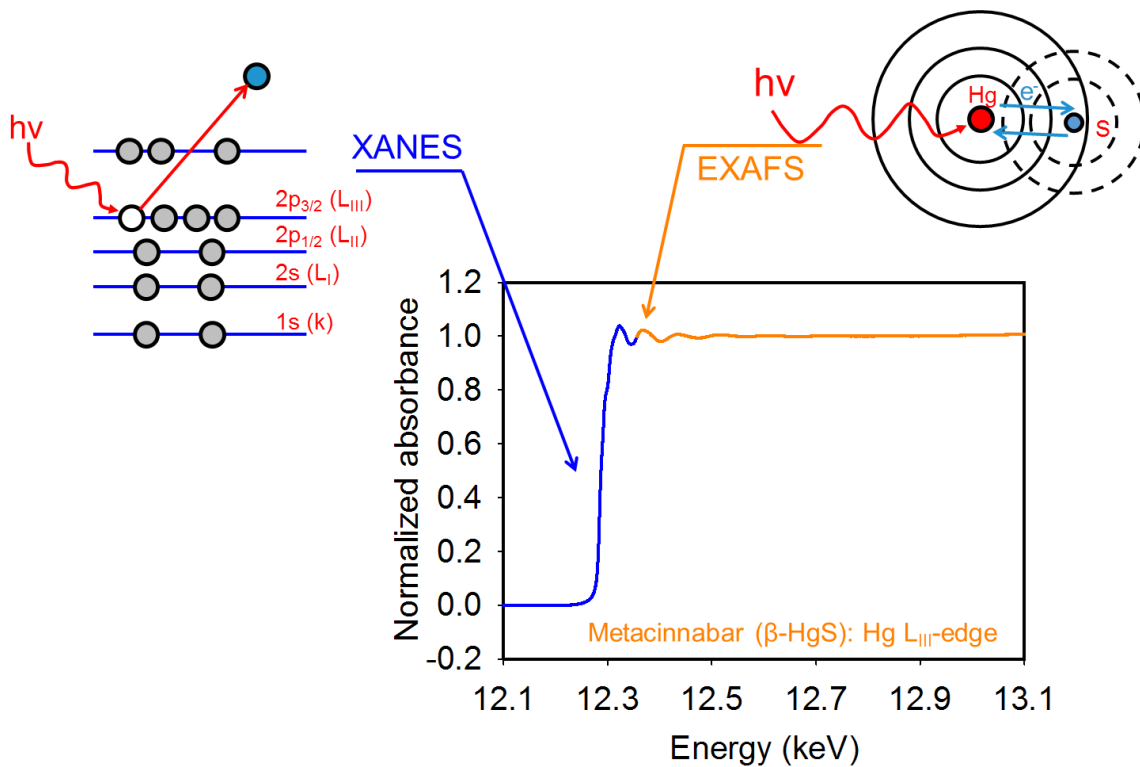


Figure 1.5 Principle of X-ray absorption near edge structure (XANES) and extended X-ray absorption fine structure (EXAFS) spectroscopy indicated by Hg L_{III} -edge of metacinnabar

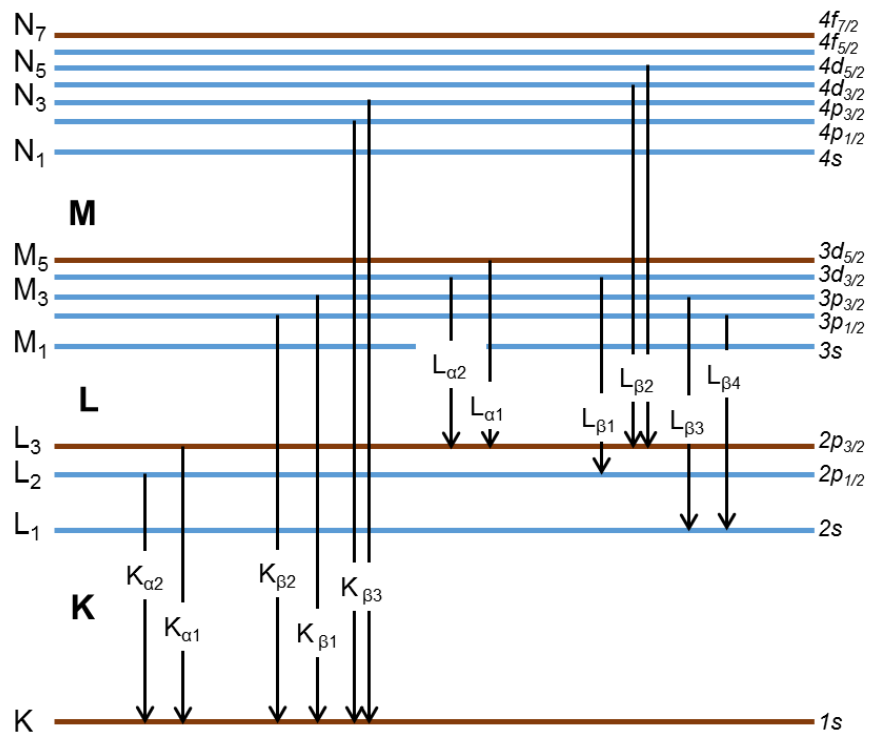


Figure 1.6 Lines for electron binding energy, X-ray emission lines, and electron configuration of elements. Bold K, L, and M are electron shell notation. The letter and number on the left side (e.g. K, L₁, L₂) are lines for electron binding energies. The letter, Greek symbol, and number with arrows are X-ray emission lines. The numbers, letters, and fractions are electron configuration.

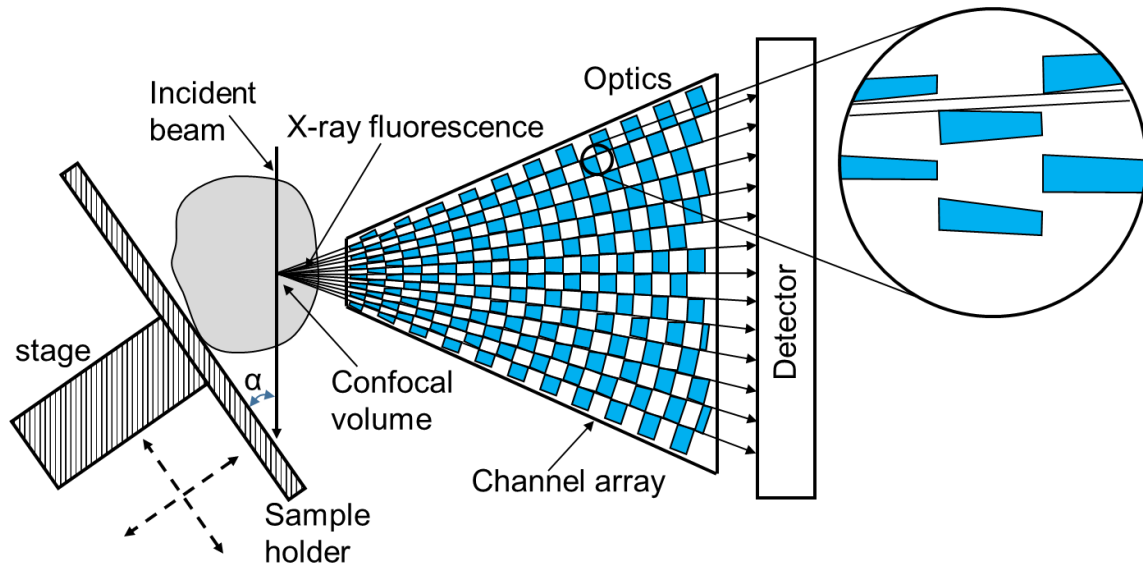


Figure 1.7 Setup of confocal X-ray micro-fluorescence imaging and schematic illustration of the optics using collimating channels. The channels are formed from a set of staggered, absorbing pillars. The inset on the left side illustrates that the pillars absorb photons by tapering away its edges from the axis of each channel. The α (35°) represents the angle between the sample holder and incident beam. The dashed lines with arrow at both ends represents the stage moving direction. Modified from Woll et al. (2014)

Chapter 2: *Aqueous Leaching of Organic Acids and Dissolved Organic Carbon from Various Biochars Prepared at Different Temperatures*

Reproduced with permission from: Liu, P., Ptacek, C.J., Blowes, D.W., Berti, W.R., Landis, R.C., 2015. Aqueous leaching of organic acids and dissolved organic carbon from various biochars prepared at different temperatures. *J. Environ. Qual.* 44(2), 684-695. Copyright ©2015 by the American Society of Agronomy, Crop Science Society of America, and Soil Science Society of America, Inc., License Number 3691450520614. Editorial and formatting changes have been made to accommodate reproduction in this thesis.

2.1 Executive Summary

Biochar has been utilized as a soil amendment, a water treatment material, and for carbon (C) sequestration. Thirty-six biochars, produced from wood, agricultural residue, and manure feedstocks at different temperatures, were evaluated for the aqueous leaching of different forms of soluble C. The release of inorganic C (alkalinity), organic acids (OAs) and dissolved organic C (DOC) was highly variable and dependent on the feedstock and pyrolysis temperature. The pH and alkalinity increased for the majority of samples. Higher pH values were associated with high-T (600 and 700 °C) biochars. Statistically significant differences in alkalinity were not observed between low-T (300 °C) and high-T biochars, whereas alkalinity released from wood-based biochar was significantly lower than from others. Concentrations of OAs and DOC released from low-T biochars were greater than from high-T biochars. The C in the OAs represented 1-60% of the DOC released, indicating the presence of other DOC forms. The C released as DOC represented up to 3% (majority <0.1%) of the total C in the biochar. SEM/EDX examination showed the high-T biochars had a greater proportion of micro-pores. FT-IR spectroscopy showed that hydroxyl, aliphatic, and quinone were the predominant functional groups of all biochars, and that the abundance of other functional groups was dependent on the feedstock. The release of DOC, especially bio-available forms such as OAs, may promote growth of organisms and heavy metal complexation, and diminish the potential effectiveness of various biochars for C sequestration.

2.2 Introduction

Biochars, or waste organic matter pyrolyzed under low oxygen and low temperature (<700 °C) conditions, are attracting substantial interest globally for possible use in a broad range of applications (Lehmann & Joseph, 2009). Biochar can be produced from

many types of carbonaceous materials, such as plants, grasses, municipal sludge, agricultural residue, manures, food waste, paper mill waste, rubber, and many others (Cantrell et al., 2012; Hale et al., 2012b; Lehmann & Joseph, 2009; Shen et al., 2012) to reduce organic waste or for biofuel production. The resulting biochars can be used as soil amendments to improve soil quality and increase crop yields by improving water retention and nutrient availability (Akhtar et al., 2014; Jeffery et al., 2011), and as adsorbents to stabilize organic and inorganic pollutants (Beesley et al., 2010; Shen et al., 2012) and bacteria as *E. coli* (Mohanty et al., 2014). However, in some cases, the application of biochars to soil may fail to increase crop yields under common agricultural practices (Borchard et al., 2014a).

The relatively stable form of C in biochar results in resistance to oxidation reactions and therefore formation of CO₂, potentially lessening the release of CO₂ to the atmosphere (Lehmann, 2007b; Lehmann & Joseph, 2009; Spokas et al., 2012). The stability of biochar and its benefits during different applications depend on the properties of the biochars, including the forms of solid-phase C and other chemical and physical properties. Studies on the forms of C in biochars are limited to a small number of biochars with minimal attention focused on the release of alkalinity, short-chain organic acids (OA) and dissolved organic C (DOC), which are important properties controlling the biogeochemical cycling of C (Anderson et al., 2011; Riedel et al., 2014), the transport of pollutants (Ngueleu et al., 2014), and the potential use for biochar in C sequestration (Jones et al., 2011). For example, soluble charcoal represents approximately 10% of the global riverine flux of DOC (Jaffé et al., 2013). Some biochars can release a sizable portion of CO₂ (e.g., 3-12% of the C in biochar during 115 days; Bruun et al. (2011))

during incubation studies. A portion (~ 1%) of black C applied to soils can be mobilized by percolating water as DOC (Major et al., 2010). The fractions of water-extractable organic C in biochars prepared from *Acacia saligna* (Labill.) H.L.Wendl. (Coojong), sawdust containing mostly *Eucalyptus pilularis* Sm. (blackbutt wood), and *Eucalyptus marginata* Donn ex Sm. (Jarrah) are dependent on feedstock types and pyrolysis temperatures (Lin et al., 2012).

Thermally desorbable organic compounds were detected in biochars produced from wood at 550 °C (Borchard et al., 2014b). UV-visible absorption and excitation-emission matrix (EEM) fluorescence spectroscopy have been used to characterize humic- and protein-like components in biochar-derived DOC (Jamieson et al., 2014). Parallel factor analysis (PARAFAC) modeling of EEM spectra indicates that the labile DOC released from biochars pyrolyzed at 350-500 °C includes (poly)phenolic pyrolysis products, water-soluble aromatic structures similar to fulvic- and humic-like soil organic matter, carboxyl and other transient thermochemical conversion intermediates, and a thermally stable DOC fraction (Uchimiya et al., 2013). Finally, Hale et al. (2012b) indicated that the mass of bioavailable polycyclic aromatic hydrocarbons (0.17 to 10.0 ng g⁻¹) and dioxins (<92 pg g⁻¹) present in biochars is dependent on the type of feedstock used in their preparation.

Characterization of a wide range of biochar types produced under comparable conditions is needed to evaluate their potential for release of inorganic and organic C. The study described here provides information on the potential release of inorganic and organic C from various biochars produced from different feedstocks and pyrolyzed at different temperatures. The results facilitate the future application of biochar for different

purposes based on their properties, *e.g.*, potential release of high concentrations of DOC. Some biochars may need to be washed before use as an amendment to soils containing elevated concentrations of heavy metals, because of the potential to enhance the transport of these metals by the leached DOC (Ngueleu et al., 2014). If C sequestration is the primary objective of a biochar application, then a biochar with a low potential to leach inorganic and organic C would be preferred.

The objectives of this study were to (1) characterize the solid-phase C content of biochars prepared from a variety of feedstocks and produced at different temperatures, (2) examine their potential to release alkalinity, OAs and DOC through aqueous leaching studies, and (3) evaluate the implications of their use in different applications in the environment. Solid-phase characterization and leaching studies were conducted on a total of 36 biochar samples derived from three major groups of feedstock materials.

2.3 Materials and Methods

2.3.1 Preparation of Biochar Source Materials

The application of biochars is proposed within the watershed of South River near Waynesboro, VA, USA. The feedstocks used in this study were selected based on their availability from local and other sources. River water was used in the experiments as an aqueous leaching media because areas where biochar may be applied are susceptible to flooding. Cocoa and cotton husks, corn cobs and stover, grasses, pine mulch and bark, poultry manures, cattle manure, and mushroom soils obtained from different suppliers were dried at room temperature and cut into small pieces (<10 cm). The kiln was preheated to either 300 °C (low T) or 600 °C (high T) and the feedstocks were pyrolyzed for 2-3 h at temperature under a limited O₂ supply. The resulting biochars were allowed to cool at room temperature overnight. Three commercial charcoals (rejects of product)

pyrolyzed at approximately 700 °C were purchased from Wicked Good Charcoal Co. (CL1), US, Cowboy Charcoal Co. (CL2), US, and Biochar Engineering Corp. (CL5), US. Two batches of activated carbon (Sigma-Aldrich Corp., St. Louis, US) were used as a benchmark because it is widely available and frequently studied. The biochars were grouped into three categories, agricultural residue (Cocoa and cotton husks, corn cobs and stover, three types of grasses); manure (poultry manures, mushroom soils derived from poultry manure and cattle manure); and wood (pine mulch and bark and charcoal). All biochar samples were ground in the same manner and sieved (<2 mm) prior to further study.

2.3.2 Characterization of Solid-Phase Biochar

The total C content was measured using a resistance furnace in an Eltra CS-2000 Infrared C/S Apparatus (ELTRA GmbH, Germany). Samples were oven-dried at 105 °C for 24 h before analysis. Standard materials used for instrument calibration included coal, graphite, and sucrose (Alpha Canada Inc., Canada). The total C analyses for the standard materials and samples were determined three times and if the three measurements deviated by >5%, a fourth measurement was conducted.

Surface functional groups were characterized using Fourier transform infrared spectroscopy (FT-IR). Samples were first dried for 24 h at 105 °C. Samples were then ground and mixed with dried KBr (Fisher Scientific Co., US) at a ratio of 1:100 in an agate mortar. The mixture was prepared in the form of thin discs (~1 mm) under 34-41 kPa (5-6 psi) using a hydraulic press (Chemplex Industries Inc., US). Spectra were recorded at a resolution of 4 cm⁻¹ from 500 to 4000 cm⁻¹ with 20 scans per sample using a Tensor 27 FT-IR spectrometer (Bruker Optics Inc., Germany).

Surface investigations were performed using a field emission scanning electron microscope (FE-SEM) (LEO 1530, LEO, Germany) equipped with an energy dispersive X-ray (EDX) detector (EDAX Pegasus 1200, EDAX Inc., US). Samples were mounted on aluminium stubs with conductive carbon tape, and coated with gold to maintain conductivity. A beam energy of 20 kV was employed to obtain backscatter electron imaging and semi-quantitative energy dispersive spectroscopy (EDS) data.

2.3.3 Release of Alkalinity, OAs and DOC from Biochar to Aqueous Solutions

Batch-style experiments were conducted to evaluate the potential for release of alkalinity, OAs and DOC from the different biochar samples through single step and multi-step release experiments.

2.3.3.1 Single-Step Release Experiments

Biochars were added at a 1:75 mass ratio to river water that had concentrations of OAs and DOC below analytical detection limits (0.01 and 0.5 mg L⁻¹ or 0.0003 and 0.04 as C mmol L⁻¹, respectively). The chemical composition of the river water is presented in Table 2.1, including pH, alkalinity, ionic strength, DOC, OAs, anions, and major cations. Ionic strength (I) is calculated using equation $I=0.5*\sum C_iZ_i^2$, where C_i is the molar concentration of i^{th} ion in solution and Z_i is its valence. Concentrations of anions were determined on unacidified samples using ion-chromatography (Dionex DX-600, Dionex Corp., Sunnyvale, USA) with an IonPac AS9-HC 4x250 mm column guarded by an AG9-HC 4x50 mm column. Concentrations of cations were determined by inductively-coupled plasma atomic emission spectroscopy (Thermo Scientific iCAP 6000, Waltham, USA).

The water and biochar were mixed thoroughly, then allowed to settle and equilibrate at room temperature (25 ± 2 °C) for 2 d. After equilibration, the mixtures were gently shaken and sampled for chemical analyses. Water samples were collected in Norm-Ject[®] syringes (Henke Sass Wolf, Germany) and passed through 0.45 µm filters (Acrodisc[®] hydrophilic polyethersulfone syringe filters; Pall Corp., UK). The first 5 mL was discarded and the remaining solution was collected for alkalinity, OAs and DOC analysis. This procedure yielded undetectable leaching of alkalinity, OAs and DOC into ultra-pure water. Duplicate mixtures of the river water and high-T biochars were equilibrated in the same manner and sampled for pH and alkalinity.

At the termination of the experiments, unfiltered water samples were collected and analyzed for pH. The pH electrode (Thermo Orion, Beverly, US) was calibrated with pH 7 and pH 4 standards buffers, and checked against pH 10 standard buffer. Alkalinity was determined in duplicate by titration of filtered samples using a HACH digital titrator, bromocresol green indicator, and 0.16 N H₂SO₄ and mean values were reported.

Concentrations of OAs were determined on unacidified samples using ion chromatography (Dionex DX-600, Dionex Corp., US) with an IonPac AS11 4×250 mm column guarded by IonPac AG17 4×50 mm (Morales et al., 1998). The analytical procedure is capable of separating more than 20 common organic acids, however standards were only prepared for lactate, acetate, propionate, and formate. The flow rate was 1 mL min⁻¹ using potassium hydroxide (EluGen Cartridge, EGCII KOH) as the eluent. The mobile phase was operated in gradient mode as 0.5 to 1 mM from 0 to 4 min, 1 to 15 mM from 4 to 8 min, 15 to 40 mM from 8 to 15 min, 40 mM from 15 to 16 min, and 40 to 0.5 mM from 16 to 17 min. The detector was a CD25 Conductivity Detector

using suppressed conductivity mode. The samples were analyzed in duplicate using different dilution factors. The standard curve was calibrated with five points for each OA at concentrations ranging from 0.05 to 5 mg L⁻¹; correlation coefficients (R²) were >99.9% for each standard curve.

The DOC was determined on samples acidified with ultra-pure H₂SO₄ to pH <2 using an automated TOC analyzer (Aurora 1030W, OI Analytical, US) following EPA Method 415.3. The QA/QC steps included ultra-pure water blanks (<0.2 mg L⁻¹), laboratory duplicates (0-20% relative standard deviation, most <5%), standards check every 10-15 samples (80-120% recovery, most 98-102%), and two matrix spikes per run (80-120% recovery, most 98-102%). Each sample was analyzed three times and the mean values were reported.

2.3.3.2 Multi-Step Release Experiments

Seven biochars were selected from the three categories (agricultural residue, manure, and wood) for multi-step release experiments. The biochars were CL2 and low-T and high-T biochars derived from switchgrass, poultry manure and mushroom soil. Activated carbon was used as a benchmark. CL2 and activated carbon from the wood-based biochar group represented high C content and potential for release of low concentrations of OAs and DOC. The switchgrass biochars from the agricultural residue-based biochar group represented the low and high-T biochar and potential for release of intermediate concentrations of OAs and DOC. The poultry manure and mushroom soil biochars from the manure-based biochar group represented low and high-T biochars and potential for release of high concentrations of OAs and DOC.

The biochars and activated carbon were mixed with ultra-pure water (Millipore Milli-Q purification system, Millipore, Billerica, US) at a 1:10 mass ratio (15 g : 150 mL), following the same procedure as the single-step release experiments, except that the mixtures were filtered using pre-washed 0.45 filters after 2 hours. The aqueous samples were analyzed for OAs and DOC using the above methods. The solid phase was mixed with ultra-pure water again and then filtered after 2 hours. The process was repeated for 6 or 12 steps. After the 4th step, the solid phase was left on the filter for 10 hours and then the solid phase was mixed with ultra-pure water again for the remaining steps.

2.3.4 Statistical Analysis

To identify statistically significant impacts of feedstock type and pyrolysis temperature on pH values and concentrations of alkalinity, OAs, and DOC in aqueous solution after mixing with biochars, data were analyzed using a two-way ANOVA procedure for independent samples using Microsoft Excel. If significant differences were observed among factors, as indicated by the F-ratio, the post hoc testing using Tukey's HSD (honestly significant difference) test was performed to determine which pairwise interactions were significantly different at $P < 0.05$.

The correlation between alkalinity, OAs, and DOC with the FT-IR functional groups was evaluated by Pearson product-moment correlation coefficients (r). The significance of a correlation, r , was tested using a t-test with a 95% confidence level ($P < 0.05$).

2.4 Results and Discussion

2.4.1 Total C Contents in Biochar

The charcoal and activated carbon samples had the highest C contents, ranging from 76.6-99.9%; the manure biochars had the lowest C contents, ranging from 22.8-63.5%

(Table 2.2). The other biochars had C contents ranging from 63.6-99.7%; these data are consistent with published values for non-herbaceous biochars (Dumroese et al., 2011; Lin et al., 2012).

The measured solid-phase C contents were dependent on both pyrolysis temperatures and feedstock types ($P < 0.05$). Specifically, the C contents of the high-T biochars were greater than for the low-T biochars ($P < 0.05$), consistent with findings reported by Gaskin et al. (2008). As pyrolysis temperature increases, light elements (e.g., hydrogen) are released, leading to enrichment of C (Bandosz, 2006). The feedstock also was an important factor influencing the C content ($P < 0.05$). Statistically significant differences of C contents were observed between agricultural residue-based and manure-based biochars ($P < 0.05$). For example, the manure had a greater mass of minerals than other feedstocks (see §3.5), resulting in a relative decrease in C content.

2.4.2 One-Time Release of Short-Chain OAs and DOC

The concentrations of OAs observed in the aqueous solutions equilibrated with the biochar samples decreased following the general order: acetate > formate > propionate > lactate (Fig. 2.1 a, b). No other organic acids were observed during IC analysis, therefore these other organic acids were not quantified. Concentrations of OAs varied as a function of feedstock and pyrolysis temperature. The highest concentrations of formate, acetate, and propionate were observed in the batch mixture containing high-T cocoa husk biochar (0.4, 3.8, and 0.94 as C mmol L⁻¹). Relatively high concentrations of all four OAs were observed in the batch mixtures containing low-T agricultural-residue and manure biochars, while lower concentrations were observed in the samples containing wood-based biochars ($P < 0.05$). Low

concentrations of OAs were leached from charcoal and activated carbon. Large differences in the concentrations of OAs were observed between low-T and high-T biochars ($P < 0.05$). Concentrations of acetate, lactate, and propionate released by most high-T biochars were below the analytical detection limit (0.01 mg L^{-1} or $0.0003 \text{ as C mmol L}^{-1}$); formate concentrations of high-T biochars were also far lower than for low-T biochars, with the exception of cocoa husk biochars. This temperature dependence of OA release is consistent with the greater release observed for low-T sawdust biochars relative to high-T biochars (Lin et al., 2012). No statistically significant differences of OA concentrations were observed among the three categories (wood-based, agricultural residue-based and manure-based) and from the interaction of pyrolysis temperatures and different groups ($P < 0.05$).

The DOC concentrations in the batch equilibration solutions showed the same trend as the OA concentrations (Fig. 2.1 a, b). The DOC concentrations ranged from less than the analytical detection limit (0.5 mg L^{-1} or $0.04 \text{ as C mmol L}^{-1}$) for hop, poultry manure, and mushroom soil biochars prepared at $600 \text{ }^\circ\text{C}$ to a high value of $12.4 \text{ as C mmol L}^{-1}$ for corn stover biochar prepared at $300 \text{ }^\circ\text{C}$. Cocoa husk biochars pyrolyzed at both high and low T had the highest mean DOC concentrations and wood biochars had the lowest. Statistically significant differences were observed in the DOC concentrations between the low-T and high-T biochars, whereas differences among wood-based, agricultural residue-based and manure-based biochars were not statistically significant ($P < 0.05$). Differences for the DOC concentrations were not statistically significant from the interaction of pyrolysis temperature and feedstock types ($P < 0.05$). In general, higher pyrolysis temperatures resulted in lower DOC concentrations ($P < 0.05$). These

observations are in keeping with Mukherjee and Zimmerman (2013), who noted higher concentrations of DOC were released by oak and grass biochars produced at 250 °C compared to those produced at 650 °C.

The C in the OAs accounted for 1-60 % of the C in the DOC, with the exception of the high-T wood-based biochars (Fig. 2.1 c, d). Although OAs released by biochars prepared at high T accounted for a lower percentage of DOC than those prepared at low T, no other clear patterns are discernible among different biochar groups. This observation is in contrast to previous observations that indicate the percentage of the low molecular weight OA component of TOC increases at higher temperatures (Lin et al., 2012). Specifically, DOC released from biochars may include biopolymers, humic substances, building blocks (oxidation or breakdown products of humic substances), low molecular weight neutral compounds, and low molecular weight acids (Huber et al., 2011; Lin et al., 2012). Hundreds of compounds with molecular masses >150 Da are released from biochar amended soil, and many of which are likely phenolics and polycyclic aromatics (Riedel et al., 2014). Lin et al. (2012) also found that while the concentrations of low molecular weight acids decrease as pyrolysis temperature increases, the percent of the C in DOC that is OAs increases from 3.2 % to 41.9% as a result of a much greater decrease in DOC concentration. Other low molecular weight OAs not evaluated in this study, such as phenolic acids, may also be released.

The lower proportions of OAs released by wood-based biochars compared to the other biochars may be due to the composition of these feedstocks. Wood-based feedstocks have higher percentages of lignin, while other feedstocks have higher percentages of hemicellulose and cellulose (Tiwari & Mishra, 2011). The decomposition

of hemicellulose occurs around 220 °C; cellulose decomposes between 315 and 400 °C; and lignin is difficult to pyrolyze (from 160 to 900 °C) (Yang et al., 2007). The products of polysaccharide decomposition include low molecular weight sugar derivatives; however, as pyrolysis temperature increases the products that are formed earlier may undergo further rearrangement through decomposition, condensation, cyclization, and polymerization in a series of consecutive reactions (secondary reactions) (Shafizadeh, 1985), leading to the formation of new compounds. The lower concentrations of OAs and DOC for the higher T biochars observed in this study may be due to similar secondary reactions.

The short chain OAs and the other labile fractions in DOC can be utilized by microbes as carbon and energy sources (Lehmann et al., 2011). The biochar may be further decomposed by microbes. For example, Kuzyakov et al. (2009) observed a strong increase in black carbon decomposition rates after adding glucose into a mixture of soil and black carbon during incubation.

2.4.3 pH and Alkalinity in One-Time Release Experiments

The measured pH values were observed to increase for the majority of the batch mixtures compared with that of the river water (Table 2.1 and Fig. 2.2), with the exception of the batch mixtures of low-T mulch, pine bark, and poultry manure biochars (Fig. 2.2). The greatest increase in pH was observed for water equilibrated with mushroom soil-based biochar produced at 600 °C with a value of 11.0. Generally, the pH values of water in contact with manure and mushroom soil biochars increased the greatest, whereas the pH value of water in contact with wood-based biochars increased the least, which is

consistent with other studies on oak wood and poultry litter biochars (Lehmann et al., 2011).

No clear patterns were observed among different biochar groups, but a large difference was observed between the high-T and low-T biochar samples ($P < 0.05$). The pH values increased from as low as 7.11 to as high as 11.0 as pyrolysis temperature increased from 300 °C to 600 °C.

This increase in pH is consistent with previous studies on oak wood, corn stover, poultry litter, dairy manure, canola straw, soybean straw, and peanut straw biochars (Cao & Harris, 2010; Lehmann et al., 2011; Yuan et al., 2011). Biochars typically have amphoteric surfaces, with both acidic and basic functional groups (Bandosz, 2006). The acidic groups include carboxyl, hydroxyl and phenolic groups. The basic groups include pyrone-like and chromene-like groups, and the delocalized π -electrons of the basal planes (Bandosz, 2006). The pH values observed in this study indicate that the majority of the biochars released more base than acid. The increase of pH is also likely related to the dissolution of oxides, including CaO, K₂O, MgO, and Na₂O generated during the pyrolysis process (Brewer et al., 2009; Rafiq et al., 2016). As the pyrolysis temperature increased, biochars convert to more graphite-like structures with more basal planes (Bandosz, 2006), which may cause the pH to increase.

The alkalinity values in water in contact with the biochar ranged from 44.5 (hop 300 °C) to 462 (cocoa husk 300 °C) mg L⁻¹ as CaCO₃ (Fig. 2.2). The alkalinity increased as the pyrolysis temperature increased for husk, corn, and grass group biochars, while the alkalinity decreased as the pyrolysis temperature increased for wood, manure, and mushroom soil biochars. The measured pH values of the aqueous solutions in contact

with the biochars ranged from 7.11 to 11, therefore the dominant carbonate species in this pH range is the bicarbonate ion. The pH and alkalinity of the river water were 7.8 and 46 mg L⁻¹ as CaCO₃ (Table 2.1). It is likely that both the pH and alkalinity were buffered during the experiments by the initial composition of the river water. Statistically significant differences of alkalinities were not observed between low-T and high-T biochars, whereas significant differences were observed among the three groups ($P < 0.05$). The alkalinities of wood-based biochar were significantly lower than those of agricultural residue-based and manure-based biochars ($P < 0.05$).

The released alkalinity accounted for 0.1-1.7 % and 0.1-1.3 % of the initial solid-phase C for the low-T and high-T biochars. This leached inorganic C can contribute to the abiotic loss of CO₂ from biochar amended in soil (especially in acidic soil). Previous investigations showed that the CO₂ emitted from soil amended with biochar is partly derived from the inorganic C component of biochar (Jones et al., 2011).

2.4.4 Continuous Release of OAs and DOC

During the continuous leaching experiment, an instantaneous release of DOC and OAs and a secondary slower release were observed (Fig. 2.3). Elevated concentrations of acetate and formate were released from CL2 and low-T biochars, which decreased exponentially with repeated washing steps. Concentrations of acetate and formate released by CL2 and low-T biochars in the first leaching step ranged from 0.34 to 12 and 0.01 to 0.67 as C mmol L⁻¹; for the third leaching step, the concentrations of acetate and formate ranged from 0.03 to 0.34 and 0.002 to 0.03 as C mmol L⁻¹. After 12 leaching steps, the concentrations of acetate and formate released by low-T poultry manure and mushroom soil biochars were below analytical detection limits. The initial release of

acetate was greater than formate (approximately ten times higher). On average, the concentrations of acetate and formate released from low-T mushroom soil biochar were approximately ten times higher than the amount released from the high-T switchgrass and poultry manure biochars. The concentrations of acetate and formate released by activated carbon and high-T biochars were below analytical detection limits, with the exception of CL2.

The concentrations of DOC showed the same trends as observed for acetate and formate. Elevated concentrations of DOC were released from CL2 and low-T biochars. The concentrations decreased with repeated washing steps, with the exception that DOC leached by low-T poultry manure biochar decreased more slowly than the OAs. The DOC concentrations leached by low-T biochars prepared from switchgrass, poultry manure and mushroom soil were 2.1, 15 and 17 as C mmol L⁻¹ in the first washing step. The DOC concentrations of high-T biochars were all below 0.83 as C mmol L⁻¹ with the majority less than 0.17 as C mmol L⁻¹ during all washing steps. After 12 washing steps, the DOC concentrations released by low-T poultry manure and mushroom soil biochars were 0.34 and 0.92 as C mmol L⁻¹. The DOC concentrations of the last washing steps for the high-T biochars were mostly below the analytical detection limit (0.04 as C mmol L⁻¹).

The release of OAs and DOC was approximated by calculating a first-order rate constant using $C = C_0 \exp(-k t)$, where C is the concentrations of OAs and DOC (C mmol L⁻¹), C_0 is the initial concentration (C mmol L⁻¹), k is the first-order rate constant (step⁻¹), and t is the number of washing steps (Table 2.3; Fig. 2.3). Use of this equation assumed that the number of washing steps, each 2 hours duration, represented time. The OAs and DOC released by activated carbon and high-T biochars were not modeled due to

the low concentrations of OAs and DOC. The initial concentration (C_0) ranged from 0.6-108 as C mmol L⁻¹ for acetate, 0.02-5 as C mmol L⁻¹ for formate, and 1-121 as C mmol L⁻¹ for DOC. The rate constants ranged from -2.28 to -0.618 step⁻¹ for acetate, -1.98 to -0.659 step⁻¹ for formate, and -1.29 to -0.378 step⁻¹ for DOC.

These rate constants were used to calculate the cumulative releases of OAs and DOC from the representative biochars. Cumulative releases of DOC from fresh biochar in batch extractions were in the range of 800-7000 mg kg⁻¹ for low-T biochars (0.1-3 % of C in biochar) and 50-200 mg kg⁻¹ for high-T biochars (0-0.02 % of C in biochar) (Table 2.3). This finding is consistent with previous studies (Jones et al., 2011; Mukherjee & Zimmerman, 2013). However, given that biochar is highly heterogeneous (Mukherjee & Zimmerman, 2013; Zimmerman, 2010), no single measureable parameter is likely to represent the OAs and DOC release behaviour of a sample.

The OAs and DOC released by biochars may cause an increase in the CO₂ output of soil following the addition of the amendment. Jones et al. (2011) reported a 2.5-fold increase in CO₂ output in the presence of biochar compared to the CO₂ release from an unamended soil which persisted for more than 1 month. This increase in CO₂ output is attributed to the breakdown of DOC and inorganic C (alkalinity) contained in the biochar. This observation is unlikely the case for long term amendments, as indicated by the very low contributions of black carbon to the CO₂ fluxes observed in a 3.2-year incubation experiment of soil and black carbon derived from perennial ryegrass residues (Kuzyakov et al., 2009). However, the DOC released from the biochar represented only 0.1-3% and less than 0.03% of total C in low-T and high-T biochars respectively, suggesting that longer time may be required for more extensive mineralization of biochars.

2.4.5 SEM/EDX

The SEM/EDX measurements for six representative samples are presented in Fig. 2.4. Corn-cob biochar prepared at 300 °C had a small number of micro-pores (<1 μm) and a larger number of meso-pores (1-10 μm) through visual observation, including some dead-end pores. The high-T biochars had meso-pores as well as extensive micro-pores inside the meso-pores. Micro-porous samples with open pores are expected to have high surface areas. The concentrations of alkalinity, OAs, and DOC leached from the samples and the pore structures observed during the SEM imaging varied considerably across the biochars. Although these observations suggest that there is an association between the pore-structure and the leachability of alkalinity, OAs and DOC, the relationship is not obvious. This lack of correlation is consistent with a previous study (Lin et al., 2012).

The EDX results indicate the corn-cob biochars prepared at 600 °C had mineral particles on the surface and higher percentages of P, Cl, and K than biochars from other feedstocks. These mineral particles may represent detrital minerals originally present in the biochar feedstock or phases newly formed during high-T pyrolysis. The surface structures and elemental composition of the poultry manure and mushroom soil biochars were notably different than the biochars prepared from other agricultural residues and from wood; specifically, the poultry manure and mushroom soil biochars had a greater abundance of mineral particles, and the manure biochar had higher concentrations of alkali and alkaline earth metals (Ca, K, Cl, S, Si, Al, and Mg). Images of the manure biochars prepared at 600 °C show that the mineral particles were aggregated with large particles on the surface.

The mineral particles formed during heating may act as catalysts during the pyrolysis of the biochars and may have an effect on the formation and conversion of the inorganic C (alkalinity) and short chain organic C (OAs and DOC) in the biochars (Xu & Sheng, 2012; Zolin et al., 2001). These minerals may catalyze the conversion of short chain organic C substances to inorganic C when the pyrolysis temperature increases. Relatively high alkalinity and low OAs and DOC were observed in solutions mixed with some high-T biochars. When biochars are mixed with river water, the mineral particles can dissolve, influencing aqueous concentrations of alkalinity, OAs, and DOC. The observed increase in pH in the solution mixed with biochars compared with the river water control may also be due to the release of alkali and alkaline earth metal oxides from the biochars. The greatest increase in pH values were associated with higher contents of alkali and alkaline earth metals in the high-T biochar compared with low-T biochar. This correlation is consistent with a previous study (Yao et al., 2010).

2.4.6 FT-IR

The FT-IR spectra showed that all of the biochar samples likely contained hydroxyl (-OH, 3449 cm^{-1}), aliphatic (-CH, -CH₂, or -CH₃, 2920 and 2847 cm^{-1}), and quinone (-CO-, 1630 cm^{-1}) functional groups (Fig. 2.5), based on wave numbers assigned by Mayo et al. (2004). The charcoal and activated carbon had the fewest different types of functional groups, whereas manure biochars had the most. The hydroxyl group peak may be a result of the overlap of hydroxyl groups and a small fraction of surface chemisorbed water (Biniak et al., 1997), while the quinone group peak may be a combination of carboxyl, ketone, and aldehyde groups (Moreno-Castilla et al., 1998). Carbonate functional groups (870 cm^{-1} ; Mayo et al. (2004)) were observed in most biochars

prepared at 600 °C. Sulfate peaks (1114, 615 cm^{-1} ; Mayo et al. (2004)) were evident in all manure biochars, consistent with the EDX results (Fig. 2.4). Phosphorus-containing functional groups (1039 cm^{-1} ; Cantrell et al. (2012) and Mayo et al. (2004)) also were evident in poultry manure and mushroom soil biochars prepared at 600 °C. Both inorganic (orthophosphate and its oligomers) and organic phosphate (mono- and diesters) contribute to the intense band observed at $\sim 1039 \text{ cm}^{-1}$ (Jiang et al., 2004). Thiol and C-S functional groups (2511 cm^{-1} and 713 cm^{-1} , respectively; Mayo et al. (2004)) were evident in the mushroom soil biochars prepared at 600 °C.

Due to the complexity of biochars, aromatic ring structures may also be present as indicated by peaks at 1630 (aromatic C=C) and 713 (aromatic C-H) cm^{-1} , based on wave numbers assigned by Chen et al. (2008) and Mayo et al. (2004). Chen et al. (2008) also observed aromatic ring structure in biochars prepared from pine needles.

Fewer peaks were observed and the peak intensity decreased when the pyrolysis temperature increased from 300 to 600 °C; the exception was for phosphate, thiol, and C-S functional groups. For the hydroxyl and quinone peaks, these reductions may be due to the desorption of chemisorbed water and degradation of quinone structures. With increasing temperature, the biochars became more similar in structure to graphite, which is much simpler than the biochar feedstocks (Bandosz, 2006). Cantrell et al. (2012) observed a similar trend for poultry manure, wood, and grass chars.

Hydrogen ions can associate with oxygen-containing functional groups (hydroxyl, carboxylic, quinone, and carbonate) (Yuan et al., 2011). The alkalinity of the biochars may be associated with a combination of the oxygen-containing functional groups. The hydroxyl at 3449 cm^{-1} , quinone at 1630 cm^{-1} , and carbonate at 870 cm^{-1} intensities were

examined to assess the degree of correlation to the release of alkalinity, OAs, and DOC from the biochars. No significant correlations were observed between functional group intensities and alkalinity. A negative correlation was observed between hydroxyl functional groups with OAs and DOC. A positive correlation was observed between quinone and carbonate functional groups with OAs and DOC ($P < 0.05$).

The functional groups or structures observed in the biochars, including hydroxyl, quinone, carbonate, P- and S-containing groups, and aromatic rings, play a key role in organic and inorganic pollutant removal (Cao & Harris, 2010). These functional groups also contribute to the pH and alkalinity change in the aqueous solution due to ion exchange or dissolution of carboxylic functional groups.

2.4.7 Environmental Relevance

This study showed that elevated concentrations of alkalinity, OAs and DOC were observed for the tested biochars, which may compromise a portion of the C sequestration benefit due to the reactive nature of these C forms. The four low-molecular weight OAs evaluated in this study are readily utilized by soil microbes (Neilson & Allard, 2012). The activity of the soil microbial community may be enhanced and the community structure may shift in response to the addition of biochars with elevated concentration of soluble organic acids (Anderson et al., 2011). The enhanced microbial activity could also accelerate the decomposition of biochar. Due to the high affinity among dissolved organic matter and heavy metals (Ravichandran, 2004), and the potential for reductive dissolution of metal-bearing Fe and Mn (oxy)hydroxides, the mobility of heavy metals may also be enhanced after amendment with biochars. For example, Beesley et al. (2010) reported a 30-fold increase of Cu and As concentrations released from a contaminated

soil in pore water after adding biochars. The interplay between all of these factors must be considered prior to the application of biochars in the environment. As a starting point for determining the appropriate biochar for C sequestration, agricultural application, and contaminated site remediation projects, feedstock types and pyrolysis temperature should be taken into consideration. Further experiments should focus on measuring long-term rates of alkalinity, OAs and DOC leaching from biochar-amended soil, taking care to test a spectrum of biochar and soil types and representative species of DOC.

2.5 Conclusions

The one-time and multi-step release experiments showed that elevated concentrations of alkalinity, OAs, and DOC were released from some biochars during water leaching. The agricultural residue and manure-based biochars had a relatively higher potential to release alkalinity, short-chain OAs and DOC than wood-based biochars. The manure biochars had the most complex FT-IR spectra and surface composition. The biochars produced from different feedstocks at 600 °C tended to have similar properties—low potential to release OAs and DOC and higher C content—than those pyrolyzed at 300 °C. The FT-IR spectra for these biochar types also were characterized by relatively fewer peaks. The high-T biochars had similar pore structures as characterized by SEM/EDX. Overall, feedstock type and pyrolysis temperature play key roles in the properties of biochars and their potential to release short-chain OAs and DOC, and these properties may influence future environmental applications.

Table 2.1 Chemical composition of river water from South River near Waynesboro, VA, USA (Unit mg L⁻¹, except ionic strength as mol L⁻¹)

Parameter	Value	Parameter	Value
pH	7.8	NO ₂ ⁻	<0.01
Alkalinity (as CaCO ₃)	46	Br ⁻	<0.01
Ionic strength	0.0004	NO ₃ ⁻	3.9
DOC	<0.5	SO ₄ ²⁻	7.6
Lactate	<0.01	Al	0.09
Acetate	<0.01	Ca	16.7
Propionate	<0.01	K	0.79
Formate	<0.01	Mg	6.8
F ⁻	0.07	Na	3.5
Cl ⁻	5.7	Si	4.3

Table 2.2 C contents of all biochars as a function of biochar feedstocks and pyrolysis temperatures.

Group	Raw material	C (%)	
		Low-T ^a	High-T ^b
Agricultural residue	Cocoa husk	63.6±1.5	70.4±1.4
	Cotton seed	78.2±2.5	99.7±1.3
	Corn cob1	79.2±1.9	98.5±1.1
	Corn cob2	76.3±1.1	98.4±4.1
	Corn stover1	71.9±1.4	81.6±4.6
	Corn stover2	71.8±1.2	78.5±0.0
	Wheat straw	77.4±2.5	89.9±1.3
	Hop bract	74.5±1.0	80.9±2.8
	Switchgrass	70.2±1.7	94.5±1.4
Manure	Cow manure	52.0±2.1	63.5±1.8
	Poultry manure1	22.8±0.0	18.5±1.4
	Poultry manure2*	52.1±0.2	-
	Poultry manure3**	-	41.5±0.3
	Mushroom soil1	27.4±0.1	37.6±2.1
	Mushroom soil2	46.1±2.4	48.5±0.3
	Mushroom soil3**	-	60.1±3.3
Wood	Mulch	46.1±3.4	63.3±3.6
	Pine bark	76.6±1.0	99.6±1.2
	CL1 ^c **	-	89.0±5.2
	CL2 ^c **	-	99.9±0.6
	CL5 ^c **	-	99.5±0.4
	Activated carbon1 ^d **	-	98.0±0.8
	Activated carbon2 ^d **	-	98.1±0.1

^a Low-T biochars were produced at 300 °C

^b high-T biochars were produced at 600 °C, except ^c 700 °C and ^d products from Sigma; Numbers after name, different sources

- no sample at this temperature

* indicates no data was available for high-T biochar

** indicates no data was available for low-T biochar.

Table 2.3 Calculated first-order rate constants for the release of OAs and DOC as a function of number of washing steps and percentages of DOC in total C of biochars ^a

Sample	C type	C_0 (C mmol L ⁻¹)	k (step ⁻¹)	R ²	% of total C in biochar ^b
CL2	Acetate	0.663	-0.618	0.989	0.009
	Formate	0.025	-0.743	0.962	0.000
	DOC	1.04	-0.567	0.958	0.016
Switchgrass (300 °C)	Acetate	2.32	-0.628	0.969	0.045
	Formate	0.179	-0.659	0.975	0.003
	DOC	2.90	-0.400	0.910	0.101
Poultry manure (300 °C)	Acetate	4.46	-1.63	0.999	0.057
	Formate	0.446	-1.54	0.995	0.006
	DOC	23.1	-0.378	0.984	2.65
Mushroom soil (300 °C)	Acetate	108	-2.28	1.00	0.539
	Formate	4.66	-1.98	0.996	0.033
	DOC	121	-1.29	0.993	2.01

^a a first-order model ($C = C_0 \exp(-k t)$) was used to calculate approximate rate constants by assuming the number of washing steps represents time, where each step was equal to 2 hours.

^b % of total C in biochar calculated using $(\sum C_i * V)/(m * \% C) * 100$ ($i = 1, 2, 3 \dots$), where C_i is the concentration of OA or DOC calculated from the fitted equation, V is the volume of ultra-pure water used in each step (0.15 L), m is the mass of biochar used in the experiment (15 g), and % C is the C content of the biochars (Table 2.2).

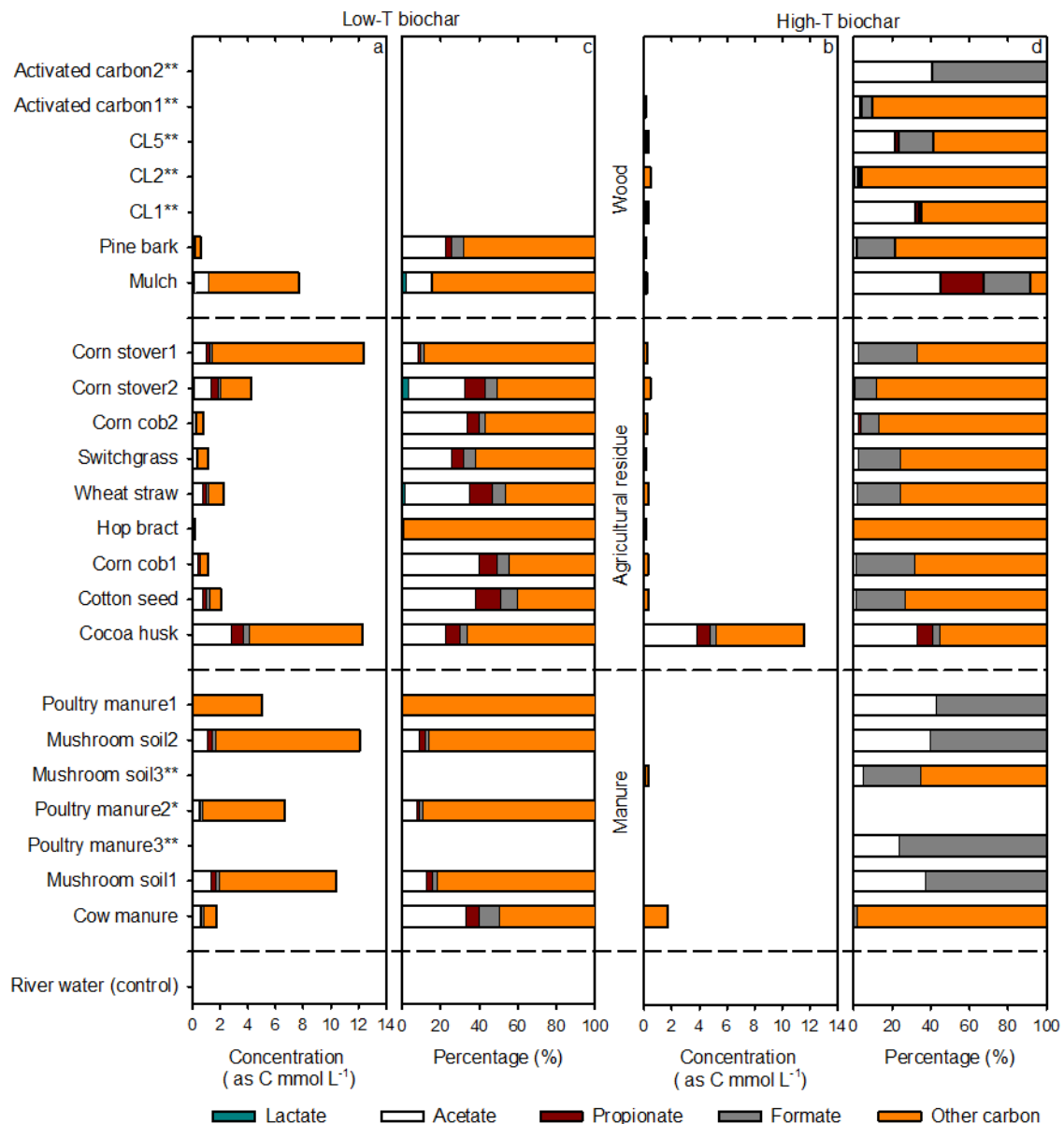


Figure 2.1 Concentration of organic acids and DOC in aqueous solution leached from each biochar sample (a, b), and the percentage of total dissolved C composed of five components (c, d). The other C was the difference between DOC and organic acids. * after biochar name indicates no data was available for high-T biochar; ** after biochar name indicates no data was available for low-T biochar.

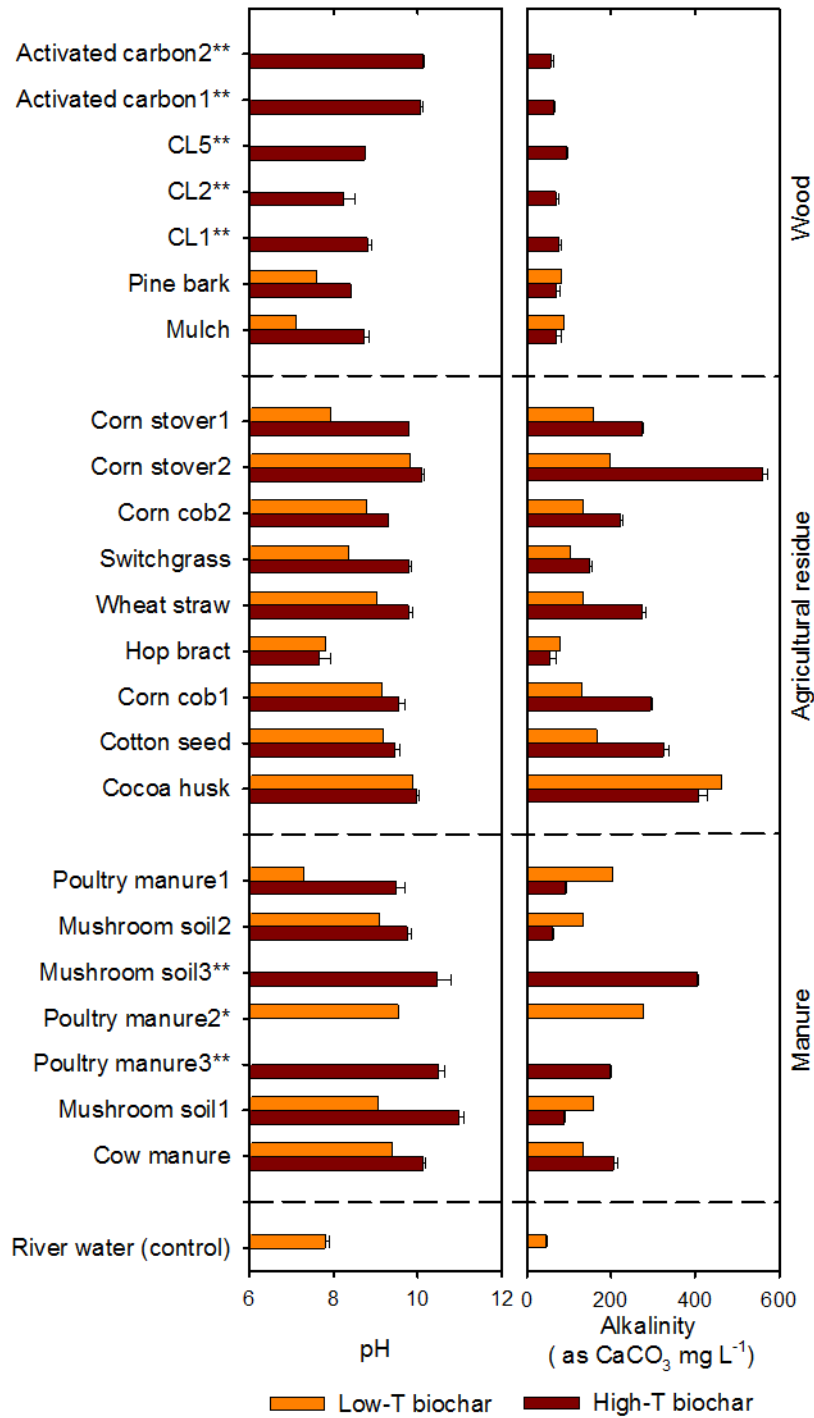


Figure 2.2 pH and alkalinity values of aqueous solutions mixed with low-T and high-T biochars. * after biochar name indicates no data was available for high-T biochar; ** after biochar name indicates no data was available for low-T biochar.

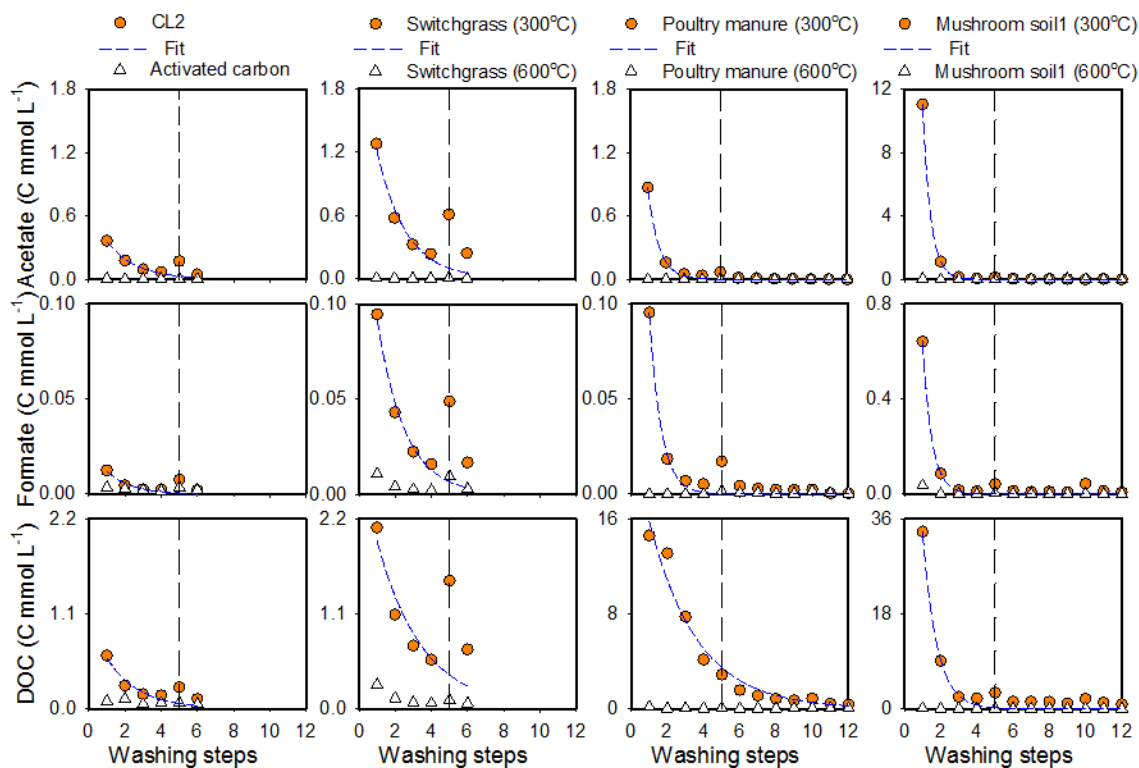


Figure 2.3 Concentrations of acetate, formate and DOC released by activated carbon, wood, switchgrass, poultry manure, and mushroom soil biochars during sequential leaching. The dashed vertical line indicates the solid phase was left on the filter for 10 hours prior to the 5th washing step. The dashed blue lines represent the regression curves of the C release using $C = C_0 \exp(-k t)$ for the orange circle data points by excluding the 5th step. The calculated regression coefficients are provided in Table 2.3.

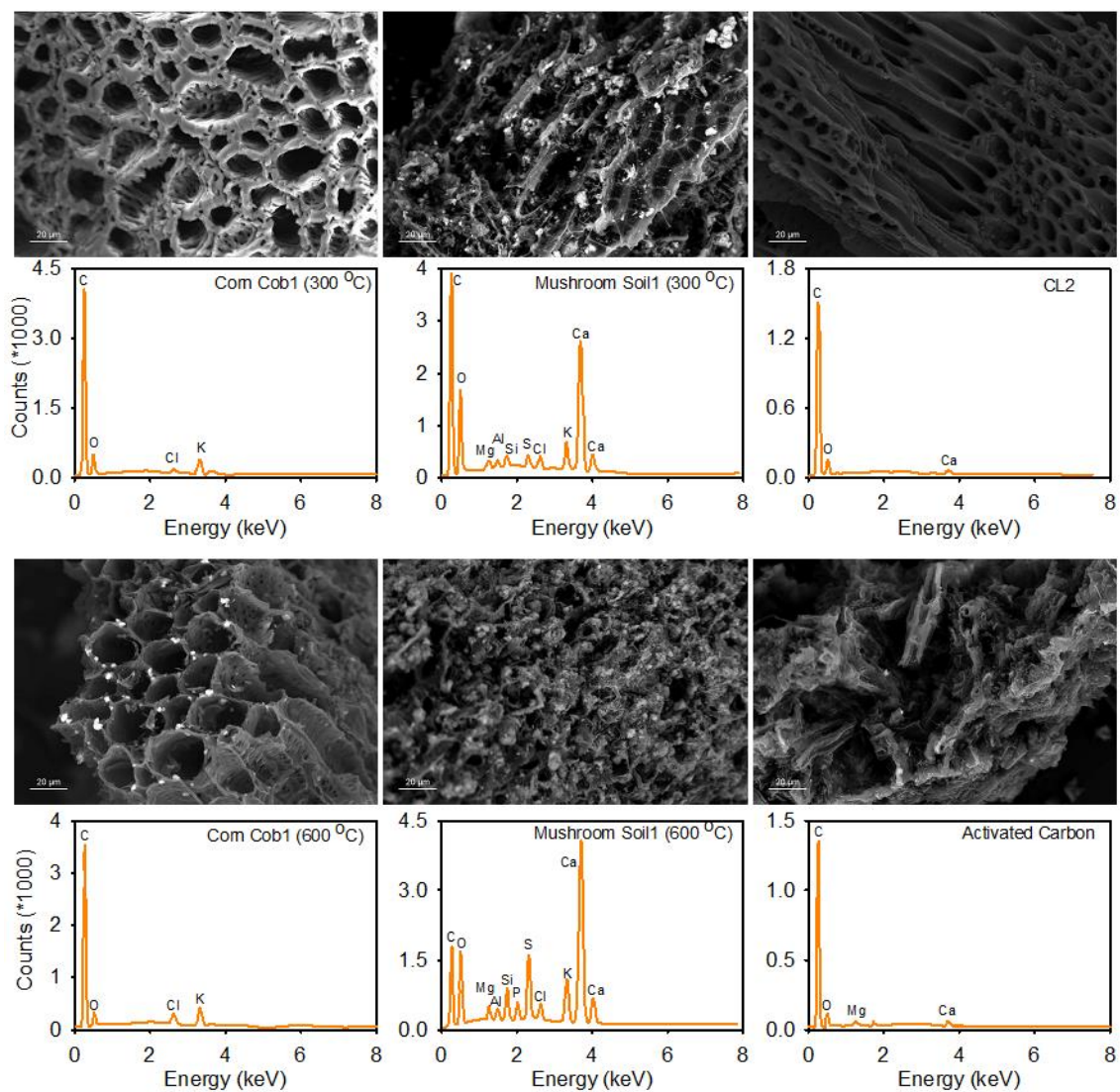


Figure 2.4 SEM/EDX images of representative biochar samples.

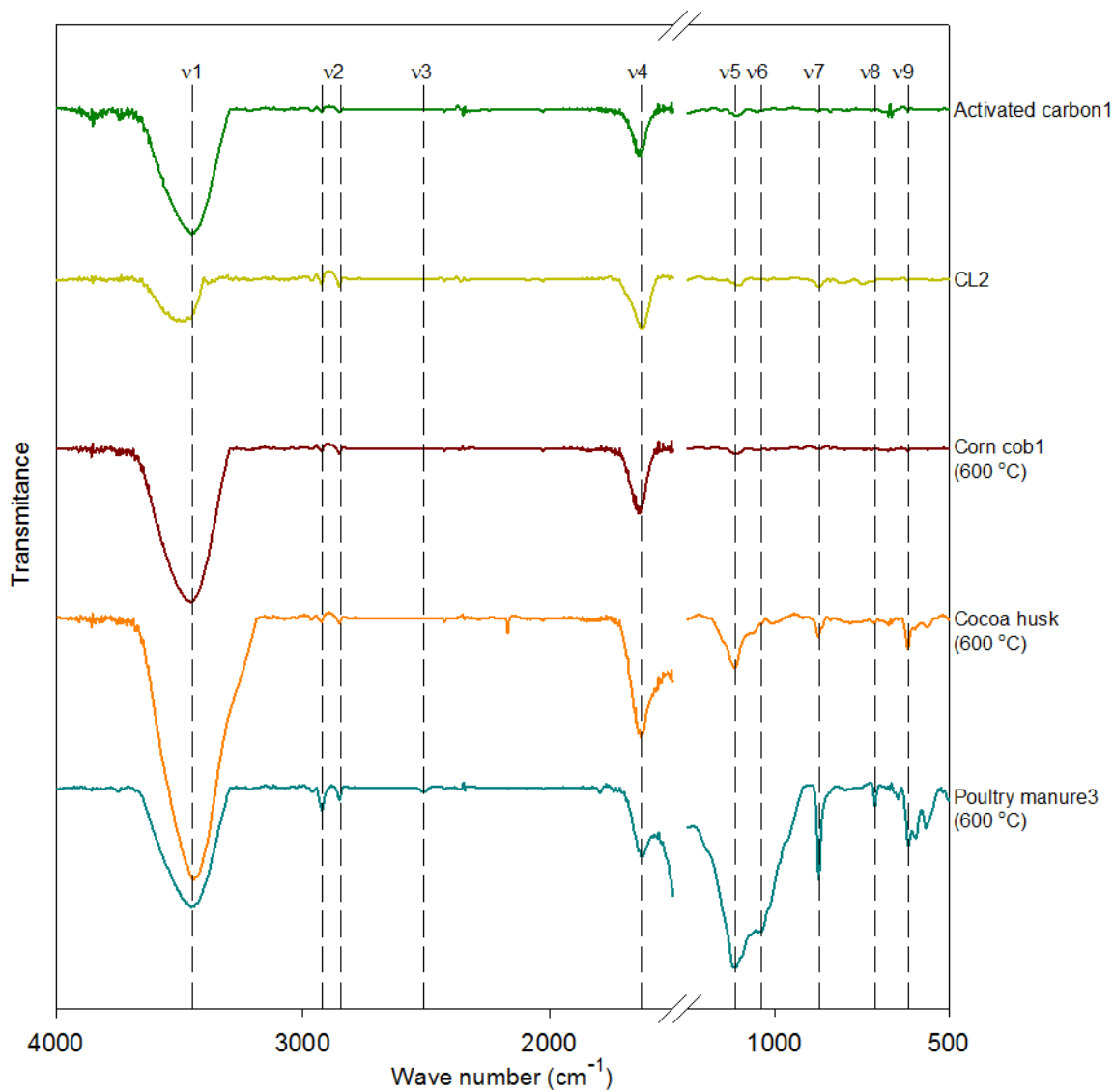


Figure 2.5 FTIR spectra of representative biochar and activated carbon samples. Dashed lines represent the following functional groups: v1, hydroxyl (-OH, 3449 cm^{-1}); v2, aliphatic (-CH, -CH₂, or -CH₃, 2920 and 2847 cm^{-1}); v3, thiol (2511 cm^{-1}); v4, quinone (-CO-, 1630 cm^{-1}); v5 v9, sulfate (1114, 615 cm^{-1}); v6, Phosphorus-containing (1039 cm^{-1}); v7, carbonate (870 cm^{-1}); v8, C-S (713 cm^{-1}).

Chapter 3: *Mechanisms of Mercury Removal by Biochars Produced from Different Feedstocks Determined using X-ray Absorption Spectroscopy*

Reproduced from: Liu, P.; Ptacek, C. J.; Blowes, D. W.; Landis, R. C. Mechanisms of mercury removal by biochars produced from different feedstocks determined using X-ray absorption spectroscopy. *J. Hazard. Mater.* 2016, 308, 233-242, Copyright (2016) with permission from Elsevier, License Number 3861501371976. Editorial and formatting changes have been made to accommodate reproduction in this thesis.

3.1 Executive Summary

Thirty-six biochars produced from distinct feedstocks at different temperatures were evaluated for their potential to remove mercury (Hg) from aqueous solution at environmentally relevant concentrations. Concentrations of total Hg (THg) decreased by >90% in batch systems containing biochars produced at 600 and 700 °C and by 40-90% for biochars produced at 300 °C. Elevated concentrations of SO_4^{2-} (up to 1000 mg L⁻¹) were observed in solutions mixed with manure-based biochars. Sulfur (S) X-ray absorption near edge structure (XANES) analyses indicate the presence of both reduced and oxidized S species in both unwashed and washed biochars. S XANES spectra obtained from biochars with adsorbed Hg were similar to those of washed biochars. Micro-X-ray fluorescence mapping results indicate that Hg was heterogeneously distributed across biochar particles. Extended X-ray absorption fine structure modeling indicates Hg was bound to S in biochars with high S content and to O and Cl in biochars with low S content. The predominant mechanisms of Hg removal are likely the formation of chemical bonds between Hg and various functional groups on the biochar. This investigation provides information on the effectiveness and mechanisms of Hg removal that is critical for evaluating biochar applications for stabilization of Hg in surface water, groundwater, soils, and sediments.

3.2 Introduction

Large volumes of solid-phase reactive materials are required in treatment systems to control the release of metals and other contaminants to the environment. For example, construction of permeable reactive barriers (Blowes et al., 2000; Blowes et al., 1997), containerized treatment systems (Hussain et al., 2014; Robertson et al., 2009), and alternative treatment wetlands (Barca et al., 2013; Easton et al., 2015; Hussain et al.,

2015) all require use of large volumes of adsorbents, reductants, or other treatment materials.

Biochar and other carbonaceous materials are widely used as treatment materials to remove a range of metals (e.g., As, Cd, Cr, Cu, Ni, Pb, Zn) and organic contaminants from aqueous solutions (Ahmad et al., 2016; Dong et al., 2011; Hu et al., 2015; Jiang et al., 2012; Lehmann & Joseph, 2009; Zhang et al., 2013). Biochar has also been evaluated with respect to Hg stabilization (Boutsika et al., 2014; Bundschuh et al., 2015; Mohan et al., 2014). The majority of Hg removal studies have focused on the determination of sorption isotherms, kinetic rate constants, or factors influencing sorption. Most of the studies have been conducted in experimental systems with relatively high initial Hg concentrations (5-2000 mg L⁻¹) (Boutsika et al., 2014; Das et al., 2007; Kadirvelu et al., 2004; Namasivayam & Kadirvelu, 1999), which is typical of industrial wastewater but much higher than commonly observed in the environment. Additional studies have been conducted for Hg removal at environmental concentrations (Bostick & Klasson, 1998; Hollerman et al., 1999; Klasson et al., 2000; Klasson & Bostick, 1998; Klasson et al., 2003). For example, Klasson and Bostick (1998) and Hollerman et al. (1999) reported that Hg concentrations decreased from 1 µg L⁻¹ to <12 ng L⁻¹ in batch experiments (Klasson & Bostick, 1998) and to <51 ng L⁻¹ in column experiments (Hollerman et al., 1999) using functionalized resins.

Speciation of Hg in the environment is strongly dependent on the presence of thiol functional groups (Yin et al., 1997). Therefore, understanding the S speciation in biochars is important with respect to potential removal approaches. X-ray absorption near-edge structure (XANES) spectroscopy is a non-destructive technique widely used

for the characterization and quantification of S species in various materials (Bisson et al., 2012; Fleet, 2005; Manceau & Nagy, 2012; Prietzel et al., 2003; Wang et al., 2013; Zeng et al., 2013). XANES analysis of biochar produced from corn stover and oak has indicates the presence of both organic and inorganic forms of S (Cheah et al., 2014; Churka Blum et al., 2013). Micro X-ray fluorescence (μ -XRF) maps and extended X-ray absorption fine structure (EXAFS) are powerful techniques for providing spatial localization of Hg, its correlation with other elements of interest, and local structural information including binding elements, bond distances, and coordination numbers. Hg L_{III} edge EXAFS analysis has been used to evaluate mechanisms of Hg removal using various treatment media, including brominated biomass ash (Bisson et al., 2012), cupric chloride-impregnated sorbents (Li et al., 2012), granular iron (Weisener et al., 2005a), activated carbon, thiol-containing materials, and modified attapulgite clay (Gibson et al., 2011).

As described in Liu et al. (2015), the biochar samples investigated in this study release different masses and forms of soluble carbon, including short-chain organic acids, dissolved organic carbon (DOC), and alkalinity. The current study describes the removal of Hg from aqueous solution by these biochars and the release of additional components that could influence Hg cycling and methylation or limit the use of the biochars for environmental applications. To evaluate the binding mechanisms, X-ray absorption spectroscopy (XAS) was applied to determine the distribution of Hg and the local coordination geometry of Hg bound to biochar particles. Combined, these analyses assist in understanding how Hg is bound to biochar, and what substances might co-occur in the biochar to potentially influence transformation of Hg in field applications.

3.3 Materials and Methods

3.3.1 Biochars Employed

Thirty-six biochar samples were prepared from three groups of feedstocks: wood, agricultural residue, and manure (Table 3.1). Two activated carbons (Sigma-Aldrich Corp., St. Louis, US) were used as a benchmark. The feedstocks were air dried and pyrolyzed using a kiln at either 300 °C (low T) or 600 °C (high T) for 2-3 h under limited O₂ conditions. The biochars were cooled overnight to room temperature. Liu et al. (2015) provide detailed methods used for preparation of the biochars.

3.3.2 Batch Experiments for Hg Removal

A stock solution of 200 mg L⁻¹ of Hg²⁺ was prepared by dissolving reagent-grade HgCl₂ in ultra-pure water (Milli-Q purification system). The stock solution was diluted with river water (South River, Waynesboro, VA) to a concentration of ~10 µg L⁻¹, representative of environmental levels (Ranchou-Peyruse et al., 2009). A series of batch-style experiments was conducted by adding 2 g of biochar to 150 mL of Hg(II)-spiked water. The mixtures were shaken thoroughly and allowed to equilibrate at room temperature for 2 d. Ultrapure water was used as a control to assess potential Hg contamination during laboratory procedures. Samples containing river water only and biochar mixed with unspiked river water were also used as controls.

At the termination of the experiment, water samples were filtered using 0.45 µm cellulose-acetate filters (Pall Corp.). For a subset of samples, six sequential aliquots (5@1 mL followed by 1@ 15 mL) of filtrate were analyzed, and concentrations of THg were observed to stabilize after the third aliquot. Therefore, for the majority of the samples, the first 5 mL aliquot of sample was discarded and subsequent aliquots were placed in an amber borosilicate glass bottle for analysis of total Hg (THg). These samples were

acidified to pH <2 using ultra-pure HNO₃. Additional samples were collected in polypropylene bottles and left unacidified for anion analyses. All samples were stored at 4 °C until analysis. The anion samples were analyzed within 72 h of collection.

3.3.3 Water Analyses

THg concentrations were determined by cold vapor atomic fluorescence spectroscopy (Tekran Instruments) after digestion following US-EPA Method 1631 (EPA, 2002a). The method detection limit (MDL) was 0.19 ng L⁻¹ as determined following the EPA procedure (40 CFR, Part 136). Quality assurance/quality control steps taken included analysis of laboratory blanks (<MDL), duplicate samples for each set of 10 samples (0-20% relative standard deviation, most < 5%), one matrix spike sample for each set of 10 samples (85-115% recovery, most 95-105%), and a NIST standard (80-120% recovery, most 95-105%) for each run. Concentrations of anions were determined on unacidified samples using ion chromatography (Dionex DX-600) with an IonPac AS9-HC 4×250 mm column.

3.3.4 S Content

Solid-phase S content of the biochar samples was measured using a resistance furnace (Eltra CS-2000). Samples were oven-dried at 105 °C for 24 h before analysis and were analyzed three times; mean values of these analyses are reported.

3.3.5 X-ray Absorption Spectroscopy (XAS)

Eight unwashed and washed biochars without Hg and five biochars with adsorbed Hg were analyzed using S K-edge XANES. Thin-sections of five biochars with adsorbed Hg were characterized by μ-XRF mapping and Hg L_{III}-edge EXAFS.

3.3.5.1 Reference Materials

Organic S reference compounds included dibenzyl disulfide (DibDis), L-cysteine, dibenzyl sulfide (DibSu), dibenzo thiophene (DibTh), and butyl sulfone (BuSu) (all from Sigma-Aldrich); tetramethylene sulfoxide (TeSu) (from Acros Organics); and sodium methane sulfonate (NaMeSu) (from Alfa Aesar). Pyrrhotite, cinnabar (α -HgS, Excalibur Mineral), metacinnabar (β -HgS), pyrite, Na tetrathionate ($\text{Na}_2\text{S}_4\text{O}_8$), NaS_2O_3 , K_2SO_4 , and HgSO_4 were selected as inorganic S reference materials. The spectrum of thianthrene was obtained from an online database (ID21-ESRF, 2016). Hg reference materials included cinnabar, HgO (Sigma-Aldrich), and HgCl_2 (Fisher Scientific). The spectra of Hg_2Cl_2 was obtained from an online database (NSLS, 2016) and metacinnabar from the Hephaestus utility of the Demeter software package (Ravel & Newville, 2005).

3.3.5.2 Hg EXAFS

Hg EXAFS analysis was conducted on the batch test samples; however, the concentrations of adsorbed Hg were too low to collect high quality spectra. To obtain improved EXAFS spectra, additional Hg was loaded onto the biochar samples by mixing 0.8 g biochar with 200 mL of a 50 mg L⁻¹ Hg(II) solution. The mixture was separated onto a filter after 48 h and the solid phase freeze-dried for polished thin-section preparation. The thin-sections were prepared by mounting grains of biochar within epoxy cement on a quartz slide 26×26 mm in size to a thickness of 30 μm (Vancouver Petrographics Ltd., Canada).

EXAFS spectra were collected for samples and reference materials on Beamline 13-ID-E (GSECARS) and Beamline 20-ID-B (PNC/XSD) at the Advanced Photon Source (APS; Illinois, USA). A focused beam approximately 2×2 μm in size was used for

XAS data collection. The μ -XRF maps were collected with a photon energy for excitation of 12.6 keV. The step size (pixel) was $2 \times 2 \mu\text{m}$ for fine maps and $25 \times 25 \mu\text{m}$ for coarse maps. Areas with elevated Hg intensity were identified for acquisition of EXAFS spectra.

The XRF mapping was analysed using X-ray Microprobe Map Viewer (Newville, 2016) for data from the GSECARS beamline and 2D QScanPlot for data from the PNC/XSD beamline. The XAS spectra were analysed using Athena, and EXAFS model calculations were made using Artemis (Ravel & Newville, 2005). The modeling was performed following the method described by Gibson et al. (2011). Briefly, the crystal structures of reference materials were obtained from an online database (AMCSD, 2016) and ATOMS.INP website (ATOMS, 2016). Weak oscillations in the EXAFS data were enhanced by applying a k weighting of 3 to the spectra. Coordination numbers (CNs) were considered as a constant during refinement of the first one or two shells for the reference materials to obtain the amplitude reduction factor (S_0^2) and static disorder (σ^2). S_0^2 and σ^2 were then kept invariant for refinement of the first shell of Hg bound to biochar to model the CNs .

3.3.5.3 S XANES

Preliminary XANES analysis indicates a pronounced intensity for sulfate and suppression of the intensity for other reduced S peaks; therefore, a separate set of biochar samples was washed to lessen the intensity of the sulfate signal. The biochar samples were mixed with ultrapure water at a 1:10 mass ratio following the same procedure as the batch experiment, except that the mixtures were filtered after 2 h; this procedure was repeated for a total of 6 or 12 times. Liu et al. (2015) provide details of the washing steps.

Biochar samples after washing and samples after contact with Hg were freeze-dried and ground into fine powders to decrease self-adsorption effects.

XANES spectra were collected on samples and reference materials at both the GSECARS beamline and at the Soft X-ray Microcharacterization Beamline (SXRMB) at the Canadian Light Source (CLS; Saskatchewan, Canada). At GSECARS, homogenized powders of samples and reference materials (mixed with high-purity graphite with a S content of ~5%) were placed into an acrylic holder covered with 2.5- μm thick Mylar film (Chemplex Industries). Sample holders were placed in a He bag during analysis. A Si(111) monochromator was detuned to 70% to reduce higher-order harmonics. An unfocused beam of $\sim 50 \times 50 \mu\text{m}$ was employed and data were collected using a Vortex ME4 silicon drift diode array detector. At the CLS-SXRMB, homogenized samples and pure reference materials were smeared as a thin film on conductive double-side tape mounted to a copper sample holder. The holder was placed inside a chamber under vacuum. Spectra were collected using fluorescence yield for biochar samples and total electron yield for the reference materials.

One to six scans were collected for biochars and reference materials. Data processing was performed with Athena (Ravel & Newville, 2005). The spectra of the samples were compared with reference materials, and spectra of reference materials with peaks at the same peak energy were selected for linear combination fitting (LCF) in Athena to calculate the relative percentages of S species in a given sample.

3.3.6 Statistical Analysis

Statistically significant correlations among feedstock type, pyrolysis temperature, THg, anion concentrations, and S content were determined using a two-fractional ANOVA.

Correlation analyses were evaluated by Pearson product-moment correlation coefficients.

3.4 Results and Discussion

3.4.1 Removal of Hg

Biochar treatment reduced concentrations of THg in river water from 9800 ng L⁻¹ to as low as 21 ng L⁻¹, for a removal of up to 99.8% (Fig. 3.1). THg concentrations in the water treated by most high-T biochars were lower than the 2000 ng L⁻¹ US-EPA drinking water standard and 73% of the high-T biochars were lower than the 770 ng L⁻¹ concentration recommended by the US-EPA to protect aquatic life (EPA, 2009; EPA, 2015).

Concentrations of THg decreased by >95% in the batch mixtures containing charcoals, activated carbons, low-T biochars produced from poultry manure and mushroom soils, and high-T biochars produced from corn cobs, corn stover, mixed grass, hop grass, switchgrass, pine mulch, pine bark, poultry manure, and mushroom soils. The highest THg concentration (5800 ng L⁻¹) was observed for biochar produced from pine bark prepared at 300 °C. The THg concentration decreased by 29% for the Hg-spiked river water after 2 d; possibly due to uptake of Hg by organic matter. The THg concentrations in other controls containing ultrapure water alone, river water alone, and biochar mixed with river water were less than 10 ng L⁻¹.

THg concentrations of the aqueous solution equilibrated with high-T biochars were significantly lower than those observed for low-T biochars ($P < 0.05$). No significant differences in THg concentrations were observed among different biochar groups and from the interaction of pyrolysis temperatures and different groups. Hg removal

efficiencies were consistently greater than 80% (majority >90%) in samples treated by manure-based biochars and high-T wood-based biochars. These treatment efficiencies are comparable to those reported for other carbonaceous materials. For example, Hg removal efficiencies of 86 to 75% using 2 to 250 $\mu\text{g L}^{-1}$ Hg^{2+} were observed for a biochar produced from soybean stalk (Kong et al., 2011).

3.4.2 SO_4^{2-}

SO_4^{2-} concentrations in the mixtures with biochars ranged from 6.0 to 1000 mg L^{-1} (Fig. 3.2), all of which exceed the concentration in the control (5.9 mg L^{-1}). The highest concentrations of SO_4^{2-} (range 72-1000 mg L^{-1} , median >400 mg L^{-1}) were consistently observed in river water mixed with mushroom soil and poultry manure biochars, whereas lower concentrations were observed with wood-based biochars. The concentrations of SO_4^{2-} in mixtures containing CL2, high-T pine bark (SW2H), corn cob (CC2H), and spent hops (GR3H) biochars were only slightly higher than that measured in river water (range 6.0-7.1 mg L^{-1}).

The elevated concentrations in the poultry manure and mushroom soil biochars are consistent with earlier studies (Hass et al., 2012) and likely due to high inorganic S content in the feedstocks (Guo & Chorover, 2006). The statistical analysis indicates no significant differences of SO_4^{2-} concentrations between the low-T and high-T biochars, whereas the SO_4^{2-} concentrations of manure-based biochars were significantly higher than the agricultural residue-based biochars.

The elevated concentrations of SO_4^{2-} released from the biochar may be problematic for applications of biochar for Hg stabilization at contaminated sites if reducing conditions are established, because the added SO_4^{2-} can be utilized as an

electron acceptor by sulfate-reducing bacteria (SRB) known to be major Hg methylators (Hsu-Kim et al., 2013) and MeHg is much more toxic than other forms of Hg. Liu et al. (2015) report that organic acids and DOC are released by some of the biochars. In combination with SO_4^{2-} , these organic acids and other forms of DOC may act as electron donors further stimulating growth of Hg methylators. The elevated SO_4^{2-} concentrations released from the biochar may affect the aqueous-phase speciation of Hg, especially for biochar samples prepared from the mushroom soil and poultry manure. The released DOC can also affect the aqueous-phase speciation of Hg, because Hg can strongly bind to DOC (Wallschläger et al., 1996). Speciation calculations were made for all batch samples using PHREEQCi. For these calculations, thermodynamic constants for Hg-Dissolved organic matter (Hg-DOM) (Dong et al., 2010; Gissera et al., 2007; Martell & Smith, 2004; Temminghoff et al., 2000) were added into the database. These calculations indicate that the aqueous solutions for all the samples were strongly undersaturated with respect to HgSO_4 , HgO , HgCl_2 phases, and that the Hg-DOM complexes accounted for >90% of the THg.

3.4.3 S Content

The solid-phase S content of the biochar samples ranged from <0.01 to 3.4% (Table 3.2). Solid-phase S content was highest for the manure-based biochars, at 0.48-3.40%, and lowest for the wood-based biochars, at <0.01-0.18%. These observations are consistent with SO_4^{2-} concentrations in the aqueous phase (Fig. 3.2). The S content of two high-T corn stover biochars (CS1H, 0.82%; CS2H, 0.37%) are close to the value reported for a corn stover biochar produced at 500 °C (~0.8%) (Cheah et al., 2014).

The statistical analysis indicates differences in S content between low-T and high-T biochar are insignificant. Generally, light elements (e.g., hydrogen) are vaporized as pyrolysis temperature increases, leading to enrichment of S (Bandosz, 2006), i.e., S content of high-T biochars is greater than for low-T biochars (Cheah et al., 2014; Gaskin et al., 2008). The lack of correlation here may be due to the variety of biochar samples evaluated. A significant difference in S content among the three groups is evident, i.e., the S content of manure-based biochar is significantly greater than for agricultural residue-based biochar, which is consistent with a previous study (Cheah et al., 2014). Correlation analysis indicates that SO_4^{2-} concentrations in the aqueous phase are not significantly correlated with S content in the biochars. This observation suggests that other forms of S are likely present in the biochars.

3.4.4 S XANES Analyses

Due to the complexity of S species in nature, a variety of S reference materials were characterized. The XANES spectra collected (Fig. 3.3a,b) are consistent with the presence of reduced S (v1- v5) and oxidized S (v6, SO_4^{2-}) species in all biochar samples (Fig. 3.3c,d), in agreement with other studies (Cheah et al., 2014). The peak positions of v3 (thianthrene-like) and v4 (thiophene-like) are at the same energy (2474.3 eV), and therefore are expressed as v3/4. The presence of v3/4 and v6 (sulfate-like, 2482.5 eV) peaks is evident in all samples. Elemental S-like peaks (v2, 2472.7 eV) are evident in unwashed and washed activated carbon (AC) and high-T mushroom soil (MU1H) biochars, which is consistent with reduced S peaks occurring in the energy range of 2472 to 2473 eV for brominated and non-brominated activated carbon (Bisson et al., 2012). Spectra consistent with the presence of thiophene-like (2nd peak) or sulfoxide-like (v5,

2476.2 eV) species were collected for CL2 and GR4H biochars. Evidence of sulfide-like S species (v1, 2470.4 eV) is present in the spectra of washed MP1H.

Comparison of the spectra obtained for the low-T and high-T biochars indicates that the intensity increased for the reduced S (Table 3.3). In addition, new peaks of reduced S phases are observed in the spectra for the high-T biochars, e.g., v2 for the MU1H biochar and v5 for the GR4H biochar. The intensities of reduced S peaks in washed biochars are also higher than for unwashed biochars (Fig. 3.3c,d). These results indicate that a portion of inorganic S (sulfate) was likely leached into the aqueous phase through the washing step relative to reduced S species, which is consistent with the elevated SO_4^{2-} data in the batch experiment (Fig. 3.2).

An LCF process was conducted to determine the similarity between the spectra of biochars and reference materials (Fig. 3.3c,d). A combination of K_2SO_4 and thiophene provides the best fit for CL2, GR4L, and GR4H biochars (Table 3.3). Addition of thianthrene and elemental S was required to provide the best fit for AC and addition of pyrrhotite was required for washed MP1H. The increase in the percentage of reduced S species in the biochar samples after washing is consistent with the intensity increase of the spectra (Fig. 3.3c,d). The percentage of reduced S species in high-T switchgrass biochar (GR4H) increased in comparison with GR4L, which is consistent with the peak intensity increase (Fig. 3.3c d).

S XANES spectra collected for pyrolyzed carbonaceous material indicate that the majority of S bonded to C is thermally decomposed during pyrolysis at 450 °C (Cheah et al., 2014; Churka Blum et al., 2013). Ester-S, and to a small extent inorganic sulfate, also accumulate (Churka Blum et al., 2013). The transformation of sulfate to reduced S occurs

at pyrolysis temperatures above 500-600 °C when hydrocarbon molecules (in pyrolysis vapor and syngas) and/or H₂ (present in syngas) are present (Cheah et al., 2014). The S transformed from sulfate is retained in the char and is presumably bound to the organic char matrix. As the biochar in this study was prepared at 300 and 600 °C, part of the sulfate was likely transformed to reduced and organic bound S at 600 °C.

Reduced S plays an important role in the binding of Hg because Hg-S complexes form with disulfide/disulfane in addition to thiol S (Xia et al., 1999). Binding of Hg to reduced S is usually favored over binding to other functional groups, e.g., hydroxyl and carboxyl groups (Bisson et al., 2012; Haitzer et al., 2002; Hesterberg et al., 2001). In this study, the S XANES spectra of biochars adsorbed with Hg are similar to the spectra of washed biochars with no adsorbed Hg; no obvious change in the intensity of the reduced and oxidized S peaks is evident (Fig. 3.3c-e). The similarity indicates that S components in the biochar are not altered by the adsorbed Hg.

3.4.5 μ -XRF Mapping

The μ -XRF results indicate Hg is distributed on the edges, inside the pores, and even inside the pore walls of the particles in all thin sections (Fig. 3.4). These observations indicate that Hg penetrates into the interior of biochar particles and does not simply sorb to the surface and pore walls. The Hg is unevenly distributed, as the greatest enrichments are close to the particle edges and within the pores in all particles. Low intensity areas on the Hg μ -XRF map are also evident within particles, especially within the low-T switchgrass (GR4L) and high-T poultry manure (MP1H) biochars. The Hg enrichment area displays a cross-channel pattern in the high-resolution mapping area on CL2-Coarse.

The Hg $L_{\alpha 1}$ peaks in the XRF spectra confirm the existence of Hg in Hg-rich areas of the maps for AC-Coarse and CL2-Coarse.

The results indicate Hg is present on the edges of and inside the particles. However, this is inconsistent with a previous study that reported Hg concentrated 0-100 μm from the exterior of the polysulfide-rubber-coated activated carbon (Kim et al., 2012). The XRF K_{α} or K_{β} lines of other elements (K, Ca, Mn, Fe, Ni, and Cu) were also collected, but their intensity is not distinguishable from the background. The S K_{α} line was filtered by Al foil because the detector was saturated without a filter.

3.4.6 Hg XANES Analysis and EXAFS Modelling

The threshold E_0 (ionization energy) of the XANES indicates the Hg oxidation state in the five samples is similar to HgCl_2 , HgO , and cinnabar, suggesting the Hg is present as Hg^{2+} (Fig. 3.5a). The XANES spectra show the absence of a distinct shoulder on the edge in the samples, in contrast to the shoulder (12.29 keV) observed for HgCl_2 and HgO reference materials.

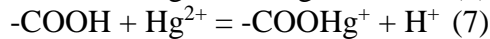
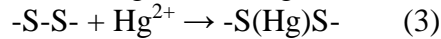
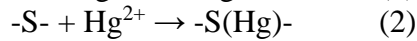
Inflection point difference (IPD) is defined as the energy difference of two distinct peaks in the first derivatives of the spectra (Huggins et al., 2003). IPD can be used as a screening method to estimate the Hg binding environment (Bisson et al., 2012). The IPDs of AC, CL2, and GR4L samples ranged from ~ 8.1 to ~ 8.4 eV, which are close to that of HgCl_2 (Fig. 3.5b). IPDs of the GR4H and MP1H samples were 7.6 and 7.7 eV, close to that of cinnabar.

EXAFS spectra were modeled against the first shell of HgCl_2 , Hg_2Cl_2 , HgO , metacinnabar, cinnabar, and their combinations. The best fit was obtained using HgO as a model compound for AC and GR4L, HgCl_2 for CL2, and cinnabar for GR4H and MP1H

(Fig. 3.5c-e; Table 3.4). The EXAFS modeling R-factors range from 0.006 to 0.015 for the reference materials and 0.005 to 0.094 for the biochar samples.

Although the IPDs of activated carbon (AC) and low-T switchgrass biochar (GR4L) are closer to HgCl₂ than HgO, negative values of coordination numbers were obtained when HgCl₂ was used as a model compound. The modeled bond distances of Hg-O in AC and GR4L are between 2.08 and 2.09 Å, which is close to the theoretical value (2.05 Å, Table 3.4) and in agreement with a previous study (Gibson et al., 2011). The O atoms bound to Hg are likely from the O-containing functional groups identified in Fourier transform infrared spectra (Liu et al., 2015) or H₂O sorbed to surfaces of activated carbon particles (Li et al., 2002). However, a study by Bisson et al. (2012) shows Hg is primarily bound to S in activated carbon used for capturing Hg from coal-fired power plants. The coordination number of Cl bound to Hg for CL2 is ~0.55, which is less than the Cl in the HgCl₂ reference compound. The modeled Hg-Cl distance is ~2.26 Å, which is close to the expected 2.29 Å for HgCl₂ but shorter than ~2.36 Å for Hg-Cl in cupric chloride-impregnated sorbents (Li et al., 2012). The Cl likely originated from the solution or possibly the biochar. The best fitting results for high-T switchgrass biochar (GR4H) and high-T poultry manure biochar (MP1H) were obtained when cinnabar was used a model compound. The coordination numbers of S bound to Hg for GR4H and MP1H are between 0.79 and 1.17, which are in the range of published values (Bisson et al., 2012; Gibson et al., 2011). The modeled Hg-S distances are ~2.24 and ~2.26 Å, shorter than 2.37±0.04 Å for the cinnabar and previous studies (Bisson et al., 2012; Li et al., 2012). The poor fitting against Hg-S for AC, CL2, and GR4L is likely due to the low S content in these samples compared with GR4H and MP1H (Table 3.2).

The S XANES data also indicate that Hg is likely bound to S in AC, CL2, and GR4L, but the percentage of Hg-S in AC, CL2, and GR4H appears to be low as Hg-S is not well represented in the EXAFS modeling for Hg. The Hg removal mechanisms by carbonaceous sorbents include coordination between Hg and functional groups on/within sorbents, reduction of Hg²⁺ to Hg(I) and precipitation (El-Shafey, 2010), and co-precipitation with anions. The predominant removal mechanisms appear to be chemical binding of Hg to functional groups (e.g., thiol, hydroxyl, carboxylic, chloride) on the surface of and within the biochars. Based on the S XANES and Hg EXAFS analyses, and published studies (Gibson et al., 2011), the following Hg removal mechanisms are proposed:



The relative importance of these individual mechanisms appears to be dependent on the biochar source material and pyrolysis temperature.

3.5 Conclusions

The majority of the biochars studied were highly effective with respect to the removal of Hg from aqueous solution and highlight the potential of biochars for this purpose. Hg distribution maps indicate that Hg is unevenly distributed across the biochar particles. Hg binds to S functional groups of the investigated biochars with elevated S content and binds to O and Cl functional groups of the biochar with low S content.

S speciation plays an important role in Hg speciation. The presence of S in the biochar samples is variable, with contents ranging from less than the analytical detection

limit to greater than 3%. The S in the biochar samples is present in both reduced and oxidized species. Variable concentrations of SO_4^{2-} leach from the biochars.

In some aquatic environments, elevated concentrations of SO_4^{2-} and labile organic matter might promote growth of SRB, the primary group of methylating bacteria. Of the biochars studied, elevated concentrations of SO_4^{2-} and labile organic compounds are evident in manure-based biochars and biochars produced from cocoa husk. The lowest concentrations of these components are released from wood-based biochars and biochars produced from cotton seed husk, corn cob and stover, and grasses, suggesting these biochars may have a lower potential to stimulate growth of SRB. The presence of DOM also might promote complexation reactions with Hg, potentially increasing Hg mobility. These results suggest that, in addition to considering the extent of Hg uptake by biochars, the presence of dissolved components that are known to promote Hg complexation and methylation reactions should be considered when selecting biochars for different environmental applications.

Table 3.1 Abbreviations, sources of feedstock, and pyrolysis temperatures for biochar samples.

Abbreviation ^a	Feedstock	T (°C)	Abbreviation	Feedstock	T (°C)
Wood			Agricultural residue		
AC1	activated carbon	- ^b	CS1H	corn stovers	600
AC2	activated carbon	- ^b	CS1L	corn stovers	300
CL1	Wicked Good Charcoal	~700	CS2H	corn stovers	600
CL2	Cowboy Charcoal	~700	CS2L	corn stovers	300
CL5	Biochar Engineering Charcoal	~700	CC1H	corn cob	600
SW1H	mulch	600	CC1L	corn cob	300
SW1L	mulch	300	CC2H	corn cob	600
SW2H	pine bark	600	CC2L	corn cob	300
SW2L	pine bark	300	CA1H	cocoa husk	600
Manure			CA1L	cocoa husk	300
MB1H	cow manure	600	CT1H	cotton seed husk	600
MB1L	cow manure	300	CT1L	cotton seed husk	300
MP1H	chicken manure	600	GR2H	wheat shaft	600
MP1L	chicken manure	300	GR2L	wheat shaft	300
MP2L	chicken manure	300	GR3H	spent hops	600
MP3H	chicken manure	600	GR3L	spent hops	300
MU1H	mushroom soil	600	GR4H	switchgrass	600
MU1L	mushroom soil	300	GR4L	switchgrass	300
MU2H	mushroom soil	600			
MU2L	mushroom soil	300			
MU3H	mushroom soil	600			

^a Number after the first two letters indicates different sources; H and L at the end represent biochar preparation at high (600 °C) vs. low (300 °C) temperature, respectively.

^b not applicable

Table 3.2 S content of biochars as a function of pyrolysis temperature.

Group	Biochar	S (%)	
		Low-T	High-T
Wood	AC2	-	0.18±0.02
	AC1	-	0.18±0.01
	CL5	-	<0.01
	CL2	-	<0.01
	CL1	-	0.14±0.01
	SW1	0.04±0.01	<0.01
	SW2	0.03±0.01	0.04±0.01
Agricultural residue	CS1	0.10±0.02	0.82±0.03
	CS2	0.11±0.02	0.37±0.02
	CC2	0.04±0.01	0.02±0.01
	GR4	0.10±0.01	0.55±0.02
	GR2	0.21±0.02	0.36±0.02
	GR3	0.13±0.02	0.34±0.02
	CC1	0.05±0.01	0.03±0.01
	CT1	0.02±0.01	0.03±0.01
	CA1	0.16±0.02	0.20±0.02
Manure	MP1	0.54±0.02	0.48±0.02
	MU2	2.4±0.05	2.4±0.04
	MU3	-	0.58±0.02
	MP2	0.67±0.02	-
	MP3	-	1.9±0.02
	MU1	3.1±0.05	3.4±0.06
	MB1	0.14±0.02	0.09±0.02

Table 3.3 Percentage (%) of different S forms calculated by LCF

Standards	AC	AC- 6 ^a	CL2	CL2- 6	GR4L	GR4L- 6	GR4H	GR4H -6	MP1H	MP1H- 12
K ₂ SO ₄	27	26	29	16	36	53	18	13	91	62
Dibenzo thiophene	44	23	71	84	64	47	82	87	9	27
Thianthrene	11	27	-	-	-	-	-	-	-	-
Elemental S	18	24	-	-	-	-	-	-	-	-
Pyrrhotite	-	-	-	-	-	-	-	-	-	11
Reduced χ^2	0.11	0.08	0.03	0.03	0.13	0.15	0.02	0.02	0.39	0.04

^a labels -6 and -12 indicate number of washes

Table 3.4 Hg EXAFS fitting results ^a

sample	path	CN	R (Å)	S ₀ ²	σ ² (Å ²)	ΔE ₀ (eV)	R-factor
AC	Hg-O	1.17 (±0.16)	2.08 (±0.03)	0.962 ^b	0.004 ^b	0.64	0.09
CL2	Hg-Cl	0.55 (±0.06)	2.26 (±0.01)	0.967 ^b	0.002 ^b	-6.9	0.013
GR4L	Hg-O	1.69 (±0.22)	2.09 (±0.04)	0.962 ^b	0.004 ^b	8.1	0.094
GR4H	Hg-S	0.83 (±0.18)	2.24 (±0.05)	0.841 ^b	0.005 ^b	-2.5	0.064
MP1H	Hg-S	1.17 (±0.07)	2.26 (±0.03)	0.841 ^b	0.005 ^b	-1.5	0.005
Cinnabar	Hg-S	2	2.37	0.841 (±0.123)	0.005 (±0.001)	3.51	0.015
HgO	Hg-O	2	2.04	0.962 (±0.126)	0.004 (±0.001)	-2.62	0.009
	Hg-O	3	2.79	0.962(±0.126)	0.025(±0.006)	-2.62	0.009
HgCl ₂	Hg-Cl	2	2.29	0.967 (±0.107)	0.002 (±0.001)	-0.6	0.006

^a CN = coordination number, R = bond length, and R-factor = fitting statistic.

^b fixed values from model compounds

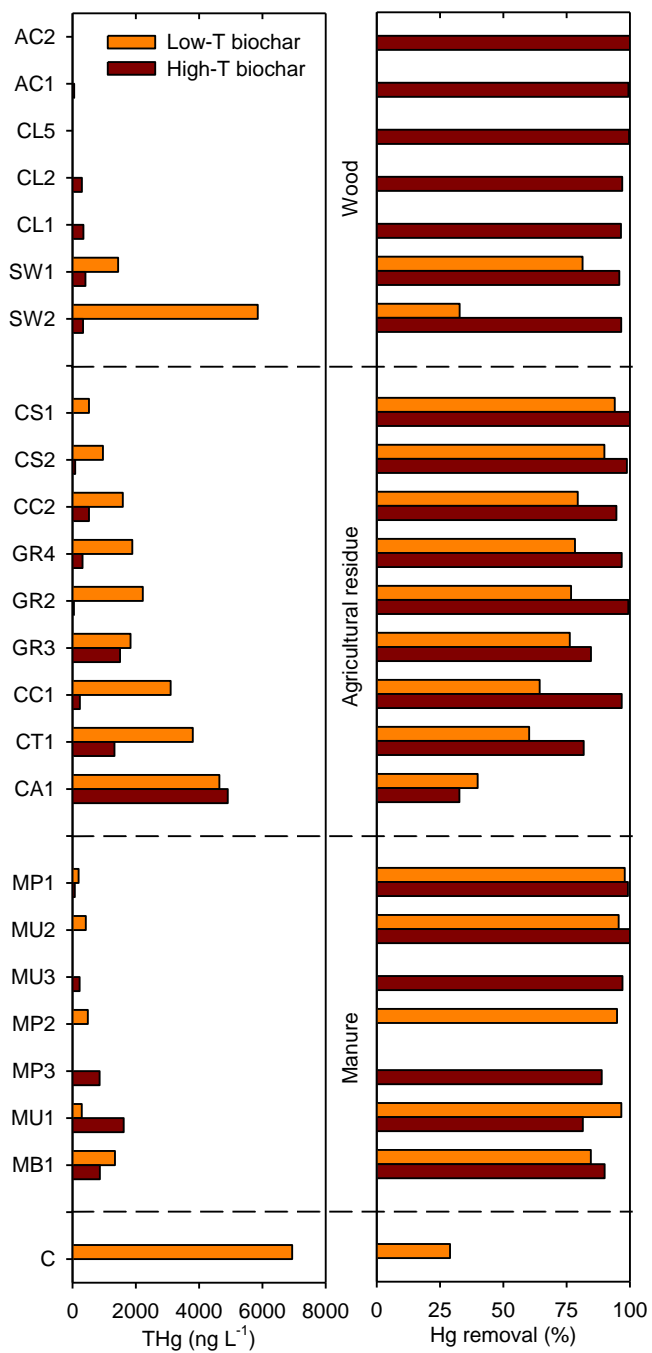


Figure 3.1 THg concentrations and % Hg removal from aqueous solution in batch tests containing biochar and river water spiked with Hg. C represents the control containing Hg-spiked river water with no biochar added.

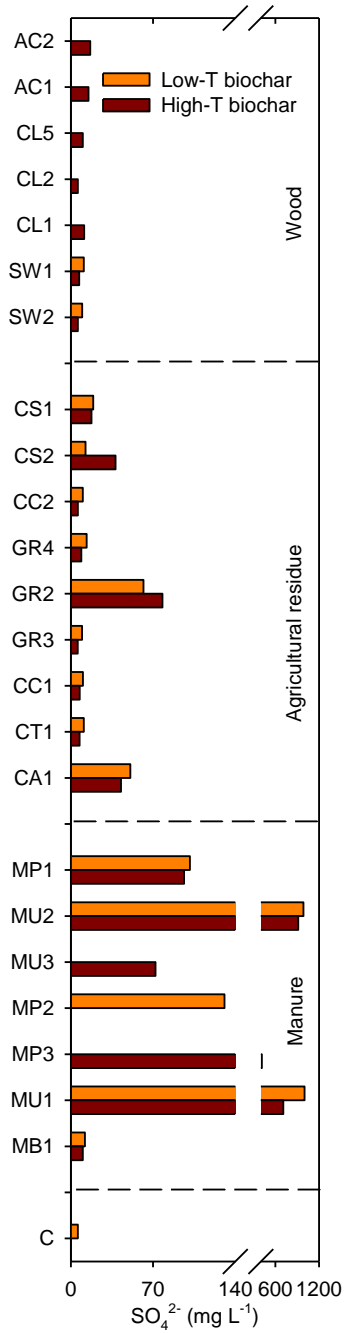


Figure 3.2 Concentrations of SO_4^{2-} in river water (control C) versus concentrations in batch mixtures containing river water and biochar.

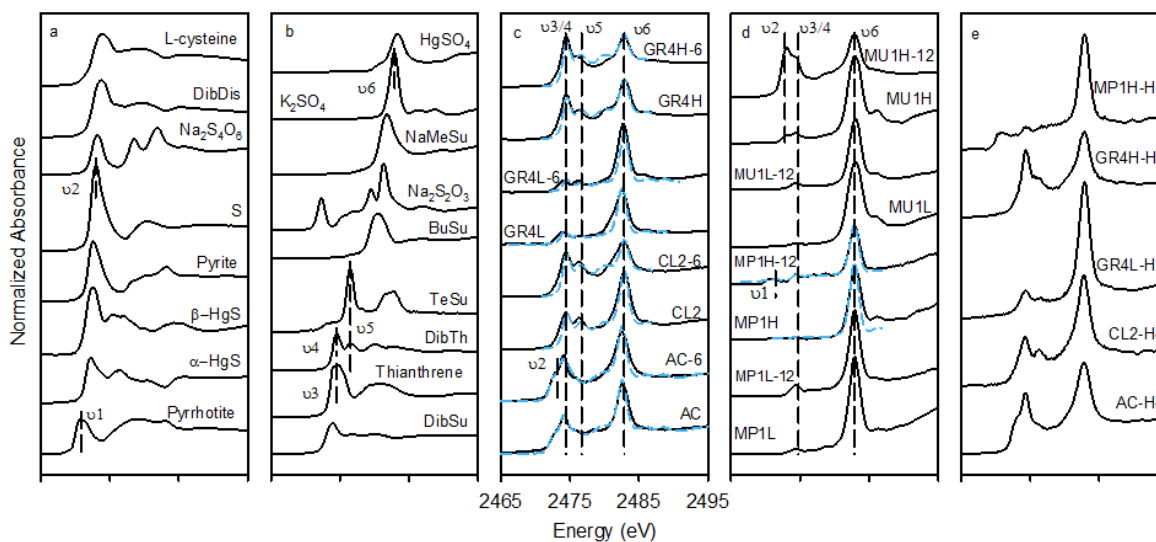


Figure 3.3 ^{a b} S XANES spectra for 17 S standards. ^{c d} S XANES spectra for unwashed and washed biochars; the number after the sample name indicates the number of times that the sample was washed. The dashed blue line indicates the fitted curves for samples using LCF. Spectra identifications displayed on the left side of subplots b, c, and d indicate samples where the spectra were reduced by half for ease of display. ^e S XANES spectra for activated carbon and biochars with adsorbed Hg(II).

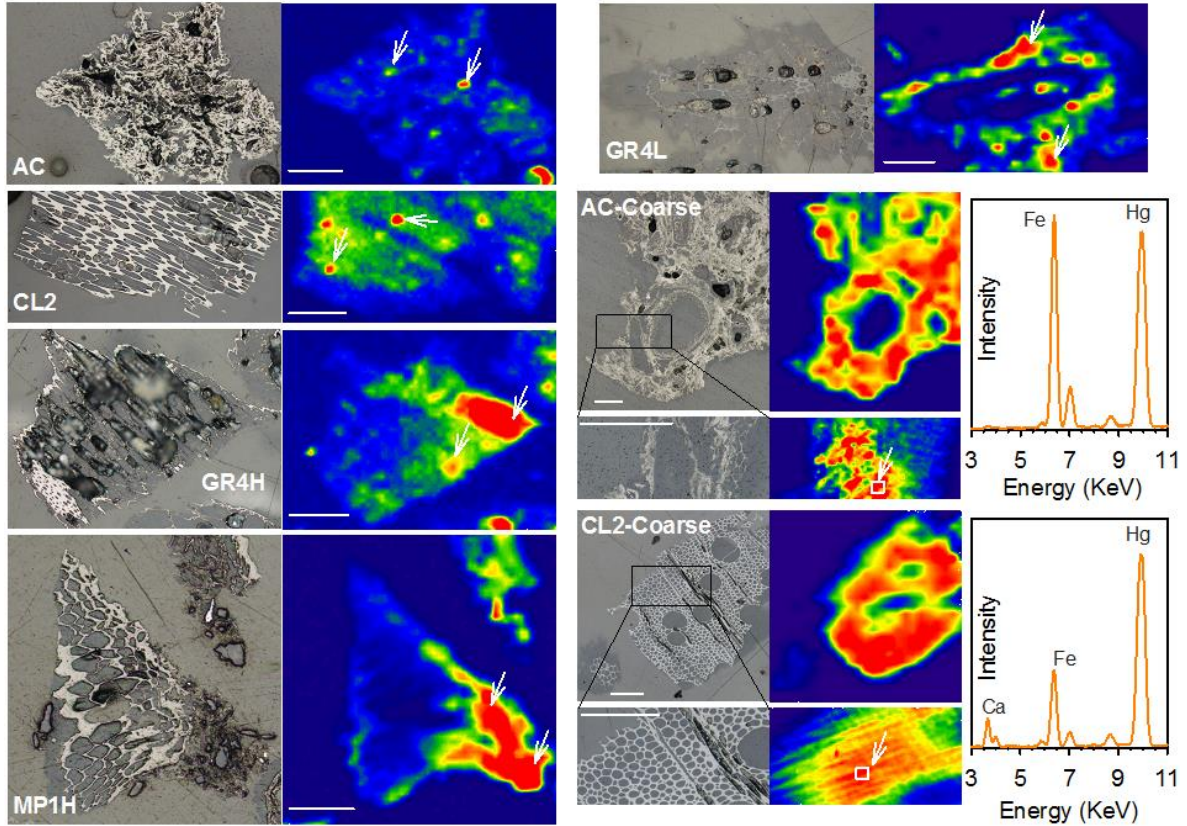


Figure 3.4 Microscope photos under reflection mode (left) and Hg L_{α} line μ -XRF maps (right) in thin sections. The white bars represent 100 μm . The EXAFS spectra for modeling were collected at the locations indicated by white arrows. Note: For AC-Coarse and CL2-Coarse, a high resolution mapping area is displayed directly below each map. The XRF spectra displayed on the right side were collected over the areas identified by white squares in the maps directly to the left of the XRF spectra.

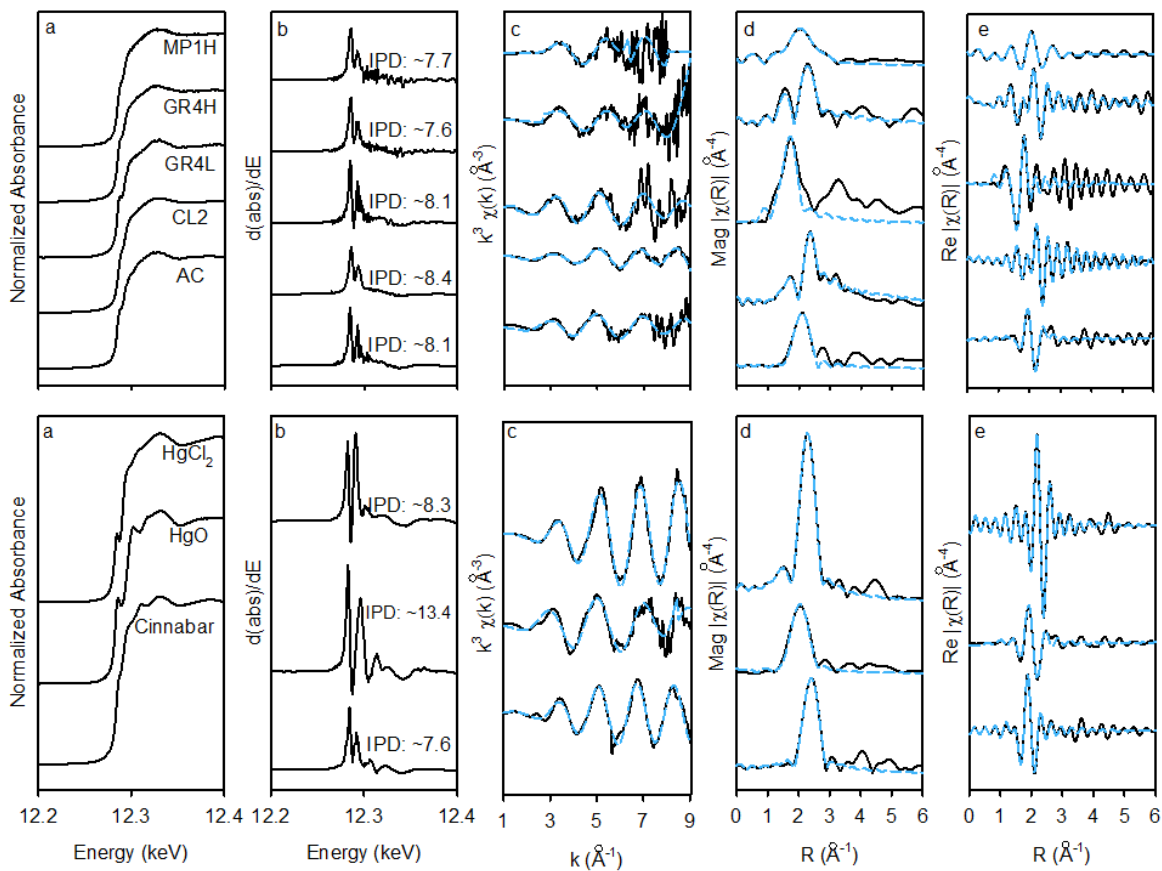


Figure 3.5 ^a Normalized Hg XANES spectra. ^b First-derivative spectra, where IPD is the inflection point difference. ^c k^3 -weighted chi spectra (black line) and best fit (light blue-dash line). ^d Fourier-transformed magnitude spectra. ^e Fourier-transformed real part.

Chapter 4: *Evaluation of Mercury Stabilization in Sediment by Biochars under Reducing Conditions*

Reproduced from: Liu, P., Ptacek, C.J., Blowes, D.W., Finfrock, Y.Z., Gordon, R.A., 2016. Stabilization of mercury in sediment by using biochars under reducing conditions. *J. Hazard. Mater.* 10.1016/j.jhazmat.2016.11.033, Copyright (2016) with permission from Elsevier, License Number 3994800488881. Editorial and formatting changes have been made to accommodate reproduction in this thesis.

4.1 Executive Summary

Mercury (Hg) is widely distributed in different localities around the world and poses a serious health threat to humans, especially when ingested in the form of methylmercury (MeHg). Efforts have been directed toward decreasing the production of MeHg by converting Hg to stable forms. Activated carbon and biochar have been evaluated as stabilization agents for Hg in contaminated sediments. However, the long-term fate of Hg stabilized by these materials remains unclear. Here, we compare the effectiveness of Hg stabilization using two biochars prepared from switchgrass at 300°C (low T) and 600°C (high T). Experiments were conducted by co-blending biochars and sediment for 600 d under anaerobic conditions. Aqueous concentrations of total Hg and MeHg were greatly reduced in the presence of biochars, with the exception of a spike in MeHg concentration observed at ~440 d in the high-T biochar system. Hg co-occurs with S, Fe, Cu, and other elements within low-T biochar particles and primarily on the surfaces of high-T biochar particles. Our results indicate that the stabilization of Hg may be through early diagenesis, suggesting that this stabilization may be effective over long time frames.

4.2 Introduction

Hg is widely distributed in the environment, and poses serious health risks to humans. MeHg, an organic form of Hg, is much more toxic than inorganic Hg and can cause central nervous system defects (Tchounwou et al., 2003). Inorganic forms of Hg can be converted to MeHg by microbes (Gilmour et al., 1992; Hu et al., 2013; Kerin et al., 2006; Yu et al., 2013) under anaerobic conditions (*e.g.*, sediments and wetlands), especially in the benthic zone of lakes, rivers, and oceans just below the oxic/anoxic interface (Benoit et al., 2003). Many efforts have focused on decreasing the direct release of Hg and the production of MeHg by dredging Hg-contaminated sediment (Bloom &

Lasorsa, 1999), *in situ* capping (Randall et al., 2013), or by converting Hg to less bioaccessible forms (Gilmour et al., 2013; Gomez-Eyles et al., 2013; Serrano et al., 2012b). Pyrogenic carbonaceous materials, including activated carbon, are widely used for Hg removal from aqueous solutions (Bailey et al., 1999) and less extensively for Hg stabilization in sediments (Gilmour et al., 2013; Gomez-Eyles et al., 2013).

Biochar, a type of black carbon with properties similar to charcoal, is a low-cost alternative to activated carbon. Biochar can be produced on site and can be used as a soil amendment to improve soil fertility (Liu et al., 2013), to sequester carbon (Lehmann, 2007b; Spokas et al., 2012), and in water and soil treatment applications (Ahmad et al., 2014). Black carbon can remain stable in the environment for an extended period of time, ranging from decades to centuries or longer (Mann, 2002; Spokas, 2010).

Despite the increasing utilization of biochar for water treatment (Bailey et al., 1999) and stabilization in contaminated sediments (Gomez-Eyles et al., 2013), the long-term fate of Hg after uptake by biochars remains unclear. We hypothesize that amending contaminated sediment with biochar can reduce aqueous concentrations of Hg and MeHg and can convert a fraction of the Hg to stable forms within the biochar particles. We also hypothesize that the degree of uptake by the biochar is dependent on the pyrolysis temperature used to prepare the biochar. Our specific objective was to investigate the correlation between filtered total Hg (THg) and MeHg with 1) the evolution of aqueous indicators of biogeochemical processes (*e.g.*, Fe, SO_4^{2-} , organic carbon); 2) the evolution of microbial communities; and 3) the changes in binding environment and distribution of Hg within the biochars after extended reaction times.

In addition to conventional XAS measurements, confocal X-ray micro-fluorescence imaging (CXMFI), which is an emerging non-destructive technique (Pushie et al., 2014), was employed. CXMFI provides compositional and structural information from precise locations on the surface of, and within, intact particles, with greater spatial precision than can be obtained using conventional micro x-ray fluorescence (μ -XRF) methods (Vincze et al., 2004). Limited applications of CXMFI are reported for natural materials; examples include the characterization of Se accumulation in fish eye lens (Choudhury et al., 2015b); W, Pt, and Fe in particles embedded in a mineralogical matrix (Cordes et al., 2015); K, Ca, and Fe in rice grains (Nakano & Tsuji, 2006); and U-Th-Pb for dating of geological materials (Schmitz et al., 2009).

Two biochars prepared at 300 and 600 °C from switchgrass, a widely available material in North America, were selected for co-blending with Hg-contaminated sediment and river water under anaerobic conditions. Samples of the aqueous and solid phases were collected as a function of time to determine shifts in chemical composition, microbial population, and Hg-binding environment through X-ray absorption spectroscopy (XAS) measurements.

4.3 Materials and Methods

4.3.1 Materials

The sediment (38° 5'46.92"N, 78°51'58.16"W) was collected from South River, Virginia, downstream of a historical point (38° 3'49.00"N, 78°53'4.65"W) of Hg release. The river water was collected 300 m upstream of the historical point. Raw switchgrass was air dried and pyrolyzed for biochar using a kiln at either 300 or 600 °C for 2-3 h under O₂-deficient conditions (Liu et al., 2015).

4.3.2 Microcosm Experiment

Microcosm experiments were conducted by mixing biochar, sediment, and river water at a ratio of 1:20:160 (5:100: 800 g) in amber bottles. Controls included ultra-pure water, river water, sediment mixed with river water, and biochar mixed with river water. The experiments were conducted in an anaerobic glovebox.

Unfiltered aqueous samples were collected for analysis of pH and Eh, and samples filtered using 0.45- μm membranes were collected for analysis of alkalinity, anions, cations, dissolved organic carbon (DOC), THg and MeHg. Sample splits were also filtered through 0.2- μm membranes for THg analyses.

Solid samples for MeHg and pyrosequencing analyses were collected with a sterilized spatula at 65, 100, 154, 235, and 387 d and stored at -20°C before analysis. Biochar particles for synchrotron analyses were separated from the solid phase by hand-picking from the amended system with a tweezer at 65, 100, 154, 235, 387, and 600 d. Biochar particles were washed three times using ultrapure water to remove fine sediment particles on the surface, freeze-dried and stored in the anaerobic chamber until analysis. The hand-picked biochar particles collected at 65, 100, 154, 235 and 387 d were mounted in epoxy on a quartz-glass slide and prepared as thin sections with a size of 26×26 mm and a thickness of 30 μm (Vancouver Petrographics Ltd., Canada). CXMFI analysis was conducted on biochar particles collected at 600 d.

4.3.3 Chemical Analyses

Determinations of pH were made using a Ross combination pH electrode (Orion 815600, Thermo Scientific), calibrated against pH 4, 7 and 10 buffers. Determinations of Eh were made using a Pt combination Eh electrode (Orion 9678, Thermo Scientific), checked

against ZoBell's (Nordstrom, 1977) and Light's (Light, 1972) solutions. Alkalinity was determined using a Hach digital titrator using bromocresol green-methyl red as an indicator and titrating to the end point using 0.16 mol L⁻¹ H₂SO₄. Concentrations of anions (including short-chain organic acids) were determined using ion chromatography (ICS-5000, Dionex Corp.) with an IonPac AS11 4×250 mm column. Cation concentrations were analyzed by inductively coupled plasma-optical emission spectrometry (Thermo Scientific iCAP 6500) and inductively coupled plasma-mass spectrometry (Thermo Scientific XSeries II). DOC was determined using an automated wet chemical oxidation method (Aurora 1030, OI Analytical).

Concentrations of THg were determined using a cold vapour atomic fluorescence spectroscopy technique (CVAFS, Tekran 2600), following EPA method 1631, with a method detection limit (MDL) of 0.2 ng L⁻¹. MeHg in the aqueous phase was analyzed through distillation (Tekran 2750), aqueous ethylation, and purge and trap using the CVAFS technique (Tekran 2700) following EPA method 1630. Determination of MDL for MeHg was performed for each run and an average MDL of 0.02 ng L⁻¹ was calculated. Solid samples for MeHg analyses underwent distillation by mixing with a solution containing 20% KCl and 8M CuSO₄ to improve recovery (Horvat et al., 1993).

The C/S content of the sediment and biochar was analyzed using a resistance furnace (Eltra CS-2000) and elemental composition was obtained following EPA Method 3052. The total organic carbon (TOC) of the sediment was analyzed using a segmented flow analyser (Skalar, Netherlands) following EPA Standard Method 5310C.

4.3.4 Pyrosequencing analysis

Genomic DNA was isolated and purified from solid-phase samples using commercial extraction kits (UltraClean Soil DNA Kit; MO BIO Laboratories). Purified DNA was shipped to MR DNA Laboratory (Shallowater, Texas) for pyrosequencing analysis. Detailed information on the selected primers (515/806 for bacteria and archaea), the processes and conditions of polymerase chain reaction and sequencing, and data processing procedures is provided in the Appendix C. Operational taxonomic units were defined as clustering at 3% divergence (97% similarity). Potential Hg methylators were extracted from the pyrosequencing results based on the methylators identified by Oak Ridge National Laboratory (2015). The potential methylators include fermentative bacteria, iron-reducing bacteria (FeRB), sulfate-reducing bacteria (SRB), methanogens, and others (Table S4.1).

4.3.5 X-Ray Absorption Spectroscopy

The separated biochar particles were prepared as thin-sections (26×26 mm in size and 30 μm thick). Micro-XRF maps were collected from thin-sections on Beamline 13-ID-E GSECARS and 20-ID-B PNC/XSD of the Advanced Photon Source. A focused beam ~2×2 μm² and step size of 2 μm were used for the μ-XRF map collection. A photon energy of 12.6 keV was applied for μ-XRF maps of Hg, Cu, Mn, Fe, Zn, Ni, Ca, and K and of 2.5 keV for S μ-XRF maps. Areas with elevated Hg intensity were identified for acquisition of extended X-ray absorption fine structure (EXAFS) spectra. The EXAFS spectra of Hg were processed using Athena, and EXAFS model calculations were made using Artemis (Ravel & Newville, 2005) following the methods described by Gibson et al. (2011) and Liu et al. (2016b).

CXRF of the Hg-bearing biochar particles at 600 d was conducted at PNC/XSD. Biochar particles were mounted on a quartz slide and oriented at 35° to the incident beam (Fig. S4.1). The XRF spectra were monitored by a Si-drift Vortex detector placed at 90° relevant to the incident beam. A Ge optical unit (lithographically fabricated spoked channel array) was mounted in front of the detector to complete the confocal geometry with a probing volume of ~2 μm (Woll et al., 2012; Woll et al., 2014).

4.3.6 Correction Method for X-Ray Fluorescence Attenuation

The intensity attenuation was calculated for the incident beam and XRF arising from the additional depth into the sample using the Beer-Lambert Law by modifying a method described by Choudhury et al. (2015b). The equation $A = \log(I_0/I) = \rho * \sigma * l$ was used to calculate the unknown I_0 and I of each pixel in each elemental intensity map, where A is absorbance, I_0 is incident intensity, I is transmitted intensity, ρ is average density along the beam path (g cm^{-3}), σ is the average total absorbance cross section along the beam path ($\text{cm}^2 \text{g}^{-1}$), and l is depth from a pixel to the edge of the intensity maps (cm). Spectral regions of interest were extracted from the spectra in an *hdf5* file for $L\alpha$ line of Hg and $K\alpha$ lines of Si, P, S, Cl, K, Ca, Ti, Cr, Mn, Fe, Co, Ni, Cu, Zn, and Se. The attenuation was calculated assuming: 1) the density distribution of the mapping area was proportional to the fraction of total intensity in each pixel over the total intensity of the entire map; and 2) the elemental mass distribution was proportional to the fraction of intensity for the corresponding element in each pixel over the intensity of the entire map. The density and elemental composition of the Hg-bearing particles were estimated based on the density and elemental composition of the sediment and biochar particles (Tables S4.2-S4.3). The density and elemental composition of each pixel were calculated based on these

assumptions. The averaged total absorbance cross section along the beam path was calculated using the McMaster table (McMaster et al., 1969) and the calculated elemental composition of each pixel along the beam path. The method was verified by a NIST reference standard material (SRM 1834) Data importing, processing, and plotting were completed in MATLAB.

4.4 Results and Discussion

4.4.1 Overview of Sediment, River Water, and Biochar

The sediment selected for this study was collected from a Hg-enriched area, and had a Hg content of $187 \mu\text{g g}^{-1}$ and was the only Hg source in the experiment, S content of $300 \mu\text{g g}^{-1}$, Fe content of $16,000 \mu\text{g g}^{-1}$, and Cu content of $150 \mu\text{g g}^{-1}$ (Table S4.2). The low-T and high-T biochars were rich in C (70.2 and 94.5%) and relatively low in S (0.1 and 0.55%) (Table S4.3). The river water contained low concentrations of THg ($<5 \text{ ng L}^{-1}$), MeHg ($<0.02 \text{ ng L}^{-1}$), and other components (Table S4.4).

4.4.2 pH, Redox Potential and Alkalinity

Values of pH for the sediment control and amended systems gradually increased from ~ 7.5 to ~ 9.0 in the first 150 d and then decreased slightly to ~ 8.5 at day 445. The redox potential (Eh) values for the sediment controls and amended systems decreased from ~ 50 to $\sim -420 \text{ mV}$ in the first 126 d, then decreased further to $\sim -440 \text{ mV}$ toward the end of the experiment at day 445 (Fig. S4.2). The Eh values indicate an anaerobic environment was maintained over the course of the experiment. The alkalinity concentrations increased from ~ 50 to $\sim 200 \text{ mg L}^{-1}$ before day 100 and then decreased to $\sim 50 \text{ mg L}^{-1}$ at day 445 in sediment controls and amended systems.

4.4.3 Aqueous THg and MeHg

Filtered (0.2 μm) THg concentrations initially increased as a function of time, ranging from 0.8 to 24 $\mu\text{g L}^{-1}$ for sediment controls (Fig. 4.1) and peaking at day 182 in the high-T (14 $\mu\text{g L}^{-1}$) and low-T (6.6 $\mu\text{g L}^{-1}$) biochar amended systems. For sediment controls, the concentrations of 0.45- μm filtered THg during the first 60 d increased from 2 to 40 $\mu\text{g L}^{-1}$, decreased to ~ 10 $\mu\text{g L}^{-1}$ at day 100, and then stabilized at ~ 40 $\mu\text{g L}^{-1}$ from day 130 until the remainder of the experiment. The 0.45- μm filtered THg concentrations in the high-T and low-T amended systems were highly variable during the first 80 d, then increased from ~ 3 to ~ 30 $\mu\text{g L}^{-1}$ from day 80 to 120 before decreasing to ~ 11 and ~ 3 $\mu\text{g L}^{-1}$, respectively. THg concentrations were < 10 ng L^{-1} in the controls of ultrapure water, river water, and biochar.

MeHg concentrations were low (< 5 ng L^{-1}) during the first 23 d (Fig. 4.1; enlarged in Fig. S4.3). After the lag phase, a pronounced increase was observed (first blue bar, Fig. 4.1), followed by a decline in concentrations and then a second spike (second blue bar, Fig. 4.1). For the two sediment controls, MeHg concentrations initially increased to 48 ng L^{-1} at day 37 and to 130 ng L^{-1} at day 47, respectively. For the amended systems, the first increase of ~ 12 ng L^{-1} was observed at day 100. A second increase in MeHg to 64 ng L^{-1} at day 265 and to 28 ng L^{-1} at day 387 was observed in the two controls, and to 27 ng L^{-1} for the low-T biochar amended system. A second peak in MeHg concentration of 260 ng L^{-1} was observed at day 445 in the high-T amended system. This value is much greater than observed in the controls and low-T amended system. The MeHg concentrations were < 0.02 ng L^{-1} in the ultrapure water, river water, and biochar controls.

The results indicate the addition of biochars resulted in lower THg and MeHg concentrations than in sediment controls, except the late MeHg concentration spike in the high-T amended system. The late MeHg concentration spike in the high-T amended system occurred without the addition of a new source of electron donors and acceptors. Concentrations of THg and MeHg in the low-T amended system were less than those in the high-T amended system. These results indicate uptake of THg and MeHg by the biochar occurred during the experiment. The results also show greater uptake of THg by the low-T biochar. This latter result contrasts observations by Liu et al. (2016b), who observed greater uptake by high-T biochar in batch-style experiments.

4.4.4 Aqueous Fe and SO₄²⁻

A lag (23 d) was observed with respect to the increase in Fe concentrations (<0.2 mg L⁻¹; Fig. 4.1, Fig. S4.3). After the lag, Fe concentrations increased to maximum values of ~1.3 mg L⁻¹ for sediment controls and 0.7 for high-T and 3.5 mg L⁻¹ for low-T biochar amended systems at day 100, before decreasing to <0.2 mg L⁻¹ after day 154. SO₄²⁻ concentrations decreased to <0.05 mg L⁻¹ after 79 d for sediment controls, and after 65 and 100 d for low-T and high-T biochar amended systems.

The increase in Fe concentrations corresponded to an increase in THg concentrations (Fig. 4.1; enlarged in Fig. S4.3). The increase in THg concentrations is attributed to the dissolution of Hg-bearing iron oxide solids originally in the sediment, where Hg often accumulates (Bernaus et al., 2006; Gu et al., 2014; Tiffreau et al., 1995). The decrease in SO₄²⁻ concentrations correspond to a decrease in concentrations of THg and Fe, which is likely due to removal associated with the formation of Hg and Fe sulfide precipitates. The concentrations of SO₄²⁻ were <0.05 mg L⁻¹ after ~75 d, after which THg

concentrations started to increase (Fig. 4.1; enlarged in Fig. S4.3). This increase in THg concentrations is likely due to the lack of formation of biogenic sulfide. This observation is consistent with a previous study (Poulin et al., 2016), in which aqueous concentrations of THg were observed to be highly variable in response to redox oscillations in a microcosm experiment containing riparian soils.

4.4.5 Solid-Phase MeHg

The MeHg contents in the low-T system (20-100 ng g⁻¹) were greater than those in sediment controls (20-40 ng g⁻¹) at all times (Fig. 4.2). The MeHg contents in the high-T amended system were less than those in sediment controls before day 154; but, much greater than the controls after day 235 (up to 260 ng g⁻¹). The high MeHg contents in the high-T system after day 235 correspond to the MeHg concentration spike in the aqueous phase (Fig. 4.1). The elevated MeHg contents in the amended systems were likely due to the adsorption of aqueous MeHg by biochars, which is consistent with previous studies (Gilmour et al., 2013; Gomez-Eyles et al., 2013).

4.4.6 Aqueous Carbon Source

Different patterns in concentration shifts of DOC, acetate, and alkalinity were observed in the sediment controls and amended systems (Fig. 4.3). The concentrations of DOC increased from ~2 to 90 mg L⁻¹ in the sediment controls and to ~60 mg L⁻¹ for the amended systems over the course of the experiment. The acetate concentrations peaked at 31 mg L⁻¹ at day ~100 in the low-T amended system and at 40 mg L⁻¹ at day ~200 in the sediment control and high-T amended system. The alkalinity concentrations increased from ~50 to ~180 mg L⁻¹ at day 100 for the sediment control, and to 260 and 200 mg L⁻¹ at day 65 for low-T and high-T amended systems; alkalinity concentrations decreased to

~50 mg L⁻¹ at the termination of the experiment. The DOC and acetate are carbon sources for microbes, for example, FeRB, SRB, and methanogens. Alkalinity (including HCO₃⁻ and CO₃²⁻) can be utilized as carbon energy sources by methanogens (McCollom, 1999).

4.4.7 Potential Methylators

The pyrosequencing results indicate the total abundances (percentages) of potential methylators was <0.5% in all samples (Fig. 4.4). The total abundances show an increasing and then decreasing pattern in the sediment control and the amended systems from day 0 to 387. The total abundances in the sediment control were lower than in the amended systems ($P < 0.05$ by t -test). At the beginning of the experiment, only *Geobacter uraniireducens* was observed. An increase in the abundance of species that are potential methylators was observed as the experiment progressed, including SRB, FeRB, and fermentative bacteria.

The early peak in MeHg concentrations is attributed to methylation of Hg by fermentative bacteria, FeRB, and SRB, as potential methylators were detected in the systems (Fig. 4.4), and concentrations of Fe peaked and concentrations of SO₄²⁻ decreased, corresponding to this MeHg peak (Fig. 4.1). The co-existence of FeRB and SRB methylators is consistent with a previous study using sediments from the same watershed (Yu et al., 2012). The second peak in MeHg concentrations toward the end of the experiment is likely due to the activity of methanogenic methylators. Although methanogenic methylators reported in other studies (Avramescu et al., 2011; Hamelin et al., 2011; Yu et al., 2013) were not observed in this study using the pyrosequencing method, other indications of methanogenesis were observed. Toward the end of the experiments, concentrations of SO₄²⁻ were <0.05 mg L⁻¹ and aqueous Fe concentrations

were stable, likely due to low activities of FeRB and SRB. Concentrations of alkalinity increased slowly and then decreased consistent with increased consumption of inorganic carbon due to methanogenic activity. Thus, the corresponding peak in MeHg may be associated with methanogenic methylators that have not yet been identified (Table S4.1).

4.4.8 μ -XRF and EXAFS

Micro-X-ray fluorescence (μ -XRF) mapping was applied to examine thin-sections prepared with biochar particles from the amended systems at 235 and 387 d (Fig. 4.5). The maps indicate the co-occurrence of Hg with Cu, Fe, S, Mn, Zn, and other elements (Figs. S4.4-S4.6). In the low-T biochar system, Hg, Cu, and Fe were distributed primarily on particle surfaces, but also penetrated into the solid phase (circled area); S was preferentially distributed along the measured planes. In the high-T biochar, Hg, Cu, and Fe were primarily distributed along the pore edges of the particles (Fig. 4.5; Figs. S4.5-S4.6). Mapping of the particles by μ -XRF for thin sections of biochar particles collected at day 65, 100, and 154 was attempted, but the intensity of the XRF signal of Hg, Fe, Cu, etc. was not distinguishable from the background.

To further understand the Hg binding environments (*e.g.*, surrounding elements, coordination numbers) at the atomic level, Hg EXAFS spectra was collected from Hg-rich areas of the high-T biochar (Fig. 4.5). Modeling results indicate that Hg is present as metacinnabar (β -HgS) with a coordination number of 3.9 and a bond length of 2.5 Å, values close to those of the reference material (Fig. 4.5; Fig. S4.7; Table S4.5). The Hg observed in biochar particles likely converted to a stable form by interaction with biogenic sulfide. These analyses are consistent with the observed shifts in aqueous phase chemistry.

4.4.9 Confocal X-Ray Micro-Fluorescence Imaging

The fluorescence intensity measured using conventional XRF mapping represents the sum of information along the measurement path (thickness of the thin sections is 30 μm) of the microbeam (Vincze et al., 2004). To overcome this limitation, CXMFI was conducted to provide spatial distributions of elements accumulated within the biochar particles at a finer scale. The porous structures of the low-T and high-T biochars collected from the amended system after 600 d can be identified using maps of K (Fig. 4.6), Ca, and other elements, which are indicative of the source plant matter (Figs. S4.8-4.9; Table S4.3). The maps indicate that Fe and Hg are distributed throughout the low-T intact biochar particles, whereas Fe and Hg are preferentially observed on the surface of the high-T biochar particles. These observations are consistent with maps of Ti, Cr, Mn, Co, Ni, Cu, Zn, and As (Figs. S4.8-S4.9). These elements coincide with the intact biochar structure. The CXMFI combined with regular μ -XRF mapping indicates that the biochar accumulated both Hg and other elements within its structure.

The co-occurrence of Hg, Mn, Fe, Co, Cu, Zn, etc. within the structure material of low-T and high-T biochar particles indicates secondary minerals were likely formed through a series of biogeochemical reactions and incorporated into the structure of the biochar (Sections 4.4.2-4 and 4.4.6). Previous studies report a size-exclusion effect on the adsorption of dissolved organic matter (DOM) to activated carbon (Agarwal et al., 2016; Ding et al., 2008; Kilduff et al., 1996; Kilduff & Wigton, 1999), and the size of fine sediment (or clay) is greater than DOM, therefore these elements observed inside the structure material of biochar particles were not due to the fine sediment (or clay). The absence of Hg, Fe, Cu, etc. associated with biochar particles collected at day 65, 100, and

154 indicates fine sediment (or clay) was also not attached to the biochar particles (Section 4.4.8).

Differences in elemental distribution patterns for low-T and high-T biochar particles are attributed to changes in the biochar composition and structure due to pyrolysis temperature. DOC and acetate determinations indicate the presence of higher concentrations and more rapid leaching of these compounds from biochar pyrolyzed at 300 °C, and suggest that this material was not as completely carbonized as the biochar pyrolyzed at 600 °C (Fig. 4.3). These results suggest that low-T biochar particles are more easily penetrated by Hg, Mn, Fe, Co, Zn, and other elements, which either precipitated or replaced the original elements within the particle under the anaerobic experimental conditions and in the presence of solutions rich in components with the potential to form minerals. This observation is also consistent with the replacement of organic material in wood chips by secondary minerals (*e.g.*, sulfides) in a permeable reactive barrier after 6 yrs of operation (Jambor et al., 2005).

Early diagenesis includes bacterial decomposition of organic matter, bacterial reduction of sulfate, dissolution and re-precipitation of minerals, bacterial regulated redox reactions, and diffusion of dissolved minerals in sediment (Berner, 1980). The time scale for early diagenesis can be <10 years (Opsahl & Benner, 1995; Torres et al., 2015; Yoshimura & Hama, 2012). In this study, Hg is likely stabilized by the low-T and high-T biochars through similar early diagenetic processes stimulated by the microbial communities.

Mercury was observed to co-occur with Cu, Fe, S, Zn, Mn, and other elements within the low-T and high-T biochar particles. Biochar can remain stable in the

environment over long time frames (Spokas, 2010). The deep penetration of Hg into the biochar structure and the possible presence of Hg as an insoluble sulfide phase suggest that the Hg contained in these particles may also be stable for long periods. We speculate that the uptake of Hg within the biochar structure may lead to a decrease in bioaccessibility and potentially a decrease in methylation of Hg present within biochar grains (Zhang et al., 2012). In addition, encapsulation of Hg within the biochar grains, as observed in our experiments, may limit its transport to other environmental compartments (Lowry et al., 2004).

4.5 Conclusions

The results indicate the evolution of Hg and MeHg in the microcosm experiment is well correlated with the evolution of Fe, SO_4^{2-} , DOC, acetate, and alkalinity in the solution and microbes in the solid phase. The μ -XRF and CXMFI analyses indicate Hg co-occurs with Fe, Cu, and other elements across the biochar particles. Low-T switchgrass biochar is likely an effective material for Hg stabilization in sediments and that the process leading to Hg stabilization is consistent with early diagenetic processes. These findings have ramifications not only for the long-term uptake of metals by biochar, but also the long-term sequestration of carbon through the potential decrease in reactivity of the biochar due to the accumulation of inorganic elements within the structure and an enhanced encapsulation process.

The microcosm experiment in this study was designed to simulate the application of biochar in a setting representative of a stagnant aquatic system with potential burial or mixing of the biochar with organic-rich sediment in a low advective setting. After application of biochar in this setting, the biochar particles are expected to initially settle at the sediment/water interface, and then slowly become incorporated within the sediment

through burial processes. Initially, the system will be oxidized, but it may become more reducing over time. The microcosm study reported here covers a progressively reducing system, from initially oxidizing to Fe(III) and SO₄-reducing to strongly methanogenic. Toward the end of the experiment, elevated MeHg concentrations were observed, suggesting precautions may be required prior to application of biochar in highly reducing systems. These results suggest that biochar amendment should be evaluated for site specific conditions including sediment composition, physical setting, and biogeochemical conditions.

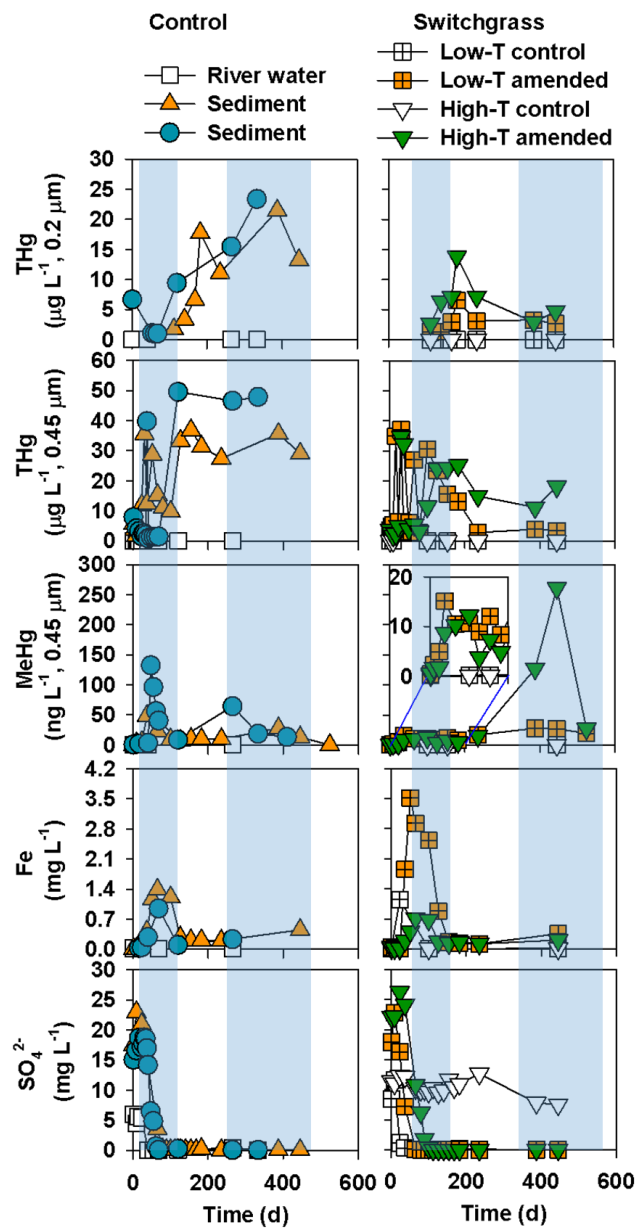


Figure 4.1 Concentrations of 0.2- and 0.45- μm filtered THg, MeHg, Fe, and SO_4^{2-} in aqueous solutions of controls and amended systems vs. time. The blue bars indicate two stages of MeHg production: a combined iron and sulfate reduction period (first) and a methanogenic period (second).

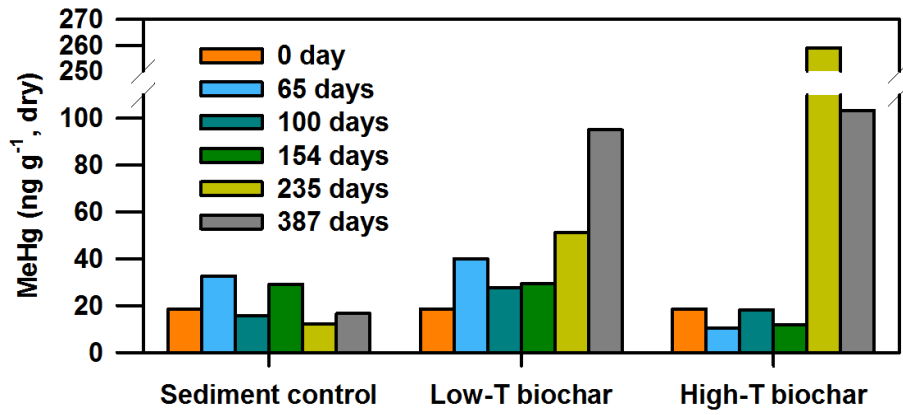


Figure 4.2 MeHg content in sediment control and amended systems (low-T and high-T switchgrass biochars) at day 0, 65, 100, 154, 235, and 387.

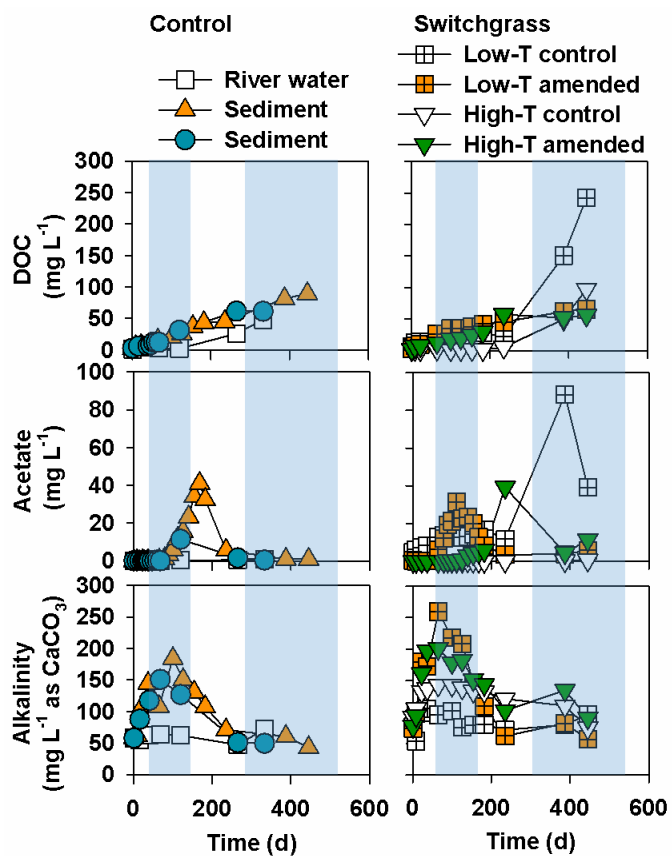


Figure 4.3 Carbon sources (dissolved organic carbon (DOC), acetate, and alkalinity) of controls and amended systems against time. The blue bars indicate two stages of MeHg production: a combined iron and sulfate reduction period (first) and a methanogenic period (second).

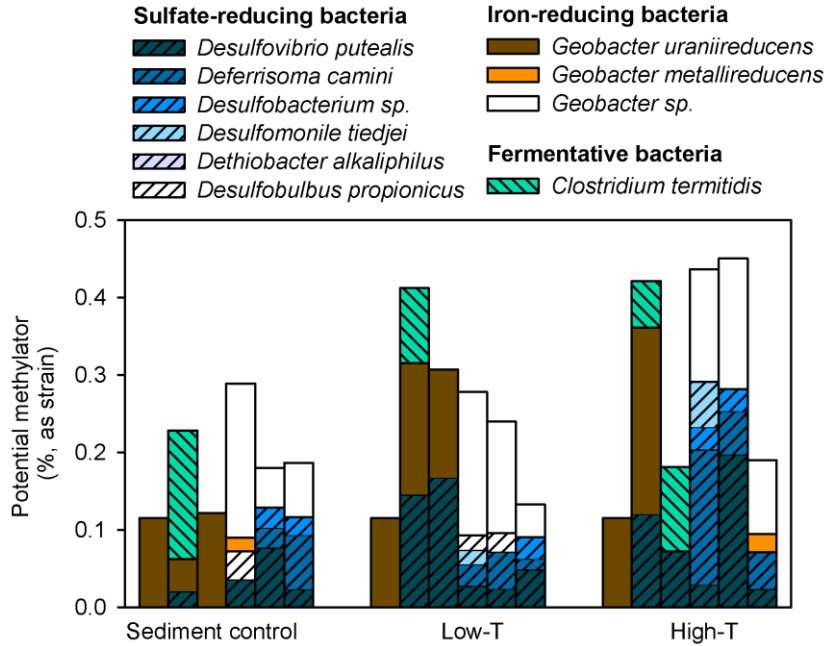


Figure 4.4 Percentages of species identified as known Hg methylators, including sulfate reducing bacteria, iron-reducing bacteria, and fermentative bacteria in sediment control and amended systems. For each sample, columns from left to right represent samples from day 0, 65, 100, 154, 235, and 387, respectively.

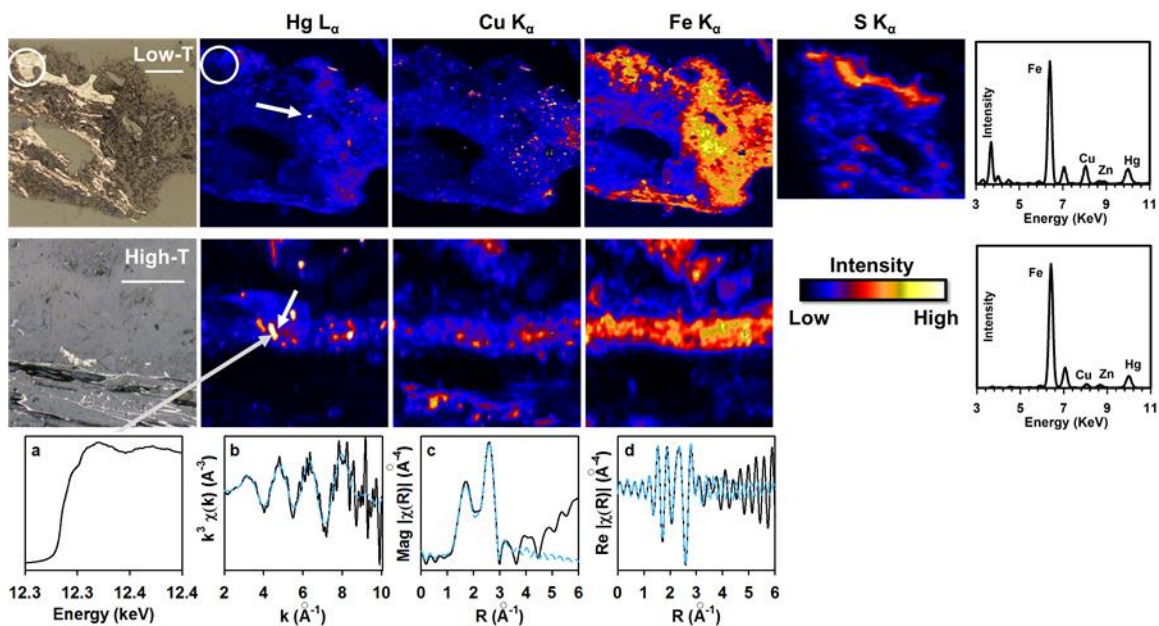


Figure 4.5 Micro-XRF maps (Hg, Cu, Fe, and S) of thin-sections of low-T (top) and high-T (intermediate) biochar particles from amended systems at days 235 and 387, respectively. The first column shows microscopic images and the last column XRF spectra were collected from the area indicated by the white arrow. The S map was collected at a different time and with a different beamline setup. The white scale represents 100 μm . ^a Edge-step normalized Hg L_{III}-edge XANES spectra were collected at the point indicated by the gray arrow. ^b k^3 -weighted chi spectra (black solid line) and the best fit data (light-blue dash line). ^c Fourier-transform magnitude spectra and the best fit data. ^d Fourier-transform real part and the best fit data.

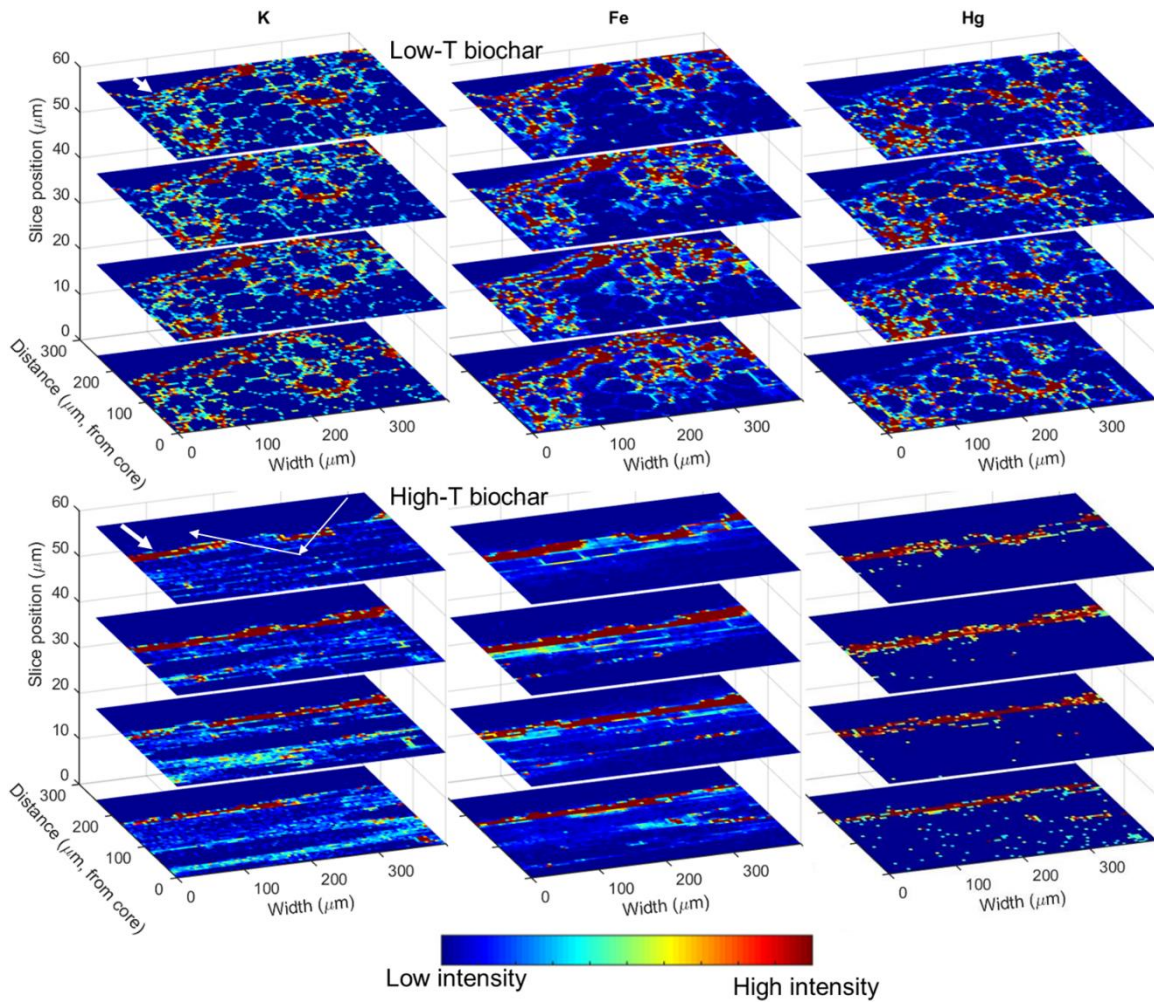


Figure 4.6 Confocal X-ray micro-fluorescence imaging showing the distribution of K, Fe, and Hg in low-T (upper) and high-T (bottom) biochar particles (not physically sectioned) collected from the amended systems after 600 d. The low-T switchgrass biochar particle was analyzed perpendicular and the high-T biochar particle was analyzed parallel to the straw, which accounts for the differences in pore structure. The thick white arrow indicates the surface of the particle. The thin white arrow indicates the incident and emitted beam paths. Note: vertical exaggeration is ~ 7 .

Chapter 5: *Control of Mercury and Methylmercury in Contaminated Sediments Using Biochars*

5.1 Executive Summary

The effectiveness of activated carbon and four-types of biochars, switchgrass (300°C and 600°C), poultry manure (600°C), and oak (~700°C) was assessed for mercury (Hg) and methylmercury (MeHg) control in microcosm experiments carried out for 524 d. At early times (< 30 d), minimal differences in concentrations of <0.45- μm total Hg (THg) in control and 5% biochar-amended systems were observed. At later stages, THg concentrations in the amended systems decreased to 8-80% of the concentrations in the sediment controls. Aqueous concentrations of MeHg were generally lower in the amended systems than in the controls, with a peak in MeHg concentration corresponding to the onset of iron and sulfate reducing (~40 d) and a second peak to methanogenic conditions (~400 d). Pyrosequencing analyses indicate the microbial communities initially associated with fermenters, shifted to iron-reducing bacteria (FeRB), sulfate-reducing bacteria (SRB), and methanogens. These analyses also indicate the existence of twelve organisms associated with Hg methylation in all systems. The community shifts were correlated to changes in concentrations of carbon sources (dissolved organic carbon (DOC), organic acids, and alkalinity) and electron acceptors (NO_3^- , Fe, and SO_4^{2-}). Co-blending of biochars with Hg-contaminated sediment provides an alternative remediation method for controlling the release of Hg and MeHg.

5.2 Introduction

A number of industrial activities, including coal combustion (Yudovich & Ketris, 2005), refuse incineration (Cheng & Hu, 2012), and Au and Hg mining, have resulted in releases of Hg and widespread contamination of receiving watersheds. In these watersheds, Hg is often observed to be unevenly distributed within sediments, soils and groundwater, and is readily cycled among different phases. Ingestion of Hg compounds can cause a series of

serious health problems in humans and animals (Clarkson & Magos, 2006). MeHg, an organic form of Hg, is much more bioaccumulative and toxic than Hg in inorganic forms (Clarkson & Magos, 2006; Tchounwou et al., 2003). Methods are available for the remediation of Hg contaminated sites (Mulligan et al., 2001; Randall & Chattopadhyay, 2013), such as sediment dredging (Han et al., 2006) and *in situ* amendment (Ahmad et al., 2014; Gilmour et al., 2013; Hilber & Bucheli, 2010; Patmont et al., 2015; Serrano et al., 2012a).

MeHg is primarily produced through biotic processes under reducing conditions. The organisms, which can methylate Hg, include SRB (Gilmour et al., 1992), FeRB (Kerin et al., 2006; Yu et al., 2011), and methanogens (Hamelin et al., 2011; Yu et al., 2013). These organisms utilize various carbon sources and electron acceptors (Fe(III), SO_4^{2-}) to methylate bioavailable Hg. Adsorbents can be applied to remove MeHg and Hg directly from the aqueous phase to minimize mass transport (Gomez-Eyles et al., 2013). Another method to control MeHg is the diminution of Hg bioavailability by converting Hg to chemically stable forms (Wang et al., 2012).

Different reactive materials are available for stabilizing Hg, including activated carbon (AC) (Gilmour et al., 2013; Hilber & Bucheli, 2010; Patmont et al., 2015), zero valent Fe (Weisener et al., 2005b), sulfurized clay (Gibson et al., 2011), sulfate-type cements (Serrano et al., 2012a), and biochars (Ahmad et al., 2014; Liu et al., 2016b). However, most of the reactive materials are expensive and not applicable for large contaminated sites, therefore there is a need to identify cost-effective materials to control Hg for remediation of large areas.

Pyrolyzed carbon, including activated carbon and biochars derived from a range of plant materials, has been applied to reduce Hg or MeHg bioaccumulation or concentrations in pore water in sediment (Bundschuh et al., 2015; Gilmour et al., 2013; Gomez-Eyles et al., 2013; Huntington et al., 2015). Gilmour et al. (2013) and Gomez-Eyles et al. (2013) applied AC and biochar for remediation of Hg-contaminated sediment. The pore water concentrations and bioaccumulation of Hg and MeHg were effectively reduced in freshwater sediment amended with AC in both of these studies. These studies reported that biochar is effective for MeHg sorption, but was less effective for control of inorganic Hg. These two studies were conducted for 15 d and focused on bioaccumulation and distribution of Hg and MeHg between aqueous and solid phase (Gilmour et al., 2013; Gomez-Eyles et al., 2013). Bundschuh et al. (2015) reported Hg bioaccumulation decreased after amending sediments with pyrolyzed carbon for up to 175 d. Huntington et al. (2015) reported the application of AC decreases pore-water MeHg concentration, but not MeHg content in sediments in field mesocosms conducted for 91 d. The decrease of MeHg concentration in pore water is attributed to adsorption by AC.

The studies that applied pyrolyzed carbon for treating Hg-contaminated sediment focus on the bioaccumulation of Hg or MeHg; most concentration decreases were attributed to adsorption; and the experimental period was relatively short (15 or up to 175 d). Sediments are often rich in organic matter and can contain various Fe- and sulfate-containing minerals. DOC, labile organic carbon, alkalinity (carbon source for methanogens), and SO_4^{2-} are released from various biochars and AC (Liu et al., 2015; Liu et al., 2016b; Riedel et al., 2014; Uchimiya et al., 2013). After applying pyrolyzed carbon

to sediment, all of these components may affect Hg speciation and MeHg evolution. For example, potential Hg methylators can methylate Hg by utilizing labile carbon as an energy source (electron donor) and Fe and SO_4^{2-} as electron acceptors; biogenic S^{2-} and Hg form Hg-S precipitation; Fe(II) from the reduction of Fe(III) and dissolved Hg compete for S^{2-} ; dissolved organic matter (DOM) and Hg form Hg-DOM complexes.

The focus of this study is to evaluate the stabilization of Hg and MeHg using AC and four distinct biochars over an extended period of time (>500 d). Microcosm experiments were conducted in an anaerobic chamber by mixing sediment, biochars, and water. Geochemical measurements and pyrosequencing analyses were conducted as a function of time to track shifts in the microbial community to provide insight into mechanisms controlling Hg and MeHg evolution after amending with biochars.

5.3 Materials and Methods

5.3.1 Materials

Sediment was collected from an Hg contaminated site at the South River, VA, US, 5.6 km downstream from a historic point of Hg release (see Supporting Information, Fig. S5.1). River water was collected upstream (~0.3 km) of the historic release point. Four biochar samples were employed in the study. Feedstocks of the biochars were air dried and pyrolyzed using a kiln at either 300°C or 600°C for 2-3 h under O_2 -deficit conditions. The biochars include switchgrass biochars (300°C, GRASS300 and 600°C, GRASS600) and poultry manure biochar (600°C, MANURE600) prepared using methods provided in detail by Liu et al. (2015), and commercial oak biochar (rejects of product, ~700°C, OAK700) from Cowboy Charcoal Co.. Commercial activated carbon (AC; Sigma-Aldrich Corp.) was used as a benchmark for comparison.

5.3.2 Anaerobic Microcosm Experiments

Microcosm experiments were conducted by mixing biochar, sediment, and river water at a ratio of 1:20:160 (mass: 5g, 100 g, and 800 g) in amber glass bottles. Controls included ultra-pure water, river water, sediment mixed with river water, and biochar mixed with river water. The sediment control and amended systems using OAK700 and MANURE600 were duplicated to facilitate statistical analysis. The experiments were conducted in an anaerobic chamber (Coy Laboratory Products Inc.) with a gas mixture of 3.5% H₂ balanced N₂. Argon was used to replace the volume removed during sampling events. The amber bottles were shaken thoroughly to remix the solid and aqueous phases after each sampling event.

Aqueous samples were collected versus time using Norm-Ject syringes (Henke Sass Wolf). Aliquots of 0.45- μ m filtered (Pall Corp.) sample were collected for the analyses of alkalinity, anions, total Hg (THg), MeHg, cations, DOC, nutrients (NH₃-N and PO₄-P), and ultraviolet (UV) absorbance at 254 nm. Additionally, unfiltered and 0.2- μ m filtered samples were collected for THg analysis. Duplicate sampling events were regularly executed for quality assurance and quality control. Samples for THg, MeHg, and DOC were stored in 15 mL amber vials (VWR International). Samples for anion, cation and UV analyses were stored in 15 mL high density polypropylene (HDPE) bottles (Thermo Scientific). Samples for anion analyses were maintained at 4°C and analyzed within 48 hrs. Samples for cation and THg analyses were acidified using 15.6N HNO₃ and stored at 4°C. Samples for determinations of MeHg (acidified with 12.1N HCl), DOC and nutrients (acidified using 8N H₂SO₄), and UV absorbance (unacidified) were stored at -20°C. The pH values of acidified samples were <2.

Solid samples were collected for MeHg analyses and pyrosequencing analyses. The sampling time and methods were the same as presented in Chapter 4.

5.3.3 Water Analyses

The pH, Eh, and alkalinity were determined inside the anaerobic chamber on unfiltered samples immediately after sample collection. The pH was determined using an Orion Ross electrode (Thermo Scientific). The performance of the Eh electrode (Orion 9678, Thermo Scientific) was checked against ZoBell's and Light's solutions. The reported value was corrected with the standard hydrogen electrode. Alkalinity was determined by adding bromocresol green-methyl red indicator and titrating to the end point using 0.16 mol L⁻¹ H₂SO₄ and a digital titrator (HACH, Loveland). Concentrations of anions (including short-chain organic acids) were determined using ion chromatography (ICS-5000, Dionex Corp.) with an IonPac AS11 4×250 mm column.

Cation concentrations were determined by inductively coupled plasma-optical emission spectrometry (ICP-OES; Thermo Scientific iCAP 6500) and inductively coupled plasma-mass spectrometry (ICP-MS; Thermo Scientific XSeries II). NH₃-N concentrations were determined using the salicylate spectrophotometric method (Hach Test Method 8155). PO₄-P concentrations were measured using the ascorbic acid spectrophotometric method (Hach Test Method 8048). DOC was determined using an automated wet chemical oxidation method (Aurora 1030, OI Analytical). UV absorbance was measured at 254 nm using a UV-Visible spectrophotometer (Evolution 260, Thermo Scientific). Specific UV absorbance (SUVA) was expressed as the ratio of absorbance at 254 nm per meter to DOC concentrations.

THg was determined using a cold vapour atomic fluorescence spectroscopy technique (CVAFS, Tekran 2600) following EPA method 1631 (EPA, 2002b). The method detection limit (MDL) of THg was 0.2 ng L⁻¹ (EPA 0.2 ng L⁻¹; Tekran 0.02 ng L⁻¹) determined following the EPA procedure (40 CFR, Part 136). MeHg was analyzed through distillation (Tekran 2750), aqueous ethylation and purge and trap with the CVAFS technique (Tekran 2700) following EPA method 1630 (EPA, 2002b). Determination of MDL for MeHg was performed for each run and an averaged MDL of 0.02 ng L⁻¹ was calculated (EPA 0.02 ng L⁻¹; Tekran 0.004 ng L⁻¹).

5.3.4 Solid Phase Analysis

Solid samples for MeHg analysis were mixed with 20% KCl, 8M H₂SO₄ and CuSO₄ for distillation to improve recovery following the method described by Horvat et al. (1993). The distilled aqueous phase was then ethylated and analyzed by CVAFS as described previously for the aqueous MeHg samples. The analysis methods for C/S content, elemental composition, and total organic carbon of the sediment and biochars are provided in the Supporting Information.

Genomic DNA was isolated and purified from solid phase using commercial extraction kits (UltraClean Soil DNA Kit; MO BIO Laboratories) following the supplier's instructions. Purified DNA was stored at -20°C prior to shipping for pyrosequencing analysis. The pyrosequencing analyses were conducted by MR DNA Laboratory (Shallowater, Texas). Detailed information on the primers used, and the processes and conditions of polymerase chain reaction and sequencing, and data processing procedures is provided in the Appendix C. Databases of fermenters, FeRB, SRB, and methanogens were assembled based on published sources. A database of

potential Hg methylators was also assembled based on the methylators identified by Oak Ridge National Laboratory (2015) (Table S4.1). A MATLAB code was written to extract fermenters, FeRB, SRB, methanogens, and methylators from the pyrosequencing data file using databases assembled from published data (Tables S5.1-S5.4).

5.3.5 Statistical Analysis

The correlation between the measured parameters was evaluated by calculation of Pearson product moment correlation coefficients (r). The significance of a correlation, r , was tested using a t test with a 95% confidence level ($P < 0.05$).

5.4 Results and Discussion

5.4.1 Overview of Sediment, River Water, and Biochar Samples

Microcosm experiments were conducted for 524 d under anaerobic conditions using sediment with a Hg concentration of $187 \mu\text{g g}^{-1}$. Total elemental concentrations in the sediment were $300 \mu\text{g g}^{-1}$ S, $16\,000 \mu\text{g g}^{-1}$ Fe, $150 \mu\text{g g}^{-1}$ Cu, and $230 \mu\text{g g}^{-1}$ Mn (Liu et al., 2016a). The concentration of total organic carbon in the sediment was $17\,600 \mu\text{g g}^{-1}$. The river water contained $<5 \text{ ng L}^{-1}$ THg and $<0.02 \text{ ng L}^{-1}$ MeHg and low concentrations of other elements (Liu et al., 2016a). The reactive materials were rich in carbon, 70.2% for GRASS300 and 94-99.9% for AC, OAK700 and GRASS600, except 18.5% for MANURE600 (Table S5.5). The S contents ranged from $<0.1\%$ for OAK700 to as high as 0.55% for GRASS600.

5.4.2 Aqueous Chemistry

Values of pH for the sediment control and amended systems gradually increased from ~ 7.5 to ~ 9.0 in the first 150 d and then decreased slightly to ~ 8.5 at 445 d (Fig. S5.2). The pH values in the biochar controls increased rapidly from ~ 8.5 to ~ 9.2 , then decreased gradually to ~ 8.5 . The pH values for AC, GRASS600 and MANURE600 controls were

greater than for other controls, which is consistent with previous observations (Liu et al., 2015). The Eh values for the controls and amended systems were similar and decreased from ~50 mV to ~-420 mV in the first 126 d, then decreased slightly to ~-440 mV until the experiments were terminated at 524 d. These Eh values indicate the environment was maintained anaerobic over the course of the experiment.

5.4.3 THg in Aqueous Phase

The 0.2- μm filtered THg concentrations ranged from 0.8 to 32 $\mu\text{g L}^{-1}$ for the sediment controls and the amended systems (Fig. 5.1). A gradual increase in concentrations of 0.2- μm filtered THg was observed over the course of the experiment in the sediment controls and MANURE600 amended system, while other amended systems showed an initial increase and slowly decreasing pattern. The 0.2- μm THg concentrations for the amended systems were less than for the sediment controls, except for the last samples collected in the MANURE600 amended systems. The THg concentrations for the duplicate systems amended with OAK700 and MANURE600 were in agreement (standard deviation <5%).

The concentrations of 0.45- μm filtered THg ranged from 1.0 to 50 $\mu\text{g L}^{-1}$ for the sediment controls and amended systems (Fig. 5.1). Compared with concentrations of 0.2- μm THg, 0.45- μm THg concentrations were highly variable during the first 100 d, with a spike in concentration observed at 30 d for both the controls and amended systems. A gradual increase THg concentrations was observed in the sediment controls after the initial 23 d, then THg concentrations stabilized at ~30 and 50 $\mu\text{g L}^{-1}$.

The effectiveness of co-blending in reducing aqueous 0.45- μm THg concentrations was not obvious at early stages. The THg concentrations decreased by 60-90% (mean 75%) compared with the sediment control for the AC amended system after

30 d, by 20-60% (mean 46%) for OAK700 after 250 d, by 30-90% (mean 69%) for GRASS300 after 100 d, by 20-70% (mean 39%) for GRASS600 after 100 d, and by 40-92% (mean 70%) for MANURE600 amended systems after 30 d. An increase in THg concentrations was observed for MANURE600 amended systems after 126 d. The 0.45- μm THg concentrations from the duplicate sampling events were in good agreement (standard deviation <5%). The THg concentrations in the ultrapure water control were <5 ng L^{-1} and <50 ng L^{-1} in river water and biochar controls.

A previous batch experiment to evaluate Hg removal by the same biochars used in this study showed rates of removals greater than 90% from Hg-spiked river water ($\sim 10 \mu\text{g L}^{-1}$) within 2 d (Liu et al., 2016b). The lower removals observed in this study are likely multi-facted and may be attributed to DOC which can retain Hg in the aqueous phase (Gomez-Eyles et al., 2013), blockage of adsorption sites by sediment particles (Mayer, 1994), competing effects for adsorption sites from other cations (Herrero et al., 2005), continuous release of Hg from the sediment (Pereira et al., 1998), and the relatively high ratio of total Hg to biochar (18.7 mg THg to 5 g biochar).

In the GRASS300 amended system, the concentrations of 0.2- μm THg, 0.45- μm THg, and MeHg were less than the corresponding concentrations of sediment controls and other amended systems. These results indicate the GRASS300 is the most promising reactive material to stabilize Hg in contaminated sediment under anaerobic condition. This observation is different from a previous batch-style experiment with respect to the addition of biochar to Hg-spiked river water (Liu et al., 2016b), which showed the least amount of THg is removed by GRASS300 compared with AC, OAK700, and GRASS600.

5.4.4 MeHg

Two peaks of temporal MeHg concentrations were observed in the sediment controls and amended systems (Fig. 5.1). Early peaks in concentrations were observed at day 37 (48 ng L⁻¹) and day 47 (130 ng L⁻¹) in the duplicated sediment controls. The MeHg concentration peaks in amended systems were lower than those in sediment controls for most data points collected at the same time, with the exception that the peak in AC amended system was greater than one of the sediment controls. The first peak concentrations were <13 ng L⁻¹ for OAK700, GRASS300 and GRASS600 amended systems, and 38 ng L⁻¹ for MANURE600 amended systems. A second peak was observed in the duplicated sediment controls with concentrations as 64 and 28 ng L⁻¹. The second peaks in AC, GRASS300, and MANURE600 amended systems were much less than those in sediment controls, while the second peaks in amended systems of OAK700 and GRASS600 were much greater with MeHg concentrations of 220 and 260 ng L⁻¹, respectively. However, due to sampling events, the water level decreased over time in the systems, and the calculated mass of MeHg at the second peak in amended systems of OAK700 and GRASS600 were less than that at the first peak of the sediment controls (Fig. S5.3). MeHg concentrations of river water and biochar controls were below the MDL.

A number of parameters affect the rates of production of MeHg, including the availability of substrates for Hg methylators and competing organisms, temperature, pH, organic material, redox conditions, and bioavailable Hg species (Ullrich et al., 2001). Correlation analyses were performed between MeHg concentrations and the other parameters measured during the experiment (pH, Eh, alkalinity, THg, cations, anions,

DOC, UV absorbance at 254 nm, SUVA, nutrients). Aqueous MeHg concentrations were negatively correlated with SO_4^{2-} concentrations in all systems. MeHg concentrations were consistently positively correlated with unfiltered THg (Fig. S5.3) in sediment controls. For most amended systems, the MeHg concentrations were positively correlated with concentrations of unfiltered THg, alkalinity, DOC, Mn, and Fe. Alkalinity and DOC are carbon energy sources for microbes (including Hg methylators). Fe, Mn, and SO_4^{2-} are electron acceptors for FeRB and SRB which are potential Hg methylators (Benoit et al., 2001a; Gilmour et al., 1992; Kerin et al., 2006; Yu et al., 2011).

The solid-phase MeHg contents ranged from 8 to 35 ng g^{-1} in the sediment control and amended systems of AC, one of the OAK700 duplicates, and a MANURE600 duplicate (Fig. 5.2). The MeHg contents in amended systems were close to those in sediment controls or even greater. A sharp increase of MeHg content was observed for the last two sampling events of amended systems of a OAK700 duplicate, GRASS300 and GRASS600 with MeHg contents of up to 260 ng g^{-1} . The elevated MeHg contents of amended systems of OAK700 and GRASS600 corresponded to the elevated aqueous MeHg concentrations (Fig. 5.1). The results indicate the application of AC and biochar does not result in an obvious decrease in MeHg content in the solid phase, unlike the aqueous MeHg concentration. This observation is consistent with previous studies (Huntington et al., 2015; Lewis et al., 2016), which suggest the application of AC results in the sorption of MeHg to AC thereby decreasing aqueous MeHg concentrations. The lower concentrations of MeHg in the aqueous phase of the amended systems compared with sediment controls were likely due to adsorption of MeHg to biochars rather than inhibition of MeHg production.

Distribution coefficients (K_d) were calculated using measured concentrations of MeHg in the solid and the aqueous phase at different times during the experiment (Fig. S5.4). The K_d values ranged from 200 to 18000 L kg⁻¹ and no clear patterns were observed for K_d values versus time. This result indicates that K_d was not likely a valid parameter to describe the distribution of MeHg between solid and aqueous phase in this study, which is inconsistent with a previous study (Gomez-Eyles et al., 2013). In this study, the distribution of MeHg between the solid and aqueous phases was likely controlled by other processes.

5.4.5 Carbon Sources for Microbes

Dissolved organic carbon, acetate, and alkalinity are potential carbon sources for microorganisms. The DOC concentrations in most systems continued to increase and concentrations of acetate and alkalinity increased and then decreased over the course of the experiment (Fig. 5.3). DOC concentrations increased from 2 to 80 mg L⁻¹ for sediment controls and amended systems, except a spike (340 mg L⁻¹) in concentrations in AC amended system which corresponded to the peaks of acetate and alkalinity concentrations. The increasing pattern versus time was similar between sediment controls and amended systems, while the concentrations of DOC in AC and MANURE600 amended systems were lower than those of sediment controls. The DOC concentrations in biochar controls were less than 2 mg L⁻¹ before day 154 and increased to as high as 400 mg L⁻¹.

A peak in acetate concentration was observed in each system, with concentrations up to 41 mg L⁻¹ for sediment controls and ranged from 21 mg L⁻¹ for OAK700 to 226 mg L⁻¹ for AC. The peak time was at day 168 for sediment control and ranged from day 112

to 387 for amended systems. No great difference was observed for acetate concentrations between sediment controls and amended systems, except the spike in AC. The acetate concentrations were $<1 \text{ mg L}^{-1}$ for most data points of biochar controls, except the spike of concentrations for AC and GRASS300 amended systems ($5.0\text{-}89 \text{ mg L}^{-1}$). Elevated formate and propionate concentrations were also observed in sediment controls and amended systems (Fig. S5.3). The alkalinity concentrations increased from ~ 50 to $\sim 200 \text{ mg L}^{-1}$ before day 100 and then decreased to $\sim 50 \text{ mg L}^{-1}$ at day 445 in sediment controls and amended systems. The alkalinity concentrations of biochar controls varied slightly between $50\text{-}100 \text{ mg L}^{-1}$.

The concentrations of acetate and DOC in the microcosm experiments were much greater than in a previous batch experiment using the same biochars (Liu et al., 2015). The results indicate the acetate and DOC released by biochars have limited contributions to the concentrations in the microcosm experiment. The increase in acetate and DOC concentrations in the microcosm experiments is likely related to the organic matter in the sediment ($17\ 600 \mu\text{g g}^{-1}$). The increase in alkalinity is a result of the microbial activities. The decrease in alkalinity is likely due to consumption by methanogens or the formation of carbonate minerals.

DOC also plays an important role in Hg speciation in the aqueous phase. Lower DOC concentrations were observed in AC and MANURE600 amended systems than those in the sediment controls, which corresponded to lower THg concentrations in AC and MANURE600 amended systems compared with sediment controls at early stage (Fig. 5.1). For OAK700, GRASS300, and GRASS600 amended systems, the DOC concentrations were similar or higher than those in the sediment controls at early stages

and THg concentrations were less than the sediment controls after extended periods. This observation is consistent with previous studies (Gilmour et al., 2013; Gomez-Eyles et al., 2013), in which aqueous inorganic Hg was controlled in sediments and reactive media (AC and biochar) co-blending experiments when DOC concentrations remained low. Hg-DOC complexes readily form in solution. These complexes are stable and can maintain elevated concentrations of Hg in the aqueous phase (Gomez-Eyles et al., 2013). The presence of DOC can also prevent the precipitation of HgS nanoparticles (Aiken et al., 2011). DOC can also be utilized as a carbon source by potential Hg methylators and can enhance the bioavailability of Hg by facilitating Hg uptake (Chiasson-Gould et al., 2014).

5.4.6 Electron Acceptors for Microbes

Concentrations of NO_3^- , Mn, Fe, and SO_4^{2-} are plotted in Fig. 5.4 in a decreasing order of energetically favourable electron accepting reactions for microbial respiration. NO_3^- concentrations decreased from $\sim 45 \text{ mg L}^{-1}$ to $< \text{MDL}$ (0.05 mg L^{-1}) within 9 d for the sediment controls and amended systems. Dissolved Mn concentrations increased from < 0.005 to $\sim 1.2 \text{ mg L}^{-1}$ within 65 d and decreased to $< 0.2 \text{ mg L}^{-1}$ after 154 d in sediment controls and amended systems. A lag stage of dissolved Fe concentrations ($< 0.2 \text{ mg L}^{-1}$) was observed for the first 23 d in sediment controls and amended systems; then Fe concentrations increased to peak concentrations ranging from 0.47 to 3.5 mg L^{-1} for sediment controls and amended systems at day 100 and then decreased to $< 0.2 \text{ mg L}^{-1}$ after 154 d. Dissolved Fe concentrations in the AC amended system were lower than in the sediment controls and other amended systems. SO_4^{2-} concentrations increased slightly at the first 37 d and then decreased to $< \text{MDL}$ (0.05 mg L^{-1}) after 79 d for the sediment controls, 65 d for GRASS300 amended system, 89 d for OAK700, 100 d for AC and

GRASS600, and 126 d for MANURE600. Due to the rapid shift to anaerobic conditions (Fig S5.2), the reduction of Fe and SO_4^{2-} occurred simultaneously.

Concentrations of NO_3^- , Mn, and Fe in the aqueous solution of the amended systems were derived from the sediment, because their concentrations were elevated in the solid phase of sediment and generally less than the analytical detection limits in the aqueous phase of biochar controls (Fig. 5.4), the river water, and solid phase of biochars. For biochar and river water controls, NO_3^- concentrations decreased from $\sim 2 \text{ mg L}^{-1}$ to $< \text{MDL}$; Mn concentrations were $< 0.05 \text{ mg L}^{-1}$, except one data point from GRASS300 control; Fe concentrations were $< 0.02 \text{ mg L}^{-1}$. A fraction of SO_4^{2-} in the aqueous solution of the amended systems was released from the biochars. The initial SO_4^{2-} concentrations of biochar controls are in the following order: MANURE600 > AC > GRASS600 > GRASS300 > OAK700, which is consistent with a previous batch-style experiment (Liu et al., 2016b). The SO_4^{2-} concentrations of biochar controls decreased only slightly over 445 d, which indicates suitable substrates for the growth of SRB was not likely provided by the biochar. The elevated SO_4^{2-} concentration in MANURE600 amended systems is likely due to the elevated S content and elevated inorganic sulfate fraction in the MANURE600 (Liu et al., 2016b).

The increase in 0.45- μm filtered THg concentrations after 23 d corresponds to the increase in dissolved Fe concentrations, which indicates that Hg is likely released from Fe minerals during reduction. The decrease in 0.45 μm filtered THg in the amended systems was likely due to a formation of Hg-sulfide precipitates as a result of SO_4^{2-} reduction. The maximum decreases in Fe and SO_4^{2-} concentrations corresponded to the first peak in MeHg in the sediment controls and amended systems; Fe concentrations

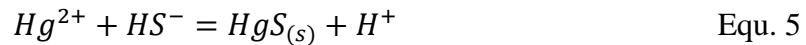
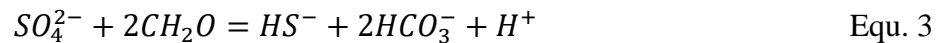
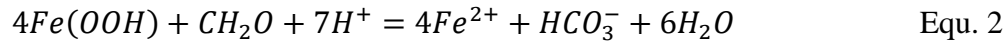
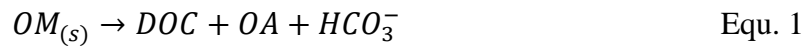
were positively correlated with MeHg concentrations ($P < 0.05$) in the amended systems of AC and MANURE600.

5.4.7 Pyrosequencing

The percentages of fermenters, FeRB, SRB, and methanogens at genus level were extracted from the pyrosequencing data and plotted in Fig. 5.5. The sum of the 16s rRNA extracted for all categories increased with time. Similar increasing and then decreasing patterns were observed over time for fermenters, FeRB, and SRB, except abundances ranged from 4.9-25%, 4.8-20%, and 0.8-3.5%, respectively. The percentages of methanogens consistently increased over time from 0% to as high as 70%. Percentages of extracted 16s rRNA in the duplicated OAK700 and MANURE600 amended systems were in good agreement. The similar patterns between sediment control and amended systems suggest that the addition of biochars had little impact on the microbial community in the system. This observation is consistent with a previous study (Noyce et al., 2015), in which soil microbial community was not affected after addition of 5 t ha⁻¹ biochar to a temperate forest soil.

Under sufficiently reducing systems, fermenters and other microorganisms can degrade organic matter (OM) in sediment to form DOC and short-chain organic acids (OA), as indicated by Equ. 1. Oxidation of organic carbon (17 600 $\mu\text{g g}^{-1}$) in the South River sediment may be an explanation for the changes in concentrations of DOC and short-chain organic acids in solution (Fig. 5.3 and Fig. S5.3). The labile organic carbon forms within DOC are key carbon and energy sources for FeRB (Lovley, 1991), SRB (Muyzer & Stams, 2008), methanogens (Deppenmeier, 2002), many of which are potential Hg methylators. The increase in alkalinity during early stages of the

experiments may be due to the respiration of these microbes (Equ. 1). The FeRB can reduce oxidized solid-phase forms of Mn and Fe and release reduced aqueous forms (Fig. 5.4; Equ. 2; Ribet et al. (1995)). The SRB can reduce SO_4^{2-} to S^{2-} (Equ. 3; Moncur et al. (2015) and Lindsay et al. (2011)); the production of S^{2-} can then be consumed by the formation of Fe- (Equ. 4; Benner et al. (2002)) and Hg-sulfide minerals (Equ. 5). The formation of these minerals explained the decrease in dissolved Fe and Hg over time (Fig. 5.1 and Fig. 5.4). Methanogens can utilize inorganic carbon as an energy source (Equ. 6) and the increase of methanogen abundances corresponds to the decrease in alkalinity (Fig. 5.3).



Twelve potential methylators at the species level were obtained from the pyrosequencing results including fermenters, FeRB, SRB, and methanogens (Fig. 5.6). Their total abundance was <0.7%. A general increasing and decreasing pattern of the total abundance of potential methylators was observed. The abundances of the potential methylators were not well correlated with concentrations of MeHg in the aqueous and solid phases, which indicates that quantification of known potential methylator abundances may not be a good indicator for net MeHg concentration in aqueous and solid phases. The late MeHg spikes in OAK700 and GRASS600 amended system do not correspond to a spike in the known potential methylators at day 387, which suggests that unknown methylators likely existed in these two systems. This discrepancy may also be a

result of the limitation of the database used for pyrosequencing data analysis. A large fraction of the microorganisms in the environment is not represented in the database (Rondon et al., 1999).

A column experiment conducted by Desrochers et al. (2015) showed that MeHg production in the South River sediment could be stimulated by increasing the concentrations of electron donors and acceptors. Here, less MeHg was observed in the aqueous phase in the amended systems using AC, GRASS300, and MANURE600 than for sediment controls even with slightly elevated carbon sources, electron acceptor (SO_4^{2-}), and percentages of methylators in the amended systems.

The following processes are proposed to describe the decrease of Hg and MeHg in the aqueous phase after addition of the amendments. First, a rapid release of dissolved Hg from the sediment and rapid adsorption by biochars occurs at the beginning of the experiment; the Hg concentrations do not decrease due to continuous dissolution of soluble Hg phases and because binding between Hg and biochar is generally weak. The second stage is an Fe-reducing period; Hg that is retained in Fe oxide minerals is released into solution after reductive dissolution of Fe oxide minerals; Hg is weakly adsorbed by biochars; MeHg is produced by FeRB (Kerin et al., 2006; Yu et al., 2011). The third stage is a sulfate reducing period; sulfate is reduced to sulfide; Hg binds with sulfide and forms precipitates on the surface or inside the pores of biochar particles; the former adsorbed Hg may also be converted to Hg-S minerals; the binding is strong between Hg and the biochar particles; less MeHg is produced by SRB (Benoit et al., 2001a; Gilmour et al., 1992) due to low bioavailability of Hg after stabilization by biochars. The fourth stage is a methanogenic period; MeHg is produced by methanogens (Hamelin et al.,

2011; Yu et al., 2013). The early peaks of MeHg concentrations in aqueous phase are attributed to the activities of fermenters, FeRB and SRB; the late peaks are attributed to activity of methanogens. Methanogens capable of methylation likely existed in the OAK700 and GRASS600 amended systems.

5.5 Implications for Remediation of Hg-contaminated Sites

These microcosm experiments indicate that biochar amended systems can be effective in reducing Hg concentrations in the aqueous phase. The presence of biochar appeared to have a limited impact on the microbial community structure. The removal of Hg using biochars is comparable to the application of AC. Previous batch experiments indicate elevated concentrations of organic acids, DOC (Liu et al., 2015), and SO_4^{2-} (Liu et al., 2016b) are released by AC, GRASS300, and MANURE600, suggesting addition of biochars may potentially stimulate the rates of MeHg production. However, the microcosm experiments indicate that at early stages MeHg concentrations increased minimally in the presence of these biochars. A MeHg concentration spike was observed at a late stage in amended systems with OAK700 and GRASS600. Thus, for the majority of the biochar types evaluated, the Hg and MeHg concentrations in the aqueous phase and potentially the bioavailability likely decrease after biochar amendment.

The results indicate GRASS300 is the most promising reactive material for Hg stabilization of contaminated sediment. If GRASS300 is applied in the field, special attention should be paid to its physical breakdown (Spokas et al., 2014b). During the experiment, GRASS300 is observed to be more fragile than wood-derived biochars. For application of most types of biochar in water bodies, another challenge is how to maintain biochar in desired locations due to its low density and settling rate (Gomez-Eyles et al., 2013). During sampling events, a large portion of the biochar particles were

observed at the interface between aqueous and solid phase and biochar particles could be easily relocated by the movement of the water. The biochar particles can be encased by using geotextile (Shackley et al., 2016), then the encased biochar can be applied in the field.

At the termination of the experiment, biochar particles were easily distinguished from the sediment, which indicates the biochar remained stable over the course of the experiment. This observation is consistent with previous studies that biochar can be stable in the environment (Mann, 2002; Spokas, 2010).

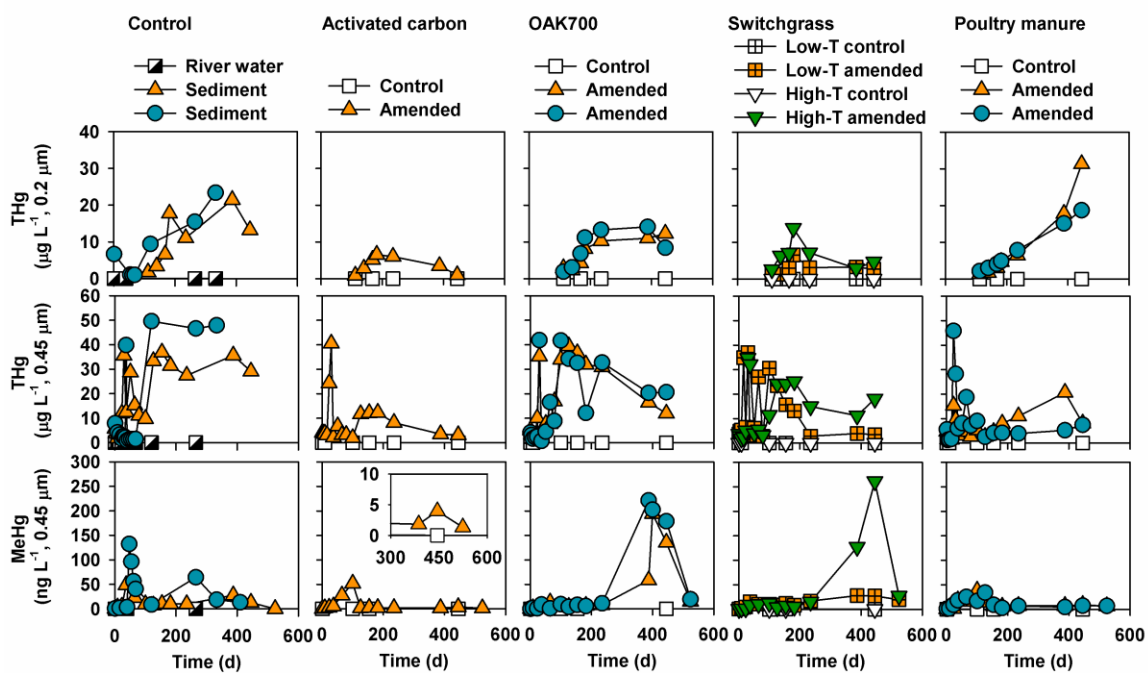


Figure 5.1 Concentrations of 0.2 and 0.45 μm filtered THg and 0.45 μm filtered MeHg in aqueous solutions of controls and amended systems against time. The data of sediment control and low-T and high-T switchgrass biochar is from Chapter 4.

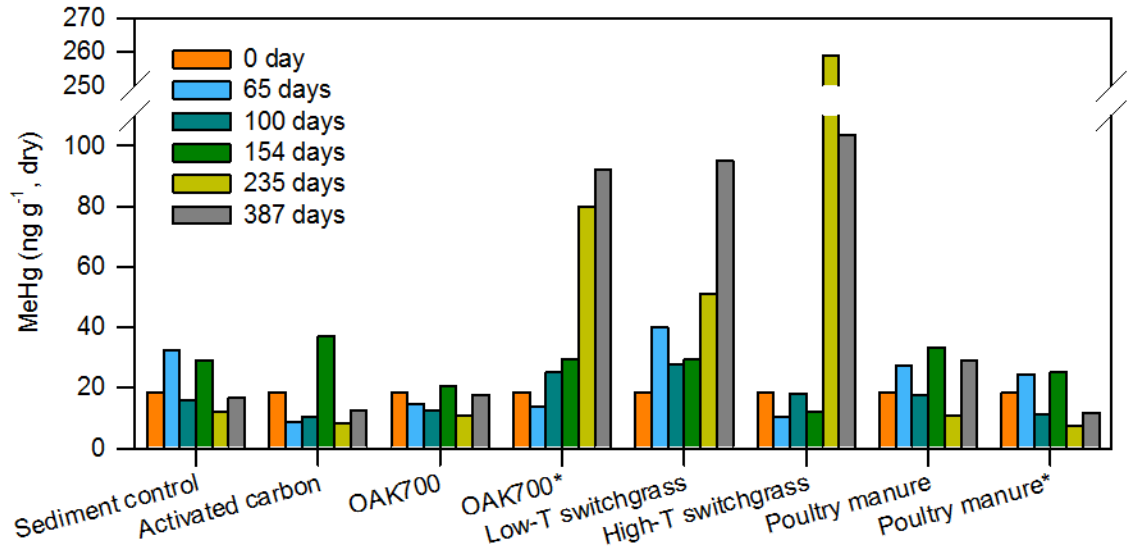


Figure 5.2 MeHg contents in sediment control and amended systems (activated carbon, OAK700, low-T and high-T switchgrass, and poultry manure) at day 0, 65, 100, 154, 235, and 387. The data of sediment control and low-T and high-T switchgrass biochar is from Chapter 4.

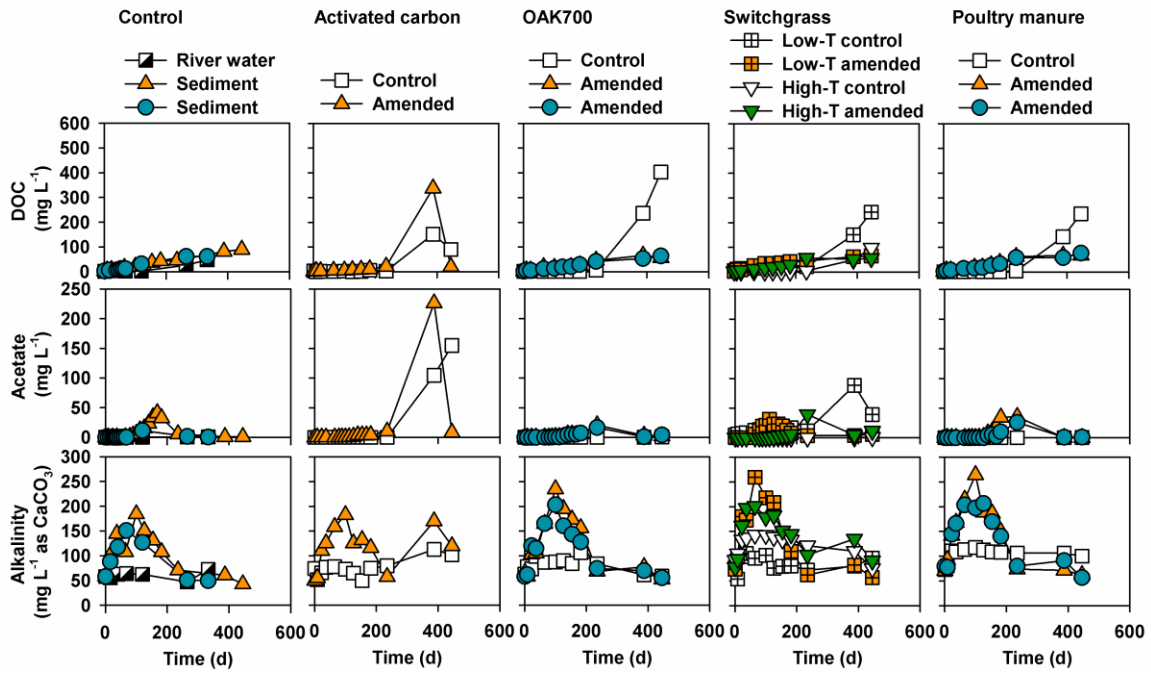


Figure 5.3 Concentration of carbon sources (DOC, acetate and alkalinity) in aqueous solutions of controls and amended systems against time. The data of sediment control and low-T and high-T switchgrass biochar is from Chapter 4.

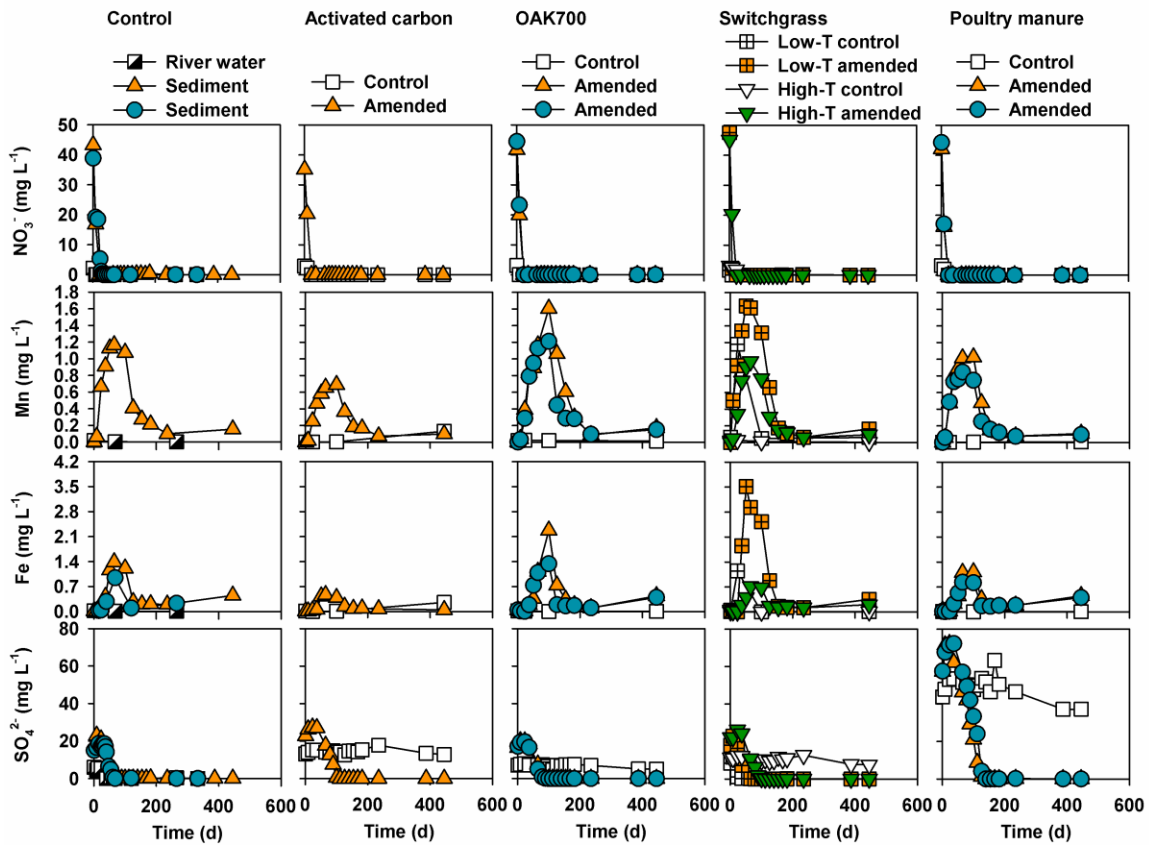


Figure 5.4 Concentration of electron acceptor (NO_3^- , Mn, Fe, and SO_4^{2-} in redox sequence) in aqueous solutions of controls and amended systems against time. The Fe and SO_4^{2-} concentrations of sediment control and low-T and high-T switchgrass biochar are from Chapter 4.

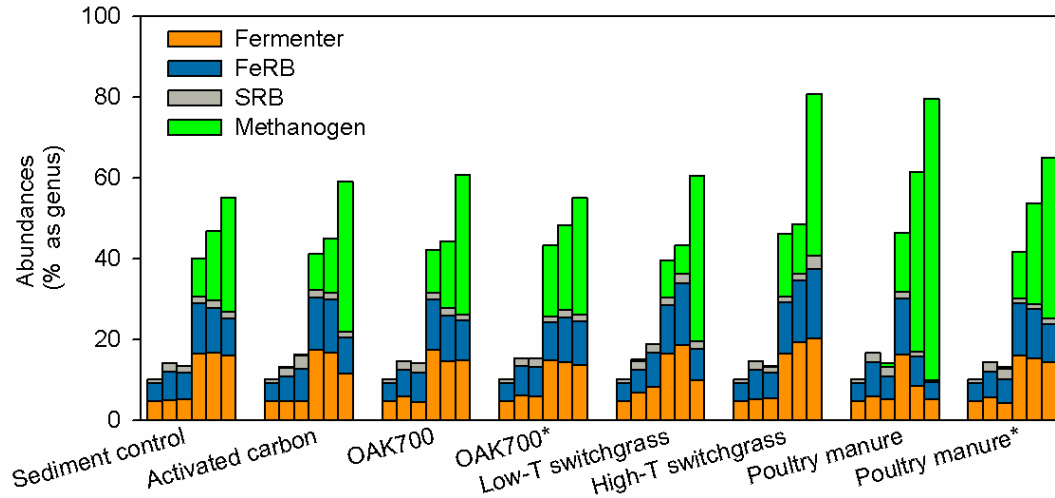


Figure 5.5 Pyrosequencing results of percentages in genus level including fermenters, FeRB, SRB, and methanogens of sediment control and amended systems of activated carbon, OAK700 (duplicate amended systems), low-T and high-T switchgrass biochar, and poultry manure biochar (duplicate amended systems). For each sample, columns from left to right represent days 0, 65, 100, 154, 235, and 387.

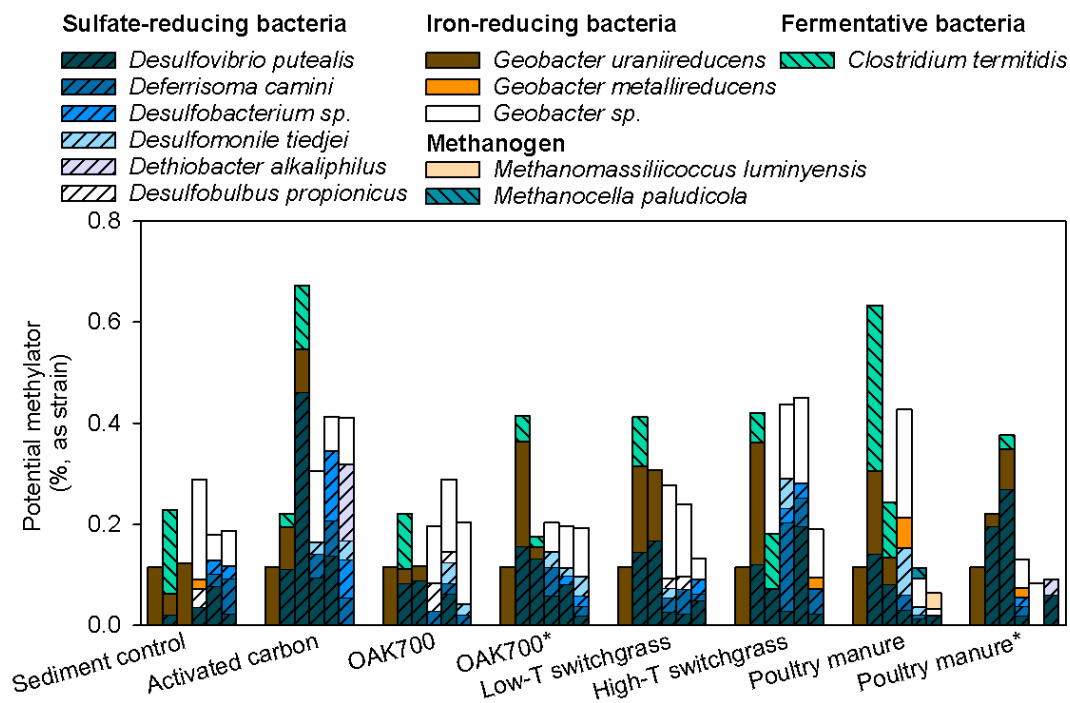


Figure 5.6 Percentages of species identified as known Hg methylators including SRB, FeRB, methanogen, and fermentative bacteria at different days from sediment control and amended systems. For each sample, columns from left to right represents day 0, 65, 100, 154, 235, and 387. The data of sediment control and low-T and high-T switchgrass biochar is from Chapter 4.

Chapter 6: *Mercury Stabilization
Mechanisms in Contaminated Sediment
Amended with Biochars Determined using
X-ray Absorption Spectroscopy*

6.1 Executive Summary

Previous results have shown that inorganic mercury (Hg) and methylmercury (MeHg) in contaminated sediment can be effectively stabilized through the addition of biochar in a 524-day microcosm experiment. This previous study indicates that concentrations of Hg in the river water in biochar amended systems were consistently lower than those in the sediment controls after several months of reaction. The removal of Hg in these studies is attributed to uptake by the biochar particles. This study focuses on identification of mechanisms controlling Hg uptake by these biochar particles to gain an improved understanding of the phases controlling Hg removal. This study utilizes X-ray absorption spectroscopy (XAS) to evaluate Hg distribution and speciation in the sediment and the biochar particles collected from the microcosm experiments after 235 and 387 days. Micro-X-ray fluorescence (μ -XRF) maps show that Hg co-exists with S, Cu, Fe, Mn, and Zn on the surface and inside the biochar particles. Extended X-ray absorption fine structure (EXAFS) modeling shows that Hg was in an oxide form on the surface of an iron (hydro)oxide particle from fresh sediment and in Hg-sulfide forms in the Hg-enriched areas of biochar particles and bulk biochar samples. S X-ray absorption near edge structure (XANES) analyses show that sulfide is present within the biochar particles from the amended systems. The results of this study suggest that after amendment with biochars, a fraction of the Hg originally present in unstable forms (dissolvable, HgO, colloidal, nano, etc.) in the sediment was likely stabilized as less soluble Hg-sulfide phases on the surface or within the biochar particles. These results suggest that Hg was accumulated by the biochar particles, suggesting that it may be less readily transported under dynamic flow conditions.

6.2 Introduction

Hg is a common contaminant in the air, oceans, lake, rivers, soils, and sediments and also occurs in different forms including elemental, Hg^{2+} , complexes with dissolved organic matter, and organomercurial forms (Selin, 2009). Organic Hg, for example methyl Hg (MeHg), is much more toxic than other forms and can cause central nervous system defects (Tchounwou et al., 2003), and can be converted from inorganic or elemental forms by microbes (Hu et al., 2013; Zhang et al., 2012). The major uptake pathway of inorganic and organic Hg is through the accumulation of dissolved species of Hg by aquatic organisms, and then Hg is biomagnified by higher level organisms in the food chain including humans. The methylation and accumulation of Hg species by organisms is primarily initiated in the aquatic environment, especially in sediments. If Hg can be stabilized and transformed to less soluble, mobile, and bioavailable forms in sediments, the health risk caused by Hg will be reduced. Laboratory studies have shown Hg is effectively removed from aqueous solution (Bundschuh et al., 2015; Dong et al., 2013; Liu et al., 2016b) and sediment (Chapter 5; Gomez-Eyles et al., 2013; Liu et al., 2016a) using biochars. Biochar may potentially be a cost-effective reactive material for application in Hg-contaminated site remediation.

We previously conducted a series of batch and long-term microcosm experiments designed to investigate Hg removal from aqueous solutions and Hg stabilization in aqueous-sediment mixtures using biochars prepared from a range of different feedstocks (Chapter 5; Liu et al., 2016a; Liu et al., 2016b). The results indicate that Hg can be effectively removed from aqueous solution in batch experiments containing biochar (Liu et al., 2016b); concentrations of Hg in contaminated sediment amended with biochar are lower than in sediment controls without biochar after 30-250

days (Chapter 5). In this study, we applied synchrotron-based techniques to characterize the biochar particles derived from the long-term microcosm experiments. The purpose of these analyses is to identify the distribution and speciation of Hg to provide an indication of mechanisms leading to Hg stabilization. The XAS techniques include micro-X-ray fluorescence (μ -XRF) mapping, Hg L_{III}-edge extended X-ray absorption fine structure (EXAFS), and S X-ray absorption near-edge structure (XANES) analyses.

6.3 Materials and Methods

6.3.1 Samples for Synchrotron Analysis

Hg-bearing biochar and sediment particles were collected from anaerobic microcosm experiments described in Chapter 5, in which contaminated sediment was amended with activated carbon (AC) and different biochars, and decreases in Hg and MeHg were observed. Biochars include oak biochar (rejects of product from Cowboy Charcoal Co., CL2), and low temperature (low-T, 300 °C, GR4L) and high temperature (high-T, 600 °C, GR4H) switchgrass biochar. Briefly, biochars, contaminated sediment, and water were mixed at a ratio of 1:20:160 on a dry mass basis in 1000 mL amber bottles. Controls included 1) biochars mixed with water (biochar control) and 2) sediment mixed with water (sediment control) at the same ratios as in the amended systems. The amber bottles were placed in an anaerobic chamber (Coy Laboratory Products Inc.) over the experimental period.

Solid-phase samples were collected from the biochar controls, sediment control and amended systems at days 65, 100, 154, 235, and 387. Solid-phase samples were collected with a scoopula. Individual biochar particles were hand-picked from the amended system using a tweezer, washed with ultra-pure water. These solid samples were freeze-dried and stored in the anaerobic chamber until analysis. Unreacted

sediment, solid-phase samples collected from the sediment control, and the biochar particles were mounted in epoxy on a quartz-glass slide and prepared as 26×26 mm thin sections with a thickness of 30 μm (Vancouver Petrographics Ltd., Canada) for μ-XRF and Hg EXAFS analyses.

Bulk samples of unreacted sediment and separated biochar particles were prepared for Hg EXAFS spectra collection. A mixture containing 3.0 g sediment with 50 mL ultrapure water was shaken for 20 minutes, and then sonicated for 10 minutes. The sand grains and other large particles were separated from this mixture by centrifuging for 2 min at 500 rpm, and then the supernatant was centrifuged a second time at 4000 rpm for 30 minutes to consolidate the fine particles. These fine particles were then freeze-dried and ground into fine powders for collection of Hg EXAFS spectra. Particles of AC and CL2 from biochar controls and the amended systems at day 387 were freeze-dried and ground into powder for bulk S XANES analysis.

6.3.2 X-ray Absorption Spectroscopy

Reference materials for XAS analyses included cinnabar, metacinnabar, and HgO for Hg, Cu₂S, CuS, CuO, and Cu foil for Cu, and cinnabar, elemental S, L-cysteine, dibenzo thiophene, Na methane sulfonate, and K₂SO₄ for S. The reference materials were ground to fine powders and smeared on polyethylene terephthalate (PET) tape (Scotch Magic Tape) for collection of EXAFS of Hg and Cu. The tape was cut, layered, and covered by Kapton tape (Furon, CHR). For collection of S XANES spectra, the reference materials were either smeared on double-sided carbon tape for analysis on Beamline SXRMB (06B1-1) at the Canadian Light Source (CLS) or mixed with graphite at 5% content for

analysis on Beamline 13-ID-E GSECARS at the Advanced Photon Source (APS). Details of method preparation are described in Gibson et al. (2011) and Liu et al. (2016b).

Micro-XRF maps were collected for thin-sections on Beamline 13-ID-E GSECARS and Beamline 20-ID-B PNC/XSD at APS following the set-up and procedures described by Liu et al. (2016b). Briefly, a focused beam approximately 2×2 μm and step size of $2 \mu\text{m}$ was used for μ -XRF map collection. A photon energy of 12.6 keV was applied for μ -XRF maps for Hg, Cu, Mn, Fe, Zn, Ni, Ca, and K and of 2.5 keV for S μ -XRF maps. Areas with elevated Hg, Cu, and S intensity were identified for acquisition of micro-EXAFS (μ -EXAFS) or XANES spectra.

Hg EXAFS spectra of bulk fresh sediment and biochar particles were collected using the same set-up for EXAFS spectra collection of Hg-enriched areas in the thin-sections, except that the beam was unfocused. S XANES spectra of bulk biochars from amendments and controls were collected on SXRMB at CLS, using the same setup and method described by Liu et al. (2016b). Briefly, the powders were smeared on a double-sided carbon tape on a copper sample holder. The sample holder was placed under a high vacuum environment. The fluorescence signal was collected and used for spectra analysis.

The XRF mapping data was analysed using X-ray Microprobe Map Viewer (Newville, 2016) for data from GSECARS and 2D QScanPlot for data from PNC/XSD. The EXAFS spectra of Hg and Cu and XANES spectra of S were first processed using Athena, and EXAFS model calculations were conducted using Artemis (Ravel & Newville, 2005). The modeling was performed following the method described by Gibson et al. (2011). The crystal structure was obtained from the American Mineralogist

Crystal Structure database and ATOMS.INP website. A k weighting of 3 was applied to enhance the weak oscillations of the EXAFS data. Amplitude reduction factor (S_0^2) and mean-square radial displacement (σ^2) were obtained by keeping the coordination numbers (CN) invariant during refinement of the first and second (only Cu₂S) shells for the reference materials. Then S_0^2 and σ^2 were kept constant during refinement of the first and second shells to obtain the CN.

6.4 Results and Discussion

6.4.1 XAS Analysis for Fresh Sediment and Sediment Control

The μ -XRF map of a fresh sediment particle shows that Hg and Cu were present at the surface of an Fe-enriched particle (Fig. 6.1). The Fe-enriched particle was assumed to be an iron (hydro)oxide phase based on microscopic images in reflection and transmission mode (Fig. S6.1). The Hg and Cu-enriched areas were located within the cavities of this particle. The X-ray fluorescence spectra of the arrow-pointed area in Hg L α line map confirmed the existence of Hg in the cavities. The spectra also indicate that Hg co-occurs with Fe, Cu, and Zn. The maps of a particle from sediment control at day 235 indicate Hg co-occurs with Fe, Ni, Cu, Zn, and Mn (Fig. 6.1 and Fig. S6.2). It was difficult to discern whether this Hg-enriched particle was newly formed during the experiment period or if it was present in the source sediment prior to the experiment. Attempts were made to collect μ -XRF maps of the two particles at 2.5 keV for S, but the intensity of S was not distinguishable from the background.

The μ -EXAFS modeling results indicate that Hg from the Hg-enriched area of the particles of fresh sediment and sediment control at day 235 were in the Hg oxide form (Fig. 6.1 and Table 6.1), with a coordination number of O atom as 2.15 and 4.97 and bond length as 1.95 and 2.21 Å. Whereas the EXAFS of bulk fresh sediment (fine or

colloidal fraction) indicate that the Hg was likely present as metacinnabar (β -HgS) with a coordination number of 3.07 for S and bond length of 2.51 Å. The modeling results indicate Hg was present in the Hg-enriched area as a Hg oxide and the majority of Hg in the sediment was in a Hg sulfide form, which is consistent with Hg sequential extraction results (Fig. S6.3) and in agreement with previous studies (Gibson et al., 2015; Lowry et al., 2004).

The observation of Hg on the surface of a (hydro)oxide phase in the natural sediment and co-occurrence of Hg with Fe, Mn, and Cu are consistent with observations in previous studies on Hg-contaminated sites (Bernaus et al., 2006; Gibson et al., 2015; Gu et al., 2014). It is also known that Hg can be effectively adsorbed by iron (hydro)oxide by forming bidentate inner-sphere complexes with the substrate surface (Collins et al., 1999; Kim et al., 2004). The Hg from the Hg-enriched area of fresh sediment was in a Hg-oxide form with a coordination number as 2.15 and bond length as 1.95 Å, which are consistent with Hg EXAFS modeling results for Hg(II) sorption onto goethite (Kim et al., 2004).

The Cu μ -EXAFS modeling results indicate the Cu from the Cu-enriched area of the iron (hydro)oxide particle of the fresh sediment was in a CuO form, with a coordination number of 2.34 and bond length of 1.94 Å (Fig. S6.4 and Table S6.1), which is in agreement with Cu(II) sorption onto goethite (Peacock & Sherman, 2004). Gibson et al. (2015) also observed that Cu co-existed with Hg in sediment with elevated Hg content, however, the Cu was present as a Cu-S forms.

6.4.2 Micro-XRF Maps of Biochar Particles from Amended Systems

The distribution of Hg, Cu, Fe, and S was indicated by the μ -XRF maps for four particles of AC and biochars collected from the amended Hg-contaminated sediment at day 387 (Fig. 6.2). The μ -XRF maps indicate Hg coexisted with Cu, Fe, S, Mn, and Zn, whereas Ni-enriched areas were located in separate spots of the particle pores (Fig. 6.2 and Fig. S6.5-S6.17). The distribution patterns of Hg, Cu, Fe, and S are different for these particles. For AC, these elements were not only distributed on the surface, but also penetrated into the particles. For CL2, the elements were primarily located in two large pores, other small pores, and the edges of the particle. For low-T switchgrass biochar (GR4L), the Hg, Cu, and Fe were primarily distributed inside of the particle, which is different from other particles. For high-T switchgrass biochar (GR4H), the Hg, Cu, and Fe were primarily observed on the surface and inside the pores of the particle based on the microscopic images collected under transmission mode (Fig. S6.16-S6.17). Collection of μ -XRF maps were also attempted for thin sections of biochar particles collected at day 65, 100, 154, and 235, but the intensity of Hg XRF was low and poor quality μ -XRF maps were obtained for the majority of the thin sections. As the experiment was continuing after 235 days, the likelihood increased for locating Hg-enriched biochar particles.

The results indicate that Hg coexisted with Cu, Fe, S, Zn, Mn, and other elements on the surface, inside the pores, or inside the particles of AC and biochars. Because of the stability of biochar (Spokas, 2010), the Hg that co-existed with these elements may also be stable for prolonged periods. Furthermore, the Hg was located and aggregated within the coarse biochar particles, potentially lessening its bioavailability.

6.4.3 Hg and Cu EXAFS

Hg EXAFS spectra were collected from the enriched areas of the mapped particles and the bulk AC and biochars separated from the amended systems (Fig. 6.3 and Fig. S6.4). The Hg EXAFS results indicate Hg was likely in cinnabar (α -HgS) form in the Hg-enriched areas of activated carbon (AC), and oak (CL2), low-T (GR4L) and high-T (GR4H) switchgrass biochar particles (Fig. 6.2; Table 6.1) and another five Hg-enriched areas from CL2 particles (Fig. S6.6, 6.9, 6.11-13 and Table S6.1).

The modelled coordination numbers (CN) ranged from 1.00 to 2.88 and modelled bond lengths ranged from 2.36 to 2.38 Å, which are in agreement with cinnabar (Fig. S6.18 and Table S6.2) and previous studies (Bisson et al., 2012; Gibson et al., 2011; Li et al., 2012; Liu et al., 2016b). For bulk biochar samples, the Hg was likely present as cinnabar for CL2 and GR4L with coordination numbers of 2.54 and 1.93 and bond lengths of 3.23 and 2.36 Å. The Hg was likely present as metacinnabar (β -HgS) for AC and GR4H, which is different for the Hg-enriched area of corresponding thin-sections; the coordination number is 3.91 and 3.24 and bond length is 2.55 and 2.49 Å, which are close to the metacinnabar reference material (Fig. S6.18 and Table S6.2).

The Cu μ -EXAFS spectra was also collected from Cu-enriched areas of AC and CL2 at day 387 (Fig. 6.2) and two more CL2 particles at day 235 and 387 (Figs. S6.7 and S6.10). The Cu EXAFS results indicate Cu was likely present as Cu₂S for the Cu-enriched area of one AC particle at day 387 (Fig. 6.2, Fig. S6.4, and Table S6.1) and two CL2 particles at day 235 and 387 (Figs. S6.7 and S6.10). Under reducing conditions, Cu(II) can be converted to Cu(I) and Cu(0) by microbes and reducing agents (For example, Fe(II) (Matocha et al., 2005) and Fe(0) (Blowes et al., 2000)), and Cu(II) and

Cu(I) can interact with biogenic sulfide and sparingly soluble Cu-sulfides can be formed (Fulda et al., 2013). During the reduction of Cu(II), Cu(II) and Cu(I) species can compete with other metal ions, for example, Hg(II) and Fe(II), for sulfide. The Cu₂S observed in the particles of AC and CL2 (except the one in Fig. 6.2) was likely formed through this process. For the Cu-enriched area in the pores of CL2 at day 387 (Fig. 6.2), the modeling results indicate that Cu was likely present as Cu(0), with a coordination number of 3.18 and bond length of 2.64 Å. The formation of Cu(0) was likely due to the lack of biogenic sulfide, because when the amounts of Cu(II) and Cu(I) exceed the amount of biogenic sulfide, more Cu(0) is formed through reduction of Cu(II) and Cu(I) and becomes the dominant species (Fulda et al., 2013). *Clostridium sp.*, which can reduce Cu(II) and Cu(I) to Cu(0) under reducing conditions (Hofacker et al., 2015), were also observed in these experimental systems at the time of sample collection for XAS analyses (Chapter 5).

The XAS and Hg sequential extraction analyses of the fresh sediment indicate that there was Hg on the surface of iron (hydro)oxide particles as Hg-oxide and soluble forms of Hg, and the majority of Hg in the sediment was in fine particles and in Hg sulfide forms (Fig. 6.1 and Fig. S6.3). The XAS results of AC and biochar particles from the amended systems indicate Hg co-occurs with Fe, Cu, S, and other elements on the surface or inside the pores of AC and biochar particles and Hg was in Hg-sulfide forms. The Hg in the bulk AC and biochar samples were also in Hg-sulfide forms. Based on the results, the Hg observed in AC and biochar particles was likely converted from soluble forms of Hg, Hg released during dissolution of iron (hydro)oxide, and Hg from colloidal or nano particles; this Hg interacted with biogenic sulfide converted from sulfate by sulfate-

reducing bacteria to form Hg sulfide; these results are consistent with the process described in Chapter 5.

6.4.4 S XANES

S XANES spectra were collected for standards and samples (Fig 6.4 and Fig. S6.19). In these spectra, the energies of lines 1-6 are 2471.9, 2472.7, 2473.5, 2474.3, 2481.4, and 2482.8 eV, which were obtained from spectra collected from the standards, cinnabar, elemental S, L-cysteine, dibenzo thiophene, Na methane sulfonate, and K₂SO₄, and correspond to inorganic-sulfide, elemental, thiol, thiophenic, sulfonate, and ester-sulfate sulfur functionalities, respectively, as assigned by Manceau and Nagy (2012) and Vairavamurthy (1998). The S XANES spectra, collected for AC and CL2 particles from control and amended systems at day 387, displayed a number of edge features. The features indicate that different S forms were present in the samples.

The thiophenic S (line 4) and ester-sulfate S (line 6) structures were observed in all spectra, while their relative intensity was low for the thin-section spot of AC amended system. The elemental S(line 2) structure was observed in the thin-section spot of CL2 amended system and bulk samples of activated carbon control and amended system. The bulk spectra from the amended system were more complex than those from the biochar control in which reactive media was only mixed with river water; sulfonate (line 5) structure was only obvious in the amended systems.

The differences between the spectra of bulk sample and the spectra of thin-section spot from the amended systems indicates the S species are highly heterogeneous; a sulfonate S peak was more pronounced than ester-sulfate peak and thiol S (line 3) peak was only observed in thin-section spot of AC amended system. The shoulder indicated by

line 1 in the thin-section spots of AC and CL2 amended systems was at a similar energy with the S peak of cinnabar (Fig. S6.19), which was assigned as inorganic sulfide. The S XANES spectra of the spots was collected on the Hg-enriched area (Fig. 6.2) and Hg EXAFS modeling results indicate Hg was likely present predominantly as Hg-S forms at these spots, and the S XANES are consistent with the modeling results.

The spectra of AC and CL2 control at day 387 are similar to the corresponding washed samples (Liu et al., 2016b), which indicate the S forms of AC and CL2 are relatively stable under the experimental conditions. The differences between the amended systems and controls were likely due to the sediment matrix. During the experiment period, sulfate is released from the biochar and sediment (Chapter 5; Liu et al., 2016b) and then sulfate is reduced by sulfate-reducing bacteria to generate sulfide. Then the reduced sulfur is co-precipitated with other elements, for example Fe, Cu, Hg, on the surface or in the pores of the amended reactive materials. The sulfate or other oxidized S forms undergo a series of reactions and are finally converted to carbon-bonded sulfide, thiol, and sulfonate forms at the end of the experimental period. The results are inconsistent with a previous study (Churka Blum et al., 2013), in which the organic S form is very rapidly converted to inorganic sulfate. This inconsistency is likely due to the differences in experimental conditions; the previous study was conducted using an “open” incubation system and the current study was conducted under anaerobic conditions.

6.5 Environmental Applications

The results indicate part of the Hg in the contaminated sediment is converted to Hg sulfide forms that co-existed with Fe, Cu, and Zn after amendment with AC and biochar particles. AC and biochar particles likely provide a host for Hg in sulfide forms to

accumulate and Hg is stabilized in these particles compared to its original forms (soluble forms, colloidal, nano, or fine particles). AC and biochars can be stable in natural environments for prolonged periods (Spokas, 2010); co-occurrence of Hg with AC and biochar particles may also lead to increased stability of Hg over the long term.

Similar results were obtained for amended systems with activated carbon and biochars, which indicate biochars may be a promising reactive material for Hg-contaminated site remediation. Biochar can be produced at low cost and on site (Coleman et al., 2010); biochar can also be used as a soil amendment to improve soil fertility (Liu et al., 2013), carbon sequestration to mitigate climate change (Lehmann, 2007b; Lehmann et al., 2006; Spokas et al., 2012), and bio-energy (Lehmann, 2007a). Biochar can also be a by-product during bio-energy (bio-fuel, bio-gas, bio-oil, etc.) production from biomass (Özçimen & Karaosmanoğlu, 2004). However, biochar particles are fragile and light, therefore biochar can be physically broken down and transported by flowing water (Spokas et al., 2014a). Full-scale applications will likely require development of engineering controls to keep biochar particles in shape and in place.

Table 6.1 EXAFS fitting results of bulk and Hg-enriched area of μ -XRF maps of sediment control (SRD) and biochar amended systems.

Sample	Model	path	CN	R (\AA)	S_0^2	σ^2 (\AA^2)	R-factor
fresh SRD_Bulk	β -HgS	Hg-S	3.07 \pm 0.29	2.51 \pm 0.01	0.718 ^a	0.009 ^a	0.01
Fresh SRD_M6	HgO	Hg-O	2.15 \pm 1.04	1.95 \pm 0.03	0.962 ^a	0.005 ^a	0.003
SRD-C-235_M6	HgO	Hg-O	4.97 \pm 1.14	2.21 \pm 0.03	0.962 ^a	0.005 ^a	0.06
AC-387_M1	α -HgS	Hg-S	2.88 \pm 0.70	2.38 \pm 0.05	0.841 ^a	0.005 ^a	0.04
CL2-387_M1	α -HgS	Hg-S	1.00 \pm 0.23	2.36 \pm 0.10	0.841 ^a	0.005 ^a	0.02
GR4L-387_M1	α -HgS	Hg-S	1.41 \pm 0.27	2.41 \pm 0.03	0.841 ^a	0.005 ^a	0.18
GR4H-387_M1	α -HgS	Hg-S	1.43 \pm 0.62	2.41 \pm 0.08	0.841 ^a	0.005 ^a	0.18
AC-387_Bulk	β -HgS	Hg-S	3.91 \pm 0.53	2.55 \pm 0.02	0.718 ^a	0.009 ^a	0.04
CL2-387_Bulk	α -HgS	Hg-S	2.54 \pm 0.62	2.32 \pm 0.04	0.841 ^a	0.005 ^a	0.18
GR4L-387_Bulk	α -HgS	Hg-S	1.93 \pm 0.14	2.36 \pm 0.01	0.841 ^a	0.005 ^a	0.01
GR4H-387_Bulk	β -HgS	Hg-S	3.24 \pm 0.70	2.49 \pm 0.03	0.718 ^a	0.009 ^a	0.17

CN = coordination number; R = modeled bond length; S_0^2 = amplitude reduction factor, σ^2 = mean-square radial displacement; R-factor = fitting statistic. ^a values obtained from model compounds (Fig. S6.18 and Table S6.2)

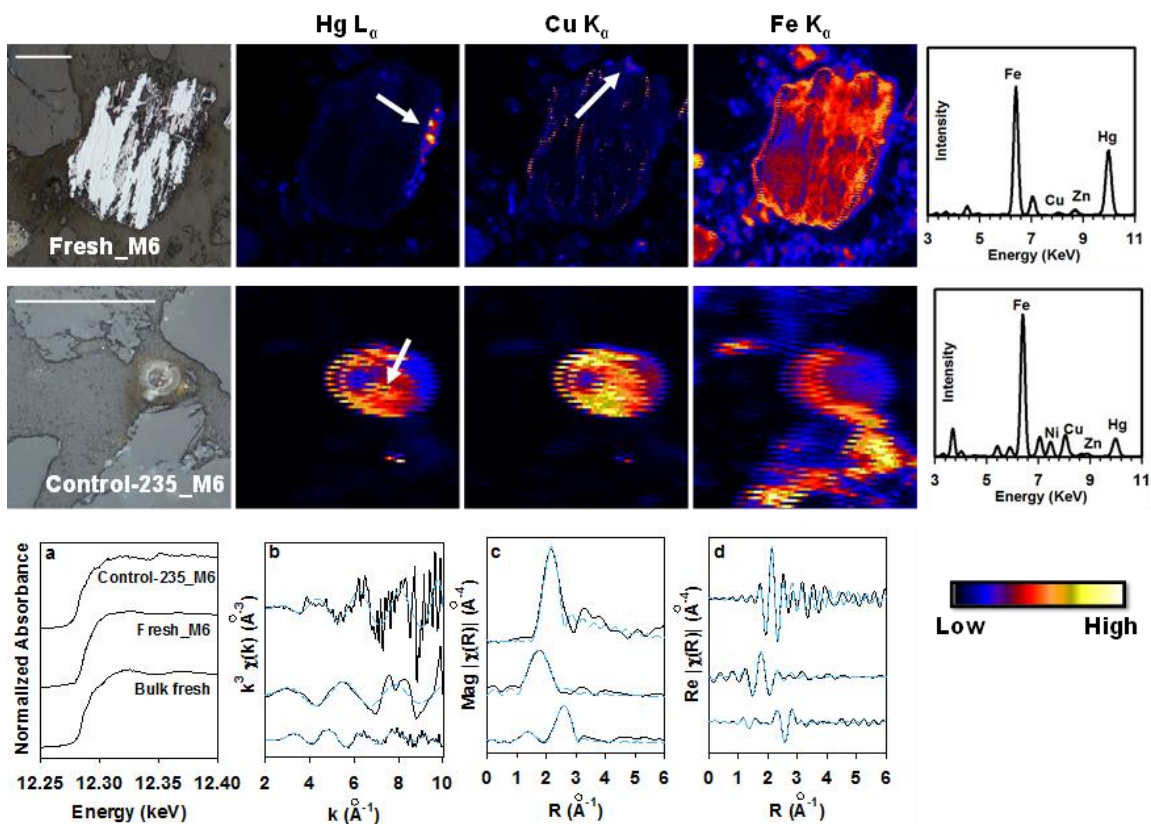


Figure 6.1 Micro-XRF maps (Hg, Cu and Fe) of particles from fresh sediment and sediment control at day 235. The first column of first two rows is the microscopic pictures and the last column is the XRF spectra collected from the area indicated by the white arrow in Hg L_α maps. The white line represents 100 μm. The points indicated by the white arrow in Hg and Cu maps mean Hg and Cu EXAFS spectra were collected. The bottom row includes ^a Edge-step normalized Hg L_{III}-edge XANES spectra of the spots indicated in the micro-XRF maps and bulk fresh sediment. ^b k³-weighted chi spectra (black solid line) and the best fit data (light-blue dash line). ^c Fourier-transform magnitude spectra and the best fit data. Fourier transform data are corrected for phase shift. ^d Fourier-transform real part and the best fit data.

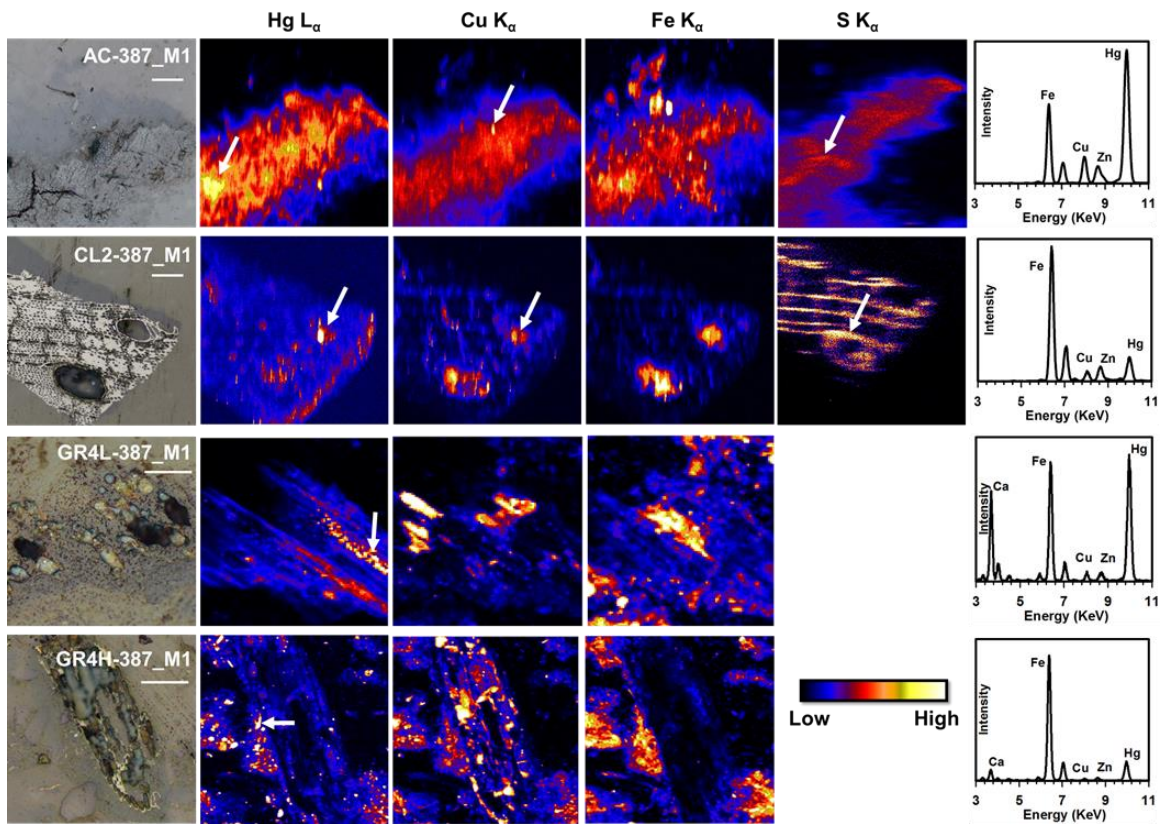


Figure 6.2 Micro XRF maps (Hg, Cu, Fe, and S) of activated carbon and biochar particles from the sediment amended systems at day 387. The first column is the microscopic pictures and the last column is the XRF spectra collected from the area indicated by the white arrow in Hg L_{α} maps. The white line represents 100 μm . The points indicated by the white arrow in Hg, Cu and S maps mean Hg and Cu EXAFS and S XANES spectra were collected. S XRF maps were collected at different time due to beamline setup, and S XRF maps were not well aligned with other maps

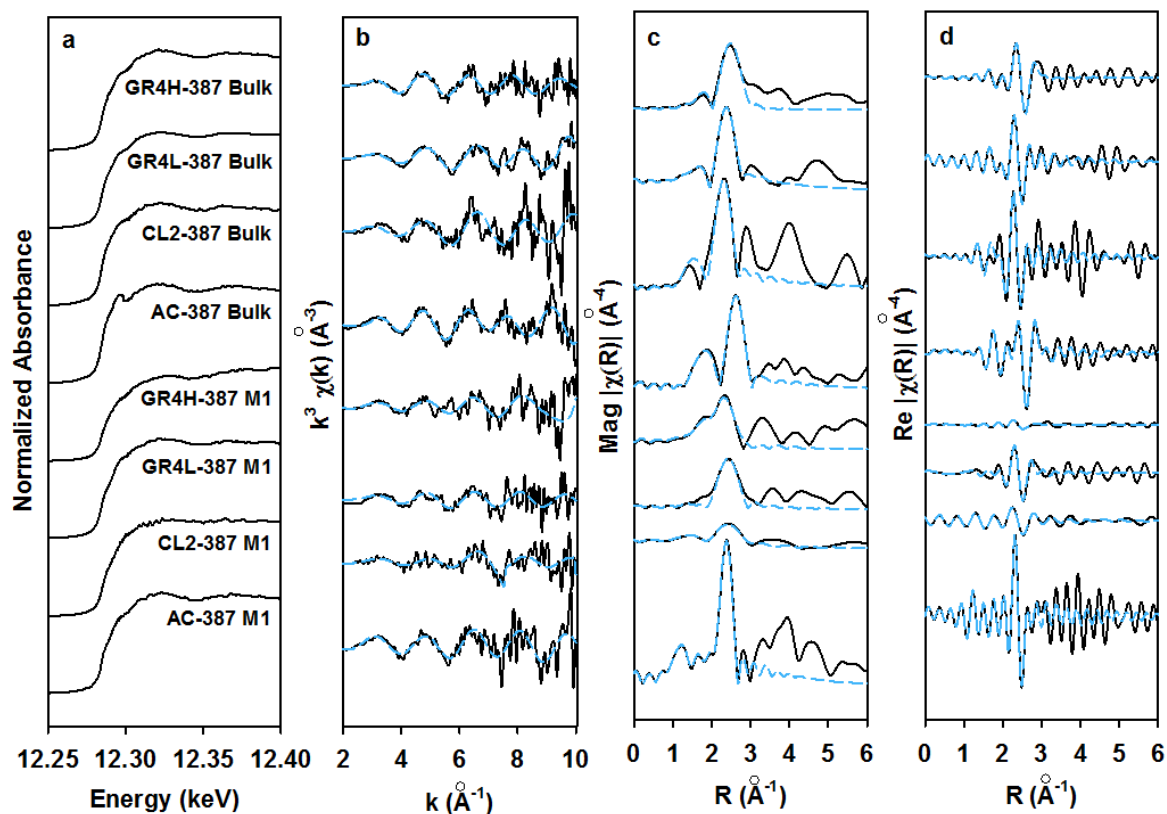


Figure 6.3 ^a Edge-step normalized Hg L_{III}-edge XANES spectra of the spots indicated in the μ -XRF maps. ^b k^3 -weighted chi spectra (black solid line) and the best fit data (light-blue dash line). ^c Fourier-transform magnitude spectra and the best fit data. Fourier transform data are corrected for phase shift. ^d Fourier-transform real part and the best fit data. M1 and bulk represent the spectra were collected from Hg-enriched area of μ -XRF maps and ground bulk biochars from amended systems.

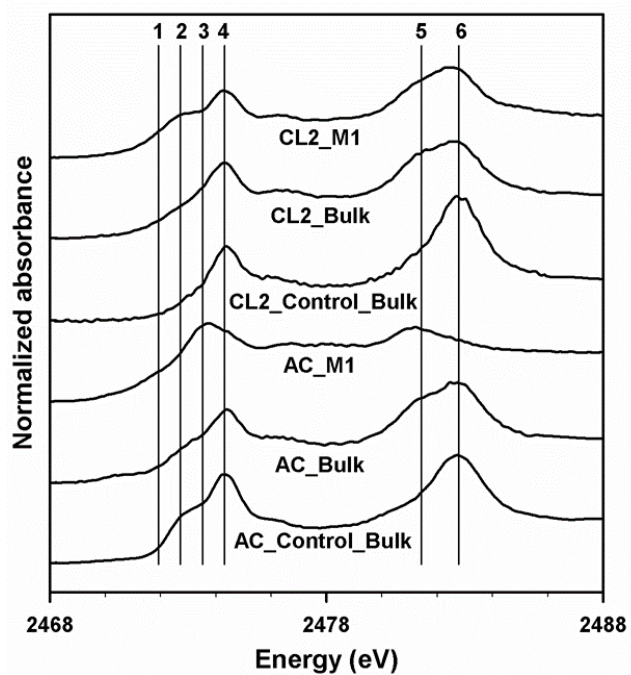


Figure 6.4 S XANES spectra of activated carbon (AC) and CL2 particles from amended systems and control at day 387. *Bulk* represents results of bulk sample analysis. *M1* represents the spectra from spots on thin-sections. S forms indicated by lines 1-6 are assigned as inorganic-sulfide, elemental, thiol, thiophenic, sulfonate, and ester-sulfate sulfur, respectively, as assigned by Manceau and Nagy (2012) and Vairavamurthy (1998).

Chapter 7: *Mechanisms of Mercury
Stabilization by Sulfurized Biochars
Determined using X-ray Absorption
Spectroscopy*

7.1 Executive Summary

The application of biochar to treat Hg in wastewater streams and contaminated soils and sediment is being proposed on an increasing basis due to its widespread availability and cost effectiveness. However, the efficiency of Hg removal by biochars is variable due to differences in source material composition and pyrolysis temperature. This study used a series of batch tests to evaluate the effectiveness of sulfurized biochar to enhance Hg removal; Hg-loaded biochars were then characterized using synchrotron-based techniques. Concentrations of Hg decreased by more than 99.5% in solutions containing biochars sulfurized by calcium polysulfide (CPS) and a dimercapto-related compound (DMC). S X-ray absorption near-edge structure (XANES) analyses indicate a polysulfur-like structure in CPS-modified biochar and a thiol-like structure (shifted compared with DMC) in the DMC-modified biochar. Micro-X-ray fluorescence (μ -XRF) mapping and confocal X-ray micro-fluorescence imaging (CXMFI) techniques indicate Hg is distributed primarily on the edges of modified biochar particles and throughout unmodified biochar particles. Hg extended X-ray absorption fine structure (EXAFS) analyses show Hg is bound to Cl in the unmodified biochar and to S in sulfurized biochars. These results indicate that Hg removal efficiency is enhanced after biochar sulfurization through the formation of strong bonds (Hg-S) with S-functional groups in the modified biochars.

7.2 Introduction

Hg is a global high-priority contaminant in water, sediment, and soils (Tchounwou et al., 2003). Extensive efforts have been devoted to removing Hg from water and to stabilize Hg in soils, sediments, and solid-wastes to decrease its impact on the environment (Randall & Chattopadhyay, 2013; Wang et al., 2012). Pyrolyzed carbonaceous materials,

including activated carbon, charcoal, and biochar, have been used as reactive media in a variety of Hg treatment systems (Gilmour et al., 2013; Gomez-Eyles et al., 2013; Liu et al., 2016b; Mohan et al., 2014; Patmont et al., 2015). For example, Hg removal from aqueous solution using biochar derived from malt spent rootlets (Boutsika et al., 2014) and activated carbons derived from sago waste (Kadirvelu et al., 2004) and coirpith (Namasivayam & Kadirvelu, 1999) have been shown to be effective; however, aqueous Hg concentrations after treatment often remain in the $\mu\text{g L}^{-1}$ to mg L^{-1} range, above those required for protection of the environment (Ullrich et al., 2001). To overcome these limitations, functionalized resins have been used to achieve final aqueous concentrations of Hg in the ng L^{-1} range (Bostick & Klasson, 1998; Hollerman et al., 1999; Klasson et al., 2000; Klasson & Bostick, 1998; Klasson et al., 2003). Synthetic chelating ligands were also used to maximize Hg removal (Blue et al., 2010; Blue et al., 2008). These specialized resins and ligands can be costly, potentially limiting their use for large-scale Hg treatment as would be required for remediation of watershed-scale contamination. There remains a need to evaluate the effectiveness of low-cost reactive materials that promote removal of Hg to ng L^{-1} levels.

The bond between Hg(II) and sulfide or thiol compounds is strong (Bisson et al., 2015; Blue et al., 2010; Blue et al., 2008; Feng et al., 2006; Olkhovyk & Jaroniec, 2005b), and binding with sulfide or thiol in solution can result in a decrease in Hg bioavailability (Slowey, 2010). However, in some cases, the presence of polysulfide in solution can lead to enhanced solubility of cinnabar and an increase in Hg bioavailability (Jay et al., 2000). Impregnation of polysulfide into carbonaceous materials can potentially reduce this adverse effect.

Calcium polysulfide (CPS) has been shown to be an effective reagent for removing Cr(VI) from water in both laboratory and field scale applications (Bewley & Clarke, 2010; Chrysochoou & Johnston, 2015; Chrysochoou et al., 2012), and dimercapto (DMC)-related compounds have been studied for Hg removal with efficient removal of Hg observed (Gibson et al., 2011; Olkhovyk & Jaroniec, 2005a; Olkhovyk & Jaroniec, 2005b). Elemental S and H₂S have also been applied for activated carbon (AC) sulfurization (Bisson et al., 2015; Feng et al., 2006), but the process requires high temperatures and the H₂S gas is corrosive and toxic.

Characterization of the form and spatial distribution of Hg within biochar particles is important for understanding Hg removal mechanisms and estimating the stability of bonded Hg. Synchrotron techniques can be used to characterize Hg speciation and S species of the sulfurized sorbent, for example to observe Hg-Br, Hg-S, and Hg-C binding environments on brominated and sulfurized sorbents (Bisson et al., 2015). Feng et al. (2006) report that elemental S, thiophene, and sulfate are likely responsible for Hg uptake in S-treated AC based on the results of S X-ray absorption near-edge structure (XANES) analyses.

Micro-X-ray fluorescence (μ -XRF) mapping has also been widely used to characterize the spatial distribution of Hg in various materials (Gu et al., 2014; Kim et al., 2000; Kim et al., 2012; Meng et al., 2014; Serrano et al., 2016). One drawback of μ -XRF mapping is that the fluorescence received by the detector is the sum of the signal along the incident beam path through the sample. Micro-XRF is often used to characterize elemental distributions in thin-sections, therefore measured distributions are representative of the sum of the elements over the thickness of a thin-section (usually $\geq 30 \mu\text{m}$) (Kim et

al., 2012; Liu et al., 2016b; Meng et al., 2014)). Confocal X-ray micro-fluorescence imaging (CXMFI), an emerging non-destructive technique, can overcome this drawback (Vincze et al., 2004). Depth compositional information can be obtained from precise locations of a particle using CXMFI (Choudhury et al., 2015b). The particle orientation can be adjusted using CXMFI, but for thin-sections, the slice of the particle is fixed.

In a previous study, Liu et al. (2016b) evaluated hardwood- (sp. *Quercus*) based biochar in its unmodified form and observed relatively effective removal of Hg from water. The current study is focused on improving Hg uptake by sulfurizing this biochar using CPS and DMC. A series of batch tests was conducted to evaluate the removal of dissolved Hg from aqueous solution using these modified biochars. Solid-phase reaction products were examined using a range of synchrotron techniques, including S XANES, μ -XRF, CXMFI, and Hg extended X-ray absorption fine structure (EXAFS) analyses, to evaluate the forms and distribution of Hg within the modified biochar particles.

7.3 Materials and Methods

7.3.1 Biochar Sulfurization

Biochar (CL2) was produced from oak wood at ~ 700 °C (rejects of the product from Cowboy Charcoal Co., Brentwood, TN, USA). CPS (23% by weight, Green Earth Sure-Gro IP Inc., Brantford, ON, Canada) and DMC (2,5-dimercapto-1,3,4-thiadiazole; 98%, Sigma-Aldrich) were used as biochar sulfurization reagents.

The biochar sulfurization was conducted under low- O_2 conditions in an anaerobic chamber (Coy Laboratory Products Inc.). CL2 was crushed and sieved to a size of 0.5-2 mm and rinsed six times with Ar-purged deionized (DI) water to remove fine particulates. The targeted S contents for the CL2 were 0.5, 2, and 5%. To achieve this, CL2 (20 g) was mixed with CPS (0.43, 1.7, and 4.2 mL) in 400 mL DI water or DMC (0.16, 0.63, and

1.56 g) in 100 mL ethanol. The mixtures were shaken thoroughly and allowed to equilibrate for 72 h. Controls were prepared by mixing CL2 with DI water and CL2 with ethanol in the same manner. The supernatants were then decanted and the reactive materials rinsed six times with DI water. The reactive materials were left to dry in the anaerobic chamber prior to the batch experiment.

7.3.2 Batch Experiments

Batch-style experiments were conducted under low-O₂ conditions. Solutions containing 25 and 250 µg L⁻¹ Hg were prepared in an anaerobic chamber by dissolving reagent-grade HgCl₂ in simulated groundwater (SG; CaCO₃-saturated DI water (Gibson et al., 2011)). Duplicate tests were conducted in 40 mL polypropylene tubes by mixing 1 g reactive material with 40 mL Hg-spiked SG. SG with and without Hg as well as ultra-purified water were used as controls. The 40 mL tubes were rotated for 48 h. Samples were then collected for total Hg (THg) analysis by filtering through 0.45 µm hydrophilic polyethersulfone membranes (Supor[®], Acrodisc[®], Pall Corp.). Samples were acidified to pH<2 with concentrated HNO₃, and stored at 4 °C until analysis.

The biochars without sulfurization and with 2% targeted S content were further tested in the same manner for removal of Hg at a higher initial concentration of Hg and for analysis with synchrotron-based X-ray techniques. The experiment was conducted by mixing 1 g of biochar with 200 mL SG with a THg concentration of 5 mg L⁻¹. Filtered samples were collected for THg and alkalinity analysis. Unfiltered samples were collected for pH analysis. Alkalinity and pH were measured immediately after sample collection. The pH was measured using an Orion Ross electrode (Orion 815600, Thermo

Scientific). Alkalinity was determined in duplicate using a Hach[®] digital titrator, bromocresol green indicator, and 0.16 N H₂SO₄, with mean values reported.

THg concentrations were determined using cold-vapor atomic fluorescence spectroscopy (Tekran 2600) according to EPA Method 1631 (EPA, 2002b). The method detection limit (MDL) was 0.19 ng L⁻¹ as determined following the EPA procedure (40 CFR, Part 136) (EPA, 2011).

7.3.3 Solid Samples for X-Ray Absorption Spectroscopy

S reference materials included CaSO₄ (Acros Organics), Na₂SO₃ (Sigma-Aldrich), CPS, and DMC. Cinnabar was used as a Hg reference material. The reference materials were ground into fine powders to decrease self-absorption effects. Unmodified and modified biochar samples with and without Hg were washed, freeze-dried, and ground into fine powders. The biochar samples loaded with Hg were prepared for thin-sections with a thickness of 30 μm (Vancouver Petrographics Ltd., Canada).

7.3.4 S X-Ray Absorption Near-Edge Structure Spectra

S XANES spectra were collected on the SXRMB beamline at the Canadian Light Source (CLS; Saskatoon, SK, Canada). Fine samples and reference compounds were spread as a thin film on a conductive double-sided tape mounted to a copper sample holder. Both total electron (TEY) and fluorescence (FY) yield data were collected. TEY data were used for reference materials and modified biochars because FY data are known to be susceptible to self-absorption at high S contents. FY data were collected for the unmodified biochars. Up to six scans were collected. Data processing was performed with ATHENA software (Ravel & Newville, 2005). Spectra for elemental S, pyrrhotite,

pyrite, L-cysteine, and Na tetrathionate were obtained from a previous study (Liu et al., 2016b). The energy for each run was calibrated with the spectrum of CaSO₄.

7.3.5 Micro-X-Ray Fluorescence Mapping

Micro-XRF maps were collected for the thin-sections on Beamline 13-ID-E (GSECARS) at the Advanced Photon Source (APS), Argonne National Laboratory (Argonne, IL, USA). A focused beam ~2×2 μm in size and a photon energy of 12.6 keV were used for μ-XRF data collection.

7.3.6 Hg Extended X-Ray Absorption Fine Structure Spectra

Hg EXAFS spectra were collected for the Hg-enriched areas of thin-sections on the GSECARS beamline and for bulk samples on Beamline 20-ID-B (PNC/XSD) at the APS. The XAS spectra were analyzed using ATHENA, and EXAFS model calculations were made using ARTEMIS (Ravel & Newville, 2005). following the method described by Gibson et al. (2011) and Liu et al. (2016b). Briefly, during the refinement of the first shell of Hg bound to biochar, the amplitude reduction factor (S_0^2) and the Debye-Waller factor (σ^2) were fixed on values determined from fits to reference compounds (Liu et al., 2016b), and the coordination number (CN) and bond distances (R) of the first shell were varied.

7.3.7 Confocal X-Ray Micro-Fluorescence Imaging

CXMFI analysis of the particles loaded with Hg was conducted at PNC/XSD. Particles were mounted on a quartz slide and placed at ~35° to the incident beam. The XRF spectra were monitored by a Si-drift Vortex detector perpendicular to the incident beam. A Ge optical unit (lithographically fabricated spoked channel array) was mounted in front of

the detector to complete the confocal geometry with a probing volume of $\sim 2 \mu\text{m}$ (Woll et al., 2012; Woll et al., 2014).

The intensity attenuation was calculated for the incident beam and XRF arising from the additional depth into the sample using the method described in Liu et al. (2016a). The elemental composition used for correction was presented in Table S7.1. Data importing, processing, and plotting were completed in MATLAB.

7.4 Results and Discussion

7.4.1 Aqueous Chemistry

Batch experiment pH values increased slightly after the addition of unmodified and modified biochars. The initial pH values were 7.9, 7.6, and 7.3 in solutions with THg concentrations of $18 \mu\text{g L}^{-1}$, $245 \mu\text{g L}^{-1}$, and 5mg L^{-1} , respectively. At the termination of the experiment, the pH values increased to ~ 8.2 in all solutions mixed with unmodified hardwood-based biochar (CL2), CPS-modified CL2 (CL2-CPS), and DMC-modified CL2 (CL2-DMC). The initial alkalinity was $\sim 95 \text{mg L}^{-1}$ as CaCO_3 , which is close to the values at the termination of the experiment. The results indicate the aqueous chemistry of the solution was only slightly altered after the addition of washed CL2 and sulfurized CL2. This was not the case for the unwashed CL2 (Liu et al., 2015), for which the pH increased from 7.8 to 8.5 and the alkalinity increased from 44 to 74mg L^{-1} .

7.4.2 Hg Removal

Substantial decreases in THg concentration were observed for solutions with added CL2, CL2-CPS, and CL2-DMC at three different initial THg concentrations (Fig. 7.1). The final THg concentrations in solutions containing modified CL2 were much lower than those with CL2. When the initial THg concentration was $17,800 \text{ng L}^{-1}$, the average final THg concentration was 370ng L^{-1} using CL2 but $<40 \text{ng L}^{-1}$ using CL2-CPS or CL2-

DMC. When the initial THg concentration was 245,000 ng L⁻¹, the final concentration was 5,700 ng L⁻¹ using CL2 but <110 ng L⁻¹ using modified CL2. When the initial THg concentration was 4,960 µg L⁻¹, the final concentration was 170 µg L⁻¹ using CL2 but <28 µg L⁻¹ using modified CL2. THg removal was >96.5 and >99.5% using CL2 and modified CL2, respectively, at the three initial concentrations.

The observed decline in Hg concentrations indicates that Hg removal is much more effective in the batch mixtures containing the modified biochar particles. No clear trend in THg concentrations is observed with respect to the use of CL2-CPS at three targeted S contents (0.5, 2, and 5%), but, in contrast, THg concentrations decrease after addition of CL2-DMC when the targeted S content increases.

Hg is more effectively removed by CL2-DMC than CL2-CPS at a low initial THg concentration, but more effectively removed by CL2-CPS at high initial concentration. The more effective Hg removal by CL2-DMC at the lowest THg concentration evaluated may be due to higher binding constants for Hg-thiol interaction than for Hg-polysulfide interaction (Skylberg, 2008). The greater Hg removal by CL2-CPS at a high concentration may be due to a higher proportion of reaction sites provided by CL2-CPS compared to CL2-DMC.

The Hg removal efficiency observed using these modified biochars is comparable to previous studies using functionalized resins and activated carbon. For example, Hg concentrations decrease from 1000 to <12 ng L⁻¹ in batch experiments and to <51 ng L⁻¹ in column experiments using functionalized resins (Hollerman et al., 1999; Klasson & Bostick, 1998); THg concentrations decrease from approximately 10,000 to 25 ng L⁻¹ in batch experiments using activated carbon (Liu et al., 2016b).

7.4.3 S XANES

S XANES spectra can help to define the oxidation state of S based on the position of the characteristic peak. The peak energy of S standards increases from 2470.3 to 2482.5 eV when the oxidation state of S increases from -2 (sulfide) to +6 (sulfate) (Fig. 7.2). The peaks in the S XANES spectra assigned to v1-5 represent the major peaks observed in CPS, DMC, CL2, and sulfurized CL2 (Fig. 7.2). Three peaks (v1, 2471.1; v2, 2472.8; v4, 2478.2 eV) are observed for CPS (Fig. 7.2a). The v1 peak is between peaks in the spectra of FeS₂ and FeS, and is due to the excitation of 1s electrons from the end members of S in the polysulfide. The v2 peak is at the same position as the peak in elemental S, and is assigned to 1s electrons in a molecular orbital σ^* (S-S) of the intermediate members of polysulfide. The v4 peak is close to that of sulfite, and another small peak is observed at higher energy in CPS and may represent an impurity. v3 (2473.6 eV) in DMC, at the same position as the peak in L-cysteine, is assigned to a $1s \rightarrow \sigma^*$ transition (S-C and S-H) (Dauphin & Salomé, 2014; Dezarnaud et al., 1990). The pre-edge small peak (2471.21 eV) in DMC is likely due to the excitation of electrons from the S between the two carbon atoms of DMC.

The two peaks at low energy and the v5 peak (sulfate, 2482.6 eV) in CL2 are not distinguishable after sulfurization to CL2-CPS and CL2-DMC (Fig. 7.2b), which is likely due to the low S content (<0.01%) in CL2 (Liu et al., 2016b). Only the v2 peak is observed in CL2-CPS, which indicates that the elemental S-like structure (polysulfur) is primarily formed during the sulfurization process. This observation also indicates that the impurities in CPS are removed during the washing process. For CL2-DMC, a shoulder at the same energy as v2 is observed on the v3⁺ peak. This shoulder is likely due to the shift

of the pre-edge small peak in DMC. The ν_3^+ means the peak is at a slightly higher energy (2474.1 eV) than ν_3 . The slight shifts of ν_3 to ν_3^+ and the pre-edge small peak are likely due to the interaction of thiol groups on DMC and functional groups on CL2. The observation of the polysulfur structure in CL2-CPS is consistent with spectra reported for activated carbon fibers treated with H_2S at 400-600 °C (Feng et al., 2006).

The disappearance of the end members of the polysulfide in the S spectra for CL2-CPS indicates the end members are likely embedded into the carbon structure of the biochar. The similarity of the S spectra between DMC and CL2-DMC indicates DMC is likely bound to biochar via π - π interactions between the ring structures as suggested by (Sandström & Wennerbeck, 1966). This type of interaction is hydrophobic and provides thiol groups that are available to bind with Hg.

The modified biochars were exposed to air for 10 and 60 d to evaluate the stability of the deposited S. The spectra collected for the modified biochars exposed to air for 10 or 60 d are similar to those for the fresh materials (Fig. 7.2c), except for a slight increase in the sulfate peak. These results suggest that the modified biochars are stable under the aerobic conditions of the experiments.

The form of S in reactive materials (*e.g.*, elemental, cysteine, and thiophene) plays an important role in the Hg removal process (Aboufazeli et al., 2013; Feng et al., 2006; Meng et al., 2014). The S XANES spectra of modified biochars loaded with Hg are similar to those without Hg (Fig. 7.2b), except the peak height is slightly different. This observation indicates the S forms are not altered by the adsorption of Hg, similar to previous findings by Liu et al. (2016b) for unmodified CL2 with and without Hg exposure.

7.4.4 Hg μ -XRF Maps

The μ -XRF maps indicate differences in the Hg distribution in thin-sections prepared using CL2, CL2-CPS, and CL2-DMC particles loaded with Hg (Fig. 7.3): Hg is located inside the pores and channels within the CL2 particles; is primarily distributed on the surface with less observed within the pores of CL2-CPS particles; and is mostly located on the surface of and also penetrating less extensively into the CL2-DMC particles. The presence of Hg is confirmed in the XRF spectra collected from an Hg-enriched area (Fig. 7.3).

The difference in Hg distribution patterns between unmodified (CL2) and modified (CL2-DMC and CL2-CPS) biochars is likely due to impregnation of S in the modified biochars. The primary distribution of Hg on the surface of modified biochars indicates the S likely impregnated the surface, which is consistent with a previous study that reported Hg concentrated on the exterior of a polysulfide-rubber-coated activated carbon, but diffused up to 100 μm into the particle after 3 months (Kim et al., 2012). Results from this study indicate the Hg is distributed up to 10 μm into the modified biochar particles after 2 d of treatment. The Hg distribution within the channel-like shape in CL2 is consistent with the observation of another thin-section of the same biochar in a previous study (Liu et al., 2016b).

7.4.5 Confocal X-Ray Micro-Fluorescence Imaging

Large differences in Hg distribution are evident for unmodified and modified biochars based on CXMFI (Fig. 7.4). Hg is distributed across and deep into CL2 particles but primarily accumulates on the surface of CL2-CPS particles. The Hg penetrates slightly deeper into CL2-DMC than CL2-CPS. Additional CXMFI results for Hg distribution

within unmodified and modified biochar particles are provided in Figs. S7.1-S7.5; distribution maps of other elements (S, Cl, K, and Ca) are also presented. Consistent Hg distribution maps are observed for the particles presented in Fig. 7.4 and Figs. S7.1-S7.5. The observations are also consistent with the μ -XRF maps (Fig. 7.3).

The S intensity of unmodified biochar particles in the maps is undistinguishable from the background signal and therefore is not included. The distribution of S is primarily on the surface of CL2-CPS (Figs. S7.2-S7.4) and on the surface and along the pores of CL2-DMC (Fig. S7.5). The observation of S in the modified biochars indicates that it was successfully incorporated into the biochars. The Hg co-occurs with S in the modified biochars (Fig. S7.2-S5). The difference in Hg distribution between the modified biochars is likely due to the difference in S distribution.

7.4.6 Hg EXAFS

The threshold E_0 (ionization energy) is 12.285 keV for the Hg XANES spectra of bulk and Hg-enriched areas of the unmodified and modified biochars (Fig. 7.5). The XANES spectra are similar for all samples and no distinguishable features are observed among the spectra. The Hg XANES spectra of the samples indicate Hg is in the oxidized Hg(II) form, as indicated by the similarity of the E_0 and edge shape of the sample spectra and the spectra for HgO, HgCl₂, cinnabar, and metacinnabar ((Liu et al., 2016b); Chapter 4).

Modeling EXAFS spectra can help to define the local structural information (*e.g.*, binding elements, coordination number, bond length) of the atom of interest. The EXAFS spectra were modelled against the first shell of cinnabar, metacinnabar, HgCl₂, Hg₂Cl₂, and HgO. The best matches are obtained using HgCl₂ as a model compound to simulate the spectra for bulk and Hg-enriched areas of unmodified CL2. Cinnabar is the best

model compound to simulate the spectra for bulk and Hg-enriched areas of CL2-DMC and CL2-CPS. Metacinnabar is the best model compound to simulate the spectra for bulk CL2-CPS (Table 7.1). The Hg EXAFS modeling results indicate that Hg is bound to Cl in the unmodified biochar and to S in the sulfurized biochar. The EXAFS modeling R-factors range from 0.006 to 0.12, with the lower values observed for bulk samples using the unfocused beam and higher values for thin-section analyses using the focused beam.

The coordination number (*CN*) of Cl is 0.58 for Hg in the Hg-enriched area of CL2, a value that is close to previous measurements using the same biochar (Liu et al., 2016b); the bond length is 2.29 Å, which is consistent with the theoretical value for Hg-Cl bonding. The *CN* of Cl is 1.04 in the bulk CL2. The *CNs* of S bound to Hg range from 1.30 to 2.05 in Hg-enriched area of CL2-CPS, CL2-DMC, and bulk CL2-DMC, which are in the range of published values (Bisson et al., 2012; Gibson et al., 2011; Liu et al., 2016b); the modeled Hg-S distances are between 2.36 and 2.42 Å, which are similar to the theoretical value (2.37 Å). The *CN* of S bound to Hg is 4.33 and the Hg-S distance is 2.51 Å in bulk CL2-CPS; both values are close to the theoretical values for metacinnabar. Gibson et al. (2011) conducted a batch experiment using DMC to remove Hg from solution and bulk Hg EXAFS was modeled with the first path of cinnabar. The results show *CN* is 1.6 and bond length is 2.48 Å (Gibson et al., 2011). The *CN* was 2.05 in the current study and the greater *CN* was likely related to the higher Hg : thiol ratios applied in the current study.

The greater *CNs* of Cl and S in bulk samples than in Hg-enriched areas of thin-sections are likely due to greater abundance of Cl and S in bulk samples compared with Hg-enriched areas. The Hg EXAFS modelling results indicate HgS is the primary Hg

species in modified biochars, suggesting that a chemical reaction occurs between the Hg in solution and the S functional groups in the biochars. Kim et al. (2012) also report Hg removal through reaction with S in polysulfide-rubber-coated activated carbon.

7.5 Environmental Applications

Hg immobilization by reaction or complexation with S functional groups within sulfurized biochar is a potential strategy for remediating contaminated sites by limiting Hg transport and decreasing Hg bioavailability. Results of this study indicate that Hg removal is enhanced after sulfurization of an oak biochar compared with unmodified biochar. After treatment, the Hg is distributed mainly on the surface of sulfurized biochars and on the surface and within the unmodified biochar particles. The results indicate that Hg is stabilized through formation of Hg-S for the modified biochar, a potentially stronger binding mechanism relative to simple surface adsorption processes.

Contaminated-site remediation using DMC or DMC-modified reactive materials has not been reported, however, DMC-modified material has been used in the removal of metal ions from ethanol (Lessi et al., 1996). DMC has also been used for determinations of Pb, Hg, and Cu in different environmental media, due to its propensity to bind with metals (Ahmed & Mamun, 2001; Tang et al., 2015b). A potential application of CL2-DMC for Hg removal is in controlled environments such as use in containerized treatment systems for wastewater (Hussain et al., 2014; Robertson et al., 2009). Larger-scale field applications may require greater information on the potential health effects of DMC (Integrated Laboratory Systems Inc., 2005).

CPS is a low-cost reagent approved for use for remediation of Cr(VI) at contaminated sites (including Superfund sites) in the US (Federal Remediation Technologies Roundtable, 2004; Petersen et al., 2006; Underwood & Ipsen, 2008) and

UK (Bewley & Sojka, 2013). After impregnation of CPS in the biochar, stabilization of Hg is expected to be enhanced, potentially decreasing the environmental impact of Hg. Biochar can be stable under some environmental settings for long periods (Mann, 2002; Spokas, 2010), suggesting that modified biochar may also be stable over the long term.

Table 7.1 Hg EXAFS fitting results for bulk and thin-sections (micro) of unmodified and CPS and DMC modified biochars^a.

Sample	Reference	Path	CN	R (Å)	S ₀ ²	σ ² (Å ²)	R-factor
DMC_bulk	α-HgS	Hg-S	2.05 (±0.27)	2.37 (±0.02)	0.841 ^b	0.00518 ^b	0.015
CPS_bulk	β-HgS	Hg-S	4.33 (±0.19)	2.51 (±0.01)	0.718 ^b	0.00967 ^b	0.006
CL2_bulk	HgCl ₂	Hg-Cl	1.04 (±0.19)	2.31 (±0.03)	0.967 ^b	0.00234 ^b	0.052
DMC_micro	α-HgS	Hg-S	1.30 (±0.35)	2.36 (±0.04)	0.841 ^b	0.00518 ^b	0.12
CPS_micro	α-HgS	Hg-S	1.66 (±0.74)	2.42 (±0.07)	0.841 ^b	0.00518 ^b	0.11
CL2_micro	HgCl ₂	Hg-Cl	0.58 (±0.21)	2.29 (±0.07)	0.967 ^b	0.00234 ^b	0.078

^a CN = coordination number, R = bond length, and R-factor = fitting statistic.

^b fixed values from model compounds ((Liu et al., 2016b) and (Liu et al., 2016a))

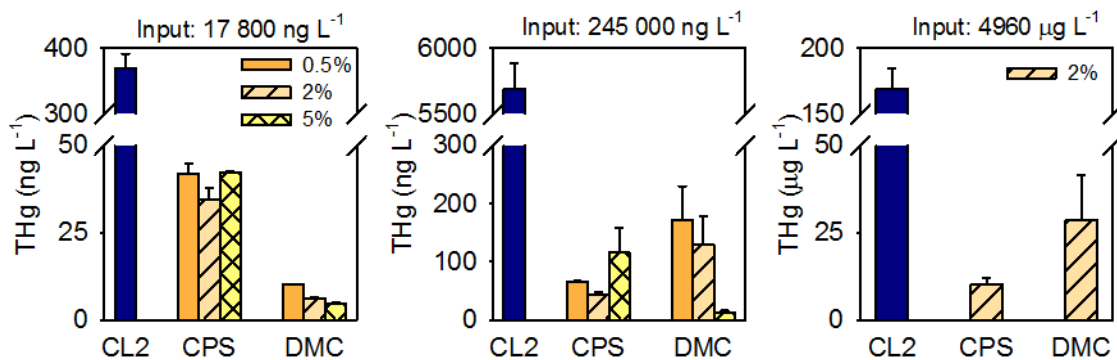


Figure 7.1 THg concentrations from aqueous solution in batch tests containing unmodified biochar (CL2) and CPS- and DMC-modified (target S contents of 0.5, 2, and 5%) biochars at three different initial concentrations. Error bars represent standard error of the mean derived from duplicate experiments.

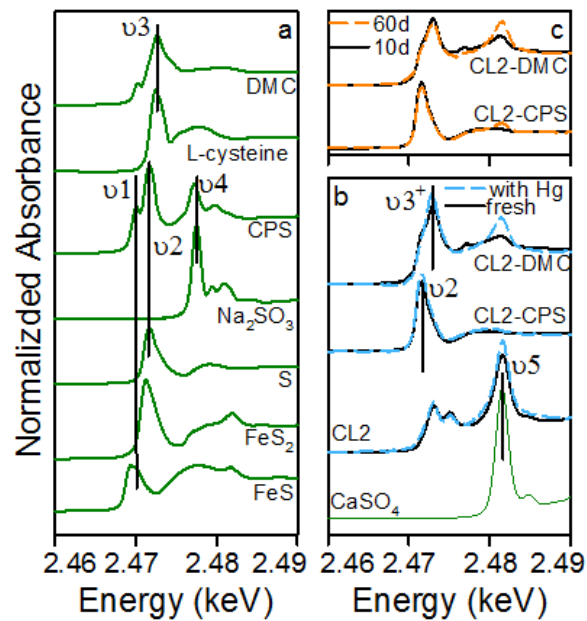


Figure 7.2 S XANES spectra of a) six reference materials (one in b), CPS, and DMC, b) unmodified and sulfurized CL2 (with and without Hg), and c) sulfurized CL2 exposed to air for 10 and 60 d. Spectra of elemental S and CaSO₄ were reduced by half for ease of display.

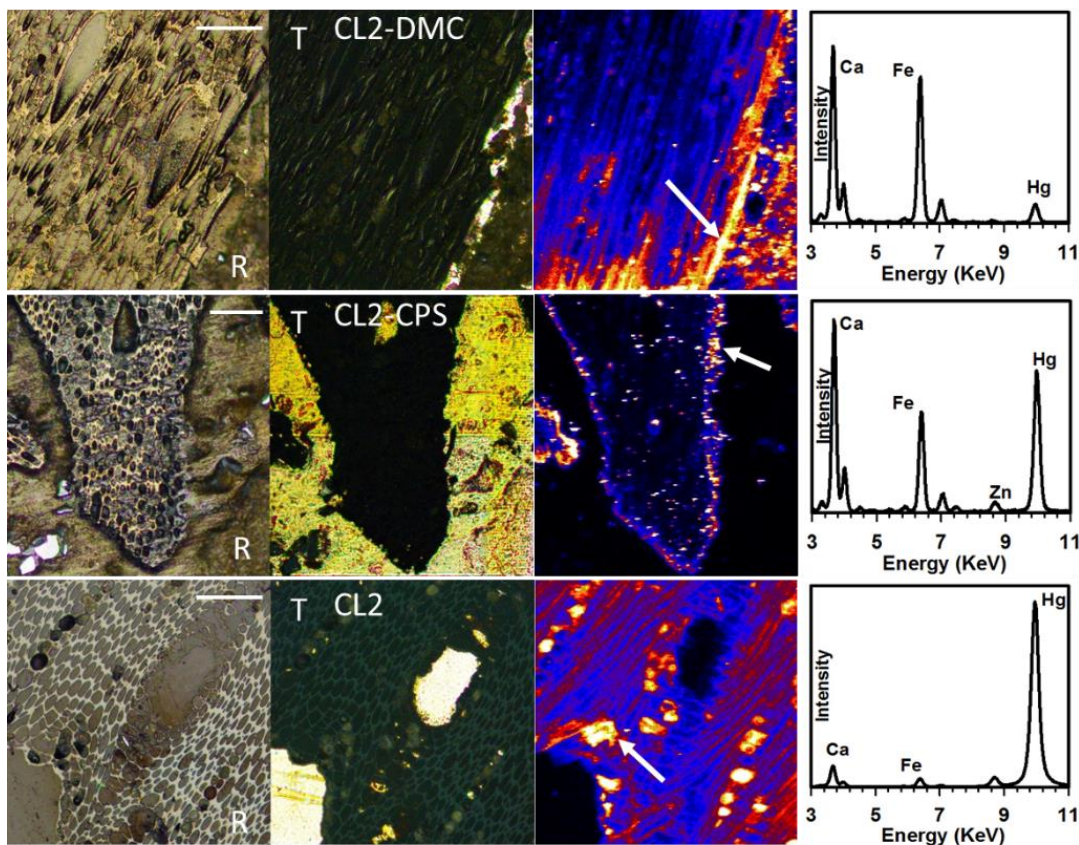


Figure 7.3 Microscope photos under reflection mode (R; 1st column), transmission mode (T; 2nd column), Hg L α line μ -XRF maps (3rd column), and the XRF spectra of the Hg-enriched area indicated by the white arrow of unmodified biochar (CL2) and CPS- and DMC-modified biochars in thin-sections. The white bar represents 100 μ m. The EXAFS spectra for modeling were also collected at the locations indicated by the white arrows.

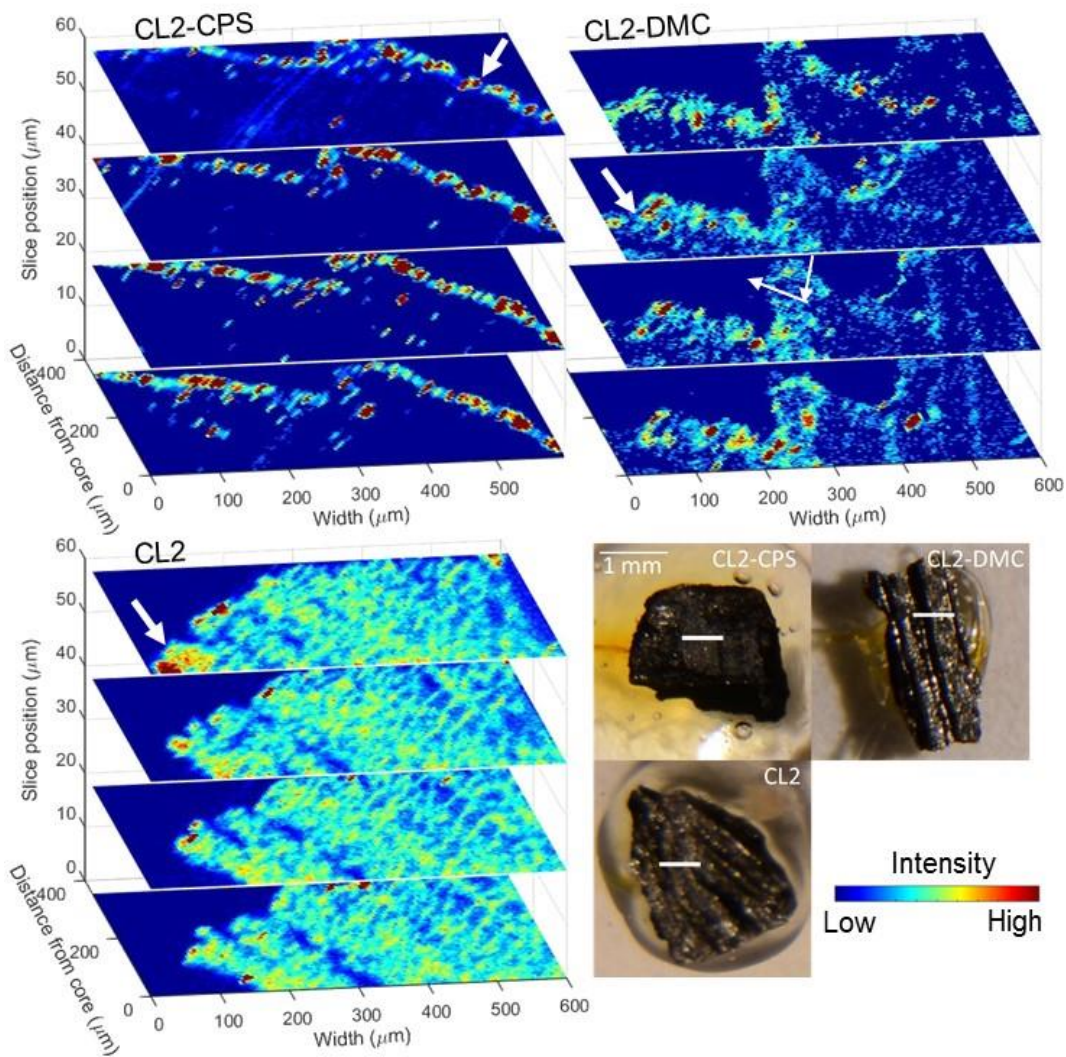


Figure 7.4 Confocal X-ray micro-fluorescence imaging showing the distribution of Hg in unmodified and modified biochar particles (not physically sectioned) with adsorbed Hg. Photos in the bottom right corner show the orientation of the particles for analysis. The white bars on the particle indicate the imaging area ($600 \times 60 \mu\text{m}^2$) with an imaging depth as $350 \mu\text{m}$. The thick white arrow indicates the surface of the particle. The thin white arrow indicates the incident and emitted beam paths. Vertical exaggeration is ~ 8 .

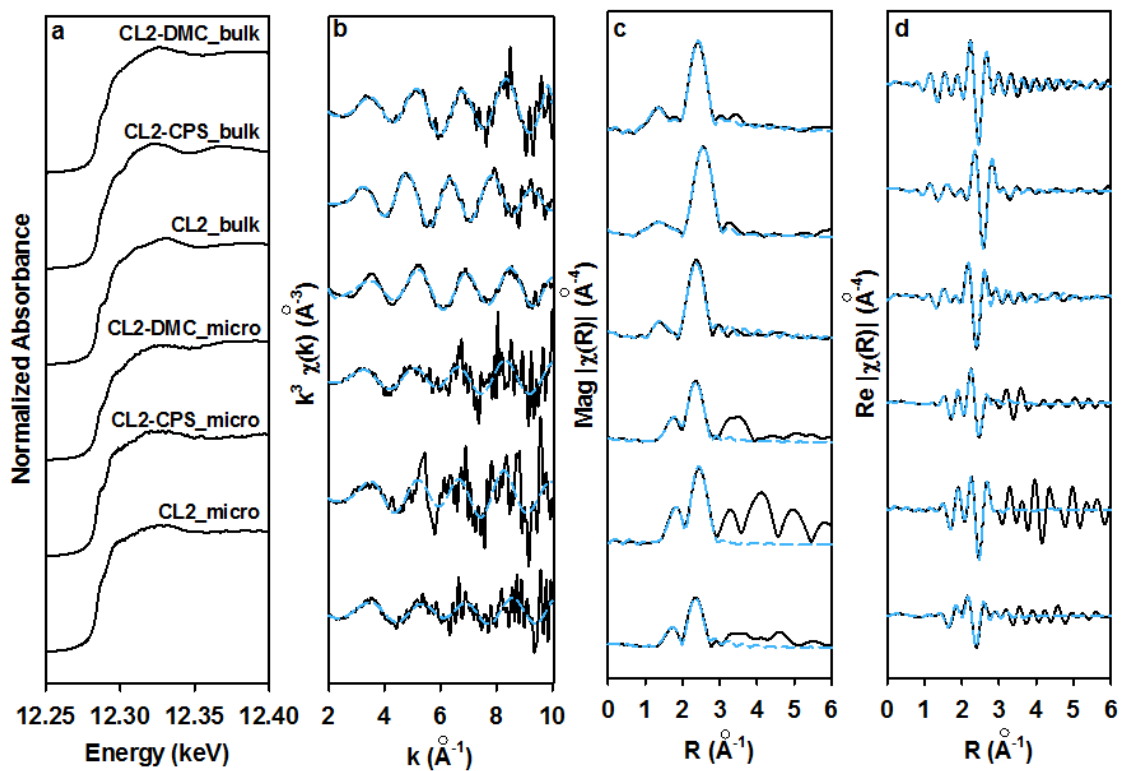


Figure 7.5 a) Normalized Hg XANES spectra collected from bulk samples and Hg-enriched areas (micro) in thin-sections of bulk unmodified (raw) and sulfurized (CPS and DMC) biochars. b) k^3 -weighted chi spectra (black line) and best fit (light blue-dash line). c) Fourier-transformed magnitude spectra. d) Fourier-transformed real part.

Chapter 8: *Conclusions*

8.1 Summary of Findings

Thirty-six biochars samples derived from a range of feedstocks and pyrolysed at different temperatures were investigated to assess their physicochemical properties, the release of OA, DOC, and nutrients to solution, the removal of Hg from solution, and the stabilization of Hg in contaminated sediment. A combination of analysis and characterization methods, including aqueous phase geochemical analysis, solid phase elemental analysis, microbial analysis, and X-ray absorption spectroscopy analysis (micro-X-ray fluorescence mapping (μ -XRF), extended X-ray absorption fine structure (EXAFS), X-ray absorption near edge structure (XANES), and confocal micro-X-ray fluorescence imaging (CXMFI)), were applied in the study. The results indicate unmodified and sulfurized biochars are effective reactive media for Hg removal from aqueous solution. The stabilization effectiveness varied among the different tested biochars.

Solid-phase C analyses indicate that charcoal and activated carbon had the highest C contents which ranged from 74.5-99.9%, manure and mushroom soil biochars had the lowest C contents which ranged from 22.8-63.5%, and C contents for the remaining biochars ranged from 63.6-99.7%. For S content, poultry manure biochars had the highest values from 0.48-3.40 %, and charcoal and activated carbon had the lowest values. The C and S contents of biochar samples prepared at 600°C were greater than for samples charred at 300°C. The results from FT-IR spectra showed all biochar samples had hydroxyl, aliphatic, and quinone functional groups. Fewer spectral peaks were observed and the intensity of the observed peaks decreased as the pyrolysis temperature was increased from 300°C to 600°C, with the exception of phosphate, and thiol functional groups.

Different short-chain organic acids (OA) (formate, acetate, lactate, and propionate) were observed in the water in contact with biochar. Concentrations of OA and dissolved organic carbon (DOC) varied with feedstock and pyrolysis temperature. The concentrations of DOC released by biochars prepared at 600°C were less than those by biochars prepared at 300°C. The concentrations of OA released by biochars prepared at 600°C were less than those by biochars prepared at 300°C. DOC concentrations showed the same trend as OA. The carbon in OA accounted for 1-90 % of DOC, which indicates other forms of carbon also were released by the biochars.

In the batch systems containing activated carbon, charcoal and biochars pyrolyzed at 600°C, concentrations of Hg were observed to decrease by >90%. In the systems containing other biochars, concentrations of Hg decreased by 40-90%. Batch test results indicate that river water equilibrated with biochars prepared at 600°C had higher pH and alkalinity and released lower concentrations of PO₄-P and NH₄-N than biochars prepared at 300°C. Higher concentrations of NO₃⁻, NO₂⁻, and SO₄²⁻ were released by biochars prepared at 300°C. Higher concentrations of Na, Al, Si, K and lower Mg, Ca, Mn, Fe were released by biochars charred at 600°C than biochars charred at 300°C. The trace elements (Ba, Cd, Cr, Co, Cu, Fe, K, Li, Mo, Na, Ni, Pb, Si, Sr and Zn) released by biochars were relatively low, and for the experimental conditions were below those deemed harmful to aquatic life.

In microcosm experiments in which biochar was co-blended with sediment and river water, determinations of aqueous concentrations of THg as a function of time showed elevated concentrations of THg in the sediment control, reaching values of approximately 40 µg L⁻¹. During the first few weeks of the experiment, small differences

were observed in THg concentrations between the control and the amended systems containing biochars. Reductions in THg concentrations of 60-90% compared with the sediment controls were observed after 30 days for activated carbon, 70-92% after 120 days for high-T poultry manure biochar, 20-92 % after 120 days for low-T and high-T switchgrass biochars, and 30-60% after 250 days for CL2 (oak wood biochar) amended systems. An increasing trend in the THg concentrations was observed for high-T poultry manure biochar amended systems after 126 days.

Concentrations of MeHg as a function of time reached maximum values of close to 40 ng L⁻¹ in the sediment control. Similar or lower concentrations of MeHg were observed in the amended systems. An initial peak in MeHg concentration in the activated carbon amendment system was higher than the sediment control. The MeHg concentrations in the duplicate CL2 amended systems were lower than those in the control and the other amendment systems in the first 300 days. The MeHg concentrations in the low-T switchgrass biochar amended system were lower than those in the sediment controls during the first 100 days. Peak concentrations in the high-T poultry manure biochar amended systems were lower than that in the sediment controls, but persisted at elevated concentrations for longer. A second peak was observed in amended systems containing CL2 and high-T switchgrass biochar with MeHg concentrations of MeHg as 220 ng L⁻¹ at day 387 and 260 ng L⁻¹ at day 445, which were much greater than other peaks.

Comparison of the concentration evolution of THg, MeHg, and Fe with SO₄²⁻ concentrations in the microcosm experiment indicates a decrease in SO₄²⁻ concentrations is correlated with an increase of THg concentrations and peak concentrations of MeHg

and Fe in the aqueous phase. Ferric Fe from (hydro)oxide and sulfate were likely reduced at the same time by FeRB and SRB utilizing carbon and energy sources, and Hg was also likely released from Fe (hydro)oxides. The sulfide derived from SO_4^{2-} reduction is expected to form sulfide precipitates with Hg and reduced Fe from the solution. After the depletion of sulfide, dissolved Hg concentrations were observed to increase. The early peak in MeHg concentration is attributed to increased activities of FeRB and SRB (Gilmour et al., 1992; Kerin et al., 2006), both of which were detected in the systems. The second peak in MeHg concentration is attributed to the activity of methanogens (Yu et al., 2013), which also were detected in the system.

μ -XRF mapping indicates Hg co-occurs with S, Cu, Fe, Mn, and Zn on the surface and inside the biochar particles. EXAFS modeling indicates Hg was in an oxide form on the surface of an Fe (hydro)oxide particle from fresh sediment and in Hg-sulfide forms for the Hg-rich areas of biochar particles after amendment with sediment. S XANES analyses indicate the presence of sulfide in these biochar particles. After amended with biochars, a fraction of the Hg in unstable forms (dissolvable, HgO, colloidal, nano, etc.) in the sediment was stabilized as Hg-sulfide forms characterized by lower potential mobility and bioavailability by biochar particles.

Compared with the pore structure of low-T and high-T switchgrass biochar, CXMFI imaging indicates that Fe and Hg were distributed throughout the particle for low-T switchgrass biochar, whereas Fe and Hg were preferentially observed on the surface of high-T biochar particles from the amended systems in the microcosm experiment. These observations are also consistent with observed distributions of Ti, Cr, Mn, Co, Ni, Cu, Zn, and As. The differences in elemental distribution patterns for low-T

and high-T biochar particles are attributed to more extensive carbonization of the biochars produced at the higher pyrolysis temperature. Biochar pyrolyzed at 300°C is not completely carbonized and has a fraction of labile C compared to biochar pyrolyzed at 600°C. For example, higher concentrations of DOC and acetate are leached from low-T biochar (Chapter 2), and were observed during the early stages of the low-T biochar amended system, but not in the high-T biochar amended system. These findings suggest that the low-T biochar structure is more easily penetrated by elements such as Hg, Mn, Fe, Co, and Zn. These elements may be either precipitated inside the particle or replace the original elements of the particle, when the conditions are anaerobic and solutions are rich in components with potential to form secondary minerals. This process is similar to an early-stage diagenesis process observed in a number of environmental systems.

The transformation of Hg in the microcosm experiment can be described by the following proposed stages, based on the aqueous geochemical and solid phase XAS analyses. During the first stage, Hg is rapidly leached from the sediment and is subsequently adsorbed to the surfaces of the biochar (Fig. 8.1); binding between Hg and biochar is weak and other cations can compete with Hg for adsorption sites on the biochar surfaces. The second stage represents the onset of Fe(III)-reducing conditions (Fig. 8.2). During this stage, Hg and other elements embedded on the surface or within Fe(III) oxides are released into solution and FeRB convert this more available Hg to MeHg. The third stage represents the onset of sulfate-reducing conditions, which overlaps with the iron-reducing stage. Sulfate is reduced to sulfide, and Hg, Fe, Cu, and other elements co-precipitate with sulfide on the surfaces or inside the biochar particles (Fig. S6.7). SRB can convert Hg to MeHg during this stage, however, to a lesser extent

due to the strong binding between Hg and the biochar. In the last stage, methanogenic conditions are established (Fig. 8.4) as indicated by utilization of alkalinity and the increase in the percentage of methanogens. During this final stage, MeHg also may be formed by methanogenic methylators.

The results indicate that Hg co-occurs with Cu, Fe, S, Zn, Mn, and other elements on the surface and inside biochar particles from the amended systems. These accumulations are well correlated with the evolution of components in the aqueous phase. Because biochar can be stable in the environment for long periods (Spokas, 2010), the Hg contained within these particles may also be stable for long time frames. The Hg was observed to be distributed within biochar particles, therefore this stabilized Hg may be less bioavailable to Hg methylators (Zhang et al., 2012). Furthermore, the transport of Hg may be limited due to the strong binding between Hg and the biochar particles (Lowry et al., 2004).

To improve the removal efficiency, the CL2 was sulfurized by the addition of calcium polysulfide (CPS) and a dimercapto (DMC)-related compound. The results of batch experiments indicate the final concentrations of Hg were much lower in solutions containing sulfurized biochars than in unmodified biochars. The final THg concentration was 5,700 ng L⁻¹ using unmodified CL2 and <110 ng L⁻¹ using sulfurized CL2 at an initial concentration of 245,000 ng L⁻¹. Polysulfur- and thiol-like structures were observed in the sulfurized biochars using S XANES. Hg was distributed primarily on the edges of sulfurized biochar particles; in contrast Hg was distributed throughout unmodified biochar particles, as indicated by μ -XRF mapping and CXMFI. EXAFS

analyses indicate that Hg was bound to Cl in the unmodified biochar and bound to S in sulfurized biochars.

The results of these studies imply that biochar may be an effective material for Hg removal from aqueous solution, and for Hg stabilization in sediments. Sulfurization of the biochar led to increased Hg removal efficiency. Hg removal from solution was through formation of Hg-S bonds for some biochar samples and for the sulfurized biochar. Stabilization of in mixtures containing biochar, sediment and river water was through the formation of Hg-S species. The formation of Hg-S is potentially a stronger binding mechanism relative to simple surface adsorption processes. The results indicate Hg may be stabilized through an early-stage diagenesis process in the microcosm experiments, especially for the low-T biochar switchgrass biochar.

8.2 Scientific Contributions

Research presented in this thesis contributed information related to removal of Hg from the aqueous phase and stabilization of Hg within contaminated sediment using various unmodified biochars and sulfurized biochars. New scientific contributions resulting from this thesis include:

- Illustration of elevated concentrations of OA, DOC, Cl⁻, SO₄²⁻, PO₄-P and NH₄-N in most river water samples equilibrated with biochars
- Demonstration of effective Hg removal from aqueous phase using biochar samples
- Investigation of Hg removal mechanisms from aqueous solution using biochars
- Demonstration of the decrease of Hg in the aqueous phase after amendment of contaminated sediment with biochars

- Illustration of MeHg evolution in the aqueous phase related to changes in Fe, SO_4^{2-} , and C source in solution and evolution of microbial activity in the solid phase
- Investigation of Hg stabilization mechanisms of contaminated sediment amended with various biochars
- Demonstration that Hg co-occurs with elements of Fe, S, Cu, Zn, and other elements on the surface or inside the biochar particles from the amended systems
- Illustration of Hg stabilization by low-T switchgrass biochars through early-stage diagenesis in a long-term amended system
- Demonstration of enhanced Hg removal by sulfurized biochar and delineation of Hg removal mechanisms using synchrotron-based techniques

8.3 Implications of Research Results

In aquatic environments, elevated concentrations of SO_4^{2-} , nutrients, and labile organic matter (short-chain OA and DOC) can lead to the formation of anoxic conditions and promote growth of FeRB, SRB, and methanogens, the primary groups of methylating bacteria. The results of batch experiments indicate that elevated concentrations of organic acids, DOC (Chapter 2), SO_4^{2-} (Chapter 3), and nutrients (Appendix G) were observed in solutions mixed with manure-based biochars and biochars produced from cocoa husk, suggesting utilization of these biochars in O_2 -limited conditions might stimulate the growth of SRB. Less elevated concentrations of these components were released from wood-based biochars and biochars produced from cotton seed husk, corn cob and stover, and grasses, suggesting these biochars can be used as amendments to control Hg in aquatic environments.

The results of the anaerobic microcosm experiments indicate that aqueous THg concentrations in biochar amended systems were lower than in the sediment controls on different days for different biochar samples. Aqueous MeHg concentrations were maintained at low levels in the early stage of the amended systems containing high-T hard-wood biochar and high-T switchgrass biochar, and in the late stage in amended systems containing activated carbon and high-T poultry manure biochar, whereas the MeHg concentrations were lower than those in sediment controls over the duration of the experiment containing low-T switchgrass biochar.

In the anaerobic microcosm experiments, both effective THg control and minimal net production of MeHg in the aqueous phase were observed in the sediment amended with the low-T switchgrass biochar. These results suggest low-T switchgrass biochar may be an effective amendment for sediment under anaerobic conditions.

The addition of biochar into the sediment did not result in obvious changes in the percentages of fermenters, FeRB, SRB, and methanogens in the amended sediment relative to the sediment control. This result suggests the biochar has a limited effect on the microbial community. The results of the microcosm experiment indicate Hg is stabilized by co-precipitation with S, Fe, Cu, etc. on the surface or inside the biochar particles. Because the Hg removal process is likely a combination of adsorption and precipitation reactions, quantifying the capacity of Hg uptake by the biochar requires information on the factors controlling the rate of Hg-S precipitation.

8.4 Future Research

The findings of this research indicate that Hg present in aqueous solutions and released from contaminated sediment can be effectively removed by biochars. However, the

following questions still remain prior to future wide-spread application of biochar to control Hg in contaminated sediment:

- The microcosm experiments were conducted under anaerobic conditions through the course of this study. The evolution of Hg under redox oscillations within amended systems is unknown. Redox oscillations may influence the release of Hg to pore waters, the production of MeHg, the activity of benthic microbes, the mobility of colloids, and the rate of aging of biochars. Previous research has shown that the concentration of Hg in pore waters and the production of MeHg are highly influenced by transitions in redox conditions (Bouchet et al., 2011; Koron & Faganeli, 2012). Benthic microbial activity also can be enhanced under redox oscillations (Bartoli et al., 2009; Frindte et al., 2012). The mobility of colloids also can be enhanced under the inducement of reducing conditions due to Fe or Mn-mineral dissolution or to shifts in solution pH (Farnsworth et al., 2012; Thompson et al., 2006). Under changing redox conditions, the rate of decomposition of biochars may be accelerated, potentially influencing the longevity of Hg stabilization by biochars. Long-term evaluation of contaminated sediment remediation using biochar under redox oscillations is required to provide more information on the robustness of biochar as a treatment media.
- A spike in MeHg concentration at ~400 days was observed in the CL2 and high-T switchgrass biochar amended systems, while no spike was observed in activated carbon, low-T switchgrass biochar, and poultry manure biochar amended systems. The mechanisms that control this spike in MeHg remains unclear. More detailed

studies are required to explore the processes controlling rates of MeHg formation in the amended systems.

- The sulfurized biochar samples should also be tested in more complicated systems, for example, within microcosm experiments and other dynamic treatment applications. The analyses in the microcosm experiment using unmodified biochars should also be conducted in the new microcosm experiment. The results will provide information about the effectiveness of Hg stabilization, evolution of MeHg, and longevity of modified biochar.
- In this research, detailed studies conducted on a subset (4 biochars) of the 36 biochars indicate partial control of THg and MeHg concentrations under anaerobic and saturated conditions at 5% (wgt/wgt) amendment over an extended time period. Additional studies should be conducted to evaluate a broader set of biochars to identify other candidate reactive materials and to evaluate higher amendment rates to more effectively control THg and MeHg.
- Due to the low density of biochar particles, they can be easily transported by flowing water. To overcome this limitation, studies should be conducted to evaluate the reactivity of biochar particles when they are encased in a mat-like filter using geotextiles or in other field applications.

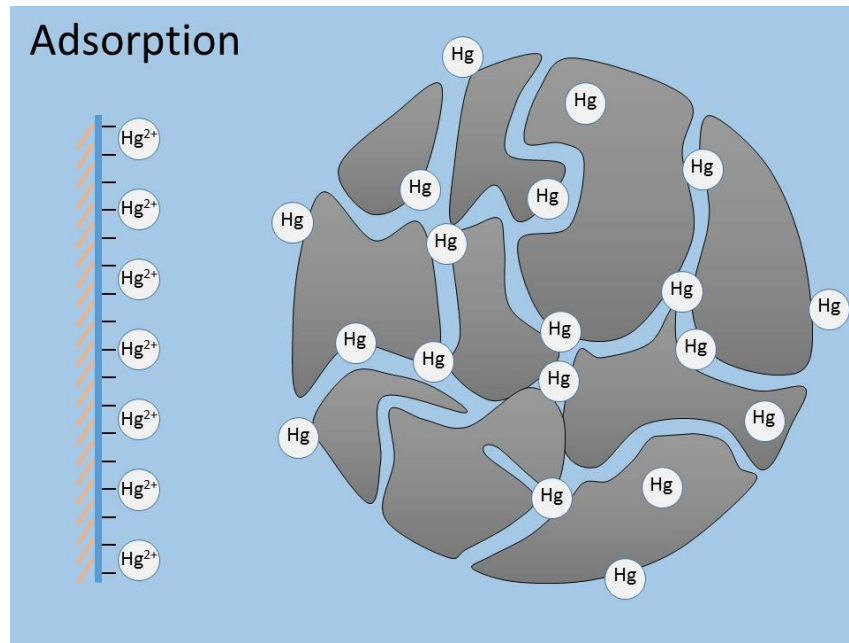


Figure 8.1 Rapid adsorption of Hg by biochar particles in the amended systems at the beginning of the experiment.

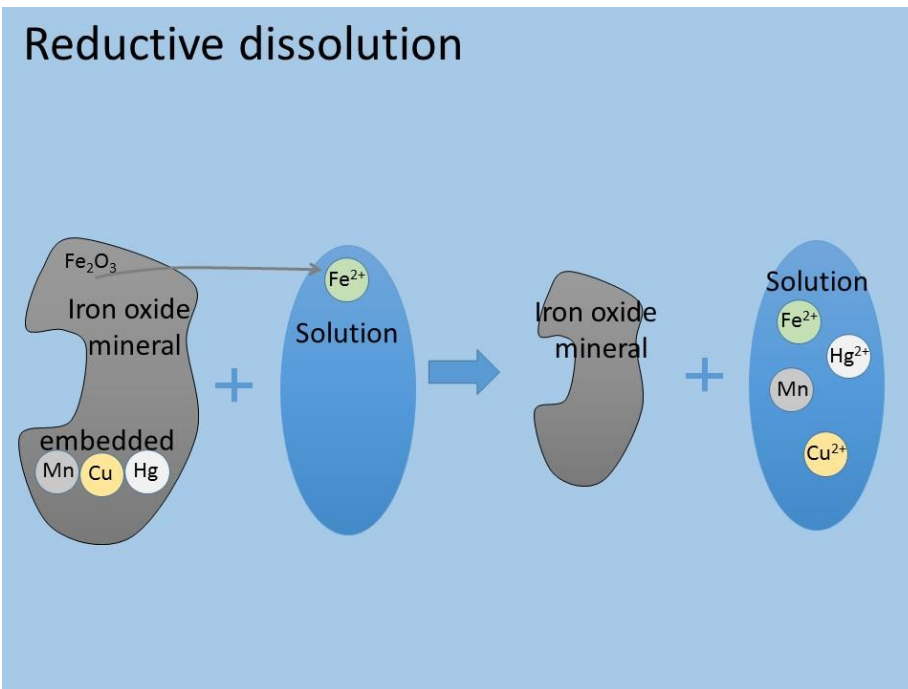


Figure 8.2 The release of Hg during the dissolution of iron oxide at the iron reducing stage.

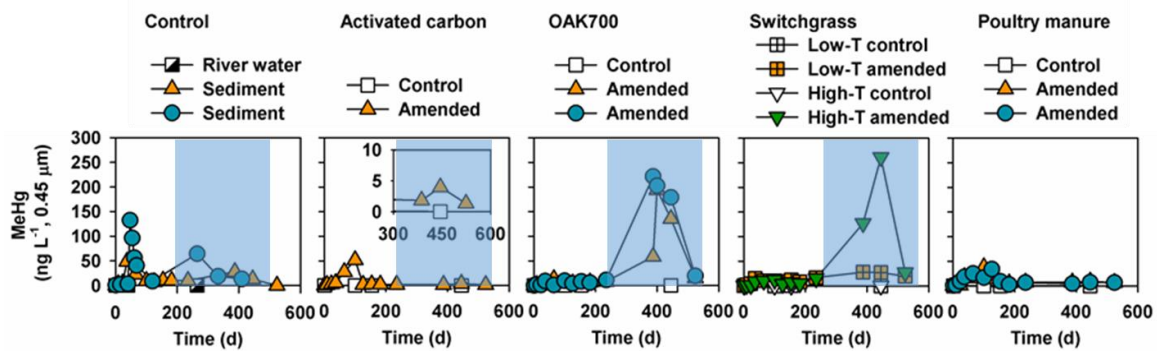


Figure 8.3 Production of MeHg during the methanogenic stage (adapted from Fig. 5.1).

References

- Aboufazeli, F., Zhad, H.R.L.Z., Sadeghi, O., Karimi, M., Najafi, E., 2013. Synthesis and characterization of novel poly-thiophene-nanoporous silica and its application for mercury removal from waste waters. *J. Macromol. Sci., Pure Appl. Chem.* 50(1), 18-24.
- Acha, D., Pabon, C.A., Hintelmann, H., 2012. Mercury methylation and hydrogen sulfide production among unexpected strains isolated from periphyton of two macrophytes of the Amazon. *FEMS Microbiol. Ecol.* 80(3), 637-45.
- Adams, C.J., Redmond, M.C., Valentine, D.L., 2006. Pure-culture growth of fermentative bacteria, facilitated by H₂ removal: bioenergetics and H₂ production. *Appl. Environ. Microbiol.* 72(2), 1079-1085.
- Adler Miserendino, R., Bergquist, B.A., Adler, S.E., Guimarães, J.R.D., Lees, P.S.J., Niquen, W., Velasquez-López, P.C., Veiga, M.M., 2013. Challenges to measuring, monitoring, and addressing the cumulative impacts of artisanal and small-scale gold mining in Ecuador. *Resources Policy.* 38(4), 713-722.
- Agarwal, S., Tyagi, I., Gupta, V.K., Ghaedi, M., Masoomzade, M., Ghaedi, A.M., Mirtamizdoust, B., 2016. Kinetics and thermodynamics of methyl orange adsorption from aqueous solutions - Artificial neural network-particle swarm optimization modeling. *J. Mol. Liq.* 218, 354-362.
- Agyarko, K., Asiedu, E., 2012. Cocoa pod husk and poultry manure on soil nutrients and cucumber growth. *Adv. Environ. Biol.* 6(11), 2870-2874.
- Ahmad, M., Ok, Y.S., Rajapaksha, A.U., Lim, J.E., Kim, B.Y., Ahn, J.H., Lee, Y.H., Al-Wabel, M.I., Lee, S.E., Lee, S.S., 2016. Lead and copper immobilization in a shooting range soil using soybean stover- and pine needle-derived biochars: Chemical, microbial and spectroscopic assessments. *J. Hazard. Mater.* 301, 179-86.
- Ahmad, M., Rajapaksha, A.U., Lim, J.E., Zhang, M., Bolan, N., Mohan, D., Vithanage, M., Lee, S.S., Ok, Y.S., 2014. Biochar as a sorbent for contaminant management in soil and water: A review. *Chemosphere.* 99, 19-23.
- Ahmed, M.J., Mamun, M.A., 2001. Spectrophotometric determination of lead in industrial, environmental, biological and soil samples using 2,5-dimercapto-1,3,4-thiadiazole. *Talanta.* 55(1), 43-54.
- Aiken, G.R., Hsu-Kim, H., Ryan, J.N., 2011. Influence of dissolved organic matter on the environmental fate of metals, nanoparticles, and colloids. *Environ. Sci. Technol.* 45(8), 3196-3201.
- Akhtar, S.S., Li, G., Andersen, M.N., Liu, F., 2014. Biochar enhances yield and quality of tomato under reduced irrigation. *Agr. Water Manage.* 138, 37-44.

Allison, J.D., Brown, D.S., Novo-Gradac, K.J. 1991. MINTEQA2/PRODEFA2: A Geochemical Assessment Model for Environmental Systems. Version 3.0 User's Manual. Environmental Protection Agency.

AMCSD, American Mineralogist Crystal Structure Database.
<http://rruff.geo.arizona.edu/AMS/amcsd.php> (Accessed by June 2016)

Anderson, C.R., Condon, L.M., Clough, T.J., Fiers, M., Stewart, A., Hill, R.A., Sherlock, R.R., 2011. Biochar induced soil microbial community change: Implications for biogeochemical cycling of carbon, nitrogen and phosphorus. *Pedobiologia*. 54(5-6), 309-320.

Anoop Krishnan, K., Anirudhan, T.S., 2002. Removal of mercury(II) from aqueous solutions and chlor-alkali industry effluent by steam activated and sulphurised activated carbons prepared from bagasse pith: Kinetics and equilibrium studies. *J. Hazard. Mater.* 92(2), 161-183.

Anto, H., Trivedi, U., Patel, K., 2006. α -Amylase production by *Bacillus cereus* MTCC 1305 using solid-state fermentation. *Food Technol. Biotech.* 44(2), 241-245.

ATOMS, The Atoms.inp Archive. <http://cars9.uchicago.edu/~newville/adb/search.html> (Accessed by June 2016)

Avramescu, M.L., Yumvihoze, E., Hintelmann, H., Ridal, J., Fortin, D., R.S. Lean, D., 2011. Biogeochemical factors influencing net mercury methylation in contaminated freshwater sediments from the St. Lawrence River in Cornwall, Ontario, Canada. *Sci. Total Environ.* 409(5), 968-978.

Babut, M.P., Delmas, H., Bray, M., Durrieu, C., Perrodin, Y., Garric, J., 2006. Characterizing the risks to aquatic ecosystems: A tentative approach in the context of freshwater dredged material disposal. *Integr. Environ. Assess. Manag.* 2(4), 330-343.

Bailey, S.E., Olin, T.J., Bricka, R.M., Adrian, D.D., 1999. A review of potentially low-cost sorbents for heavy metals. *Water Res.* 33(11), 2469-2479.

Bainotti, A., Nishio, N., 2000. Growth kinetics of *Acetobacterium sp.* on methanol - formate in continuous culture. *J. Appl. Microbiol.* 88(2), 191-201.

Bandosz, T., 2006. Activated Carbon Surfaces in Environmental Remediation. Academic Press, Amsterdam, The Netherlands.

Barca, C., Troesch, S., Meyer, D., Drissen, P., Andreis, Y., Chazarenc, F., 2013. Steel slag filters to upgrade phosphorus removal in constructed wetlands: Two years of field experiments. *Environ. Sci. Technol.* 47(1), 549-556.

Bartoli, M., Vezzulli, L., Nizzoli, D., Azzoni, R., Porrello, S., Moreno, M., Fabiano, M., Viaroli, P., 2009. Short-term effect of oxic to anoxic transition on benthic microbial

activity and solute fluxes in organic-rich phytotreatment ponds. *Hydrobiologia*. 629(1), 123-136.

Beesley, L., Moreno-Jimenez, E., Gomez-Eyles, J.L., 2010. Effects of biochar and greenwaste compost amendments on mobility, bioavailability and toxicity of inorganic and organic contaminants in a multi-element polluted soil. *Environ. Pollut.* 158(6), 2282-7.

Benner, S.G., Blowes, D.W., Gould, W.D., Herbert Jr, R.B., Ptacek, C.J., 1999. Geochemistry of a permeable reactive barrier for metals and acid mine drainage. *Environ. Sci. Technol.* 33(16), 2793-2799.

Benner, S.G., Blowes, D.W., Ptacek, C.J., Mayer, K.U., 2002. Rates of sulfate reduction and metal sulfide precipitation in a permeable reactive barrier. *Appl. Geochem.* 17(3), 301-320.

Benoit, J., Gilmour, C., Heyes, A., Mason, R., Miller, C. 2003. Geochemical and biological controls over methylmercury production and degradation in aquatic ecosystems. ACS symposium series. pp. 262-297.

Benoit, J.M., Gilmour, C.C., Mason, R.P., 2001a. Aspects of bioavailability of mercury for methylation in pure cultures of *Desulfobulbus propionicus* (1pr3). *Appl. Environ. Microbiol.* 67(1), 51-58.

Benoit, J.M., Mason, R.P., Gilmour, C.C., Aiken, G.R., 2001b. Constants for mercury binding by dissolved organic matter isolates from the Florida Everglades. *Geochim. Cosmochim. Acta.* 65(24), 4445-4451.

Bernaus, A., Gaona, X., Esbrí, J.M., Higuera, P., Falkenberg, G., Valiente, M., 2006. Microprobe techniques for speciation analysis and geochemical characterization of mine environments: The mercury district of Almadén in Spain. *Environ. Sci. Technol.* 40(13), 4090-4095.

Berner, R.A., 1980. *Early Diagenesis: A Theoretical Approach*. Princeton University Press, Princeton, New Jersey, USA.

Berthon, G., 1995. Critical evaluation of the stability-constants of metal-complexes of amino-acids with polar side-chains. *Pure Appl. Chem.* 67(7), 1117-1240.

Bewley, R., Sojka, G., 2013. In-situ 'deliverability' trials using calcium polysulphide to treat chromium contamination at Shawfield, Glasgow. CL:AIRE (Contaminated Land: Applications in Real Environments), Technology Demonstration Project Bulletin TDP30, 1-8.

Bewley, R.J.F., Clarke, S., 2010. Field application of calcium polysulphide for ex situ treatment of soils contaminated with chromite ore processing residue. *Land Contam. Reclam.* 18(1), 1-12.

- Biester, H., Gosar, M., Covelli, S., 2000. Mercury speciation in sediments affected by dumped mining residues in the drainage area of the Idrija mercury mine, Slovenia. *Environ. Sci. Technol.* 34(16), 3330-3336.
- Biniak, S., Szymanski, G., Siedlewski, J., Swiatkowski, A., 1997. The characterization of activated carbons with oxygen and nitrogen surface groups. *Carbon.* 35(12), 1799-1810.
- Bisson, T.M., MacLean, L.C.W., Hu, Y., Xu, Z., 2012. Characterization of mercury binding onto a novel brominated biomass ash sorbent by X-ray absorption spectroscopy. *Environ. Sci. Technol.* 46(21), 12186-12193.
- Bisson, T.M., Ong, Z.Q., MacLennan, A., Hu, Y., Xu, Z., 2015. Impact of sulfur loading on brominated biomass ash on mercury capture. *Energ. Fuel.* 29(12), 8110-8117.
- Bloom, N.S., Lasorsa, B.K., 1999. Changes in mercury speciation and the release of methyl mercury as a result of marine sediment dredging activities. *Sci. Total Environ.* 237-238, 379-385.
- Blowes, D.W., Ptacek, C.J., Benner, S.G., McRae, C.W.T., Bennett, T.A., Puls, R.W., 2000. Treatment of inorganic contaminants using permeable reactive barriers. *J. Contam. Hydrol.* 45(1-2), 123-137.
- Blowes, D.W., Ptacek, C.J., Jambor, J.L., 1997. In-situ remediation of Cr(VI)-contaminated groundwater using permeable reactive walls: Laboratory studies. *Environ. Sci. Technol.* 31(12), 3348-3357.
- Blue, L.Y., Jana, P., Atwood, D.A., 2010. Aqueous mercury precipitation with the synthetic dithiolate, BDTH₂. *Fuel.* 89(6), 1326-1330.
- Blue, L.Y., Van Aelstyn, M.A., Matlock, M., Atwood, D.A., 2008. Low-level mercury removal from groundwater using a synthetic chelating ligand. *Water Res.* 42(8-9), 2025-2028.
- Boening, D.W., 2000. Ecological effects, transport, and fate of mercury: A general review. *Chemosphere.* 40(12), 1335-51.
- Bolgiano, R.W., 1980. Mercury Contamination of the South, South Fork Shenandoah, and Shenandoah Rivers. Virginia State Water Control Board.
- Borchard, N., Siemens, J., Ladd, B., Möller, A., Amelung, W., 2014a. Application of biochars to sandy and silty soil failed to increase maize yield under common agricultural practice. *Soil Till. Res.* 144, 184-194.
- Borchard, N., Spokas, K., Prost, K., Siemens, J., 2014b. Greenhouse gas production in mixtures of soil with composted and noncomposted biochars is governed by char-associated organic compounds. *J. Environ. Qual.* 43(3), 971-979.

Bostick, D., Klasson, K. 1998. Multi-weight isotherm results for mercury removal in upper East Fork Poplar Creek water (Report#: ORNL/TM--13582). Oak Ridge National Laboratory, TN.

Bouchet, S., Bridou, R., Tessier, E., Rodriguez-Gonzalez, P., Monperrus, M., Abril, G., Amouroux, D., 2011. An experimental approach to investigate mercury species transformations under redox oscillations in coastal sediments. *Mar. Environ. Res.* 71(1), 1-9.

Boutsika, L.G., Karapanagioti, H.K., Manariotis, I.D., 2014. Aqueous mercury sorption by biochar from malt spent rootlets. *Water Air Soil Poll.* 225(1), 1-10.

Brewer, C.E., Chuang, V.J., Masiello, C.A., Gonnermann, H., Gao, X., Dugan, B., Driver, L.E., Panzacchi, P., Zygourakis, K., Davies, C.A., 2014. New approaches to measuring biochar density and porosity. *Biomass Bioenerg.* 66, 176-185.

Brewer, C.E., Schmidt-Rohr, K., Satrio, J.A., Brown, R.C., 2009. Characterization of biochar from fast pyrolysis and gasification systems. *Environ. Prog. Sustain. Energy.* 28(3), 386-396.

Bringer, S., Sahm, H., Swyzen, W., 1984. Ethanol production by *Zymomonas mobilis* and its application on an industrial scale. *Biotechnol. Bioeng. Symp.* 14(14), 311-319.

Brunauer, S., Emmett, P.H., Teller, E., 1938. Adsorption of gases in multimolecular layers. *J. Am. Chem. Soc.* 60(2), 309-319.

Bruun, E.W., Hauggaard-Nielsen, H., Ibrahim, N., Egsgaard, H., Ambus, P., Jensen, P.A., Dam-Johansen, K., 2011. Influence of fast pyrolysis temperature on biochar labile fraction and short-term carbon loss in a loamy soil. *Biomass Bioenerg.* 35(3), 1182-1189.

Bryan, S.E., Tipping, E., Hamilton-Taylor, J., 2002. Comparison of measured and modelled copper binding by natural organic matter in freshwaters. *Comp. Biochem. Physiol., C: Comp. Pharmacol. Toxicol.* 133(1-2), 37-49.

BSI Lab., Microbial database for bioenergy production.

<http://www4a.biotech.or.th/bioenergy/searchresult.php> (Accessed by May 2015)

Bundschuh, M., Zubrod, J.P., Seitz, F., Newman, M.C., 2015. Effects of two sorbents applied to mercury-contaminated river sediments on bioaccumulation in and detrital processing by *Hyalella azteca*. *J. Soils Sediments.* 15(5), 1265-1274.

Calvin, S., 2013. XAFS for Everyone. CRC Press, Taylor & Francis, New York.

Cantrell, K.B., Hunt, P.G., Uchimiya, M., Novak, J.M., Ro, K.S., 2012. Impact of pyrolysis temperature and manure source on physicochemical characteristics of biochar. *Bioresour. Technol.* 107, 419-28.

- Cao, X.D., Harris, W., 2010. Properties of dairy-manure-derived biochar pertinent to its potential use in remediation. *Bioresour. Technol.* 101(14), 5222-5228.
- Capone, K.A., Dowd, S.E., Stamatias, G.N., Nikolovski, J., 2011. Diversity of the human skin microbiome early in life. *J. Invest. Dermatol.* 131(10), 2026-2032.
- Carter, L.J., 1977. Chemical plants leave unexpected legacy for two virginia rivers. *Science.* 198(4321), 1015-20.
- Celo, V., Lean, D.R.S., Scott, S.L., 2006. Abiotic methylation of mercury in the aquatic environment. *Sci. Total Environ.* 368(1), 126-137.
- Chang, Y.J., Pukall, R., Saunders, E., Lapidus, A., Copeland, A., Nolan, M., del Rio, T.G., Lucas, S., Chen, F., Tice, H., Cheng, J.F., Han, C., Detter, J.C., Bruce, D., Goodwin, L., Pitluck, S., Mikhailova, N., Liolios, K., Pati, A., Ivanova, N., Mavromatis, K., Chen, A., Palaniappan, K., Land, M., Hauser, L., Jeffries, C.D., Brettin, T., Rohde, M., Göker, M., Bristow, J., Eisen, J.A., Markowitz, V., Hugenholtz, P., Kyrpides, N.C., Klenk, H.P., 2010. Complete genome sequence of *Acidaminococcus fermentans* type strain (VR4 T). *Stand. Genomic. Sci.* 3(1), 1-14.
- Cheah, S., Malone, S.C., Feik, C.J., 2014. Speciation of sulfur in biochar produced from pyrolysis and gasification of oak and corn stover. *Environ. Sci. Technol.* 48(15), 8474-80.
- Chen, B., Zhou, D., Zhu, L., 2008. Transitional adsorption and partition of nonpolar and polar aromatic contaminants by biochars of pine needles with different pyrolytic temperatures. *Environ. Sci. Technol.* 42(14), 5137-5143.
- Cheng, C.-H., Lehmann, J., Engelhard, M.H., 2008. Natural oxidation of black carbon in soils: Changes in molecular form and surface charge along a climosequence. *Geochim. Cosmochim. Acta.* 72(6), 1598-1610.
- Cheng, C.-H., Lehmann, J., Thies, J.E., Burton, S.D., Engelhard, M.H., 2006. Oxidation of black carbon by biotic and abiotic processes. *Org. Geochem.* 37(11), 1477-1488.
- Cheng, H., Hu, Y., 2012. Mercury in municipal solid waste in China and its control: A review. *Environ. Sci. Technol.* 46(2), 593-605.
- Chiasson-Gould, S.A., Blais, J.M., Poulain, A.J., 2014. Dissolved organic matter kinetically controls mercury bioavailability to bacteria. *Environ. Sci. Technol.* 48(6), 3153-3161.
- Choudhury, S., Hormes, J., Agyeman-Budu, D.N., Woll, A.R., George, G.N., Coulthard, I., Pickering, I.J., 2015a. Application of a spoked channel array to confocal X-ray fluorescence imaging and X-ray absorption spectroscopy of medieval stained glass. *J. Anal. At. Spectrom.* 30(3), 759-766.
- Choudhury, S., Thomas, J.K., Sylvain, N.J., Ponomarenko, O., Gordon, R.A., Heald, S.M., Janz, D.M., Krone, P.H., Coulthard, I., George, G.N., Pickering, I.J., 2015b.

Selenium preferentially accumulates in the eye lens following embryonic exposure: A confocal x-ray fluorescence imaging study. *Environ. Sci. Technol.* 49(4), 2255-2261.

Chrysochoou, M., Johnston, C.P., 2015. Polysulfide speciation and reactivity in chromate-contaminated soil. *J. Hazard. Mater.* 281(0), 87-94.

Chrysochoou, M., Johnston, C.P., Dahal, G., 2012. A comparative evaluation of hexavalent chromium treatment in contaminated soil by calcium polysulfide and green-tea nanoscale zero-valent iron. *J. Hazard. Mater.* 201-202, 33-42.

Churka Blum, S., Lehmann, J., Solomon, D., Caires, E.F., Alleoni, L.R.F., 2013. Sulfur forms in organic substrates affecting S mineralization in soil. *Geoderma*. 200-201, 156-164.

Clarkson, T.W., 1997. The toxicology of mercury. *Crit. Rev. Clin. Lab. Sci.* 34(4), 369-403.

Clarkson, T.W., Magos, L., 2006. The toxicology of mercury and its chemical compounds. *Crit. Rev. Toxicol.* 36(8), 609-662.

Coleman, M., Page-Dumroese, D., Archuleta, J., Badger, P., Chung, W., Venn, T., Loeffler, D., Jones, G., McElligott, K. 2010. Can portable pyrolysis units make biomass utilization affordable while using bio-char to enhance soil productivity and sequester carbon. Integrated management of carbon sequestration and biomass utilization opportunities in a changing climate: Proceedings of the 2009 National Silviculture Workshop, Fort Collins. Citeseer. pp. 159-168.

Collins, C.R., Sherman, D.M., Ragnarsdottir, K.V., 1999. Surface complexation of Hg²⁺ on goethite: Mechanism from EXAFS spectroscopy and density functional calculations. *J. Colloid Interface Sci.* 219(2), 345-350.

Compeau, G.C., Bartha, R., 1987. Effect of salinity on mercury-methylating activity of sulfate-reducing bacteria in estuarine sediments. *Appl. Environ. Microbiol.* 53(2), 261-265.

Cordes, N.L., Seshadri, S., Havrilla, G.J., Yuan, X., Feser, M., Patterson, B.M., 2015. Three dimensional subsurface elemental identification of minerals using confocal micro-X-ray fluorescence and micro-X-ray computed tomography. *Spectrochim Acta Part B At. Spectrosc.* 103-104, 144-154.

Das, S.K., Das, A.R., Guha, A.K., 2007. A study on the adsorption mechanism of mercury on *Aspergillus versicolor* biomass. *Environ. Sci. Technol.* 41(24), 8281-8287.

Dauphin, Y., Salomé, M., 2014. Chemical mapping with x-ray absorption spectroscopy, in: DiMasi, E., Gower, L.B.(Eds.), *Biom mineralization Sourcebook: Characterization of Biominerals and Biomimetic Materials*. CRC Press, Taylor & Francis Group, Boca Raton, FL, USA, pp. 73-93.

Department of Biotechnology University of Wrocław,
<http://metanogen.biotech.uni.wroc.pl/page/10/> (Accessed by May 2015)

Deppenmeier, U., 2002. The unique biochemistry of methanogenesis. *Prog. Nucleic. Acid Res. Mol. Biol.* 71, 223-283.

DeSantis, T.Z., Hugenholtz, P., Larsen, N., Rojas, M., Brodie, E.L., Keller, K., Huber, T., Dalevi, D., Hu, P., Andersen, G.L., 2006. Greengenes, a chimera-checked 16S rRNA gene database and workbench compatible with ARB. *Appl. Environ. Microbiol.* 72(7), 5069-5072.

Desrochers, K., 2013. Geochemical characterization and assessment of stabilization mechanisms for mercury-contaminated riverbank sediments from the South River, Virginia (USA). (Master of Science). University of Waterloo, Waterloo, Canada.

Desrochers, K.A.N., Paulson, K.M.A., Ptacek, C.J., Blowes, D.W., Gould, W.D., 2015. Effect of electron donor to sulfate ratio on mercury methylation in floodplain sediments under saturated flow conditions. *Geomicrobiol. J.* 32(10), 924-933.

Dezarnaud, C., Tronc, M., Hitchcock, A.P., 1990. Inner shell spectroscopy of the carbon-sulfur bond. *Chem. Phys.* 142(3), 455-462.

Ding, L., Snoeyink, V.L., Mariñas, B.J., Yue, Z., Economy, J., 2008. Effects of powdered activated carbon pore size distribution on the competitive adsorption of aqueous atrazine and natural organic matter. *Environ. Sci. Technol.* 42(4), 1227-1231.

Dong, W., Liang, L., Brooks, S., Southworth, G., Gu, B., 2010. Roles of dissolved organic matter in the speciation of mercury and methylmercury in a contaminated ecosystem in Oak Ridge, Tennessee. *Environ. Chem.* 7(1), 94-102.

Dong, X., Ma, L.Q., Li, Y., 2011. Characteristics and mechanisms of hexavalent chromium removal by biochar from sugar beet tailing. *J. Hazard. Mater.* 190(1-3), 909-15.

Dong, X., Ma, L.Q., Zhu, Y., Li, Y., Gu, B., 2013. Mechanistic investigation of mercury sorption by Brazilian pepper biochars of different pyrolytic temperatures based on x-ray photoelectron spectroscopy and flow calorimetry. *Environ. Sci. Technol.* 47(21), 12156-12164.

Donovan, P.M., Blum, J.D., Singer, M.B., Marvin-Dipasquale, M., Tsui, M.T.K., 2016. Isotopic composition of inorganic mercury and methylmercury downstream of a historical gold mining region. *Environ. Sci. Technol.* 50(4), 1691-1702.

Dowd, S.E., Callaway, T.R., Wolcott, R.D., Sun, Y., McKeehan, T., Hagevoort, R.G., Edrington, T.S., 2008a. Evaluation of the bacterial diversity in the feces of cattle using 16S rDNA bacterial tag-encoded FLX amplicon pyrosequencing (bTEFAP). *BMC Microbiol.* 8, 125.

Dowd, S.E., Sun, Y., Wolcott, R.D., Domingo, A., Carroll, J.A., 2008b. Bacterial tag-encoded FLX amplicon pyrosequencing (bTEFAP) for microbiome studies: Bacterial diversity in the ileum of newly weaned Salmonella-infected pigs. *Foodborne Pathog. Dis.* 5(4), 459-472.

Driscoll, C.T., Han, Y.J., Chen, C.Y., Evers, D.C., Lambert, K.F., Holsen, T.M., Kamman, N.C., Munson, R.K., 2007. Mercury contamination in forest and freshwater ecosystems in the northeastern United States. *Bioscience.* 57(1), 17-28.

Dumroese, R.K., Heiskanen, J., Englund, K., Tervahauta, A., 2011. Pelleted biochar: Chemical and physical properties show potential use as a substrate in container nurseries. *Biomass Bioenerg.* 35(5), 2018-2027.

Easton, Z.M., Rogers, M., Davis, M., Wade, J., Eick, M., Bock, E., 2015. Mitigation of sulfate reduction and nitrous oxide emission in denitrifying environments with amorphous iron oxide and biochar. *Ecol. Eng.* 82(0), 605-613.

Ebinghaus, R., Turner, R.R., Lacerda, L.D.d., Vasiliev, O., Salomons, W., 1999. *Mercury Contaminated Sites: Characterization, Risk Assessment and Remediation.* Springer, Berlin, Germany.

Edgar, R.C., 2010. Search and clustering orders of magnitude faster than BLAST. *Bioinformatics.* 26(19), 2460-2461.

El-Shafey, E.I., 2010. Removal of Zn(II) and Hg(II) from aqueous solution on a carbonaceous sorbent chemically prepared from rice husk. *J. Hazard. Mater.* 175(1-3), 319-327.

EPA, 2002a. Method 1631, Revision E: Mercury in water by oxidation, purge and trap, and cold vapor atomic fluorescence spectrometry. US Environmental Protection Agency Washington, DC.

EPA. 2002b. Method 1631: Revision E: Mercury in water by oxidation, purge and trap, and cold vapor atomic fluorescence spectrometry, U.S. Environmental Protection Agency. Washington DC, USA.

EPA, US-EPA National Primary Drinking Water Regulations.
<http://water.epa.gov/drink/contaminants/index.cfm> (Accessed by April 2015)

EPA. 2011. 40 CFR Appendix B to Part 136 - Definition and Procedure for the Determination of the Method Detection Limit-Revision 1.11, U.S. Environmental Protection Agency. Washington DC, USA.

EPA, US-EPA National Recommended Water Quality Criteria.
<http://water.epa.gov/scitech/swguidance/standards/criteria/current/index.cfm> (Accessed by April 2015)

- Eren, A.M., Zozaya, M., Taylor, C.M., Dowd, S.E., Martin, D.H., Ferris, M.J., 2011. Exploring the diversity of *Gardnerella vaginalis* in the genitourinary tract microbiota of monogamous couples through subtle nucleotide variation. PLoS ONE. 6(10).
- Ettler, V., Mihaljevič, M., Šebek, O., Grygar, T., 2007. Assessment of single extractions for the determination of mobile forms of metals in highly polluted soils and sediments- Analytical and thermodynamic approaches. Anal. Chim. Acta. 602(1), 131-140.
- Farnsworth, C.E., Voegelin, A., Hering, J.G., 2012. Manganese oxidation induced by water table fluctuations in a sand column. Environ. Sci. Technol. 46(1), 277-284.
- Federal Remediation Technologies Roundtable. 2004. Abstracts of Remediation Case Studies Volume 8, (Report#: EPA 542-R-04-012).
- Fellin, S.C., 2016. Mercury stabilization in contaminated sediment by co-blending with solid-phase reactive media. (Master of Science). University of Waterloo, Waterloo, Canada.
- Feng, W., Borguet, E., Vidic, R.D., 2006. Sulfurization of a carbon surface for vapor phase mercury removal - II: Sulfur forms and mercury uptake. Carbon. 44(14), 2998-3004.
- Flanders, J.R., Turner, R.R., Morrison, T., Jensen, R., Pizzuto, J., Skalak, K., Stahl, R., 2010. Distribution, behavior, and transport of inorganic and methylmercury in a high gradient stream. Appl. Geochem. 25(11), 1756-1769.
- Fleet, M.E., 2005. XANES spectroscopy of sulfur in Earth materials. Can. Mineral. 43(6), 1811-1838.
- Fleming, E.J., Mack, E.E., Green, P.G., Nelson, D.C., 2006. Mercury methylation from unexpected sources: Molybdate-inhibited freshwater sediments and an iron-reducing bacterium. Appl. Environ. Microbiol. 72(1), 457-464.
- Frindte, K., Eckert, W., Attermeyer, K., Grossart, H.P., 2012. Internal wave-induced redox shifts affect biogeochemistry and microbial activity in sediments: a simulation experiment. Biogeochemistry, 1-12.
- Fulda, B., Voegelin, A., Ehlert, K., Kretzschmar, R., 2013. Redox transformation, solid phase speciation and solution dynamics of copper during soil reduction and reoxidation as affected by sulfate availability. Geochim. Cosmochim. Acta. 123, 385-402.
- Gammons, C.H., Slotton, D.G., Gerbrandt, B., Weight, W., Young, C.A., McNearny, R.L., Cámac, E., Calderón, R., Tapia, H., 2006. Mercury concentrations of fish, river water, and sediment in the Ríó Ramis-Lake Titicaca watershed, Peru. Sci. Total Environ. 368(2-3), 637-648.

- Gaskin, J.W., Steiner, C., Harris, K., Das, K.C., Bibens, B., 2008. Effect of low-temperature pyrolysis conditions on biochar for agricultural use. *Trans. ASABE*. 51(6), 2061-2069.
- Gerbig, C.A., Kim, C.S., Stegemeier, J.P., Ryan, J.N., Aiken, G.R., 2011. Formation of nanocolloidal metacinnabar in mercury-DOM-sulfide systems. *Environ. Sci. Technol.* 45(21), 9180-9187.
- Ghosh, U., Luthy, R.G., Cornelissen, G., Werner, D., Menzie, C.A., 2011. In-situ sorbent amendments: A new direction in contaminated sediment management. *Environ. Sci. Technol.* 45(4), 1163-1168.
- Gibson, B., Ptacek, C., Blowes, D., Daugherty, S., 2015. Sediment resuspension under variable geochemical conditions and implications for contaminant release. *J. Soils Sediments*. 15(7), 1644-1656.
- Gibson, B.D., Ptacek, C.J., Lindsay, M.B.J., Blowes, D.W., 2011. Examining mechanisms of groundwater Hg(II) treatment by reactive materials: An EXAFS study. *Environ. Sci. Technol.* 45(24), 10415-21.
- Gill, G.A., Bruland, K.W., 1990. Mercury speciation in surface freshwater systems in California and other areas. *Environ. Sci. Technol.* 24(9), 1392-1400.
- Gilmour, C.C., Henry, E.A., 1991. Mercury methylation in aquatic systems affected by acid deposition. *Environ. Pollut.* 71(2-4), 131-69.
- Gilmour, C.C., Henry, E.A., Mitchell, R., 1992. Sulfate stimulation of mercury methylation in freshwater sediments. *Environ. Sci. Technol.* 26(11), 2281-2287.
- Gilmour, C.C., Riedel, G.S., Riedel, G., Kwon, S., Landis, R., Brown, S.S., Menzie, C.A., Ghosh, U., 2013. Activated carbon mitigates mercury and methylmercury bioavailability in contaminated sediments. *Environ. Sci. Technol.* 47(22), 13001-13010.
- Gismera, M.J., Procopio, J.R., Sevilla, M.T., 2007. Characterization of mercury-Humic acids interaction by potentiometric titration with a modified carbon paste mercury sensor. *Electroanal.* 19(10), 1055-1061.
- Gomez-Eyles, J.L., Yupanqui, C., Beckingham, B., Riedel, G., Gilmour, C., Ghosh, U., 2013. Evaluation of biochars and activated carbons for *in situ* remediation of sediments impacted with organics, mercury, and methylmercury. *Environ. Sci. Technol.* 47(23), 13721-13729.
- Graham, A.M., Aiken, G.R., Gilmour, C.C., 2012. Dissolved organic matter enhances microbial mercury methylation under sulfidic conditions. *Environ. Sci. Technol.* 46(5), 2715-23.

Gu, B., Mishra, B., Miller, C., Wang, W., Lai, B., Brooks, S.C., Kemner, K.M., Liang, L., 2014. X-ray fluorescence mapping of mercury on suspended mineral particles and diatoms in a contaminated freshwater system. *Biogeosciences Discuss.* 11(5), 7521-7540.

Guo, M., Chorover, J., 2006. Leachate migration from spent mushroom substrate through intact and repacked subsurface soil columns. *Waste Manage.* 26(2), 133-140.

Hadnagy, E., Gardner, K.H., Chesner, W.H., Justus, H., Forgione, M., Maxwell, G., 2014. Pilot-scale evaluation of an in situ amendment delivery and mixing device for contaminated sediment remediation applications. *J. Soils Sediments.* 15(2), 480-489.

Haitzer, M., Aiken, G.R., Ryan, J.N., 2002. Binding of mercury(II) to dissolved organic matter: The role of the mercury-to-DOM concentration ratio. *Environ. Sci. Technol.* 36(16), 3564-3570.

Haitzer, M., Aiken, G.R., Ryan, J.N., 2003. Binding of mercury(II) to aquatic humic substances: Influence of pH and source of humic substances. *Environ. Sci. Technol.* 37(11), 2436-2441.

Hale, S.E., Hanley, K., Lehmann, J., Zimmerman, A.R., Cornelissen, G., 2012a. Effects of chemical, biological, and physical aging as well as soil addition on the sorption of pyrene to activated carbon and biochar. *Environ. Sci. Technol.* 46(4), 2479-2480.

Hale, S.E., Lehmann, J., Rutherford, D., Zimmerman, A., Bachmann, R.T., Shitumbanuma, V., O'Toole, A., Sundqvist, K.L., Arp, H.P.H., Cornelissen, G., 2012b. Quantifying the total and bioavailable PAHs and dioxins in biochars. *Environ. Sci. Technol.* 46(5), 2830-2838.

Hamelin, S., Amyot, M., Barkay, T., Wang, Y., Planas, D., 2011. Methanogens: Principal methylators of mercury in lake periphyton. *Environ. Sci. Technol.* 45(18), 7693-7700.

Han, F.X., Su, Y., Monts, D.L., Waggoner, C.A., Plodinec, M.J., 2006. Binding, distribution, and plant uptake of mercury in a soil from Oak Ridge, Tennessee, USA. *Sci. Total Environ.* 368(2-3), 753-768.

Hao, X., 2010. *Water Infrastructure for Sustainable Communities: China and the World.* IWA Publishing, London, UK.

Harvey, O.R., Herbert, B.E., Kuo, L.J., Louchouart, P., 2012. Generalized two-dimensional perturbation correlation infrared spectroscopy reveals mechanisms for the development of surface charge and recalcitrance in plant-derived biochars. *Environ. Sci. Technol.* 46(19), 10641-50.

Hass, A., Gonzalez, J.M., Lima, I.M., Godwin, H.W., Halvorson, J.J., Boyer, D.G., 2012. Chicken manure biochar as liming and nutrient source for acid appalachian soil. *J. Environ. Qual.* 41(4), 1096-1106.

- Henny, C.J., Hill, E.F., Hoffman, D.J., Spalding, M.G., Grove, R.A., 2002. Nineteenth century mercury: Hazard to wading birds and cormorants of the Carson River, Nevada. *Ecotoxicology*. 11(4), 213-231.
- Herrero, R., Lodeiro, P., Rey-Castro, C., Vilariño, T., Sastre de Vicente, M.E., 2005. Removal of inorganic mercury from aqueous solutions by biomass of the marine macroalga *Cystoseira baccata*. *Water Res.* 39(14), 3199-3210.
- Hesterberg, D., Chou, J.W., Hutchison, K.J., Sayers, D.E., 2001. Bonding of Hg(II) to reduced organic sulfur in humic acid as affected by S/Hg ratio. *Environ. Sci. Technol.* 35(13), 2741-2745.
- Hethener, P., Brauman, A., Garcia, J.-L., 1992. *Clostridium termitidis* sp. nov., a cellulolytic bacterium from the gut of the wood-feeding termite, *Nasutitermes lujae*. *Syst Appl Microbiol.* 15(1), 52-58.
- Hilber, I., Bucheli, T.D., 2010. Activated carbon amendment to remediate contaminated sediments and soils: A review. *Global Nest J.* 12(3), 305-317.
- Hofacker, A.F., Behrens, S., Voegelin, A., Kaegi, R., Lösekann-Behrens, T., Kappler, A., Kretzschmar, R., 2015. Clostridium species as metallic copper-forming bacteria in soil under reducing conditions. *Geomicrobiol. J.* 32(2), 130-139.
- Hogberg, D., 2015. Removal of mercury from aqueous solutions using wood-based biochars. (Master of Science). University of Waterloo, Waterloo, Canada.
- Hollerman, W., Holland, L., Ila, D., Hensley, J., Southworth, G., Klasson, T., Taylor, P., Johnston, J., Turner, R., 1999. Results from the low level mercury sorbent test at the Oak Ridge Y-12 Plant in Tennessee. *J. Hazard. Mater.* 68(3), 193-203.
- Horvat, M., Bloom, N.S., Liang, L., 1993. Comparison of distillation with other current isolation methods for the determination of methyl mercury compounds in low-level environmental samples Part 1. Sediments. *Anal. Chim. Acta.* 281(1), 135-152.
- Hsi, H.C., Rood, M.J., Rostam-Abadi, M., Chen, S., Chang, R., 2001. Effects of sulfur impregnation temperature on the properties and mercury adsorption capacities of activated carbon fibers (ACFs). *Environ. Sci. Technol.* 35(13), 2785-2791.
- Hsu-Kim, H., Kucharzyk, K.H., Zhang, T., Deshusses, M.A., 2013. Mechanisms regulating mercury bioavailability for methylating microorganisms in the aquatic environment: A critical review. *Environ. Sci. Technol.* 47(6), 2441-56.
- Hu, H., Lin, H., Zheng, W., Tomanicek, S.J., Johs, A., Feng, X., Elias, D.A., Liang, L., Gu, B., 2013. Oxidation and methylation of dissolved elemental mercury by anaerobic bacteria. *Nat. Geosci.* 6(9), 751-754.

Hu, X., Ding, Z., Zimmerman, A.R., Wang, S., Gao, B., 2015. Batch and column sorption of arsenic onto iron-impregnated biochar synthesized through hydrolysis. *Water Res.* 68, 206-216.

Huber, S.A., Balz, A., Abert, M., Pronk, W., 2011. Characterisation of aquatic humic and non-humic matter with size-exclusion chromatography - organic carbon detection - organic nitrogen detection (LC-OCD-OND). *Water Res.* 45(2), 879-885.

Huggins, F.E., Yap, N., Huffman, G.P., Senior, C.L., 2003. XAFS characterization of mercury captured from combustion gases on sorbents at low temperatures. *Fuel Process. Technol.* 82(2-3), 167-196.

Huntington, T.G., Lewis, A., Amirbahman, A., Marvin-DiPasquale, M.C., Culbertson, C.W. 2015. Assessment of the use of sorbent amendments for reduction of mercury methylation in wetland sediments at Acadia National Park, Maine: U.S. Geological Survey Scientific Investigations Report 2014-5234. US Geological Survey. 2328-0328.

Hussain, S.I., Blowes, D.W., Ptacek, C.J., Jamieson-Hanes, J.H., Wootton, B., Balch, G., Higgins, J., 2015. Mechanisms of phosphorus removal in a pilot-scale constructed wetland/BOF slag wastewater treatment system. *Environ. Eng. Sci.* 32(4), 340-352.

Hussain, S.I., Blowes, D.W., Ptacek, C.J., Olding, D., 2014. Phosphorus removal from lake water using basic oxygen furnace slag: System performance and characterization of reaction products. *Environ. Eng. Sci.* 31(11), 631-642.

ID21-ESRF, ID21 Sulfur XANES Spectra Database of European Synchrotron Radiation Facility.

<http://www.esrf.eu/home/UsersAndScience/Experiments/XNP/ID21/php/Database-SCompounds.html> (Accessed by June 2016)

Integrated Laboratory Systems Inc. 2005. 2,5-Dimercapto-1,3,4-thiadiazole [CAS No. 1072-71-5] and its salts and esters: Review of toxicological literature (Report#: N01-ES-35515).

Jackson, A.K., Evers, D.C., Folsom, S.B., Condon, A.M., Diener, J., Goodrick, L.F., McGann, A.J., Schmerfeld, J., Cristol, D.A., 2011. Mercury exposure in terrestrial birds far downstream of an historical point source. *Environ. Pollut.* 159(12), 3302-8.

Jaffé, R., Ding, Y., Niggemann, J., Vähätalo, A.V., Stubbins, A., Spencer, R.G.M., Campbell, J., Dittmar, T., 2013. Global charcoal mobilization from soils via dissolution and riverine transport to the oceans. *Science.* 340(6130), 345-347.

Jambor, J.L., Raudsepp, M., Mountjoy, K., 2005. Mineralogy of permeable reactive barriers for the attenuation of subsurface contaminants. *Can. Mineral.* 43(6), 2117-2140.

Jamieson, T., Sager, E., Guéguen, C., 2014. Characterization of biochar-derived dissolved organic matter using UV-visible absorption and excitation-emission fluorescence spectroscopies. *Chemosphere.* 103, 197-204.

- Jay, J.A., Morel, F.M.M., Hemond, H.F., 2000. Mercury speciation in the presence of polysulfides. *Environ. Sci. Technol.* 34(11), 2196-2200.
- Jeffery, S., Verheijen, F.G.A., van der Velde, M., Bastos, A.C., 2011. A quantitative review of the effects of biochar application to soils on crop productivity using meta-analysis. *Agric. Ecosyst. Environ.* 144(1), 175-187.
- Jiang, J., Xu, R.K., Jiang, T.Y., Li, Z., 2012. Immobilization of Cu(II), Pb(II) and Cd(II) by the addition of rice straw derived biochar to a simulated polluted Ultisol. *J. Hazard. Mater.* 229-230, 145-150.
- Jiang, W., Saxena, A., Song, B., Ward, B.B., Beveridge, T.J., Myneni, S.C.B., 2004. Elucidation of functional groups on gram-positive and gram-negative bacterial surfaces using infrared spectroscopy. *Langmuir.* 20(26), 11433-11442.
- Jin, Y., Liang, X.Q., He, M.M., Liu, Y., Tian, G.M., Shi, J.Y., 2016. Manure biochar influence upon soil properties, phosphorus distribution and phosphatase activities: A microcosm incubation study. *Chemosphere.* 142, 128-135.
- John, R.P., Nampoothiri, K.M., Pandey, A., 2007. Fermentative production of lactic acid from biomass: An overview on process developments and future perspectives. *Appl. Microbiol. Biotechnol.* 74(3), 524-534.
- Jones, D.L., Murphy, D.V., Khalid, M., Ahmad, W., Edwards-Jones, G., DeLuca, T.H., 2011. Short-term biochar-induced increase in soil CO₂ release is both biotically and abiotically mediated. *Soil Biol. Biochem.* 43(8), 1723-1731.
- Jonsson, S., Mazrui, N.M., Mason, R.P., 2016. Dimethylmercury formation mediated by inorganic and organic reduced sulfur surfaces. *Sci. Rep.* 6, 27958.
- Junier, P., Junier, T., Podell, S., Sims, D.R., Detter, J.C., Lykidis, A., Han, C.S., Wigginton, N.S., Gaasterland, T., Bernier-Latmani, R., 2010. The genome of the Gram-positive metal- and sulfate-reducing bacterium *Desulfotomaculum reducens* strain MI-1. *Environ Microbiol.* 12(10), 2738-2754.
- Kadirvelu, K., Kavipriya, M., Karthika, C., Vennilamani, N., Pattabhi, S., 2004. Mercury(II) adsorption by activated carbon made from sago waste. *Carbon.* 42(4), 745-752.
- Kerin, E.J., Gilmour, C.C., Roden, E., Suzuki, M.T., Coates, J.D., Mason, R.P., 2006. Mercury methylation by dissimilatory iron-reducing bacteria. *Appl. Environ. Microbiol.* 72(12), 7919-7921.
- Kilduff, J.E., Karanfil, T., Chin, Y.P., Weber Jr, W.J., 1996. Adsorption of natural organic polyelectrolytes by activated carbon: A size-exclusion chromatography study. *Environ. Sci. Technol.* 30(4), 1336-1343.

- Kilduff, J.E., Wigton, A., 1999. Sorption of TCE by humic-preloaded activated carbon: Incorporating size- exclusion and pore blockage phenomena in a competitive adsorption model. *Environ. Sci. Technol.* 33(2), 250-256.
- Kim, C.S., Brown Jr, G.E., Rytuba, J.J., 2000. Characterization and speciation of mercury-bearing mine wastes using X-ray absorption spectroscopy. *Sci. Total Environ.* 261(1-3), 157-168.
- Kim, C.S., Rytuba, J.J., Brown Jr, G.E., 2004. EXAFS study of mercury(II) sorption to Fe- and Al-(hydr)oxides: I. Effects of pH. *J. Colloid Interface Sci.* 271(1), 1-15.
- Kim, E.A., Masue-Slowey, Y., Fendorf, S., Luthy, R.G., 2012. Intra-particle migration of mercury in granular polysulfide-rubber-coated activated carbon (PSR-AC). *Chemosphere.* 86(6), 648-654.
- King, J.K., Kostka, J.E., Frischer, M.E., Saunders, F.M., 2000. Sulfate-reducing bacteria methylate mercury at variable rates in pure culture and in marine sediments. *Appl. Environ. Microbiol.* 66(6), 2430-2437.
- Klasson, K., Bostick, D., Farr, L., McTaggart, D., Taylor, P. 2000. Demonstration of mercury sorbents to meet DOE customer needs (Report#: ORNL/TM-2000/12). Oak Ridge National Laboratory, TN.
- Klasson, K.T., Bostick, D.T. 1998. Trace-level mercury removal from surface water (Report#: ORNL/CP-98108). Oak Ridge National Laboratory, TN.
- Klasson, K.T., Kosny, K., Drescher, S.R., Southworth, G.R., Hensley, J.F. 2003. Reaching parts per trillion clean-up criterion for mercury in water. in: *Waste Management 2003 Symposium*. Tucson, AZ, pp. 23-27.
- Koku, H., Erolu, I., Gündüz, U., Yücel, M., Türker, L., 2002. Aspects of the metabolism of hydrogen production by *Rhodobacter sphaeroides*. *Int. J. Hydrogen Energy.* 27(11-12), 1315-1329.
- Kong, H., He, J., Gao, Y., Wu, H., Zhu, X., 2011. Cosorption of phenanthrene and mercury(II) from aqueous solution by soybean stalk-based biochar. *J. Agric. Food Chem.* 59(22), 12116-12123.
- Koron, N., Faganeli, J., 2012. Benthic fluxes of mercury during redox changes in pristine coastal marine sediments from the Gulf of Trieste (northern Adriatic Sea). *J. Soils Sediments*, 1-11.
- Krabbenhoft, D.P., Babiarz, C.L., 1992. The role of groundwater transport in aquatic mercury cycling. *Water Resour. Res.* 28(12), 3119-3128.
- Kupryianchyk, D., Rakowska, M.I., Reible, D., Harmsen, J., Cornelissen, G., van Veggel, M., Hale, S.E., Grotenhuis, T., Koelmans, A.A., 2015. Positioning activated carbon

- amendment technologies in a novel framework for sediment management. *Integr. Environ. Assess. Manag.* 11(2), 221-234.
- Kuzyakov, Y., Subbotina, I., Chen, H., Bogomolova, I., Xu, X., 2009. Black carbon decomposition and incorporation into soil microbial biomass estimated by ¹⁴C labeling. *Soil Biol. Biochem.* 41(2), 210-219.
- Kwon, S., Pignatello, J.J., 2005. Effect of natural organic substances on the surface and adsorptive properties of environmental black carbon (char): Pseudo pore blockage by model lipid components and its implications for N-2-probed surface properties of natural sorbents. *Environ. Sci. Technol.* 39(20), 7932-7939.
- Laglera, L.M., van den Berg, C.M.G., 2003. Copper complexation by thiol compounds in estuarine waters. *Mar. Chem.* 82(1-2), 71-89.
- Lehmann, J., 2007a. Bio-energy in the black. *Front. Ecol. Environ.* 5(7), 381-387.
- Lehmann, J., 2007b. A handful of carbon. *Nature.* 447(7141), 143-144.
- Lehmann, J., Gaunt, J., Rondon, M., 2006. Bio-char sequestration in terrestrial ecosystems - A review. *Mitig. Adapt. Strategies Glob. Chang.* 11(2), 403-427.
- Lehmann, J., Joseph, S., 2009. *Biochar for Environmental Management: Science and Technology.* Earthscan Publishers, London, UK.
- Lehmann, J., Rillig, M.C., Thies, J., Masiello, C.A., Hockaday, W.C., Crowley, D., 2011. Biochar effects on soil biota – A review. *Soil Biol. Biochem.* 43(9), 1812-1836.
- Lessi, P., Dias Filho, N.L., Moreira, J.C., Campos, J.T.S., 1996. Sorption and preconcentration of metal ions on silica gel modified with 2,5-dimercapto-1,3,4-thiadiazole. *Anal. Chim. Acta.* 327(2), 183-190.
- Lewis, A.S., Huntington, T.G., Marvin-Dipasquale, M.C., Amirbahman, A., 2016. Mercury remediation in wetland sediment using zero-valent iron and granular activated carbon. *Environ. Pollut.* 212, 366-373.
- Li, X., Lee, J.Y., Heald, S., 2012. XAFS characterization of mercury captured on cupric chloride-impregnated sorbents. *Fuel.* 93(1), 618-624.
- Li, Y.H., Lee, C.W., Gullett, B.K., 2002. The effect of activated carbon surface moisture on low temperature mercury adsorption. *Carbon.* 40(1), 65-72.
- Liang, P., Li, Y.C., Zhang, C., Wu, S.C., Cui, H.J., Yu, S., Wong, M.H., 2013. Effects of salinity and humic acid on the sorption of Hg on Fe and Mn hydroxides. *J. Hazard. Mater.* 244-245, 322-328.
- Light, T.S., 1972. Standard solution for redox potential measurements. *Anal. Chem.* 44(6), 1038-1039.

- Lin, Y., Munroe, P., Joseph, S., Henderson, R., Ziolkowski, A., 2012. Water extractable organic carbon in untreated and chemical treated biochars. *Chemosphere*. 87(2), 151-7.
- Lindsay, M.B., Blowes, D.W., Ptacek, C.J., Condon, P.D., 2011. Transport and attenuation of metal(loid)s in mine tailings amended with organic carbon: Column experiments. *J. Contam. Hydrol.* 125(1-4), 26-38.
- Liu, P., Ptacek, C.J., Blowes, D.W., Berti, W.R., Landis, R.C., 2015. Aqueous leaching of organic acids and dissolved organic carbon from various biochars prepared at different temperatures. *J. Environ. Qual.* 44(2), 684-695.
- Liu, P., Ptacek, C.J., Blowes, D.W., Finfrock, Y.Z., Gordon, R.A., 2016a. Stabilization of mercury in sediment by using biochars under reducing conditions. *J. Hazard. Mater.* 10.1016/j.jhazmat.2016.11.033.
- Liu, P., Ptacek, C.J., Blowes, D.W., Landis, R.C., 2016b. Mechanisms of mercury removal by biochars produced from different feedstocks determined using X-ray absorption spectroscopy. *J. Hazard. Mater.* 308, 233-242.
- Liu, X.Y., Zhang, A.F., Ji, C.Y., Joseph, S., Bian, R.J., Li, L.Q., Pan, G.X., Paz-Ferreiro, J., 2013. Biochar's effect on crop productivity and the dependence on experimental conditions-a meta-analysis of literature data. *Plant Soil.* 373(1-2), 583-594.
- Livingston, R.J., 2006. *Restoration Of Aquatic Systems*. CRC Press, Taylor & Francis Groups, Boca Raton, USA.
- Long, S.K., Patrick, R., 1961. Production of 2, 3-Butylene glycol from citrus wastes: I. the *Aerobacter aerogenes* fermentation. *Appl. Microbiol.* 9(3), 244.
- Lovley, D., 2013. Dissimilatory Fe(III)- and Mn(IV)-reducing prokaryotes, in: Rosenberg, E., DeLong, E., Lory, S., Stackebrandt, E., Thompson, F.(Eds.), *The Prokaryotes*. Springer Berlin Heidelberg, pp. 287-308.
- Lovley, D.R., 1991. Dissimilatory Fe(III) and Mn(IV) reduction. *Microbiol. Rev.* 55(2), 259-287.
- Lovley, D.R., Holmes, D.E., Nevin, K.P., 2004. Dissimilatory Fe(III) and Mn(IV) reduction. *Adv. Microb. Physiol.* 49, 219-286.
- Lowry, G.V., Shaw, S., Kim, C.S., Rytuba, J.J., Brown, G.E., 2004. Macroscopic and microscopic observations of particle-facilitated mercury transport from New Idria and Sulphur Bank mercury mine tailings. *Environ. Sci. Technol.* 38(19), 5101-5111.
- Lu, P., Feng, Q., Meng, Q., Yuan, T., 2012. Electrokinetic remediation of chromium- and cadmium-contaminated soil from abandoned industrial site. *Sep. Purif. Technol.* 98, 216-220.

Lu, Y.F., Allen, H.E., 2002. Characterization of copper complexation with natural dissolved organic matter (DOM) - link to acidic moieties of DOM and competition by Ca and Mg. *Water Res.* 36(20), 5083-5101.

Madigan, M.T., Clark, D.P., Stahl, D., Martinko, J.M., 2010. *Brock Biology of Microorganisms* 13th Edition.

Major, J., Lehmann, J., Rondon, M., Goodale, C., 2010. Fate of soil-applied black carbon: downward migration, leaching and soil respiration. *Glob. Chang Biol.* 16(4), 1366-1379.

Malm, O., 1998. Gold mining as a source of mercury exposure in the Brazilian Amazon. *Environ. Res.* 77(2), 73-78.

Manceau, A., Nagy, K.L., 2012. Quantitative analysis of sulfur functional groups in natural organic matter by XANES spectroscopy. *Geochim. Cosmochim. Acta.* 99, 206-223.

Mann, C.C., 2002. The real dirt on rainforest fertility. *Science.* 297(5583), 920-923.

Mao, J.D., Johnson, R.L., Lehmann, J., Olk, D.C., Neves, E.G., Thompson, M.L., Schmidt-Rohr, K., 2012. Abundant and stable char residues in soils: Implications for soil fertility and carbon sequestration. *Environ. Sci. Technol.* 46(17), 9571-6.

Martell, A.E., Smith, R.M. 2004. *Critically Selected Stability Constants of Metal Complexes*, Version 8.0. Washington DC, USA.

Mason, R.P., Reinfelder, J.R., Morel, F.M.M., 1995. Bioaccumulation of mercury and methylmercury. *Water Air Soil Poll.* 80(1-4), 915-921.

Matocha, C.J., Karathanasis, A.D., Rakshit, S., Wagner, K.M., 2005. Reduction of copper(II) by iron(II). *J. Environ. Qual.* 34(5), 1539-1546.

Mayer, L.M., 1994. Surface area control of organic carbon accumulation in continental shelf sediments. *Geochim. Cosmochim. Acta.* 58(4), 1271-1284.

Mayo, D., Miller, F., Hannah, R., 2004. *Course Notes on the Interpretation of Infrared and Raman Spectra*. John Wiley & Sons, Inc., Hoboken, NJ.

McCollom, T.M., 1999. Methanogenesis as a potential source of chemical energy for primary biomass production by autotrophic organisms in hydrothermal systems on Europa. *J. Geophys. Res.-Planet.* 104(E12), 30729-30742.

McMaster, W.H., Del Grande, N.K., Mallett, J.H., Hubbell, J.H. 1969. Compilation of x-ray cross sections. *Lawrence Livermore National Laboratory Report UCRL-50174* (section I-III).

- Meng, B., Feng, X., Qiu, G., Anderson, C.W.N., Wang, J., Zhao, L., 2014. Localization and speciation of mercury in brown rice with implications for pan-Asian public health. *Environ. Sci. Technol.* 48(14), 7974-7981.
- Menzel, K., Zeng, A.-P., Deckwer, W.-D., 1997. High concentration and productivity of 1, 3-propanediol from continuous fermentation of glycerol by *Klebsiella pneumoniae*. *Enzyme Microb. Technol.* 20(2), 82-86.
- Mohan, D., Sarswat, A., Ok, Y.S., Pittman Jr, C.U., 2014. Organic and inorganic contaminants removal from water with biochar, a renewable, low cost and sustainable adsorbent - A critical review. *Bioresour. Technol.* 160, 191-202.
- Mohanty, S.K., Cantrell, K.B., Nelson, K.L., Boehm, A.B., 2014. Efficacy of biochar to remove *Escherichia coli* from stormwater under steady and intermittent flow. *Water Res.* 61, 288-296.
- Moingt, M., Lucotte, M., Paquet, S., Ghaleb, B., 2014. Deciphering the impact of land-uses on terrestrial organic matter and mercury inputs to large boreal lakes of central Québec using lignin biomarkers. *Appl. Geochem.* 41, 34-48.
- Moncur, M.C., Ptacek, C.J., Lindsay, M.B.J., Blowes, D.W., Jambor, J.L., 2015. Long-term mineralogical and geochemical evolution of sulfide mine tailings under a shallow water cover. *Appl. Geochem.* 57, 178-193.
- Morales, J.A., de Graterol, L.S., Velásquez, H., de Nava, M.G., de Borrego, B.S., 1998. Determination by ion chromatography of selected organic and inorganic acids in rainwater at Maracaibo, Venezuela. *J. Chromatogr. A.* 804(1-2), 289-294.
- Morel, F.M.M., Kraepiel, A.M.L., Amyot, M., 1998. The chemical cycle and bioaccumulation of mercury. *Annu. Rev. Ecol. Syst.* 29, 543-566.
- Moreno-Castilla, C., Carrasco-Marin, F., Maldonado-Hodar, F.J., Rivera-Utrilla, J., 1998. Effects of non-oxidant and oxidant acid treatments on the surface properties of an activated carbon with very low ash content. *Carbon.* 36(1-2), 145-151.
- Mukherjee, A., Zimmerman, A.R., 2013. Organic carbon and nutrient release from a range of laboratory-produced biochars and biochar-soil mixtures. *Geoderma.* 193-194, 122-130.
- Mulligan, C.N., Yong, R.N., Gibbs, B.F., 2001. Remediation technologies for metal-contaminated soils and groundwater: An evaluation. *Eng. Geol.* 60(1-4), 193-207.
- Muyzer, G., Stams, A.J.M., 2008. The ecology and biotechnology of sulphate-reducing bacteria. *Nat. Rev. Microbiol.* 6(6), 441-454.
- Nakano, K., Tsuji, K., 2006. Development of confocal 3d micro XRF spectrometer and its application to rice grain. *Bunseki Kagaku.* 55(6), 427-432.

- Namasivayam, C., Kadirvelu, K., 1999. Uptake of mercury (II) from wastewater by activated carbon from an unwanted agricultural solid by-product: Coirpith. *Carbon*. 37(1), 79-84.
- Neilson, A.H., Allard, A.S., 2012. *Organic Chemicals in the Environment: Mechanisms of Degradation and Transformation*, Second Edition. CRC Press, Taylor & Francis Group, Boca Raton, FL, USA.
- Nevin, K.P., Holmes, D.E., Woodard, T.L., Covalla, S.F., Lovley, D.R., 2007. Reclassification of *Trichlorobacter thiogenes* as *Geobacter thiogenes* comb. nov. *Int. J. Syst. Evol. Microbiol.* 57(3), 463-466.
- Newville, M., Larch: X-ray Data Analysis.
<http://cars.uchicago.edu/xraylarch/contents.html> (Accessed by March 2016)
- Ngueleu, S.K., Grathwohl, P., Cirpka, O.A., 2014. Particle-facilitated transport of lindane in water-saturated tropical lateritic porous media. *J. Environ. Qual.* 43(4), 1392-1403.
- Nirmal Kumar, J.I., George, B., Kumar, R.N., Sajish, P.R., Viyol, S., 2010. Biosorption of mercury and lead by dried *Aspergillus niger* Tiegh. isolated from estuarine sediments. *Int. J. Environ. Stud.* 67(5), 735-746.
- Nordstrom, D.K., 1977. Thermochemical redox equilibria of ZoBell's solution. *Geochim. Cosmochim. Acta.* 41(12), 1835-1841.
- Norton, S., Lacroix, C., Vuilleumard, J.-C., 1994. Kinetic study of continuous whey permeate fermentation by immobilized *Lactobacillus helveticus* for lactic acid production. *Enzyme Microb. Technol.* 16(6), 457-466.
- Noyce, G.L., Basiliko, N., Fulthorpe, R., Sackett, T.E., Thomas, S.C., 2015. Soil microbial responses over 2 years following biochar addition to a north temperate forest. *Biol. Fertil. Soils.* 51(6), 649-659.
- NSLS, EXAFS Database of Standard Materials at NSLS.
<http://www.bnl.gov/ps/x18b/data.asp> (Accessed by June 2016)
- Oak Ridge National Laboratory, Predicted mercury methylators.
http://www.esd.ornl.gov/programs/rsfa/data/PredictedMethylators/PredictedMethylators_20140514.pdf (Accessed by November 30, 2015)
- Oh, Y.-K., Seol, E.-H., Lee, E.Y., Park, S., 2002. Fermentative hydrogen production by a new chemoheterotrophic bacterium *Rhodospseudomonas palustris* P4. *Int. J. Hydrogen Energy.* 27(11), 1373-1379.
- Olkhovyyk, O., Jaroniec, M., 2005a. Adsorption characterization of ordered mesoporous silicas with mercury-specific immobilized ligands. *Adsorption.* 11(1 SUPPL.), 685-690.

Olkhovyk, O., Jaroniec, M., 2005b. Ordered mesoporous silicas with 2,5-dimercapto-1,3,4-thiadiazole ligand: High capacity adsorbents for mercury ions. *Adsorption*. 11(3-4), 205-214.

Opsahl, S., Benner, R., 1995. Early diagenesis of vascular plant tissues: Lignin and cutin decomposition and biogeochemical implications. *Geochim. Cosmochim. Acta*. 59(23), 4889-4904.

Ortiz, V.L., Mason, R.P., Ward, J.E., 2015. An examination of the factors influencing mercury and methylmercury particulate distributions, methylation and demethylation rates in laboratory-generated marine snow. *Mar. Chem.* 177(Pt 5), 753-762.

Özçimen, D., Karaosmanoğlu, F., 2004. Production and characterization of bio-oil and biochar from rapeseed cake. *Renew. Energ.* 29(5), 779-787.

Parkhurst, D.L., Appelo, C. 1999. User's guide to PHREEQC (Version 2): A Computer Program for Speciation, Batch-reaction, One-dimensional Transport, and Inverse Geochemical Calculations. US Geological Survey.

Patmont, C.R., Ghosh, U., LaRosa, P., Menzie, C.A., Luthy, R.G., Greenberg, M.S., Cornelissen, G., Eek, E., Collins, J., Hull, J., Hjartland, T., Glaza, E., Bleiler, J., Quadrini, J., 2015. In situ sediment treatment using activated carbon: A demonstrated sediment cleanup technology. *Integr. Environ. Assess. Manag.* 11(2), 195-207.

Paulson, K., 2014. Methylmercury production in riverbank sediments of the South River, Virginia (USA) and assessment of biochar as a mercury treatment option. (Master of Science). University of Waterloo, Waterloo, Canada.

Paulson, K.M.A., Ptacek, C.J., Blowes, D.W., Gould, W.D., Ma, J., Landis, R.C., Dyer, J.A., 2016. Role of organic carbon sources and sulfate in controlling net methylmercury production in riverbank sediments of the South River, VA (USA). *Geomicrobiol. J.*(Accepted).

Peacock, C.L., Sherman, D.M., 2004. Copper(II) sorption onto goethite, hematite and lepidocrocite: A surface complexation model based on ab initio molecular geometries and EXAFS spectroscopy. *Geochim. Cosmochim. Acta*. 68(12), 2623-2637.

Pereira, M.E., Duarte, A.C., Millward, G.E., Vale, C., Abreu, S.N., 1998. Tidal export of particulate mercury from the most contaminated area of Aveiro's Lagoon, Portugal. *Sci. Total Environ.* 213(1-3), 157-163.

Petersen, S.W., Hedquist, K.A., Hanford, F. 2006. Teatability test report for calcium polysulfide in the 100-K area. US Department of Energy. DOE/RL-2006-17.

Poulin, B.A., Aiken, G.R., Nagy, K.L., Manceau, A., Krabbenhoft, D.P., Ryan, J.N., 2016. Mercury transformation and release differs with depth and time in a contaminated riparian soil during simulated flooding. *Geochim. Cosmochim. Acta*. 176, 118-138.

- Prietzl, J., Thieme, J., Neuhäusler, U., Susini, J., Kögel-Knabner, I., 2003. Speciation of sulphur in soils and soil particles by X-ray spectromicroscopy. *Eur. J. Soil Sci.* 54(2), 423-433.
- Pronk, J.T., De Bruyn, J.C., Bos, P., Kuenen, J.G., 1992. Anaerobic growth of *Thiobacillus ferrooxidans*. *Appl. Environ. Microbiol.* 58(7), 2227-2230.
- Pushie, M.J., Pickering, I.J., Korbas, M., Hackett, M.J., George, G.N., 2014. Elemental and chemically specific X-ray fluorescence imaging of biological systems. *Chem. Rev.* 114(17), 8499-8541.
- Qiu, M., Sun, K., Jin, J., Han, L., Sun, H., Zhao, Y., Xia, X., Wu, F., Xing, B., 2015. Metal/metalloid elements and polycyclic aromatic hydrocarbon in various biochars: The effect of feedstock, temperature, minerals, and properties. *Environ. Pollut.* 206, 298-305.
- Rachman, M.A., Furutani, Y., Nakashimada, Y., Kakizono, T., Nishio, N., 1997. Enhanced hydrogen production in altered mixed acid fermentation of glucose by *Enterobacter aerogenes*. *J. Ferment. Bioeng.* 83(4), 358-363.
- Rafiq, M.K., Bachmann, R.T., Rafiq, M.T., Shang, Z., Joseph, S., Long, R.L., 2016. Influence of pyrolysis temperature on physico-chemical properties of corn stover (zea mays l.) biochar and feasibility for carbon capture and energy balance. *PLoS ONE.* 11(6).
- Ranchou-Peyruse, M., Monperrus, M., Bridou, R., Duran, R., Amouroux, D., Salvado, J.C., Guyoneaud, R., 2009. Overview of mercury methylation capacities among anaerobic bacteria including representatives of the sulphate-reducers: Implications for environmental studies. *Geomicrobiol. J.* 26(1), 1-8.
- Randall, P.M., Chattopadhyay, S., 2013. Mercury contaminated sediment sites-An evaluation of remedial options. *Environ. Res.* 125, 131-49.
- Randall, P.M., Yates, B.J., Lal, V., Darlington, R., Fimmen, R., 2013. In-situ subaqueous capping of mercury-contaminated sediments in a fresh-water aquatic system, Part II-evaluation of sorption materials. *Environ. Res.* 125, 41-51.
- Ransom, C., Balan, V., Biswas, G., Dale, B., Crockett, E., Sticklen, M., 2007. Heterologous *Acidothermus cellulolyticus* 1, 4- β -endoglucanase E1 produced within the corn biomass converts corn stover into glucose. *Appl. Biochem. Biotechnol.* 137-140(1-12), 207-219.
- Rao, M.M., Reddy, D.H.K.K., Venkateswarlu, P., Seshaiyah, K., 2009. Removal of mercury from aqueous solutions using activated carbon prepared from agricultural by-product/waste. *J. Environ. Manage.* 90(1), 634-643.
- Ravel, B., Newville, M., 2005. ATHENA, ARTEMIS, HEPHAESTUS: Data analysis for X-ray absorption spectroscopy using IFEFFIT. *J. Synchrotron Radiat.* 12(4), 537-541.

- Ravichandran, M., 2004. Interactions between mercury and dissolved organic matter - a review. *Chemosphere*. 55(3), 319-331.
- Reuther, C., Wheeler, M., 1996. Measuring mercury. *Environ. Health Perspect.* 104(8), 826-831.
- Rhoades, E.L., O'Neal, M.A., Pizzuto, J.E., 2009. Quantifying bank erosion on the South River from 1937 to 2005, and its importance in assessing Hg contamination. *Applied Geography*. 29(1), 125-134.
- Ribet, I., Ptacek, C.J., Blowes, D.W., Jambor, J.L., 1995. The potential for metal release by reductive dissolution of weathered mine tailings. *J. Contam. Hydrol.* 17(3), 239-273.
- Riedel, T., Iden, S., Geilich, J., Wiedner, K., Durner, W., Biester, H., 2014. Changes in the molecular composition of organic matter leached from an agricultural topsoil following addition of biomass-derived black carbon (biochar). *Org. Geochem.* 69, 52-60.
- Riscassi, A.L., Scanlon, T.M., 2011. Controls on stream water dissolved mercury in three mid-Appalachian forested headwater catchments. *Water Resour. Res.* 47(12), W12512.
- Robertson, W.D., Ptacek, C.J., Brown, S.J., 2009. Rates of nitrate and perchlorate removal in a 5-year-old wood particle reactor treating agricultural drainage. *Ground Water Monit. Remediat.* 29(2), 87-94.
- Rondon, M.R., Goodman, R.M., Handelsman, J., 1999. The Earth's bounty: Assessing and accessing soil microbial diversity. *Trends Biotechnol.* 17(10), 403-409.
- Rukavina, N.A., Mudroch, A., Joshi, S.R., 1990. The geochemistry and sedimentology of the surficial sediments of Lac St-Louis, St. Lawrence River. *Sci. Total Environ.* 97-98, 481-494.
- Sandström, J., Wennerbeck, I., 1966. Tautomeric cyclic thiones. *Acta Chem. Scand.* 20(1), 57-71.
- Santoro, A., Terzano, R., Medici, L., Beciani, M., Pagnoni, A., Blo, G., 2012. Colloidal mercury (Hg) distribution in soil samples by sedimentation field-flow fractionation coupled to mercury cold vapour generation atomic absorption spectroscopy. *J. Environ. Monit.* 14(1), 138-145.
- Schiraldi, C., Marulli, F., Di Lernia, I., Martino, A., De Rosa, M., 1999. A microfiltration bioreactor to achieve high cell density in *Sulfolobus solfataricus* fermentation. *Extremophiles*. 3(3), 199-204.
- Schmitz, S., Möller, A., Wilke, M., Malzer, W., Kanngiesser, B., Bousquet, R., Berger, A., Schefer, S., 2009. Chemical U-Th-Pb dating of monazite by 3D-micro X-ray fluorescence analysis with synchrotron radiation. *Eur. J. Mineral.* 21(5), 927-945.

Scoullou, M.J., Vonkeman, G.H., Thornton, I., Makuch, Z., 2001. Mercury, Cadmium, Lead: Handbook for Sustainable Heavy Metals Policy and Regulation. Kluwer Academic Publishers, Dordrecht, The Netherlands.

Scullion, J., 2006. Remediating polluted soils. *Naturwissenschaften*. 93(2), 51-65.

Selin, N.E., 2009. Global biogeochemical cycling of mercury: A review. *Annu. Rev. Environ. Resour.* 34, 43-63.

Serrano, S., Vlassopoulos, D., Bessinger, B., O'Day, P.A., 2012a. Immobilization of Hg(II) by coprecipitation in sulfate-cement systems. *Environ. Sci. Technol.* 46(12), 6767-6775.

Serrano, S., Vlassopoulos, D., Bessinger, B., O'Day, P.A., 2012b. Immobilization of Hg(II) by coprecipitation in sulfate-cement systems. *Environ. Sci. Technol.* 46(12), 6767-6775.

Serrano, S., Vlassopoulos, D., O'Day, P.A., 2016. Mechanism of Hg(II) immobilization in sediments by sulfate-cement amendment. *Appl. Geochem.* 67, 68-80.

Shackley, S., Ruyschaert, G., Zwart, K., Glaser, B., 2016. Biochar in European Soils and Agriculture: Science and Practice. Taylor & Francis, Abingdon, Oxon, United Kingdom.

Shafizadeh, F., 1985. Pyrolytic reactions and products of biomass, in: Overend, R.P., Milne, T.A., Mudge, L.K.(Eds.), *Fundamentals of Thermochemical Biomass Conversion*. Elsevier Applied Science, London, UK.

Shen, Y.S., Wang, S.L., Tzou, Y.M., Yan, Y.Y., Kuan, W.H., 2012. Removal of hexavalent Cr by coconut coir and derived chars-the effect of surface functionality. *Bioresour. Technol.* 104, 165-72.

Shin, J.-H., Yoon, J.H., Ahn, E.K., Kim, M.-S., Sim, S.J., Park, T.H., 2007. Fermentative hydrogen production by the newly isolated *Enterobacter asburiae* SNU-1. *Int. J. Hydrogen Energy.* 32(2), 192-199.

Singh, B.P., Cowie, A.L., Smernik, R.J., 2012. Biochar carbon stability in a clayey soil as a function of feedstock and pyrolysis temperature. *Environ. Sci. Technol.* 46(21), 11770-8.

Skylberg, U., 2008. Competition among thiols and inorganic sulfides and polysulfides for Hg and MeHg in wetland soils and sediments under suboxic conditions: Illumination of controversies and implications for MeHg net production. *J. Geophys. Res.* 113(G00C03), 1-14.

Skylberg, U., Bloom, P.R., Qian, J., Lin, C.M., Bleam, W.F., 2006. Complexation of mercury(II) in soil organic matter: EXAFS evidence for linear two-coordination with reduced sulfur groups. *Environ. Sci. Technol.* 40(13), 4174-4180.

- Skylberg, U., Xia, K., Bloom, P.R., Nater, E.A., Bleam, W.F., 2000. Binding of mercury(II) to reduced sulfur in soil organic matter along upland-peat soil transects. *J. Environ. Qual.* 29(3), 855-865.
- Slowey, A.J., 2010. Rate of formation and dissolution of mercury sulfide nanoparticles: The dual role of natural organic matter. *Geochim. Cosmochim. Acta.* 74(16), 4693-4708.
- South River Science Team, <http://southriverscienceteam.org/> (Accessed by August 2015)
- Spokas, K., Novak, J.M., Masiello, C.A., Johnson, M.G., Colosky, E.C., Ippolito, J., Trigo, C., 2014a. Physical disintegration of biochar: An overlooked process. *Environ. Sci. Technol. Lett.* 1(8), 326-332.
- Spokas, K.A., 2010. Review of the stability of biochar in soils: Predictability of O:C molar ratios. *Carbon Manag.* 1(2), 289-303.
- Spokas, K.A., Cantrell, K.B., Novak, J.M., Archer, D.W., Ippolito, J.A., Collins, H.P., Boateng, A.A., Lima, I.M., Lamb, M.C., McAloon, A.J., Lentz, R.D., Nichols, K.A., 2012. Biochar: A synthesis of its agronomic impact beyond carbon sequestration. *J. Environ. Qual.* 41(4), 973-989.
- Spokas, K.A., Novak, J.M., Masiello, C.A., Johnson, M.G., Colosky, E.C., Ippolito, J.A., Trigo, C., 2014b. Physical disintegration of biochar: An overlooked process. *Environ. Sci. Technol. Lett.* 1(8), 326-332.
- Stal, L.J., Moezelaar, R., 1997. Fermentation in cyanobacteria. *FEMS Microbiol. Rev.* 21(2), 179-211.
- Steinbuechel, A., Kuhn, M., Niedrig, M., Schlegel, H.G., 1983. Fermentation enzymes in strictly aerobic bacteria: Comparative studies on strains of the *Genus Alcaligenes* and on *Nocardia opaca* and *Xanthobacter autotrophicus*. *J. Gen. Microbiol.* 129(9), 2825-2835.
- Sud, D., Mahajan, G., Kaur, M.P., 2008. Agricultural waste material as potential adsorbent for sequestering heavy metal ions from aqueous solutions - A review. *Bioresour. Technol.* 99(14), 6017-6027.
- Swanson, K.S., Dowd, S.E., Suchodolski, J.S., Middelbos, I.S., Vester, B.M., Barry, K.A., Nelson, K.E., Torralba, M., Henrissat, B., Coutinho, P.M., Cann, I.K., White, B.A., Fahey Jr, G.C., 2011. Phylogenetic and gene-centric metagenomics of the canine intestinal microbiome reveals similarities with humans and mice. *ISME J.* 5(4), 639-649.
- Takaoka, S., Fujino, T., Hotta, N., Ueda, K., Hanada, M., Tajiri, M., Inoue, Y., 2013. Signs and symptoms of methylmercury contamination in a First Nations community in Northwestern Ontario, Canada. *Sci. Total Environ.* 468-469, 950-957.
- Tang, J., Lv, H., Gong, Y., Huang, Y., 2015a. Preparation and characterization of a novel graphene/biochar composite for aqueous phenanthrene and mercury removal. *Bioresour. Technol.* 196, 355-363.

- Tang, W., Bruce Chase, D., Sparks, D.L., Rabolt, J.F., 2015b. Selective and quantitative detection of trace amounts of mercury(II) Ion (Hg^{2+}) and Copper(II) Ion (Cu^{2+}) using surface-enhanced raman scattering (SERS). *Appl. Spectrosc.* 69(7), 843-849.
- Tchounwou, P.B., Ayensu, W.K., Ninashvili, N., Sutton, D., 2003. Environmental exposure to mercury and its toxicopathologic implications for public health. *Environ. Toxicol.* 18(3), 149-175.
- Temminghoff, E.J.M., Plette, A.C.C., Van Eck, R., Van Riemsdijk, W.H., 2000. Determination of the chemical speciation of trace metals in aqueous systems by the Wageningen Donnan Membrane Technique. *Anal. Chim. Acta.* 417(2), 149-157.
- Thompson, A., Chadwick, O.A., Boman, S., Chorover, J., 2006. Colloid mobilization during soil iron redox oscillations. *Environ. Sci. Technol.* 40(18), 5743-5749.
- Tiffreau, C., Lützenkirchen, J., Behra, P., 1995. Modeling the adsorption of mercury(II) on (hydr)oxides. I. amorphous iron oxide and α -quartz. *J. Colloid Interface Sci.* 172(1), 82-93.
- Tiwari, G.N., Mishra, R.K., 2011. *Advanced Renewable Energy Sources*. Royal Society of Chemistry, Cambridge, UK.
- Torres, E., Couture, R.M., Shafei, B., Nardi, A., Ayora, C., Van Cappellen, P., 2015. Reactive transport modeling of early diagenesis in a reservoir lake affected by acid mine drainage: Trace metals, lake overturn, benthic fluxes and remediation. *Chem. Geol.* 419, 75-91.
- Uchimiya, M., Ohno, T., He, Z., 2013. Pyrolysis temperature-dependent release of dissolved organic carbon from plant, manure, and biorefinery wastes. *J. Anal. Appl. Pyrol.* 104, 84-94.
- Uchimiya, M., Wartelle, L.H., Klasson, K.T., Fortier, C.A., Lima, I.M., 2011. Influence of pyrolysis temperature on biochar property and function as a heavy metal sorbent in soil. *J. Agric. Food Chem.* 59(6), 2501-2510.
- Ullrich, S.M., Tanton, T.W., Abdrashitova, S.A., 2001. Mercury in the aquatic environment: A review of factors affecting methylation. *Crit. Rev. Environ. Sci. Technol.* 31(3), 241-293.
- Underwood, C., Ipsen, E.C. 2008. DRAFT Focused Feasibility Study: *Groundwater source control interim remedial measure Arkema Chemicals Facility, Portland, Oregon* Project No. 0065572
- US-EPA. 1996. Method 3052: Microwave assisted acid digestion of siliceous and organically based matrices, U.S. Environmental Protection Agency. Washington DC, USA.

- Vairavamurthy, A., 1998. Using X-ray absorption to probe sulfur oxidation states in complex molecules. *Spectrochim. Acta Mol. Biomol. Spectrosc.* 54(12), 2009-2017.
- Vandieken, V., Mußmann, M., Niemann, H., Jørgensen, B.B., 2006. *Desulfuromonas svalbardensis* sp. nov. and *Desulfuromusa ferrireducens* sp. nov., psychrophilic, Fe(III)-reducing bacteria isolated from Arctic sediments, Svalbard. *Int. J. Syst. Evol. Microbiol.* 56(5), 1133-1139.
- Veiga, M.M., Hinton, J.J., 2002. Abandoned artisanal gold mines in the Brazilian Amazon: A legacy of mercury pollution. *Nat. Resour. Forum.* 26(1), 15-26.
- Vincze, L., Vekemans, B., Brenker, F.E., Falkenberg, G., Rickers, K., Somogyi, A., Kersten, M., Adams, F., 2004. Three-dimensional trace element analysis by confocal X-ray microfluorescence imaging. *Anal. Chem.* 76(22), 6786-6791.
- Virginia Department of Environmental Quality, Fish Tissue Mercury in South River, South Fork Shenandoah River, and Shenandoah River in 2007. http://www.deq.virginia.gov/Portals/0/DEQ/Water/WaterQualityMonitoring/FishSedimentMonitoring/2007_Fish_Hg_Results.pdf (Accessed by September 2015)
- Virkutyte, J., Sillanpää, M., Latostenmaa, P., 2002. Electrokinetic soil remediation - Critical overview. *Sci. Total Environ.* 289(1-3), 97-121.
- Wallschläger, D., Desai, M.V.M., Wilken, R.D., 1996. The role of humic substances in the aqueous mobilization of mercury from contaminated floodplain soils. *Water Air Soil Poll.* 90(3-4), 507-520.
- Wang, J., Feng, X., Anderson, C.W.N., Xing, Y., Shang, L., 2012. Remediation of mercury contaminated sites - A review. *J. Hazard. Mater.* 221-222, 1-18.
- Wang, M.J., Hu, Y.F., Wang, J.C., Chang, L.P., Wang, H., 2013. Transformation of sulfur during pyrolysis of inertinite-rich coals and correlation with their characteristics. *J. Anal. Appl. Pyrol.* 104, 585-592.
- Wang, Q., Kim, D., Dionysiou, D.D., Sorial, G.A., Timberlake, D., 2004. Sources and remediation for mercury contamination in aquatic systems - A literature review. *Environ. Pollut.* 131(2), 323-336.
- Weber, K.A., Achenbach, L.A., Coates, J.D., 2006. Microorganisms pumping iron: Anaerobic microbial iron oxidation and reduction. *Nat. Rev. Microbiol.* 4(10), 752-764.
- Weisener, C.G., Sale, K.S., Smyth, D.J.A., Blowes, D.W., 2005a. Field column study using zerovalent iron for mercury removal from contaminated groundwater. *Environ. Sci. Technol.* 39(16), 6306-6312.
- Weisener, C.G., Sale, K.S., Smyth, D.J.A., Blowes, D.W., 2005b. Field column study using zerovalent iron for mercury removal from contaminated groundwater. *Environ. Sci. Technol.* 39(16), 6306-6312.

Wiederhold, J.G., Skyllberg, U., Drott, A., Jiskra, M., Jonsson, S., Björn, E., Bourdon, B., Kretzschmar, R., 2014. Mercury isotope signatures in contaminated sediments as a tracer for local industrial pollution sources. *Environ. Sci. Technol.* 49(1), 177-185.

Wikipedia, *Desulfovibrio*. <http://en.wikipedia.org/wiki/Desulfovibrio> (Accessed by May 2015)

Woll, A.R., Agyeman-Budu, D., Bilderback, D.H., Dale, D., Kazimirov, A.Y., Pfeifer, M., Plautz, T., Szebenyi, T., Untracht, G. 2012. 3D x-ray fluorescence microscopy with 1.7 μm resolution using lithographically fabricated micro-channel arrays. *Advances in X-Ray/EUV Optics and Components VII*, Proceedings of SPIE, San Diego, California, USA. pp. 85020K-1-85020K-14.

Woll, A.R., Agyeman-Budu, D., Choudhury, S., Coulthard, I., Finnefrock, A.C., Gordon, R., Hallin, E., Mass, J., 2014. Lithographically-fabricated channel arrays for confocal x-ray fluorescence microscopy and XAFS. *J. Phys. Conf. Ser.* 493(1), 012028.

Wong, H.K.T., Gauthier, A., Nriagu, J.O., 1999. Dispersion and toxicity of metals from abandoned gold mine tailings at Goldenville, Nova Scotia, Canada. *Sci. Total Environ.* 228(1), 35-47.

Xia, K., Skyllberg, U.L., Bleam, W.F., Bloom, P.R., Nater, E.A., Helmke, P.A., 1999. X-ray absorption spectroscopic evidence for the complexation of Hg(II) by reduced sulfur in soil humic substances. *Environ. Sci. Technol.* 33(2), 257-261.

Xie, T., Sadasivam, B.Y., Reddy, K.R., Wang, C., Spokas, K., 2016. Review of the effects of biochar amendment on soil properties and carbon sequestration. *J. Hazard. Toxic Radioact. Waste.* 20(1), 04015013-1-14.

Xu, M., Sheng, C., 2012. Influences of the heat-treatment temperature and inorganic matter on combustion characteristics of cornstalk biochars. *Energ. Fuel.* 26(1), 209-218.

Yang, H., Yan, R., Chen, H., Lee, D.H., Zheng, C., 2007. Characteristics of hemicellulose, cellulose and lignin pyrolysis. *Fuel.* 86(12-13), 1781-1788.

Yao, F.X., Arbestain, M.C., Virgel, S., Blanco, F., Arostegui, J., Maciá-Agulló, J.A., Macías, F., 2010. Simulated geochemical weathering of a mineral ash-rich biochar in a modified Soxhlet reactor. *Chemosphere.* 80(7), 724-732.

Yargicoglu, E.N., Sadasivam, B.Y., Reddy, K.R., Spokas, K., 2015. Physical and chemical characterization of waste wood derived biochars. *Waste Manage.* 36, 256-268.

Yin, Y., Allen, H.E., Huang, C.P., Sparks, D.L., Sanders, P.F., 1997. Kinetics of mercury(II) adsorption and desorption on soil. *Environ. Sci. Technol.* 31(2), 496-503.

Yoshimura, K., Hama, T., 2012. Degradation and dissolution of zooplanktonic organic matter and lipids in early diagenesis. *J. Oceanogr.* 68(1), 205-214.

- Yu, R., Flanders, J.R., Mack, E.E., Turner, R., Mirza, M.B., Barkay, T., 2011. Contribution of coexisting sulfate and iron reducing bacteria to methylmercury production in freshwater river sediments. *Environ. Sci. Technol.* 46(5), 2684–2691.
- Yu, R.Q., Flanders, J.R., Mack, E.E., Turner, R., Mirza, M.B., Barkay, T., 2012. Contribution of coexisting sulfate and iron reducing bacteria to methylmercury production in freshwater river sediments. *Environ. Sci. Technol.* 46(5), 2684-91.
- Yu, R.Q., Reinfelder, J.R., Hines, M.E., Barkay, T., 2013. Mercury methylation by the methanogen *Methanospirillum hungatei*. *Appl. Environ. Microbiol.* 79(20), 6325-6330.
- Yuan, J.H., Xu, R.K., Zhang, H., 2011. The forms of alkalis in the biochar produced from crop residues at different temperatures. *Bioresour. Technol.* 102(3), 3488-3497.
- Yudovich, Y.E., Ketris, M.P., 2005. Mercury in coal: A review. Part 1. Geochemistry. *Int. J. Coal Geol.* 62(3), 107-134.
- Zabihi, M., Haghghi Asl, A., Ahmadpour, A., 2010. Studies on adsorption of mercury from aqueous solution on activated carbons prepared from walnut shell. *J. Hazard. Mater.* 174(1-3), 251-256.
- Zeng, T., Arnold, W.A., Toner, B.M., 2013. Microscale characterization of sulfur speciation in lake sediments. *Environ. Sci. Technol.* 47(3), 1287-1296.
- Zhang, P., Sun, H., Yu, L., Sun, T., 2013. Adsorption and catalytic hydrolysis of carbaryl and atrazine on pig manure-derived biochars: Impact of structural properties of biochars. *J. Hazard. Mater.* 244-245, 217-224.
- Zhang, T., Kim, B., Levard, C., Reinsch, B.C., Lowry, G.V., Deshusses, M.A., Hsu-Kim, H., 2012. Methylation of mercury by bacteria exposed to dissolved, nanoparticulate, and microparticulate mercuric sulfides. *Environ. Sci. Technol.* 46(13), 6950-8.
- Zhu, X.F., Wu, X.Y., Dai, Y., 2003. Fermentation conditions and properties of a chitinase from *Acinetobacter* sp. C-17. *Biosci., Biotechnol., Biochem.* 67(2), 284-290.
- Zimmerman, A.R., 2010. Abiotic and microbial oxidation of laboratory-produced black carbon (biochar). *Environ. Sci. Technol.* 44(4), 1295-301.
- Zolin, A., Jensen, A., Jensen, P.A., Frandsen, F., Dam-Johansen, K., 2001. The influence of inorganic materials on the thermal deactivation of fuel chars. *Energ. Fuel.* 15(5), 1110-1122.
- Zornoza, R., Moreno-Barriga, F., Acosta, J.A., Muñoz, M.A., Faz, A., 2016. Stability, nutrient availability and hydrophobicity of biochars derived from manure, crop residues, and municipal solid waste for their use as soil amendments. *Chemosphere.* 144, 122-130.

Appendix A: *Summary of Data Presented
in Chapter 2*

Table S2.1 Summary of organic acids (OAs) and dissolved organic carbon (DOC) concentrations (as C mmol L⁻¹) in aqueous solution leached from low-T biochar samples for batch experiments.

Group	Raw material	Lactate	Acetate	Propionate	Formate	Other	DOC
Wood	Activated carbon2**	-	-	-	-	-	-
	Activated carbon1**	-	-	-	-	-	-
	Biochar Engineering Charcoal**	-	-	-	-	-	-
	Cowboy Charcoal**	-	-	-	-	-	-
	Wicked Good Charcoal**	-	-	-	-	-	-
	Pine bark	<0.0003	0.14	0.019	0.039	0.42	0.63
	Mulch	0.20	0.98	0.058	<0.0003	6.4	7.7
Agricultural residue	Corn stover1	0.011	1.0	0.20	0.21	11	12
	Corn stover2	0.15	1.3	0.46	0.24	2.2	4.3
	Corn cob2	<0.0003	0.26	0.052	0.024	0.44	0.78
	Switchgrass	0.005	0.28	0.068	0.071	0.68	1.1
	Wheat straw	0.046	0.75	0.26	0.15	1.0	2.2
	Hop bract	<0.0003	<0.0003	<0.0003	0.0017	0.18	0.18
	Corn cob1	0.007	0.45	0.10	0.07	0.50	1.1
	Cotton seed	<0.0003	0.79	0.27	0.19	0.81	2.1
	Cocoa husk	0.045	2.8	0.90	0.40	8.2	12
Manure	Poultry manure1	<0.0003	<0.0003	<0.0003	<0.0003	5.0	5.0
	Mushroom soil2	0.0083	1.1	0.35	0.29	10	12
	Mushroom soil3**	-	-	-	-	-	-
	Poultry manure2*	0.0093	0.52	0.10	0.11	5.9	6.6
	Poultry manure3**	-	-	-	-	-	-
	Mushroom soil1	0.037	1.3	0.36	0.26	8.5	10
	Cow manure	0.0023	0.58	0.12	0.18	0.85	1.7
control	River water	<0.0003	<0.0003	<0.0003	<0.0003	<0.04	<0.04

The other carbon was the difference between DOC and OAs. ** after biochar name indicates no data was available for low-T biochar.

Table S2.1 continued. Percentages of carbon components released from low-T biochar samples.

Group	Raw material	Lactate	Acetate	Propionate	Formate	Other
Wood	Activated carbon2**	-	-	-	-	-
	Activated carbon1**	-	-	-	-	-
	Biochar Engineering Charcoal**	-	-	-	-	-
	Cowboy Charcoal**	-	-	-	-	-
	Wicked Good Charcoal**	-	-	-	-	-
	Pine bark	0	23.1	2.98	6.15	67.8
	Mulch	2.55	12.7	0.756	0	83.9
Agricultural residue	Corn stover1	0.0886	8.43	1.64	1.68	88.2
	Corn stover2	3.51	29.4	10.8	5.67	50.7
	Corn cob2	0	33.8	6.65	3.01	56.5
	Switchgrass	0.454	25.5	6.15	6.48	61.4
	Wheat straw	2.04	33.5	11.5	6.6	46.4
	Hop bract	0	0	0	0.975	99
	Corn cob1	0.619	39.5	9.32	6.19	44.4
	Cotton seed	0	38.4	12.9	9.03	39.6
Cocoa husk	0.363	22.8	7.31	3.28	66.2	
Manure	Poultry manure1	-	-	-	-	-
	Mushroom soil2	0.0689	9.1	2.92	2.41	85.5
	Mushroom soil3**	-	-	-	-	-
	Poultry manure2*	0.14	7.77	1.5	1.71	88.9
	Poultry manure3**	-	-	-	-	-
	Mushroom soil1	0.352	12.5	3.47	2.52	81.2
	Cow manure	0.135	33.4	6.86	10.6	49
control	River water	0	0	0	0	0

The other carbon was the difference between DOC and OAs. ** after biochar name indicates no data was available for low-T biochar.

Table S2.1 continued. Summary of OAs and DOC concentrations (as C mmol L⁻¹) in aqueous solution leached from high-T biochar samples for batch experiment.

Group	Raw material	Lactate	Acetate	Propionate	Formate	Other	DOC
Wood	Activated carbon2**	<0.0003	0.004	<0.0003	0.0059	<0.04	<0.04
	Activated carbon1**	<0.0003	0.004	0.0012	0.0059	0.105	0.12
	Biochar Engineering Charcoal**	<0.0003	0.066	0.0049	0.056	0.18	0.31
	Cowboy Charcoal**	0.0037	0.0057	0.0045	0.0054	0.43	0.45
	Wicked Good Charcoal**	<0.0003	0.10	0.0061	0.0035	0.21	0.32
	Pine bark	<0.0003	0.0027	<0.0003	0.029	0.11	0.14
	Mulch	<0.0003	0.086	0.043	0.047	<0.04	0.19
Agricultural residue	Corn stover1	<0.0003	0.0063	<0.0003	0.072	0.15	0.23
	Corn stover2	<0.0003	0.006	<0.0003	0.050	0.40	0.45
	Corn cob2	<0.0003	0.0080	0.0028	0.022	0.21	0.24
	Switchgrass	<0.0003	0.005	<0.0003	0.038	0.13	0.17
	Wheat straw	<0.0003	0.0069	<0.0003	0.067	0.22	0.30
	Hop bract	<0.0003	<0.0003	<0.0003	<0.0003	0.12	0.12
	Corn cob1	<0.0003	0.004	<0.0003	0.085	0.18	0.27
	Cotton seed	<0.0003	0.00533	<0.0003	0.079	0.22	0.31
Cocoa husk	0.061	3.8	0.94	0.40	6.3	12	
Manure	Poultry manure1	<0.0003	0.01	<0.0003	0.014	<0.04	<0.04
	Mushroom soil2	<0.0003	0.0093	<0.0003	0.014	<0.04	<0.04
	Mushroom soil3**	<0.0003	0.018	<0.0003	0.098	0.21	0.33
	Poultry manure2*	-	-	-	-	-	-
	Poultry manure3**	<0.0003	0.017	<0.0003	0.053	<0.04	0.0697
	Mushroom soil1	<0.0003	0.014	<0.0003	0.023	<0.04	<0.04
	Cow manure	<0.0003	0.011	<0.0003	0.028	1.6	1.7
Control	River water	<0.0003	<0.0003	<0.0003	<0.0003	<0.0003	<0.04

The other carbon was the difference between DOC and OAs. * after biochar name indicates no data was available for high-T biochar.

Table S2.1 continued. Percentages of carbon components released from high-T biochar samples.

Group	Raw material	Lactate	Acetate	Propionate	Formate	Other
Wood	Activated carbon2**	0	40.5	0	59.5	0
	Activated carbon1**	0	3.45	1.05	5.06	90.4
	Biochar Engineering Charcoal**	0	21.6	1.58	18.2	58.6
	Cowboy Charcoal**	0.82	1.26	0.99	1.21	95.7
	Wicked Good Charcoal**	0	32.1	1.91	1.09	64.9
	Pine bark	0	1.86	0	19.9	78.3
	Mulch	0	45	22.2	24.5	8.32
Agricultural residue	Corn stover1	0	2.7	0	30.7	66.6
	Corn stover2	0	1.31	0	11	87.7
	Corn cob2	0	3.21	1.14	8.98	86.7
	Switchgrass	0	2.83	0	21.6	75.5
	Wheat straw	0	2.31	0	22.3	75.3
	Hop bract	0	0	0	0	100
	Corn cob1	0	1.44	0	30.7	67.9
	Cotton seed	0	1.7	0	25.3	73
Cocoa husk	0.53	33	8.09	3.48	54.9	
Manure	Poultry manure1	0	43	0	57	0
	Mushroom soil2	0	40.1	0	59.9	0
	Mushroom soil3**	0	5.58	0	29.9	64.5
	Poultry manure2*	-	-	-	-	-
	Poultry manure3**	0	23.9	0	76.1	0
	Mushroom soil1	0	37.6	0	62.4	0
	Cow manure	0	0.63	0	1.7	97.7
control	River water	0	0	0	0	0

The other carbon was the difference between DOC and OAs. * after biochar name indicates no data was available for high-T biochar.

Table S2.2 Summary of pH and alkalinity values of aqueous solutions mixed with low-T and high-T biochars.

Group	Raw material	pH		Alkalinity (as CaCO ₃ mg L ⁻¹)	
		Low T ^a	High T ^b	Low T ^a	High T ^b
Wood	Activated carbon2 ^{d**}	-	10.1	-	56.3
	Activated carbon1 ^{d**}	-	10.1	-	63.6
	Biochar Engineering	-	8.75	-	-
	Charcoal ^{d**}	-	-	-	95.1
	Cowboy Charcoal ^{d**}	-	8.25	-	69
	Wicked Good	-	8.81	-	-
	Charcoal**	-	-	-	76.9
	Pine bark	7.59	8.4	82.8	69.7
	Mulch	7.11	8.73	88	68.7
Agricultural residue	Corn stover1	7.93	9.79	157	274
	Corn stover2	9.82	10.1	197	562
	Corn cob2	8.78	9.3	133	222
	Switchgrass	8.36	9.79	102	150
	Wheat straw	9.02	9.78	133	274
	Hop bract	7.81	7.65	78.9	52.9
	Corn cob1	9.16	9.56	131	294
	Cotton seed	9.18	9.46	166	324
	Cocoa husk	9.89	9.98	462	408
Manure	Poultry manure1	7.28	9.49	203	90.5
	Mushroom soil2	9.1	9.75	133	60.2
	Mushroom soil3**	-	10.5	-	406
	Poultry manure2*	9.53	-	277	-
	Poultry manure3**	-	10.5	-	198
	Mushroom soil1	9.05	11	159	89.1
	Cow manure	9.38	10.1	133	205
Control	River water	7.8	-	44.1	-

^a Low-T biochars were produced at 300 °C

^b high-T biochars were produced at 600 °C, except ^c 700 °C and ^d products from Sigma; Numbers after name, different sources

- no sample at this temperature

* indicates no data was available for high-T biochar

** indicates no data was available for low-T biochar.

Table S2.3 Summary of concentrations of acetate, formate and DOC released by activated carbon, wood, switchgrass, poultry manure, and mushroom soil biochars during sequential leaching.

	Washing steps	Acetate	Formate	DOC
	Unit	C mmol L ⁻¹	C mmol L ⁻¹	C mmol L ⁻¹
Activated Carbon	1	0.0066	0.0035	0.088
	2	0.0032	0.0027	0.11
	3	0.0021	0.0021	0.052
	4	0.0022	0.0015	0.065
	5	0.0026	0.0035	0.070
	6	0.0020	0.0023	0.054
Cowboy Charcoal	1	0.37	0.012	0.62
	2	0.18	0.0046	0.27
	3	0.096	0.0026	0.17
	4	0.069	0.0024	0.16
	5	0.17	0.0076	0.25
	6	0.047	0.0021	0.12
Low-T switchgrass biochar	1	1.3	0.095	2.1
	2	0.58	0.043	1.1
	3	0.33	0.022	0.73
	4	0.23	0.016	0.57
	5	0.61	0.049	1.5
	6	0.24	0.017	0.69
High-T switchgrass biochar	1	0.0041	0.011	0.28
	2	0.003	0.003	0.12
	3	0.0023	0.0025	0.071
	4	0.0022	0.002	0.067
	5	0.0058	0.0092	0.10
	6	0.0026	0.0028	0.064
Low-T poultry manure biochar	1	0.87	0.096	15
	2	0.16	0.019	13
	3	0.049	0.0070	7.8
	4	0.035	0.0052	4.1
	5	0.072	0.017	2.9
	6	0.015	0.0044	1.6
	7	0.0092	0.0029	1.1
	8	0.007	0.0024	0.86
	9	0.0058	0.0023	0.71

	10	0.0045	0.0024	0.87
	11	0.0003	0.0005	0.43
	12	<0.0003	0.0003	0.34
High-T poultry manure biochar	1	<0.0003	<0.0003	0.16
	2	<0.0003	<0.0003	<0.04
	3	<0.0003	<0.0003	<0.04
	4	<0.0003	<0.0003	<0.04
	5	0.0020	0.0016	0.056
	6	<0.0003	0.0006	<0.04
	7	0.0012	0.0006	<0.04
	8	0.0009	<0.0003	<0.04
	9	0.0007	0.0003	<0.04
	10	0.0018	0.0015	<0.04
	11	0.0011	0.00055	0.041
	12	0.00084	<0.0003	<0.04
Low-T mushroom soil biochar	1	11	0.64	34
	2	1.1	0.086	9.1
	3	0.16	0.017	2.2
	4	0.055	0.013	2.0
	5	0.14	0.042	3.1
	6	0.041	0.013	1.3
	7	0.027	0.0088	1.4
	8	0.027	0.0099	1.3
	9	0.023	0.0078	1.0
	10	0.0039	0.044	1.9
	11	0.026	0.013	1.2
	12	<0.0003	0.0075	0.91
High-T mushroom soil biochar	1	0.039	0.036	0.11
	2	<0.0003	<0.0003	<0.04
	3	<0.0003	<0.0003	<0.04
	4	<0.0003	<0.0003	0.043
	5	<0.0003	0.0034	0.045
	6	<0.0003	0.0012	<0.04
	7	0.0017	0.0006	<0.04
	8	0.0012	0.0004	<0.04
	9	0.0007	0.0006	<0.04
	10	0.0051	0.002	0.049
	11	0.0014	0.0006	<0.04
	12	<0.0003	0.0004	<0.04

Appendix B: *Summary of Data Presented in Chapter 3*

Table S3.1 Summary of THg concentrations and % Hg removal from aqueous solution in batch tests containing biochar and river water spiked with Hg.

Group	Raw material	THg (ng L ⁻¹)		Removal %	
		Low T ^a	High T ^b	Low T ^a	High T ^b
Wood	Activated carbon2 ^{d**}	-	4.38	-	99.9
	Activated carbon1 ^{d**}	-	55.6	-	99.4
	Biochar Engineering Charcoal ^{d**}	-	21	-	99.7
	Cowboy Charcoal ^{d**}	-	297	-	97.0
	Wicked Good Charcoal ^{**}	-	346	-	96.5
	Pine bark	1440	409	81.3	95.8
	Mulch	5850	333	32.8	96.6
	Agricultural residue	Corn stover1	521	21.2	94
Corn stover2		963	86.8	89.9	98.8
Corn cob2		1590	521	79.4	94.7
Switchgrass		1890	317	78.3	96.8
Wheat straw		2220	46.7	76.8	99.4
Hop bract		1830	1500	76.3	84.6
Corn cob1		3100	234	64.4	96.8
Cotton seed		3800	1330	60.2	81.8
Cocoa husk		4640	4910	39.9	32.7
Manure	Poultry manure1	194	72.7	98	99.2
	Mushroom soil2	422	21.7	95.6	99.8
	Mushroom soil3 ^{**}	-	225	-	97.1
	Poultry manure2 [*]	484	-	94.9	-
	Poultry manure3 ^{**}	-	859	-	88.9
	Mushroom soil1	292	1620	96.6	81.4
	Cow manure	1340	867	84.6	90.0
Control	River water	6940		29	

^a Low-T biochars were produced at 300 °C

^b high-T biochars were produced at 600 °C, except ^c 700 °C and ^d products from Sigma; Numbers after name, different sources

- no sample at this temperature

* indicates no data was available for high-T biochar

** indicates no data was available for low-T biochar.

Table S3.2 Summary of concentrations of SO_4^{2-} in river water versus concentrations in batch mixtures containing river water and biochar.

Group	Raw material	SO_4^{2-} (mg L ⁻¹)	
		Low T ^a	High T ^b
Wood	Activated carbon2 ^{d**}	-	16.5
	Activated carbon1 ^{d**}	-	15.1
	Biochar Engineering Charcoal ^{d**}	-	10.2
	Cowboy Charcoal ^{d**}	-	5.99
	Wicked Good Charcoal ^{**}	-	11.3
	Pine bark	11	7.11
	Mulch	9.72	5.96
	Agricultural residue	Corn stover1	19.1
Corn stover2		12.5	38.1
Corn cob2		10.2	6
Switchgrass		13.4	8.94
Wheat straw		61.8	78
Hop bract		9.54	5.91
Corn cob1		10.3	7.54
Cotton seed		11	7.46
Cocoa husk		50.6	42.7
Manure	Poultry manure1	101	96.4
	Mushroom soil2	987	914
	Mushroom soil3 ^{**}	-	72.1
	Poultry manure2 [*]	131	-
	Poultry manure3 ^{**}	-	415
	Mushroom soil1	1000	709
	Cow manure	12	10.2
Control	River water	5.96	

^a Low-T biochars were produced at 300 °C

^b high-T biochars were produced at 600 °C, except ^c 700 °C and ^d products from Sigma; Numbers after name, different sources

- no sample at this temperature

* indicates no data was available for high-T biochar

** indicates no data was available for low-T biochar.

Appendix C: *Supplementary Information in
Chapter 4*

Pyrosequencing Analysis. 16S rRNA polymerase chain reaction (PCR) primers 515/806 (for bacteria and archaea) were applied in a single-step 30 cycle PCR using HotStarTaq Plus Master Mix Kit (Valencia, CA), under the following conditions: 94 °C for 3 min, followed by 28 cycles of 94 °C for 30 seconds; 53 °C for 40 seconds and 72 °C for 1 minute; after which a final elongation step at 72 °C for 5 minutes was performed. Following PCR, all barcoded amplicon products from the different samples were mixed in equal concentrations and purified using Agencourt Ampure beads (Agencourt Bioscience Corporation, MA). A Roche 454 FLX titanium instrument and reagents were used for sequencing.

The sequence data derived from the sequencing process was processed using a proprietary analysis pipeline (www.mrdnalab.com), MR DNA, Shallowater, TX). Sequences are depleted of barcodes and primers then short sequences <200bp are removed, sequences with ambiguous base calls removed, and sequences with homopolymer runs exceeding 6bp removed. Sequences are then denoised and operational taxonomic units were defined as clustering at 3% divergence (97% similarity) followed by removal of singleton sequences and chimeras (Capone et al., 2011; Dowd et al., 2008a; Dowd et al., 2008b; Edgar, 2010; Eren et al., 2011; Swanson et al., 2011). Final OTUs were taxonomically classified into genus/species using BLASTn against a curated database derived from GreenGenes, RDPII and NCBI (DeSantis et al. (2006), <http://rdp.cme.msu.edu>).

Solid Phase Analysis. Solid-phase C/S content of the sediment and biochar samples was measured using a resistance furnace (Eltra CS-2000). The elemental composition of the sediment and biochars were obtained by digestion following EPA Method 3052 (multi-

acid digest with microwave assist) and analyzed by inductively coupled plasma-optical emission spectrometry (ICP-OES) and inductively coupled plasma-mass spectrometry (ICP-MS). The analysis of total organic carbon (TOC) of the sediment followed these steps: 1) 0.5 g sediment was digested with 40 mL of 10% H₂SO₄ for 30 minutes; 2) the extract was passed through a glass fibre filter; 3) the filtrate was analyzed by a Skalar segmented flow analyzer using Standard Methods 5310C to derive the value for total organic carbon of the sediment.

Table S4.1. Potential Hg methylators identified by Oak Ridge National Laboratory.

SRB	Methanogen	FeRB	Fermenters	Other
<i>Desulfovibrio desulfuricans</i>	<i>Methanoregula boonei</i>	<i>Geobacter sulfurreducens</i>	<i>Syntrophus aciditrophicus</i>	<i>Syntrophorhabdus aromaticivorans</i>
<i>Desulfovibrio aespoeensis</i>	<i>Methanoregula formicicum</i>	<i>Geobacter metallireducens</i>	<i>Clostridium termitidis</i>	<i>Deferrisoma camini</i>
<i>Desulfovibrio africanus</i>	<i>Methanosphaerula palustris</i>	<i>Geobacter sp.</i>		<i>Syntrophobotulus glycolicus</i>
<i>Desulfovibrio oxyclinae</i>	<i>Methanofollis liminatans</i>	<i>Geobacter sp.</i>		<i>Dehalobacter restrictus</i>
<i>Desulfovibrio longus</i>	<i>Methanospirillum hungatei</i>	<i>Geobacter uraniireducens</i>		<i>Dehalobacter sp.</i>
<i>Desulfovibrio putealis</i>	<i>Methanocorpusculum bavaricum</i>	<i>Geobacter bemidjensis bem</i>		<i>Ethanoligenens harbinense</i>
<i>Desulfovibrio inopinatus</i>	<i>Methanolobus tindarius</i>	<i>Geobacter bremensis</i>		<i>Acetivibrio cellulolyticus</i>
<i>Desulfomicrobium baculatum</i>	<i>Methanomethylovorans hollandica</i>	<i>Geopsychrobacter electrodiphilus</i>		<i>Dethiobacter alkaliphilus</i>
<i>Desulfomicrobium escambiense</i>	<i>Methanolobus psychrophilus</i>			<i>Acetonema longum</i>
<i>Desulfobulbus propionicus</i>	<i>Methanocella arvoryzae</i>			<i>Dehalococcoides mccartyi</i>
<i>Desulfobulbus mediterraneus</i>	<i>Methanocella paludicola</i>			<i>Chrysiogenes arsenatis</i>
<i>Desulfobulbus japonicus</i>	<i>Methanomassiliicoccus luminyensis</i>			<i>Atribacteria bacterium</i>
<i>Desulfospira joergensenii</i>				
<i>Desulfotignum phosphitoxidans</i>				
<i>Desulfotignum balticum</i>				
<i>Desulfobacterium sp.</i>				
<i>Desulfonatronospira thiodismutans</i>				
<i>Desulfonatronum lacustre</i>				
<i>Desulfomonile tiedjei</i>				
<i>Desulfitobacterium dehalogenans</i>				
<i>Desulfitobacterium dichloroeliminans</i>				
<i>Desulfitobacterium metallireducens</i>				
<i>Desulfitobacterium sp.</i>				
<i>Desulfosporosinus acidiphilus</i>				
<i>Desulfosporosinus orientis</i>				
<i>Desulfosporosinus sp.</i>				
<i>Desulfosporosinus youngiae</i>				

Table S4.2. Elemental composition of sediment ($\mu\text{g g}^{-1}$)

Parameter	Concentration
Hg	187
S	300
TOC	17600
TIC	1700
Fe	16000
Cu	150
Mn	230
Ca	2000
Al	5000
Mg	1200
P	360
Zn	80
K	760
Na	35
Ni	8.2
Pb	21
As	2.2
Cd	0.43
Cr	59
V	16
Se	< 0.7
Co	6.5
Mo	0.6
Sr	11
Ti	94
Ba	65

TOC: total organic carbon

TIC: total inorganic carbon

Table S4.3. Elemental composition of low-T and high-T switchgrass biochars

Element	Low T	High T
C, %	70.2±1.7	94.5±1.4
S, %	0.10±0.01	0.55±0.02
Ag, µg g ⁻¹	0.06	0.87
Al, µg g ⁻¹	160	240
Ar, µg g ⁻¹	< 0.5	< 0.5
Ba, µg g ⁻¹	22	37
Be, µg g ⁻¹	< 0.02	< 0.02
Bi, µg g ⁻¹	< 0.09	< 0.09
Ca, µg g ⁻¹	9200	14000
Cd, µg g ⁻¹	0.03	< 0.02
Co, µg g ⁻¹	0.16	0.21
Cr, µg g ⁻¹	3.4	5.4
Cu, µg g ⁻¹	7.2	12
Fe, µg g ⁻¹	2100	1700
K, µg g ⁻¹	9300	11000
Li, µg g ⁻¹	< 2	< 2
Mg, µg g ⁻¹	2100	3500
Mn, µg g ⁻¹	210	260
Mo, µg g ⁻¹	0.2	0.4
Na, µg g ⁻¹	18	29
Ni, µg g ⁻¹	0.6	1.2
P, µg g ⁻¹	930	1600
Pb, µg g ⁻¹	0.47	1.2
Sb, µg g ⁻¹	< 0.8	< 0.8
Se, µg g ⁻¹	< 0.7	< 0.7
Sn, µg g ⁻¹	7.0	130
Sr, µg g ⁻¹	18	30
Ti, µg g ⁻¹	11	27
Tl, µg g ⁻¹	< 0.02	< 0.02
U, µg g ⁻¹	0.008	0.012
V, µg g ⁻¹	< 1	< 1
Y, µg g ⁻¹	0.38	0.39
Zn, µg g ⁻¹	23	35

Table S4.4. Chemical composition of river water employed in the study

Parameter	Value	Unit	Parameter	Value	Unit
THg	< 5	ng L ⁻¹	Be	<0.08	µg L ⁻¹
MeHg	<0.02	ng L ⁻¹	B	100	µg L ⁻¹
pH	7.8		S	2.9	mg L ⁻¹
Alkalinity (as CaCO ₃)	46	mg L ⁻¹	P	<100	µg L ⁻¹
DOC	<0.5	mg L ⁻¹	Ti	<0.50	µg L ⁻¹
Lactate	<0.01	mg L ⁻¹	V	0.38	µg L ⁻¹
Acetate	<0.01	mg L ⁻¹	Cr	<0.30	µg L ⁻¹
Propionate	<0.01	mg L ⁻¹	Mn	<0.50	µg L ⁻¹
Formate	<0.01	mg L ⁻¹	Fe	22	µg L ⁻¹
F ⁻	0.07	mg L ⁻¹	Co	<0.20	µg L ⁻¹
Cl ⁻	5.7	mg L ⁻¹	Ni	<0.50	µg L ⁻¹
NO ₂ ⁻	<0.01	mg L ⁻¹	Cu	<0.50	µg L ⁻¹
Br ⁻	<0.01	mg L ⁻¹	Zn	1.0	µg L ⁻¹
NO ₃ ⁻	3.9	mg L ⁻¹	As	0.3	µg L ⁻¹
SO ₄ ²⁻	7.6	mg L ⁻¹	Se	<1	µg L ⁻¹
Al	0.09	mg L ⁻¹	Sr	69	µg L ⁻¹
Ca	17	mg L ⁻¹	Mo	0.33	µg L ⁻¹
K	0.79	mg L ⁻¹	Ag	<0.15	µg L ⁻¹
Mg	6.8	mg L ⁻¹	Cd	0.10	µg L ⁻¹
Na	3.5	mg L ⁻¹	Sn	<1.0	µg L ⁻¹
Si	4.3	mg L ⁻¹	Sb	0.19	µg L ⁻¹
NH ₃ -N	<0.01	mg L ⁻¹	Ba	27	µg L ⁻¹
PO ₄ -P	<0.02	mg L ⁻¹	Tl	0.03	µg L ⁻¹
Li	2.8	µg L ⁻¹	Pb	0.09	µg L ⁻¹

Table S4.5. EXAFS analysis of Hg L_{III}-edge

Sample	Model	Path	CN	R (Å)	S ₀ ²	σ ² (Å ²)	R-factor
High-T biochar	β-HgS	Hg-S	3.90 (±1.11)	2.50 (±0.03)	0.718 ^a	0.009 ^a	0.02
HgO		Hg-O	2	2.05	0.962 (±0.126)	0.004 (±0.001)	0.009
α-HgS		Hg-S	2	2.37	0.841 (±0.123)	0.005 (±0.001)	0.015
β-HgS		Hg-S	4	2.52	0.718 (±0.035)	0.009 (±0.0007)	0.0008

CN = coordination number; R = modeled bond length; S₀² = amplitude reduction factor, σ² = mean-square radial displacement; R-factor = fitting statistic. ^a values obtained from reference materials.

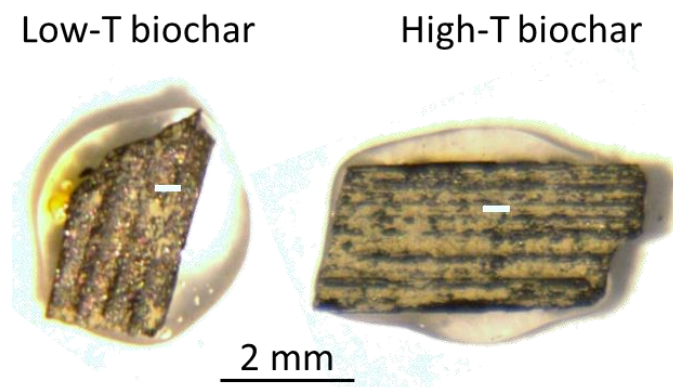


Figure S4.1. Photos of low-T and high-T biochar particles for confocal X-ray fluorescence imaging analysis. The white bars on the particle indicate the imaging area ($400 \times 60 \mu\text{m}^2$ or $0.4 \times 0.06 \text{ mm}^2$, respectively). The imaging depth is $250 \mu\text{m}$.

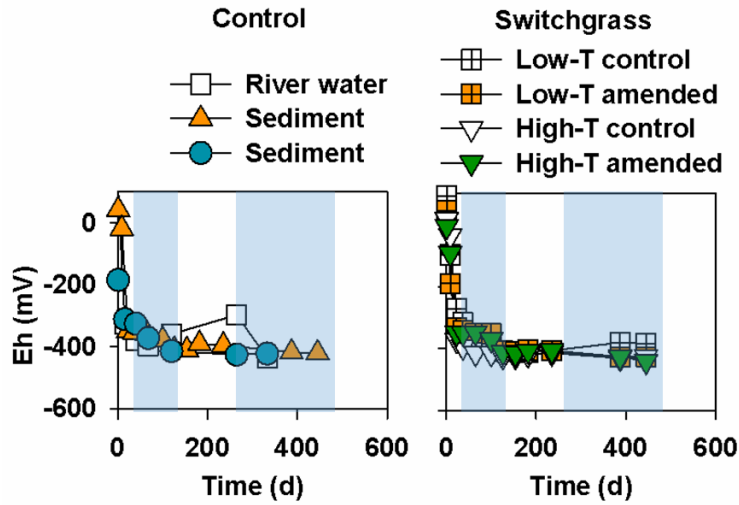


Figure S4.2. Eh values of controls and amended systems vs. time. The blue bars indicate two stages of MeHg production: a combined Fe and SO_4^{2-} reduction period (first) and a methanogenic period (second).

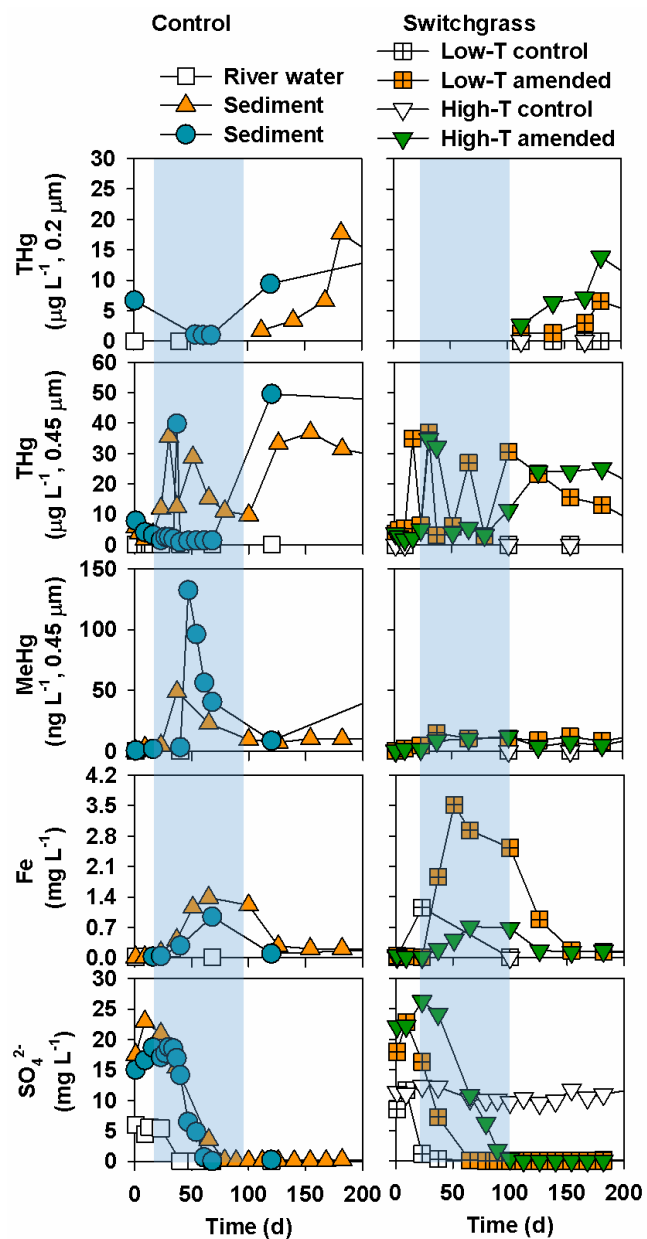


Figure S4.3. Concentrations of 0.2- and 0.45-µm filtered THg, 0.45-µm filtered MeHg, Fe, and SO₄²⁻ in aqueous solutions of controls and amended systems vs. time (first 200 days). The blue bar indicates the combined Fe and SO₄²⁻ reduction stage of MeHg production.

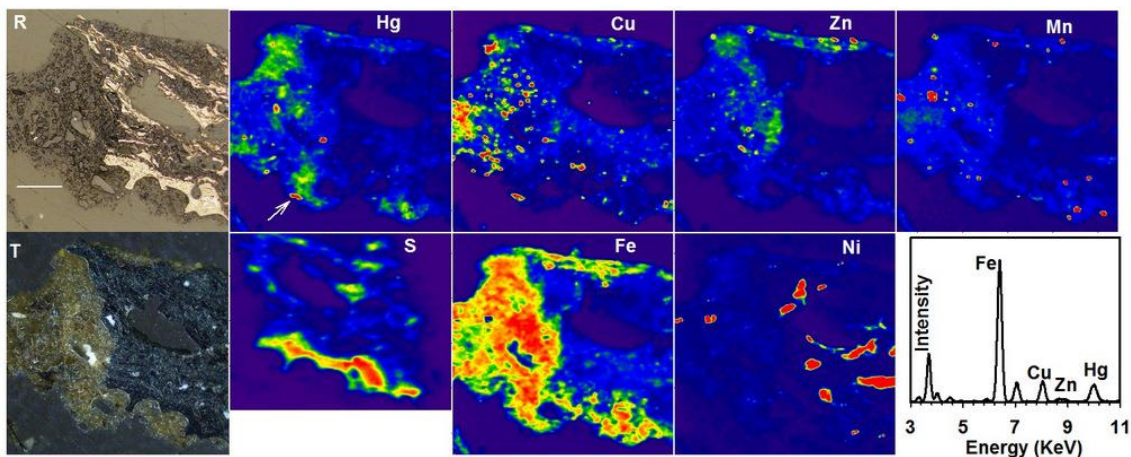


Figure S4.4. Micro-XRF Hg L_{α} , Fe K_{α} , Cu K_{α} , Zn K_{α} , Mn K_{α} , and Ni K_{α} maps of grains from the low-T switchgrass biochar amended system on day 235. R and T represent pictures taken in reflection and transmission mode, respectively. The white bar represents 100 μm . The arrow in the Hg map indicates the position where XRF spectra were collected. The maps were collected at Sector 13-ID-E at the Advanced Photon Source, Argonne National Laboratory.

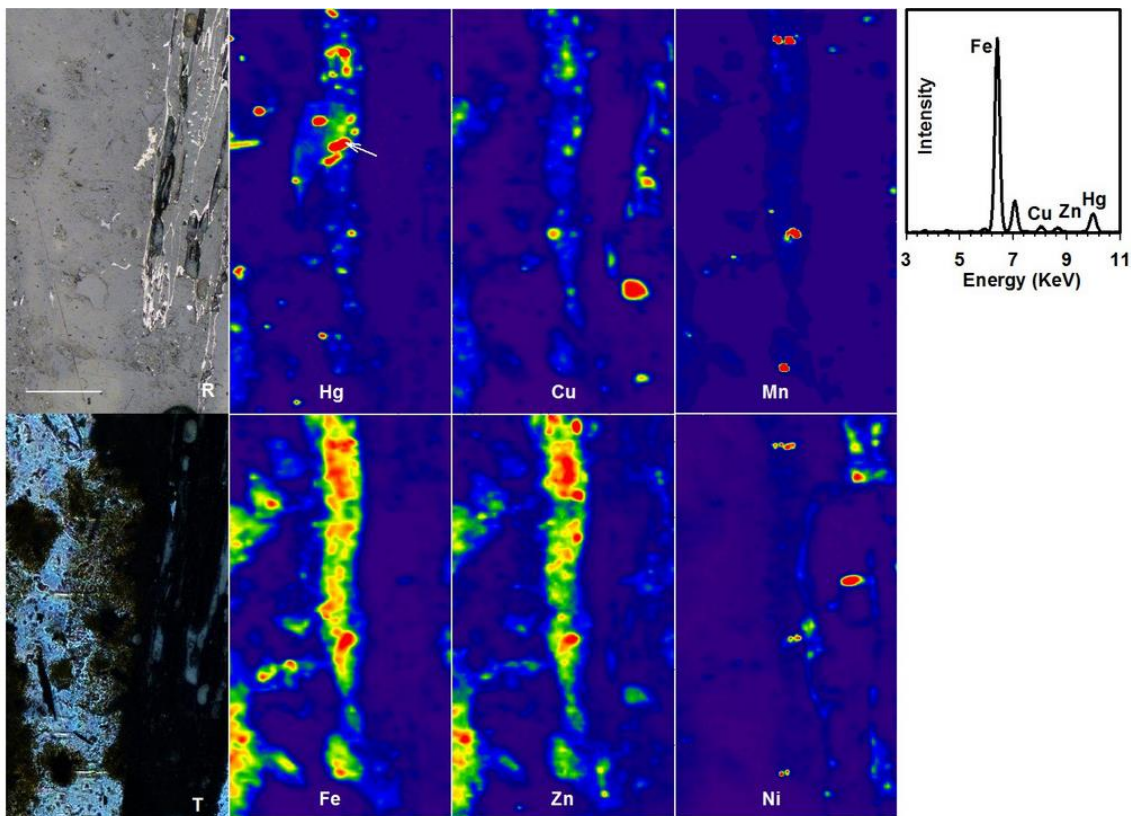


Figure S4.5. Micro-XRF Hg L_{α} , Fe K_{α} , Cu K_{α} , Zn K_{α} , Mn K_{α} , and Ni K_{α} maps of grains from high-T biochar amended system on day 387. R and T represent pictures taken in reflection and transmission mode, respectively. The white bar represents 100 μm . The arrow in the Hg map indicates the position where XRF spectra and Hg EXAFS data were collected. The maps were collected at Sector 13-ID-E at the Advanced Photon Source, Argonne National Laboratory.

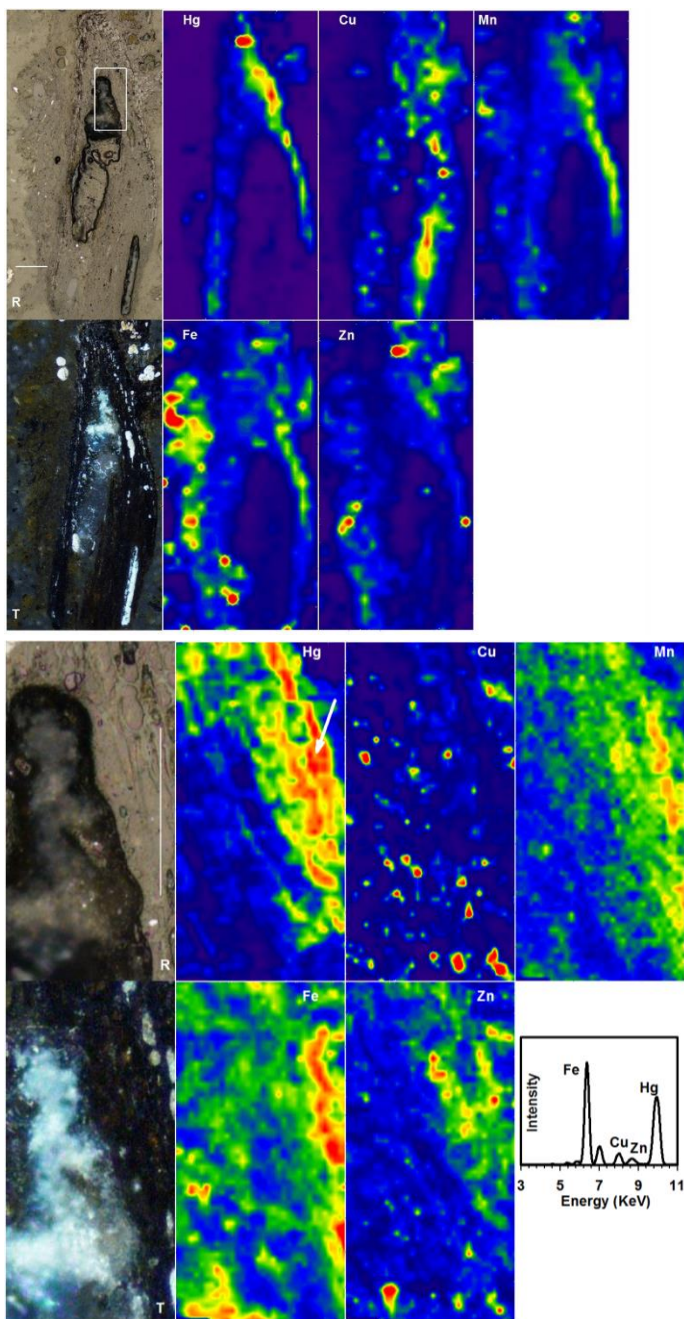


Figure S4.6. Micro-XRF Hg L_{α} , Fe K_{α} , Cu K_{α} , Zn K_{α} , and Mn K_{α} maps of grains from high-T switchgrass biochar amended system on day 387. R and T represent pictures taken in reflection and transmission mode, respectively. The white bar represents 100 μm . The area of the lower $\mu\text{-XRF}$ maps is indicated by the white box in the microscope picture of the upper $\mu\text{-XRF}$ maps. The arrow in the Hg map indicates the position where XRF spectra were collected. The maps were collected at Sector 20-ID-B at the Advanced Photon Source, Argonne National Laboratory.

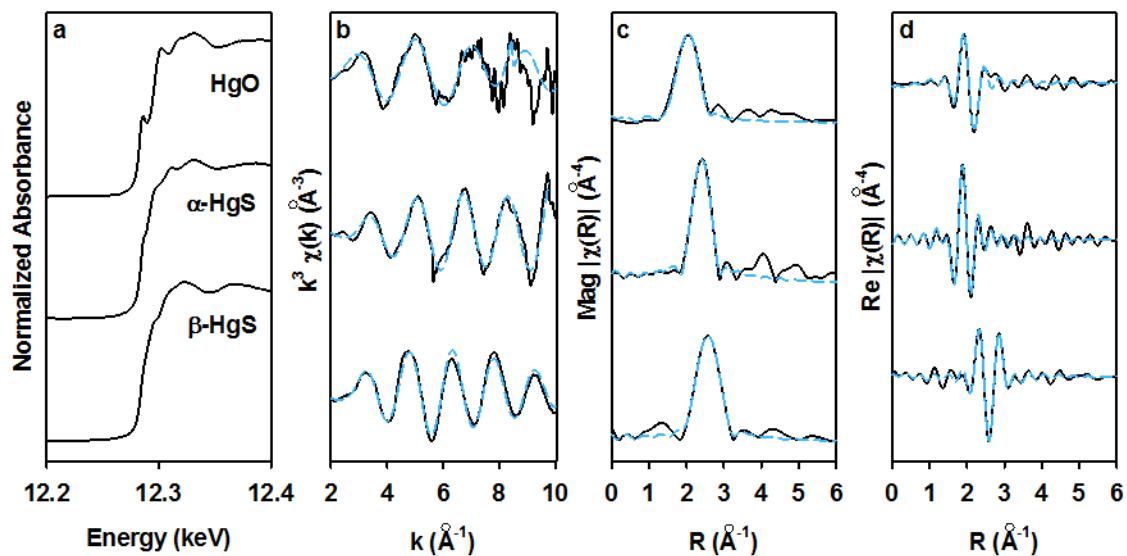
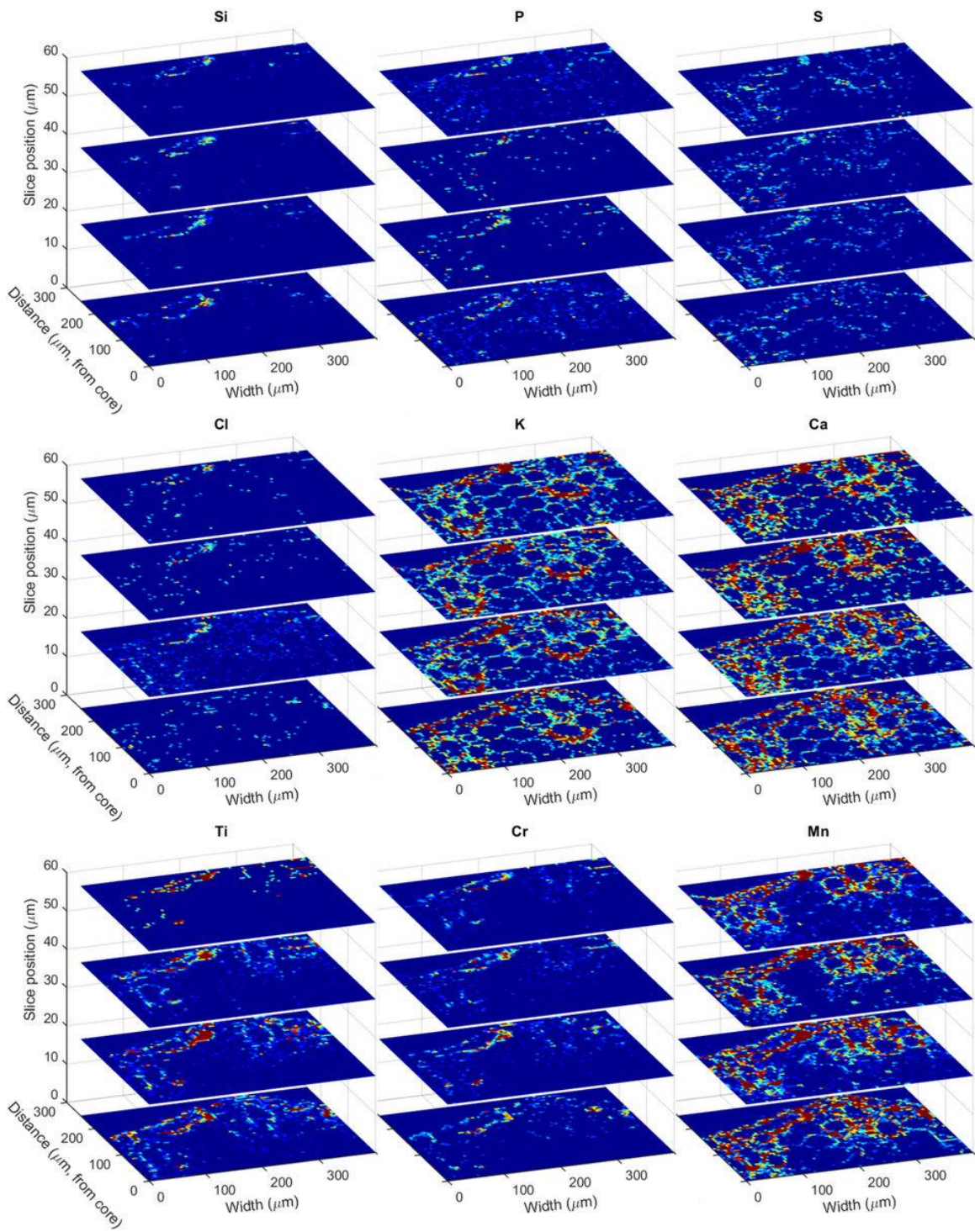


Figure S4.7. ^a Edge-step normalized Hg L_{III}-edge XANES spectra of Hg reference materials (HgO, mercury oxide; α -HgS, cinnabar; β -HgS, metacinnabar.). ^b k^3 -weighted chi spectra (black solid line) and the best fit data (light-blue dash line). ^c Fourier-transform magnitude spectra and the best fit data. ^d Real part of the Fourier transform and best fit data.



Continued

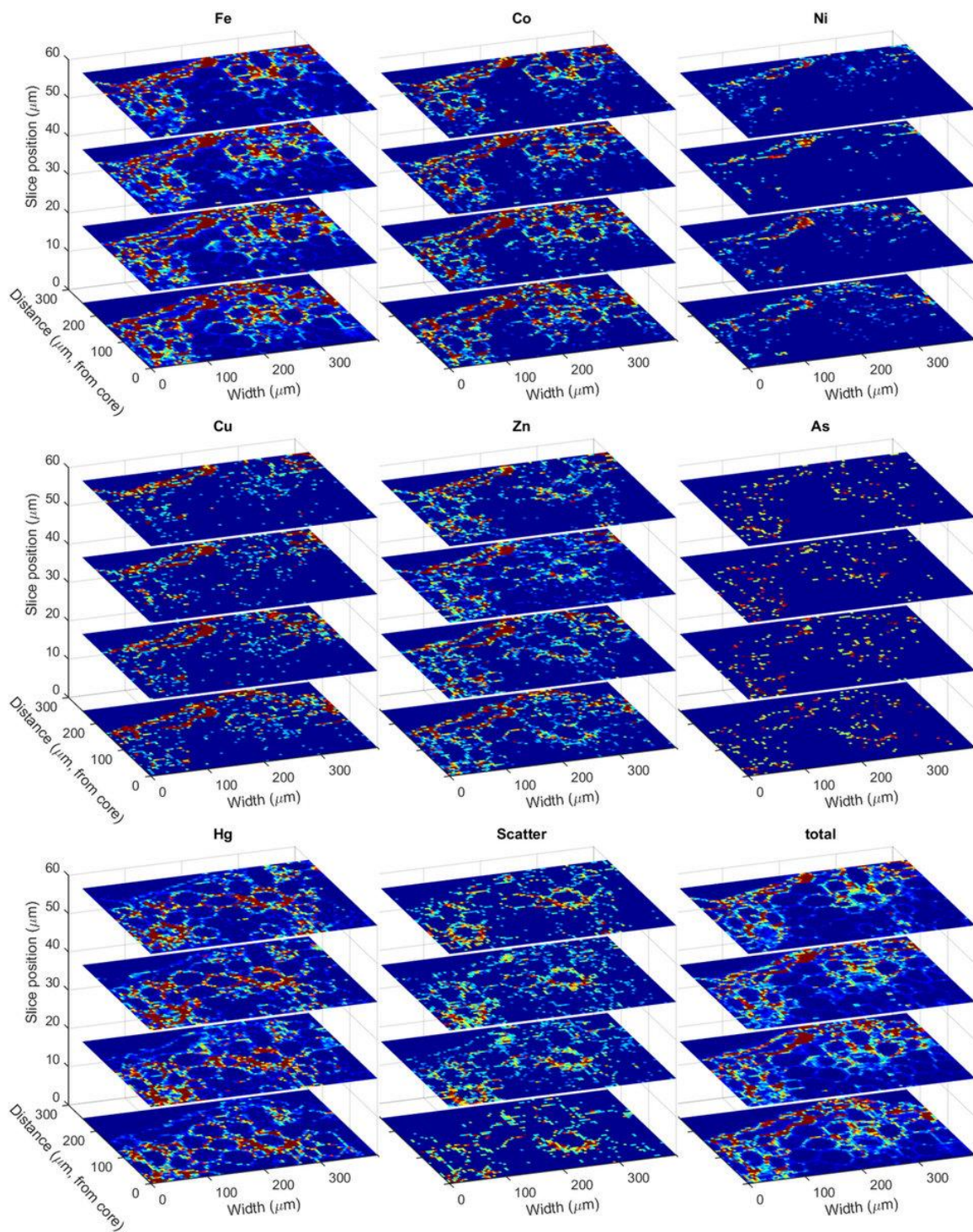
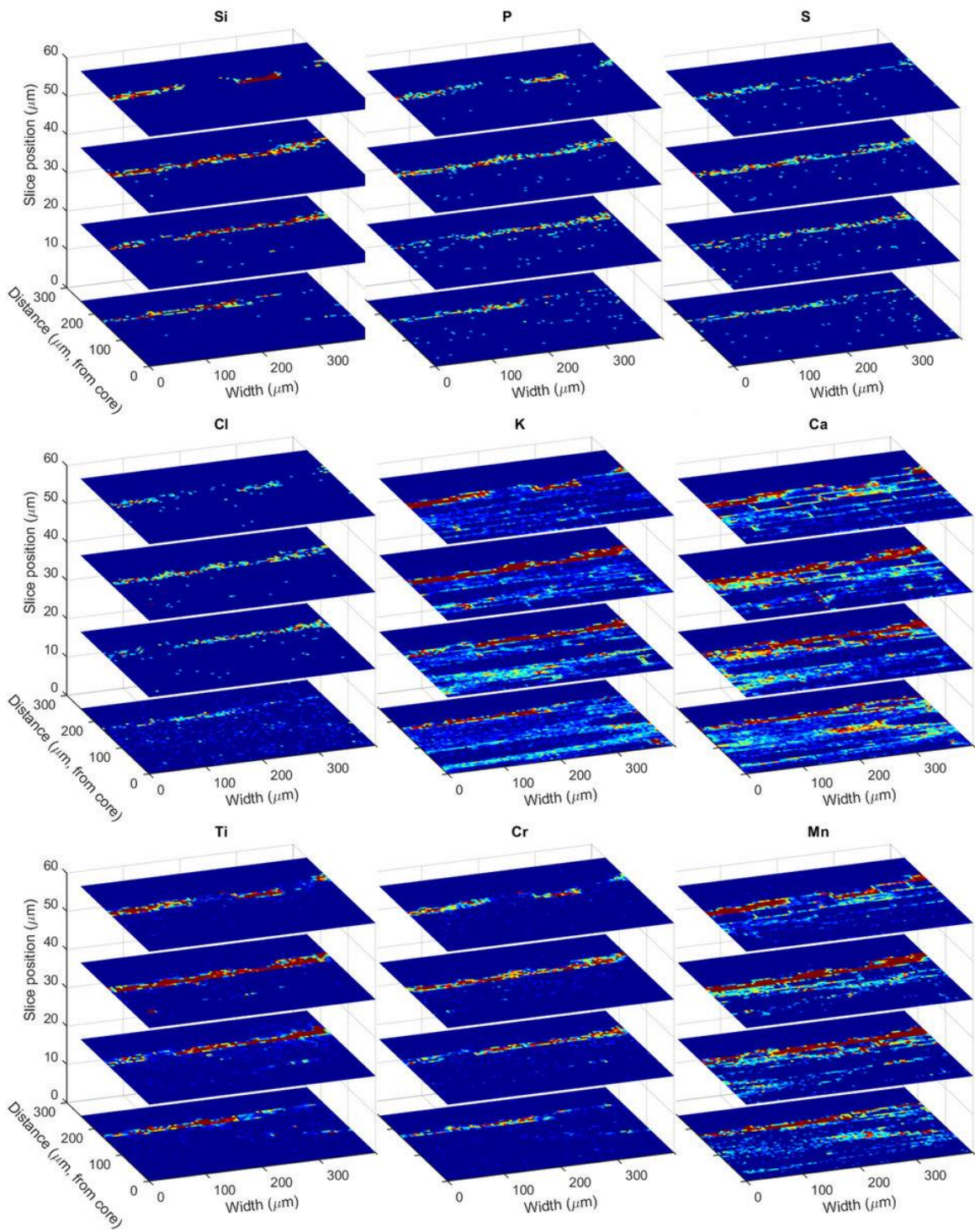


Figure S4.8. Confocal X-ray fluorescence imaging showing the distribution of Si, P, S, Cl, K, Ca, Ti, Cr, Mn, Fe, Co, Ni, Cu, Zn, As, Hg, intensity of scattered incident beam, and intensity sum of all elements in a low-T biochar particle (not physically sectioned) collected from the amended system after 600 days. The particle was analyzed perpendicular to the orientation of the straw.



Continued

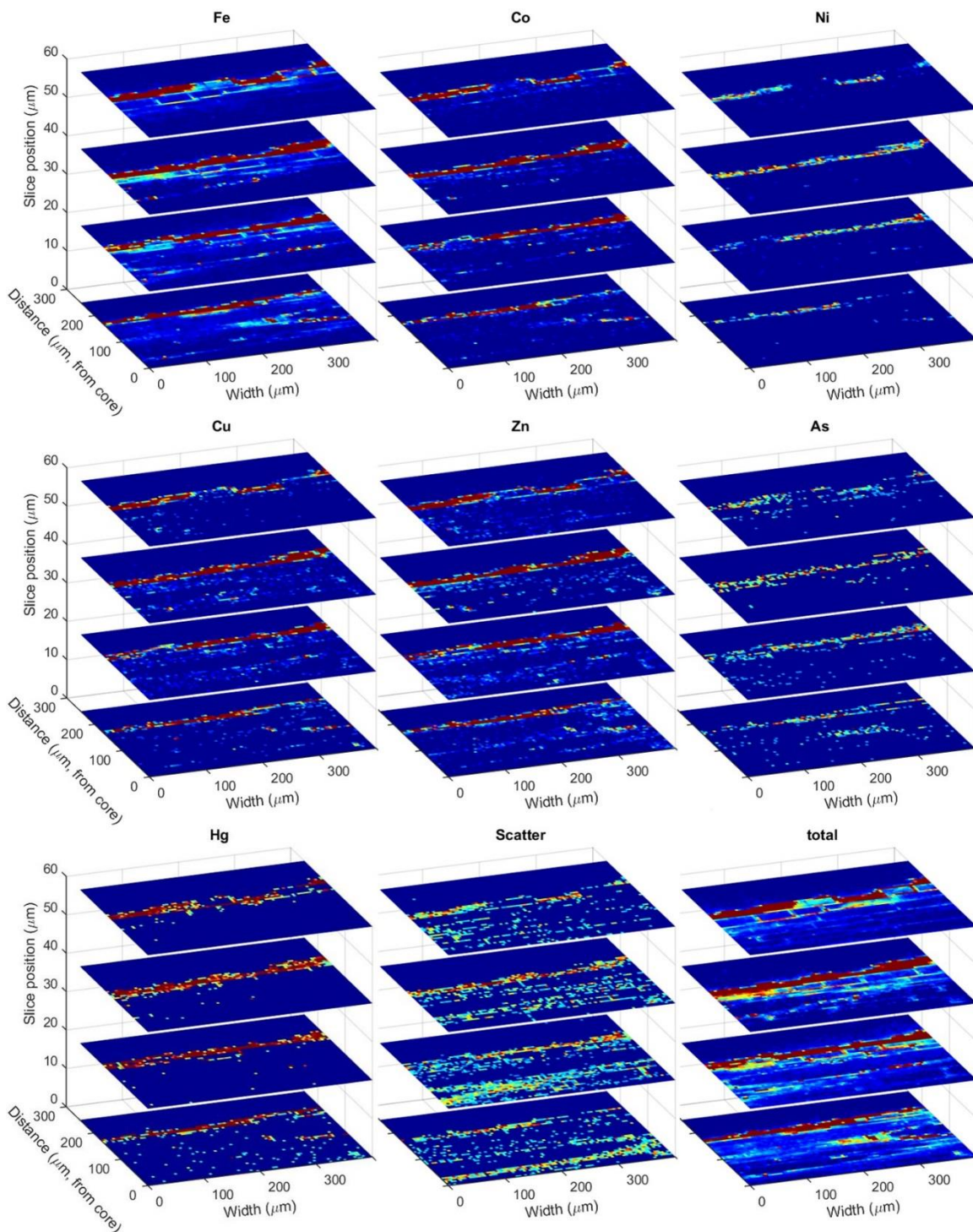


Figure S4.9. Confocal X-ray microfluorescence imaging showing the distribution of Si, P, S, Cl, K, Ca, Ti, Cr, Mn, Fe, Co, Ni, Cu, Zn, As, Hg, intensity of scattered incident beam, and intensity sum of all the elements in a high-T biochar particle (not physically sectioned) collected from the amended system after 600 days. The particle was analyzed perpendicular to the orientation of the straw.

Appendix D: *Supplementary Information in
Chapter 5*

Aqueous Phase Analysis

The pH was determined using an Orion Ross electrode (Thermo Scientific). The performance of the Eh electrode (Orion 9678, Thermo Scientific) was checked against ZoBell's (Nordstrom, 1977) and Light's (Light, 1972) solutions. NH₃-N concentrations were determined using the salicylate spectrophotometric method (Hach Test Method 8155). PO₄-P concentrations were measured using the ascorbic acid spectrophotometric method (Hach Test Method 8048). DOC was determined using an automated wet chemical oxidation method (Aurora 1030, OI Analytical). UV absorbance was measured at 254 nm using a UV-Visible spectrophotometer (Evolution 260, Thermo Scientific). Specific UV absorbance (SUVA) was expressed as the ratio of absorbance at 254 nm per meter to DOC concentrations.

Solid Phase Analysis

Samples were oven-dried at 105 °C for 24 h before analysis for C/S content, elemental composition, and total organic carbon. Each sample was analyzed three times; mean values of the three analyses are reported. Solid-phase C/S content of the sediment and biochar samples was measured using a resistance furnace (Eltra CS-2000). The elemental composition of the sediment and biochars were obtained by digestion following EPA Method 3052 (multi-acid digest with microwave assist) and analyzed by inductively coupled plasma-optical emission spectrometry (ICP-OES) and inductively coupled plasma-mass spectrometry (ICP-MS). The analysis of total organic carbon (TOC) of the sediment followed these steps: 1) 0.5 g sediment was digested with 40 mL of 10% H₂SO₄ for 30 minutes; 2) the extract was passed through a glass fibre filter; 3) the filtrate was

analyzed by a Skalar segmented flow analyzer using Standard Methods 5310C to derive the value for total organic carbon of the sediment.

Table S5.1 Assembled fermenters

king	phylum	class	order	family	genus	strain	reference
Bacteria	Firmicutes	Clostridia	Clostridiales	Eubacteriaceae	Acetobacterium	<i>Acetobacterium sp.</i>	(Bainotti & Nishio, 2000)
Bacteria	Firmicutes	Negativicutes	Selenomonadales	Acidaminococcaceae	Acidaminococcus	<i>Acidaminococcus fermentans</i>	(Chang et al., 2010)
Bacteria	Actinobacteria	Actinobacteria	Acidothermales	Acidothermaceae	Acidothermus	<i>Acidothermus cellulolyticus</i>	(Ransom et al., 2007)
Bacteria	Proteobacteria	Gammaproteobacteria	Pseudomonadales	Moraxellaceae	Acinetobacter	<i>Acinetobacter sp.</i>	(Zhu et al., 2003)
Fungi	Zygomycota	Mucoromycotina	Mucorales	Mucoraceae	Actinomucor	<i>Actinomucor repens</i>	(Lovley et al., 2004)
Bacteria	Proteobacteria	Gammaproteobacteria	Enterobacteriales	Enterobacteriaceae	Enterobacter	<i>Aerobacter aerogenes</i>	(Long & Patrick, 1961)
Bacteria	Proteobacteria	Betaproteobacteria	Burkholderiales	Alcaligenaceae	Alcaligenes	<i>Alcaligenes hydrogenophilus</i>	(Steinbuechel et al., 1983)
Bacteria	Proteobacteria	Gammaproteobacteria	Oceanospirillales	Alcanivoracaceae	Alcanivorax	<i>Alcanivorax borkumensis</i>	(BSI Lab., 2015)
Fungi	Ascomycota	Dothideomycetes	Pleosporales	Pleosporaceae	Alternaria	<i>Alternaria tenuis</i>	(Lovley et al., 2004)
Bacteria	Synergistetes	Synergistia	Synergistales	Synergistaceae	Aminobacterium	<i>Aminobacterium colombiense</i>	(Adams et al., 2006)
Bacteria	Cyanobacteria	Cyanophyceae	Nostocales	Nostocaceae	Trichormus	<i>Anabaena azollae</i>	(Stal & Moezelaar, 1997)
Bacteria	Cyanobacteria	Cyanophyceae	Nostocales	Nostocaceae	Trichormus	<i>Anabaena siarnensis</i>	(Stal & Moezelaar, 1997)
Bacteria	Cyanobacteria	Cyanophyceae	Nostocales	Nostocaceae	Trichormus	<i>Anabaena sp.</i>	(Stal & Moezelaar, 1997)
Bacteria	Cyanobacteria	Cyanophyceae	Nostocales	Nostocaceae	Trichormus	<i>Anabaena variabilis</i>	(BSI Lab., 2015)
Bacteria	Cyanobacteria	Cyanophyceae	Nostocales	Nostocaceae	Anabaenopsis	<i>Anabaenopsis circularis</i>	(Stal & Moezelaar, 1997)
Bacteria	Cyanobacteria	Cyanophyceae	Oscillatoriophyceidae	Chroococcales	Aphanocapsa	<i>Aphanocapsa sp.</i>	(Stal & Moezelaar, 1997)

Bacteria	Actinobacteria	Actinobacteria	Micrococcales	Micrococcaceae	Arthrobacter	<i>Arthrobacter aurescens</i>	(BSI Lab., 2015)
Fungi	Ascomycota	Eurotiomycetes	Eurotiales	Trichocomaceae	Aspergillus	<i>Aspergillus aculeatus</i>	(BSI Lab., 2015)
Fungi	Ascomycota	Eurotiomycetes	Eurotiales	Trichocomaceae	Aspergillus	<i>Aspergillus awamori</i>	(John et al., 2007)
Fungi	Ascomycota	Eurotiomycetes	Eurotiales	Trichocomaceae	Aspergillus	<i>Aspergillus nidulans</i>	(BSI Lab., 2015)
Fungi	Ascomycota	Eurotiomycetes	Eurotiales	Trichocomaceae	Aspergillus	<i>Aspergillus niger</i>	(BSI Lab., 2015)
Bacteria	Proteobacteria	Gammaproteobacteria	Pseudomonadales	Pseudomonadaceae	Azotobacter	<i>Azotobacter chroococcum</i>	(BSI Lab., 2015)
Bacteria	Proteobacteria	Gammaproteobacteria	Pseudomonadales	Pseudomonadaceae	Azotobacter	<i>Azotobacter vinelandii</i>	(BSI Lab., 2015)
Bacteria	Firmicutes	Bacilli	Bacillales	Bacillaceae	Bacillus	<i>Bacillus cereus</i>	(Anto et al., 2006)
Bacteria	Firmicutes	Bacilli	Bacillales	Bacillaceae	Bacillus	<i>Bacillus circulans</i>	(Lovley et al., 2004)
Bacteria	Firmicutes	Bacilli	Bacillales	Bacillaceae	Bacillus	<i>Bacillus licheniformis</i>	(BSI Lab., 2015)
Bacteria	Firmicutes	Bacilli	Bacillales	Bacillaceae	Bacillus	<i>Bacillus mesentericus</i>	(Lovley et al., 2004)
Bacteria	Firmicutes	Bacilli	Bacillales	Bacillaceae	Bacillus	<i>Bacillus polymyxa</i>	(Lovley et al., 2004)
Bacteria	Firmicutes	Bacilli	Bacillales	Bacillaceae	Bacillus	<i>Bacillus pumilus</i>	(Lovley et al., 2004)
Bacteria	Firmicutes	Bacilli	Bacillales	Bacillaceae	Bacillus	<i>Bacillus sp.</i>	(Lovley et al., 2004)
Bacteria	Firmicutes	Bacilli	Bacillales	Bacillaceae	Bacillus	<i>Bacillus subtilis</i>	(Lovley et al., 2004)
Bacteria	Bacteroidetes	Bacteroidetes	Bacteroidales	Bacteroidaceae	Bacteroides	<i>Bacteroides hypermegas</i>	(Lovley et al., 2004)
Bacteria	Firmicutes	Bacilli	Bacillales	Bacillaceae	Bacillus	<i>Bacteroides sp.</i>	(Madigan et al., 2010)
Bacteria	Bacteroidetes	Bacteroidetes	Bacteroidales	Bacteroidaceae	Bacteroides	<i>Bradyrhizobium japonicum</i>	(BSI Lab., 2015)

Bacteria	Proteobacteria	Alphaproteobacteria	Rhizobiales	Bradyrhizobiaceae	Bradyrhizobium	<i>Bradyrhizobium sp.</i>	(BSI Lab., 2015)
Bacteria	Proteobacteria	Betaproteobacteria	Burkholderiales	Burkholderiaceae	Burkholderia	<i>Burkholderia capacia</i>	(BSI Lab., 2015)
Bacteria	Cyanobacteria	Cyanophyceae	Nostocales	Rivulariaceae	Calothrix	<i>Calothrix brevissima</i>	(Stal & Moezelaar, 1997)
Bacteria	Cyanobacteria	Cyanophyceae	Nostocales	Rivulariaceae	Calothrix	<i>Calothrix marchica</i>	(Stal & Moezelaar, 1997)
Bacteria	Cyanobacteria	Cyanophyceae	Nostocales	Rivulariaceae	Calothrix	<i>Calothrix membranacea</i>	(Stal & Moezelaar, 1997)
Bacteria	Actinobacteria	Actinobacteria	Micrococcales	Cellulomonadaceae	Cellulomonas	<i>Cellulomonas fimi</i>	(BSI Lab., 2015)
Bacteria	Cyanobacteria	Cyanophyceae	Stigonematales	Chlorogloeopsaceae	Chlorogloeopsis	<i>Chlorogloeopsis fritschii</i>	(Stal & Moezelaar, 1997)
Bacteria	Cyanobacteria	Cyanophyceae	Stigonematales	Chlorogloeopsaceae	Chlorogloeopsis	<i>Chlorogloeopsis sp.</i>	(Stal & Moezelaar, 1997)
Bacteria	Firmicutes	Clostridia	Clostridiales	Clostridiaceae	Clostridium	<i>Clostridium acetobutylicum</i>	(BSI Lab., 2015)
Bacteria	Firmicutes	Clostridia	Clostridiales	Clostridiaceae	Clostridium	<i>Clostridium beijerinckii</i>	(BSI Lab., 2015)
Bacteria	Firmicutes	Clostridia	Clostridiales	Clostridiaceae	Clostridium	<i>Clostridium butyricum</i>	(Lovley et al., 2004)
Bacteria	Firmicutes	Clostridia	Clostridiales	Clostridiaceae	Clostridium	<i>Clostridium cellulolyticum</i>	(BSI Lab., 2015)
Bacteria	Firmicutes	Clostridia	Clostridiales	Clostridiaceae	Clostridium	<i>Clostridium pasteurianum</i>	(BSI Lab., 2015)
Bacteria	Firmicutes	Clostridia	Clostridiales	Clostridiaceae	Clostridium	<i>Clostridium polymyxa</i>	(Lovley et al., 2004)
Bacteria	Firmicutes	Clostridia	Clostridiales	Clostridiaceae	Clostridium	<i>Clostridium saccharobutyricum</i>	(Lovley et al., 2004)
Bacteria	Firmicutes	Clostridia	Clostridiales	Clostridiaceae	Clostridium	<i>Clostridium saccharobutylicum</i>	(BSI Lab., 2015)
Bacteria	Firmicutes	Clostridia	Clostridiales	Clostridiaceae	Clostridium	<i>Clostridium sporogenes</i>	(Lovley et al., 2004)

Bacteria	Firmicutes	Clostridia	Clostridiales	Clostridiaceae	Clostridium	<i>Clostridium stercorarium</i>	(BSI Lab., 2015)
Bacteria	Firmicutes	Clostridia	Clostridiales	Ruminococcaceae	Ruminiclostridium	<i>Clostridium termitidis</i>	(Hethener et al., 1992)
Bacteria	Firmicutes	Clostridia	Clostridiales	Clostridiaceae	Clostridium	<i>Clostridium thermocellum</i>	(BSI Lab., 2015)
Bacteria	Cyanobacteria	Oscillatoriothycideae	Chroococcales	Chroococcales	Cyanothece	<i>Cyanothece sp.</i>	(Stal & Moezelaar, 1997)
Bacteria	Bacteroidetes	Cytophagia	Cytophagales	Cytophagaceae	Cytophaga	<i>Cytophaga hutchinsonii</i>	(BSI Lab., 2015)
Bacteria	Chloroflexi	Dehalococcoidia	Dehalococcoidales	Dehalococcoidaceae	Dehalococcoides	<i>Dehalococcoides ethenogenes</i>	(BSI Lab., 2015)
Bacteria	Chloroflexi	Dehalococcoidia	Dehalococcoidales	Dehalococcoidaceae	Dehalococcoides	<i>Dehalococcoides sp.</i>	(BSI Lab., 2015)
Bacteria	Proteobacteria	Deltaproteobacteria	Desulfovibrionales	Desulfomicrobiaceae	Desulfomicrobium	<i>Desulfovibrio baculatum</i>	(BSI Lab., 2015)
Bacteria	Proteobacteria	Deltaproteobacteria	Desulfovibrionales	Desulfomicrobiaceae	Desulfomicrobium	<i>Desulfovibrio desulfuricans</i>	(BSI Lab., 2015)
Bacteria	Proteobacteria	Deltaproteobacteria	Desulfovibrionales	Desulfomicrobiaceae	Desulfomicrobium	<i>Desulfovibrio gigas</i>	(BSI Lab., 2015)
Bacteria	Proteobacteria	Deltaproteobacteria	Desulfovibrionales	Desulfomicrobiaceae	Desulfomicrobium	<i>Desulfovibrio vulgaris</i>	(BSI Lab., 2015)
Bacteria	Proteobacteria	Gammaproteobacteria	Enterobacteriales	Enterobacteriaceae	Enterobacter	<i>Enterobacter aerogenes</i>	(Rachman et al., 1997)
Bacteria	Proteobacteria	Gammaproteobacteria	Enterobacteriales	Enterobacteriaceae	Enterobacter	<i>Enterobacter asburiae</i>	(Shin et al., 2007)
Bacteria	Proteobacteria	Gammaproteobacteria	Enterobacteriales	Enterobacteriaceae	Enterobacter	<i>Enterobacter sp.</i>	(Lovley et al., 2004)
Bacteria	Proteobacteria	Gammaproteobacteria	Enterobacteriales	Enterobacteriaceae	Escherichia	<i>Escherichia coli</i>	(Lovley et al., 2004)
Bacteria	Proteobacteria	Gammaproteobacteria	Enterobacteriales	Enterobacteriaceae	Escherichia	<i>Escherichia sp.</i>	(Lovley et al., 2004)
Bacteria	Actinobacteria	Actinobacteria	Frankiales	Frankiaceae	Frankia	<i>Frankia alni</i>	(BSI Lab., 2015)
Bacteria	Cyanobacteria	Nostocales	Microchaetaceae	Microchaete	Microchaete	<i>Fremyella diplosiphon</i>	(Stal & Moezelaar, 1997)

Fungi	Ascomycota	Sordariomycetes	Hypocreales	Nectriaceae	Fusarium	<i>Fusarium oxysporum</i>	(Lovley et al., 2004)
Fungi	Ascomycota	Sordariomycetes	Hypocreales	Nectriaceae	Fusarium	<i>Fusarium solani</i>	(Lovley et al., 2004)
Fungi	Ascomycota	Sordariomycetes	Hypocreales	Nectriaceae	Fusarium	<i>Fusarium sp.</i>	(Lovley et al., 2004)
Bacteria	Firmicutes	Bacilli	Bacillales	Bacillaceae	Geobacillus	<i>Geobacillus stearothermophilus</i>	(BSI Lab., 2015)
Bacteria	Proteobacteria	Deltaproteobacteria	Desulfuromonadales	Geobacteraceae	Geobacter	<i>Geobacter sulfurreducens</i>	(BSI Lab., 2015)
Bacteria	Proteobacteria	Alphaproteobacteria	Rhodospirillales	Acetobacteraceae	Gluconacetobacter	<i>Gluconacetobacter diazotrophicus</i>	(BSI Lab., 2015)
Bacteria	Proteobacteria	Alphaproteobacteria	Rhodospirillales	Acetobacteraceae	Gluconobacter	<i>Gluconobacter oxydans</i>	(BSI Lab., 2015)
Bacteria	Actinobacteria	Actinobacteria	Kineosporiales	Kineosporiaceae	Kineococcus	<i>Kineococcus radiotolerans</i>	(BSI Lab., 2015)
Bacteria	Proteobacteria	Gammaproteobacteria	Enterobacteriales	Enterobacteriaceae	Klebsiella	<i>Klebsiella pneumoniae</i>	(Menzel et al., 1997)
Bacteria	Firmicutes	Bacilli	Lactobacillales	Lactobacillaceae	Lactobacillus	<i>Lactobacillus amylophilus</i>	(John et al., 2007)
Bacteria	Firmicutes	Bacilli	Lactobacillales	Lactobacillaceae	Lactobacillus	<i>Lactobacillus amylovorus</i>	(John et al., 2007)
Bacteria	Firmicutes	Bacilli	Lactobacillales	Lactobacillaceae	Lactobacillus	<i>Lactobacillus casei</i>	(John et al., 2007)
Bacteria	Firmicutes	Bacilli	Lactobacillales	Lactobacillaceae	Lactobacillus	<i>Lactobacillus delbrueckii</i>	(John et al., 2007)
Bacteria	Firmicutes	Bacilli	Lactobacillales	Lactobacillaceae	Lactobacillus	<i>Lactobacillus helveticus</i>	(Norton et al., 1994)
Bacteria	Firmicutes	Bacilli	Lactobacillales	Lactobacillaceae	Lactobacillus	<i>Lactobacillus manihotivorans</i>	(John et al., 2007)
Bacteria	Firmicutes	Bacilli	Lactobacillales	Lactobacillaceae	Lactobacillus	<i>Lactobacillus sp.</i>	(John et al., 2007)
Bacteria	Firmicutes	Bacilli	Lactobacillales	Lactobacillaceae	Lactobacillus	<i>Lactobacillus spp.</i>	(John et al., 2007)

Bacteria	Firmicutes	Bacilli	Lactobacillales	Lactobacillaceae	Lactobacillus	<i>Lactococcus lactis</i>	(John et al., 2007)
Bacteria	Proteobacteria	Deltaproteobacteria	Desulfuromonadales	Pelobacteraceae	Malonomonas	<i>Malonomonas rubra</i>	(Madigan et al., 2010)
Archaea	Euryarchaeota	Methanobacteria	Methanobacteriales	Methanobacteriaceae	Methanothermobacter	<i>Methanobacterium thermoautotrophicum</i>	(BSI Lab., 2015)
Archaea	Euryarchaeota	Methanobacteria	Methanobacteriales	Methanobacteriaceae	Methanobrevibacter	<i>Methanobrevibacter smithii</i>	(BSI Lab., 2015)
Archaea	Euryarchaeota	Methanococci	Methanococcales	Methanocaldococcales	Methanocaldococcus	<i>Methanocaldococcus jannaschii</i>	(BSI Lab., 2015)
Archaea	Euryarchaeota	Methanomicrobia	Methanosarcinales	Methanosarcinaceae	Methanococoides	<i>Methanococoides burtonii</i>	(BSI Lab., 2015)
Archaea	Euryarchaeota	Methanococci	Methanococcales	Methanococcaceae	Methanococcus	<i>Methanococcus aeolicus</i>	(BSI Lab., 2015)
Archaea	Euryarchaeota	Methanococci	Methanococcales	Methanococcaceae	Methanococcus	<i>Methanococcus maripaludis</i>	(BSI Lab., 2015)
Archaea	Euryarchaeota	Methanococci	Methanococcales	Methanococcaceae	Methanococcus	<i>Methanococcus vannieli</i>	(BSI Lab., 2015)
Archaea	Euryarchaeota	Methanomicrobia	Methanomicrobiales	Methanocorpusculaceae	Methanocorpusculum	<i>Methanocorpusculum labreanum</i>	(BSI Lab., 2015)
Archaea	Euryarchaeota	Methanopyri	Methanopyrales	Methanopyraceae	Methanopyrus	<i>Methanopyrus kandleri</i>	(BSI Lab., 2015)
Archaea	Euryarchaeota	Methanomicrobia	Methanosarcinales	Methanosaetaceae	Methanosaeta	<i>Methanosaeta thermophila</i>	(BSI Lab., 2015)
Archaea	Euryarchaeota	Methanomicrobia	Methanosarcinales	Methanosarcinaceae	Methanosarcina	<i>Methanosarcina acetivorans</i>	(BSI Lab., 2015)
Archaea	Euryarchaeota	Methanomicrobia	Methanosarcinales	Methanosarcinaceae	Methanosarcina	<i>Methanosarcina barkeri</i>	(BSI Lab., 2015)
Archaea	Euryarchaeota	Methanomicrobia	Methanosarcinales	Methanosarcinaceae	Methanosarcina	<i>Methanosarcina mazei</i>	(BSI Lab., 2015)
Archaea	Euryarchaeota	Methanobacteria	Methanobacteriales	Methanobacteriaceae	Methanosphaera	<i>Methanosphaera stadtmanae</i>	(BSI Lab., 2015)

Archaea	Euryarchaeota	Methanomicrobia	Methanomicrobiales	Methanospirillaceae	Methanospirillum	<i>Methanospirillum hungatei</i>	(BSI Lab., 2015)
Bacteria	Proteobacteria	Gammaproteobacteria	Methylococcales	Methylococcaceae	Methylococcus	<i>Methylococcus capsulatus</i>	(BSI Lab., 2015)
Bacteria	Cyanobacteria	Nostocales	Microchaetaceae	Microchaete	Microchaete	<i>Microchaete diplosiphon</i>	(Stal & Moezelaar, 1997)
Bacteria	Cyanobacteria	Cyanophyceae	Oscillatoriothricaceae	Oscillatoriales	Coleofasciculus	<i>Microcoleus chthonoplastes</i>	(Stal & Moezelaar, 1997)
Bacteria	Cyanobacteria	Cyanophyceae	Oscillatoriothricaceae	Chroococcales	Microcystis	<i>Microcystis aeruginosa</i>	(Stal & Moezelaar, 1997)
Bacteria	Cyanobacteria	Cyanophyceae	Nostocales	Nostocaceae	Nostoc	<i>Nostoc commune</i>	(Stal & Moezelaar, 1997)
Bacteria	Cyanobacteria	Cyanophyceae	Nostocales	Nostocaceae	Nostoc	<i>Nostoc MAC</i>	(Stal & Moezelaar, 1997)
Bacteria	Cyanobacteria	Cyanophyceae	Nostocales	Nostocaceae	Nostoc	<i>Nostoc purrctiforme</i>	(Stal & Moezelaar, 1997)
Bacteria	Cyanobacteria	Cyanophyceae	Nostocales	Nostocaceae	Nostoc	<i>Nostoc sp.</i>	(BSI Lab., 2015)
Bacteria	Proteobacteria	Alphaproteobacteria	Rhizobiales	Bradyrhizobiaceae	Oligotropha	<i>Oligotropha carboxidovorans</i>	(BSI Lab., 2015)
Bacteria	Cyanobacteria	Cyanophyceae	Oscillatoriothricaceae	Oscillatoriales	Planktothrix	<i>Oscillatoria agardhii</i>	(Stal & Moezelaar, 1997)
Bacteria	Cyanobacteria	Cyanophyceae	Oscillatoriothricaceae	Oscillatoriales	Planktothrix	<i>Oscillatoria limosa</i>	(Stal & Moezelaar, 1997)
Bacteria	Cyanobacteria	Cyanophyceae	Oscillatoriothricaceae	Oscillatoriales	Planktothrix	<i>Oscillatoria sp.</i>	(Stal & Moezelaar, 1997)
Bacteria	Cyanobacteria	Cyanophyceae	Oscillatoriothricaceae	Oscillatoriales	Planktothrix	<i>Oscillatoria terebriformia</i>	(Stal & Moezelaar, 1997)
Bacteria	Proteobacteria	Betaproteobacteria	Burkholderiales	Oxalobacteraceae	Oxalobacter	<i>Oxalobacter formigenes</i>	(Madigan et al., 2010)
Bacteria	Proteobacteria	Gammaproteobacteria	Enterobacteriales	Enterobacteriaceae	Paracolobactrum	<i>Paracolobactrum sp.</i>	(Lovley et al., 2004)
Bacteria	Proteobacteria	Deltaproteobacteria	Desulfuromonadales	Pelobacteraceae	Pelobacter	<i>Pelobacter acetylenicus</i>	(Madigan et al., 2010)
Bacteria	Proteobacteria	Deltaproteobacteria	Desulfuromonadales	Pelobacteraceae	Pelobacter	<i>Pelobacter acidigallici</i>	(Madigan et al., 2010)

Bacteria	Proteobacteria	Deltaproteobacteria	Desulfuromonadales	Pelobacteraceae	Pelobacter	<i>Pelobacter massiliensis</i>	(Madigan et al., 2010)
Bacteria	Cyanobacteria	Cyanophyceae	Oscillatoriophycideae	Oscillatoriales	Leptolyngbya	<i>Phormidium luridum</i>	(Stal & Moezelaar, 1997)
Bacteria	Cyanobacteria	Cyanophyceae	Oscillatoriophycideae	Oscillatoriales	Leptolyngbya	<i>Plectonema boryanum</i>	(Stal & Moezelaar, 1997)
Bacteria	Cyanobacteria	Cyanophyceae	Oscillatoriophycideae	Oscillatoriales	Leptolyngbya	<i>Plectonema calothrioides</i>	(Stal & Moezelaar, 1997)
Bacteria	Fusobacteria	Fusobacteriia	Fusobacteriales	Fusobacteriaceae	Propionigenium	<i>Propionigenium modestum</i>	(Madigan et al., 2010)
Bacteria	Proteobacteria	Gamma Proteobacteria	Pseudomonadales	Pseudomonadaceae	Pseudomonas	<i>Pseudomonas aeruginosa</i>	(Lovley et al., 2004)
Bacteria	Proteobacteria	Gamma Proteobacteria	Pseudomonadales	Pseudomonadaceae	Pseudomonas	<i>Pseudomonas denitrificans</i>	(Lovley et al., 2004)
Bacteria	Proteobacteria	Gamma Proteobacteria	Pseudomonadales	Pseudomonadaceae	Pseudomonas	<i>Pseudomonas fluorescens</i>	(BSI Lab., 2015)
Bacteria	Proteobacteria	Gamma Proteobacteria	Pseudomonadales	Pseudomonadaceae	Pseudomonas	<i>Pseudomonas liquefaciens</i>	(Lovley et al., 2004)
Bacteria	Proteobacteria	Gamma Proteobacteria	Pseudomonadales	Pseudomonadaceae	Pseudomonas	<i>Pseudomonas putida</i>	(BSI Lab., 2015)
Bacteria	Proteobacteria	Gammaproteobacteria	Pseudomonadales	Pseudomonadaceae	Pseudomonas	<i>Pseudomonas sp.</i>	(Lovley et al., 2004)
Bacteria	Proteobacteria	Gamma Proteobacteria	Pseudomonadales	Pseudomonadaceae	Pseudomonas	<i>Pseudomonas stutzeri</i>	(BSI Lab., 2015)
Bacteria	Proteobacteria	Gamma Proteobacteria	Pseudomonadales	Pseudomonadaceae	Pseudomonas	<i>Pseudomonas wisconsinensis</i>	(BSI Lab., 2015)
Bacteria	Proteobacteria	Betaproteobacteria	Burkholderiales	Burkholderiaceae	Cupriavidus	<i>Ralstonia eutropha</i>	(BSI Lab., 2015)
Bacteria	Proteobacteria	Alphaproteobacteria	Rhizobiales	Rhizobiaceae	Rhizobium	<i>Rhizobium leguminosarum</i>	(BSI Lab., 2015)
Bacteria	Proteobacteria	Alphaproteobacteria	Rhodobacterales	Rhodobacteraceae	Rhodobacter	<i>Rhodobacter capsulatus</i>	(Lovley et al., 2004)
Bacteria	Proteobacteria	Alphaproteobacteria	Rhodobacterales	Rhodobacteraceae	Rhodobacter	<i>Rhodobacter sphaeroides</i>	(Koku et al., 2002)
Bacteria	Proteobacteria	Alphaproteobacteria	Rhizobiales	Bradyrhizobiaceae	Rhodopseudomonas	<i>Rhodopseudomonas palustris</i>	(Oh et al., 2002)

Bacteria	Proteobacteria	Alphaproteobacteria	Rhizobiales	Bradyrhizobiaceae	Rhodopseudomonas	<i>Rhodopseudomonas sp</i>	(Norton et al., 1994)
Bacteria	Proteobacteria	Alphaproteobacteria	Rhodospirillales	Rhodospirillaceae	Rhodospirillum	<i>Rhodospirillum rubrum</i>	(BSI Lab., 2015)
Bacteria	Proteobacteria	Betaproteobacteria	Burkholderiales	Burkholderiales	Rubrivivax	<i>Rubrivivax gelatinosus</i>	(BSI Lab., 2015)
Bacteria	Firmicutes	Clostridia	Clostridiales	Ruminococcaceae	Ruminococcus	<i>Ruminococcus albus</i>	(BSI Lab., 2015)
Bacteria	Proteobacteria	Gammaproteobacteria	Alteromonadales	Alteromonadaceae	Saccharophagus	<i>Saccharophagus degradans</i>	(BSI Lab., 2015)
Bacteria	Firmicutes	Clostridia	Clostridiales	Clostridiaceae	Sarcina	<i>Sarcina ventriculi</i>	(BSI Lab., 2015)
Bacteria	Cyanobacteria	Cyanophyceae	Nostocales	Scytonemataceae	Scytonema	<i>Scytonema schmidlei</i>	(Stal & Moezelaar, 1997)
Bacteria	Proteobacteria	Gammaproteobacteria	Enterobacteriales	Enterobacteriaceae	Serratia	<i>Serratia marcescans</i>	(Lovley et al., 2004)
Bacteria	Fibrobacteres	Acidobacteria	Solibacteres	Solibacterales	Solibacteraceae	<i>Solibacter usitatus</i>	(BSI Lab., 2015)
Bacteria	Cyanobacteria	Cyanophyceae	Oscillatoriophyceidae	Oscillatoriales	Arthrospira	<i>Spirulina minosa</i>	(Stal & Moezelaar, 1997)
Bacteria	Cyanobacteria	Cyanophyceae	Oscillatoriophyceidae	Oscillatoriales	Arthrospira	<i>Spirulina platensis</i>	(Stal & Moezelaar, 1997)
Bacteria	Firmicutes	Negativicutes	Selenomonadales	Veillonellaceae	Sporomusa	<i>Sporomusa malonica</i>	(Madigan et al., 2010)
Bacteria	Firmicutes	Bacilli	Lactobacillales	Streptococcaceae	Lactococcus	<i>Streptococcus lactis</i>	(John et al., 2007)
Archaea	Crenarchaeota	Thermoprotei	Sulfolobales	Sulfolobaceae	Sulfolobus	<i>Sulfolobus acidocaldarius</i>	(Schiraldi et al., 1999)
Bacteria	Cyanobacteria	Cyanophyceae	Oscillatoriophyceidae	Chroococcales	Synechocystis	<i>Synechocystis sp.</i>	(Stal & Moezelaar, 1997)
Bacteria	Firmicutes	Clostridia	Clostridiales	Syntrophomonadaceae	Syntrophothermus	<i>Syntrophothermus lipocalidus</i>	(Adams et al., 2006)
Bacteria	Proteobacteria	Deltaproteobacteria	Syntrophobacteriales	Syntrophaceae	Syntrophus	<i>Syntrophus aciditrophicus</i>	(Madigan et al., 2010)
Bacteria	Firmicutes	Clostridia	Thermoanaerobacterales	Thermoanaerobacteraceae	Caldanaerobacter	<i>Thermoanaerobacter Brockii</i>	(BSI Lab., 2015)

Bacteria	Firmicutes	Clostridia	Thermoanaerobacterales	Thermoanaerobacteraceae	Caldanaerobacter	<i>Thermoanaerobacter ethanolicus</i>	(BSI Lab., 2015)
Bacteria	Firmicutes	Clostridia	Thermoanaerobacterales	Thermoanaerobacteraceae	Caldanaerobacter	<i>Thermoanaerobacter tengcongensis</i>	(BSI Lab., 2015)
Bacteria	Actinobacteria	Actinobacteria	Streptosporangiales	Nocardiopsaceae	Thermobifida	<i>Thermobifida fusca</i>	(BSI Lab., 2015)
Bacteria	Thermotogae	Thermotogae	Thermotogales	Thermotogaceae	Thermotoga	<i>Thermotoga maritima</i>	(BSI Lab., 2015)
Bacteria	Thermotogae	Thermotogae	Thermotogales	Thermotogaceae	Thermotoga	<i>Thermotoga neapolitana</i>	(BSI Lab., 2015)
Eubacteria	Proteobacteria	Acidithiobacillia	Acidithiobacillales	Acidithiobacillaceae	Acidithiobacillus	<i>Thiobacillus thiooxidans</i>	(Lovley et al., 2004)
Bacteria	Cyanobacteria	Cyanophyceae	Nostocales	Microchaetaceae	Tolypothrix	<i>Tolypothrix tenuis</i>	(Stal & Moezelaar, 1997)
Fungi	Ascomycota	Sordariomycetes	Hypocreales	Hypocreaceae	Trichoderma	<i>Trichoderma reesei</i>	(BSI Lab., 2015)
Fungi	Ascomycota	Sordariomycetes	Hypocreales	Hypocreaceae	Trichoderma	<i>Trichoderma viride</i>	(BSI Lab., 2015)
Bacteria	Proteobacteria	Gammaproteobacteria	Vibrionales	Vibrionaceae	Vibrio	<i>Vibrio sp.</i>	(Lovley et al., 2004)
Bacteria	Cyanobacteria	Cyanophyceae	Stigonematales	Stigonemataceae	Westiellopsis	<i>Westiellopsis prolifica</i>	(Stal & Moezelaar, 1997)
Bacteria	Proteobacteria	Epsilonproteobacteria	Campylobacteriales	Helicobacteraceae	Wolinella	<i>Wolinella succinogenes</i>	(Lovley et al., 2004)
Fungi	Ascomycota	Saccharomycetes	Saccharomycetales	Dipodascaceae	Yarrowia	<i>Yarrowia lipolytica</i>	(BSI Lab., 2015)
Bacteria	Proteobacteria	Gammaproteobacteria	Oceanospirillales	Halomonadaceae	Zymobacter	<i>Zymobacter palmae</i>	(BSI Lab., 2015)
Bacteria	Proteobacteria	Alphaproteobacteria	Sphingomonadales	Sphingomonadaceae	Zymomonas	<i>Zymomonas mobilis</i>	(Bringer et al., 1984)

Table S5.2 Assembled iron-reducing bacteria

king	phylum	class	order	family	genus	strain	reference
Bacteria	Actinobacteria	Actinobacteria	Acidimicrobiales	Acidimicrobiaceae	Acidimicrobium	<i>Acidimicrobium ferroxidans</i>	(Lovley et al., 2004)
Bacteria	Proteobacteria	Alphaproteobacteria	Rhodospirillales	Acetobacteraceae	Acidiphilium	<i>Acidiphilium acidophilum</i>	(Weber et al., 2006)
Bacteria	Proteobacteria	Alphaproteobacteria	Rhodospirillales	Acetobacteraceae	Acidiphilium	<i>Acidiphilium cryptum</i>	(Lovley et al., 2004)
Eubacteria	Proteobacteria	Acidithiobacillia	Acidithiobacillales	Acidithiobacillaceae	Acidithiobacillus	<i>Acidithiobacillus ferroxidans</i>	(Lovley et al., 2004)
Fungi	Zygomycota	Mucoromycotina	Mucorales	Mucoraceae	Actinomucor	<i>Actinomucor repens</i>	(Lovley, 2013)
Bacteria	Proteobacteria	Gammaproteobacteria	Enterobacteriales	Enterobacteriaceae	Enterobacter	<i>Aerobacter aerogenes</i>	(Lovley, 2013)
Bacteria	Proteobacteria	Gammaproteobacteria	Aeromonadales	Aeromonadaceae	Aeromonas	<i>Aeromonas hydrophila</i>	(Lovley, 2013)
Bacteria	Firmicutes	Bacilli	Bacillales	Alicyclobacillaceae	Alicyclobacillus	<i>Alicyclobacillus sp.</i>	(Weber et al., 2006)
Bacteria	Firmicutes	Clostridia	Clostridiales	Clostridiaceae	Alkaliphilus	<i>Alkaliphilus metalliredigensis</i>	(Weber et al., 2006)
Fungi	Ascomycota	Dothideomycetes	Pleosporales	Pleosporaceae	Alternaria	<i>Alternaria tenuis</i>	(Lovley, 2013)
Bacteria	Firmicutes	Clostridia	Clostridiales	Proteinivoraceae	Anaerobranca	<i>Anaerobranca californiensis</i>	(Weber et al., 2006)
Bacteria	Proteobacteria	Deltaproteobacteria	Myxococcales	Myxococcaceae	Anaeromyxobacter	<i>Anaeromyxobacter dehalogenans</i>	(Weber et al., 2006)
Bacteria	Proteobacteria	Deltaproteobacteria	Myxococcales	Myxococcaceae	Anaeromyxobacter	<i>Anaeromyxobacter dehalogens</i>	(Lovley et al., 2004)
Bacteria	Proteobacteria	Deltaproteobacteria	Myxococcales	Myxococcaceae	Anaeromyxobacter	<i>Anaeromyxobacter sp.</i>	(Lovley et al., 2004)
Archaea	Euryarchaeota	Archaeoglobi	Archaeoglobales	Archaeoglobaceae	Archaeoglobus	<i>Archaeoglobus fulgidus</i>	(Lovley, 2013)

Bacteria	Firmicutes	Bacilli	Bacillales	Bacillaceae	Bacillus	<i>Bacillus arseniciselenatis</i>	(Lovley et al., 2004)
Bacteria	Firmicutes	Bacilli	Bacillales	Bacillaceae	Bacillus	<i>Bacillus cereus</i>	(Lovley, 2013)
Bacteria	Firmicutes	Bacilli	Bacillales	Bacillaceae	Bacillus	<i>Bacillus circulans</i>	(Lovley, 2013)
Bacteria	Firmicutes	Bacilli	Bacillales	Bacillaceae	Bacillus	<i>Bacillus infernus</i>	(Lovley, 2013)
Bacteria	Firmicutes	Bacilli	Bacillales	Bacillaceae	Bacillus	<i>Bacillus mesentericus</i>	(Lovley, 2013)
Bacteria	Firmicutes	Bacilli	Bacillales	Bacillaceae	Bacillus	<i>Bacillus polymyxa</i>	(Lovley, 2013)
Bacteria	Firmicutes	Bacilli	Bacillales	Bacillaceae	Bacillus	<i>Bacillus pumilus</i>	(Lovley, 2013)
Bacteria	Firmicutes	Bacilli	Bacillales	Bacillaceae	Bacillus	<i>Bacillus sp.</i>	(Lovley, 2013)
Bacteria	Firmicutes	Bacilli	Bacillales	Bacillaceae	Bacillus	<i>Bacillus subterraneus</i>	(Lovley et al., 2004)
Bacteria	Firmicutes	Bacilli	Bacillales	Bacillaceae	Bacillus	<i>Bacillus subtilis</i>	(Lovley, 2013)
Bacteria	Bacteroidetes	Bacteroidetes	Bacteroidales	Bacteroidaceae	Bacteroides	<i>Bacteroides hypermegas</i>	(Lovley, 2013)
Bacteria	Firmicutes	Clostridia	Thermoanaerobacterales	Thermoanaerobacteraceae	Thermoterrabacterium	<i>Carboxydotherrmus ferrireducens</i>	(Weber et al., 2006)
Bacteria	Firmicutes	Clostridia	Clostridiales	Clostridiaceae	Clostridium	<i>Clostridium beijerinckii</i>	(Weber et al., 2006)
Bacteria	Firmicutes	Clostridia	Clostridiales	Clostridiaceae	Clostridium	<i>Clostridium butyricum</i>	(Lovley, 2013)
Bacteria	Firmicutes	Clostridia	Clostridiales	Clostridiaceae	Clostridium	<i>Clostridium polymyxa</i>	(Lovley, 2013)
Bacteria	Firmicutes	Clostridia	Clostridiales	Clostridiaceae	Clostridium	<i>Clostridium saccarobutyricum</i>	(Lovley, 2013)
Bacteria	Firmicutes	Clostridia	Clostridiales	Clostridiaceae	Clostridium	<i>Clostridium sp.</i>	(Lovley et al., 2004)

Bacteria	Firmicutes	Clostridia	Clostridiales	Clostridiaceae	Clostridium	<i>Clostridium sporogenes</i>	(Lovley, 2013)
Bacteria	Deferribacteres	Deferribacteres	Deferribacterales	Deferribacteraceae	Deferribacter	<i>Deferribacter abyssi</i>	(Lovley et al., 2004)
Bacteria	Deferribacteres	Deferribacteres	Deferribacterales	Deferribacteraceae	Deferribacter	<i>Deferribacter thermophilus</i>	(Lovley, 2013)
Bacteria	Firmicutes	Clostridia	Clostridiales	Peptococcaceae	Desulfotobacterium	<i>Desulfotobacterium frappieri</i>	(Weber et al., 2006)
Bacteria	Firmicutes	Clostridia	Clostridiales	Peptococcaceae	Desulfotobacterium	<i>Desulfotobacterium hafniense</i>	(Lovley et al., 2004)
Bacteria	Firmicutes	Clostridia	Clostridiales	Peptococcaceae	Desulfotobacterium	<i>Desulfotobacterium metallireducens</i>	(Lovley et al., 2004)
Bacteria	Firmicutes	Clostridia	Clostridiales	Peptococcaceae	Desulfotobacterium	<i>Desulfotobacterium sp.</i>	(Lovley et al., 2004)
Bacteria	Proteobacteria	Deltaproteobacteria	Desulfobacterales	Desulfobacteraceae	Desulfobacter	<i>Desulfobacter postgatei</i>	(Lovley, 2013)
Bacteria	Proteobacteria	Deltaproteobacteria	Desulfobacterales	Desulfobacteraceae	Desulfobacterium	<i>Desulfobacterium autotrophicum</i>	(Lovley, 2013)
Bacteria	Proteobacteria	Deltaproteobacteria	Desulfobacterales	Desulfobulbaceae	Desulfobulbus	<i>Desulfobulbus propionicus</i>	(Lovley, 2013)
Bacteria	Firmicutes	Clostridia	Clostridiales	Peptococcaceae	Desulfotomaculum	<i>Desulfotomaculum reducens</i>	(Lovley et al., 2004)
Bacteria	Firmicutes	Negativicutes	Selenomonadales	Veillonellaceae	Desulfosporomusa	<i>Desulfosporomusa polytropa</i>	(Weber et al., 2006)
Bacteria	Firmicutes	Clostridia	Clostridiales	Peptococcaceae	Desulfosporosinus	<i>Desulfosporosinus meridiei</i>	(Weber et al., 2006)
Bacteria	Firmicutes	Clostridia	Clostridiales	Peptococcaceae	Desulfotomaculum	<i>Desulfotomaculum nigrificans</i>	(Lovley, 2013)
Bacteria	Firmicutes	Clostridia	Clostridiales	Peptococcaceae	Desulfotomaculum	<i>Desulfotomaculum reducens</i>	(Weber et al., 2006)
Bacteria	Proteobacteria	Delta Proteobacteria	Desulfovibrionales	Desulfovibrionaceae	Desulfovibrio	<i>Desulfovibrio baarsii</i>	(Lovley, 2013)
Bacteria	Proteobacteria	Delta Proteobacteria	Desulfovibrionales	Desulfovibrionaceae	Desulfovibrio	<i>Desulfovibrio baculatus</i>	(Lovley, 2013)

Bacteria	Proteobacteria	Delta Proteobacteria	Desulfovibrionales	Desulfovibrionaceae	Desulfovibrio	<i>Desulfovibrio desulfuricans</i>	(Lovley, 2013)
Bacteria	Proteobacteria	Delta Proteobacteria	Desulfovibrionales	Desulfovibrionaceae	Desulfovibrio	<i>Desulfovibrio profundus</i>	(Weber et al., 2006)
Bacteria	Proteobacteria	Delta Proteobacteria	Desulfovibrionales	Desulfovibrionaceae	Desulfovibrio	<i>Desulfovibrio sulfodismutans</i>	(Lovley, 2013)
Bacteria	Proteobacteria	Delta Proteobacteria	Desulfovibrionales	Desulfovibrionaceae	Desulfovibrio	<i>Desulfovibrio vulgaris</i>	(Lovley, 2013)
Bacteria	Proteobacteria	Deltaproteobacteria	Desulfuromonadales	Desulfuromonadaceae	Desulfuromonas	<i>Desulfuromonas acetexigens</i>	(Lovley, 2013)
Bacteria	Proteobacteria	Deltaproteobacteria	Desulfuromonadales	Desulfuromonadaceae	Desulfuromonas	<i>Desulfuromonas acetoxidans</i>	(Lovley, 2013)
Bacteria	Proteobacteria	Deltaproteobacteria	Desulfuromonadales	Desulfuromonadaceae	Desulfuromonas	<i>Desulfuromonas chloroethenica</i>	(Lovley, 2013)
Bacteria	Proteobacteria	Deltaproteobacteria	Desulfuromonadales	Desulfuromonadaceae	Desulfuromonas	<i>Desulfuromonas michiganensis</i>	(Lovley et al., 2004)
Bacteria	Proteobacteria	Deltaproteobacteria	Desulfuromonadales	Desulfuromonadaceae	Desulfuromonas	<i>Desulfuromonas palmitatis</i>	(Lovley, 2013)
Bacteria	Proteobacteria	Deltaproteobacteria	Desulfuromonadales	Desulfuromonadaceae	Desulfuromonas	<i>Desulfuromonas svalbardensis</i>	(Vandieken et al., 2006)
Bacteria	Proteobacteria	Deltaproteobacteria	Desulfuromonadales	Desulfuromonadaceae	Desulfuromusa	<i>Desulfuromusa bakii</i>	(Lovley, 2013)
Bacteria	Proteobacteria	Deltaproteobacteria	Desulfuromonadales	Desulfuromonadaceae	Desulfuromusa	<i>Desulfuromusa ferrireducens</i>	(Vandieken et al., 2006)
Bacteria	Proteobacteria	Deltaproteobacteria	Desulfuromonadales	Desulfuromonadaceae	Desulfuromusa	<i>Desulfuromusa kysingii</i>	(Lovley, 2013)
Bacteria	Proteobacteria	Deltaproteobacteria	Desulfuromonadales	Desulfuromonadaceae	Desulfuromusa	<i>Desulfuromusa succinoxidans</i>	(Lovley, 2013)
Bacteria	Proteobacteria	Deltaproteobacteria	Desulfuromonadales	Desulfuromonadaceae	Desulfuromusa	<i>Desulfuromusa succnoxidans</i>	(Lovley et al., 2004)
Bacteria	Proteobacteria	Gammaproteobacteria	Enterobacteriales	Enterobacteriaceae	Enterobacter	<i>Enterobacter sp.</i>	(Lovley, 2013)
Bacteria	Proteobacteria	Gammaproteobacteria	Enterobacteriales	Enterobacteriaceae	Escherichia	<i>Escherichia coli</i>	(Lovley, 2013)

Bacteria	Proteobacteria	Gammaproteobacteria	Enterobacteriales	Enterobacteriaceae	Escherichia	<i>Escherichia sp.</i>	(Lovley, 2013)
Bacteria	Proteobacteria	Betaproteobacteria	Rhodocyclales	Rhodocyclaceae	Ferribacterium	<i>Ferribacterium limneticum</i>	(Lovley, 2013)
Bacteria	Proteobacteria	Gammaproteobacteria	Alteromonadales	Ferrimonadaceae	Ferrimonas	<i>Ferrimonas balearica</i>	(Lovley, 2013)
Archaea	Euryarchaeota	Archaeoglobi	Archaeoglobales	Archaeoglobaceae	Ferroglobus	<i>Ferroglobus placidus</i>	(Weber et al., 2006)
Fungi	Ascomycota	Sordariomycetes	Hypocreales	Nectriaceae	Fusarium	<i>Fusarium oxysporum</i>	(Lovley, 2013)
Fungi	Ascomycota	Sordariomycetes	Hypocreales	Nectriaceae	Fusarium	<i>Fusarium solani</i>	(Lovley, 2013)
Fungi	Ascomycota	Sordariomycetes	Hypocreales	Nectriaceae	Fusarium	<i>Fusarium sp.</i>	(Lovley, 2013)
Bacteria	Proteobacteria	Deltaproteobacteria	Desulfuromonadales	Geobacteraceae	Geobacter	<i>Geobacter metallireducens</i>	(Lovley et al., 2004)
Bacteria	Proteobacteria	Deltaproteobacteria	Desulfuromonadales	Geobacteraceae	Geobacter	<i>Geobacter akaganaitreducens</i>	(Lovley, 2013)
Bacteria	Proteobacteria	Deltaproteobacteria	Desulfuromonadales	Geobacteraceae	Geobacter	<i>Geobacter arculus</i>	(Lovley, 2013)
Bacteria	Proteobacteria	Deltaproteobacteria	Desulfuromonadales	Geobacteraceae	Geobacter	<i>Geobacter argillaceus</i>	(Lovley et al., 2004)
Bacteria	Proteobacteria	Deltaproteobacteria	Desulfuromonadales	Geobacteraceae	Geobacter	<i>Geobacter bemidjensis</i>	(Lovley et al., 2004)
Bacteria	Proteobacteria	Deltaproteobacteria	Desulfuromonadales	Geobacteraceae	Geobacter	<i>Geobacter bremensis</i>	(Lovley et al., 2004)
Bacteria	Proteobacteria	Deltaproteobacteria	Desulfuromonadales	Geobacteraceae	Geobacter	<i>Geobacter chappellei</i>	(Lovley, 2013)
Bacteria	Proteobacteria	Deltaproteobacteria	Desulfuromonadales	Geobacteraceae	Geobacter	<i>Geobacter grbiciae</i>	(Lovley et al., 2004)
Bacteria	Proteobacteria	Deltaproteobacteria	Desulfuromonadales	Geobacteraceae	Geobacter	<i>Geobacter grbicum</i>	(Lovley, 2013)
Bacteria	Proteobacteria	Deltaproteobacteria	Desulfuromonadales	Geobacteraceae	Geobacter	<i>Geobacter humireducens</i>	(Lovley, 2013)

Bacteria	Proteobacteria	Deltaproteobacteria	Desulfuromonadales	Geobacteraceae	Geobacter	<i>Geobacter hydrogenophilus</i>	(Lovley, 2013)
Bacteria	Proteobacteria	Deltaproteobacteria	Desulfuromonadales	Geobacteraceae	Geobacter	<i>Geobacter metallireducens</i>	(Lovley, 2013)
Bacteria	Proteobacteria	Deltaproteobacteria	Desulfuromonadales	Geobacteraceae	Geobacter	<i>Geobacter pelophilus</i>	(Lovley et al., 2004)
Bacteria	Proteobacteria	Deltaproteobacteria	Desulfuromonadales	Geobacteraceae	Geobacter	<i>Geobacter pickeringii</i>	(Lovley et al., 2004)
Bacteria	Proteobacteria	Deltaproteobacteria	Desulfuromonadales	Geobacteraceae	Geobacter	<i>Geobacter sp.</i>	(Lovley, 2013)
Bacteria	Proteobacteria	Deltaproteobacteria	Desulfuromonadales	Geobacteraceae	Geobacter	<i>Geobacter sulfurreducens</i>	(Lovley, 2013)
Bacteria	Proteobacteria	Deltaproteobacteria	Desulfuromonadales	Geobacteraceae	Geobacter	<i>Geobacter thiogenes</i>	(Nevin et al., 2007)
Archaea	Crenarchaeota	Thermoprotei	Desulfurococcales	Pyrodictiaceae	Geogemma	<i>Geogemma barossii</i>	(Lovley et al., 2004)
Archaea	Crenarchaeota	Thermoprotei	Desulfurococcales	Pyrodictiaceae	Geogemma	<i>Geogemma hydrogenophila</i>	(Lovley et al., 2004)
Archaea	Euryarchaeota	Archaeoglobi	Archaeoglobales	Archaeoglobaceae	Geoglobus	<i>Geoglobus ahangari</i>	(Lovley et al., 2004)
Bacteria	Proteobacteria	Deltaproteobacteria	Desulfuromonadales	Geobacteraceae	Geopsychrobacter	<i>Geopsychrobacter electrodiphlos</i>	(Lovley et al., 2004)
Bacteria	Proteobacteria	Deltaproteobacteria	Desulfuromonadales	Geobacteraceae	Geopsychrobacter	<i>Geopsychrobacter electriphilus</i>	(Lovley et al., 2004)
Bacteria	Proteobacteria	Deltaproteobacteria	Desulfuromonadales	Geobacteraceae	Geopsychrobacter	<i>Geopsychrobacter electrodiphilus</i>	(Weber et al., 2006)
Bacteria	Thermodesulfobacteria	Thermodesulfobacteria	Thermodesulfobacteriales	Thermodesulfobacteriaceae	Geothermobacterium	<i>Geothermobacter ehrlichii</i>	(Weber et al., 2006)
Bacteria	Thermodesulfobacteria	Thermodesulfobacteria	Thermodesulfobacteriales	Thermodesulfobacteriaceae	Geothermobacterium	<i>Geothermobacterium ferrireducens</i>	(Weber et al., 2006)
Bacteria	Acidobacteria	Holophagae	Holophagales	Holophagaceae	Geothrix	<i>Geothrix fermentans</i>	(Lovley, 2013)

Bacteria	Deferribacteres	Deferribacteres	Deferribacterales	Deferribacteraceae	Geovibrio	<i>Geovibrio ferrireducens</i>	(Lovley, 2013)
Archaea	Crenarchaeota	Thermoprotei	Desulfurococcales	Pyrodictiaceae	Hyperthermus	<i>Hyperthermus butylicus</i>	(Weber et al., 2006)
Archaea	Euryarchaeota	Methanococci	Methanococcales	Methanococcaceae	Methanococcus	<i>Methanococcus thermolithotrophicus</i>	(Lovley, 2013)
Archaea	Euryarchaeota	Methanopyri	Methanopyrales	Methanopyraceae	Methanopyrus	<i>Methanopyrus kandleri</i>	(Lovley, 2013)
Bacteria	Proteobacteria	Gamma Proteobacteria	Enterobacteriales	Enterobacteriaceae	Pantoea	<i>Pantoea agglomerans</i>	(Weber et al., 2006)
Bacteria	Proteobacteria	Gammaproteobacteria	Enterobacteriales	Enterobacteriaceae	Paracolobactrum	<i>Paracolobactrum sp.</i>	(Lovley, 2013)
Bacteria	Proteobacteria	Deltaproteobacteria	Desulfuromonadales	Pelobacteraceae	Pelobacter	<i>Pelobacter carbinolicus</i>	(Lovley, 2013)
Bacteria	Proteobacteria	Deltaproteobacteria	Desulfuromonadales	Pelobacteraceae	Pelobacter	<i>Pelobacter propionicus</i>	(Lovley, 2013)
Bacteria	Proteobacteria	Deltaproteobacteria	Desulfuromonadales	Pelobacteraceae	Pelobacter	<i>Pelobacter venetianus</i>	(Lovley, 2013)
Bacteria	Proteobacteria	Gamma Proteobacteria	Pseudomonadales	Pseudomonadaceae	Pseudomonas	<i>Pseudomonas aeruginosa</i>	(Lovley, 2013)
Bacteria	Proteobacteria	Gamma Proteobacteria	Pseudomonadales	Pseudomonadaceae	Pseudomonas	<i>Pseudomonas denitrificans</i>	(Lovley, 2013)
Bacteria	Proteobacteria	Gamma Proteobacteria	Pseudomonadales	Pseudomonadaceae	Pseudomonas	<i>Pseudomonas liquefaciens</i>	(Lovley, 2013)
Bacteria	Proteobacteria	Gammaproteobacteria	Pseudomonadales	Pseudomonadaceae	Pseudomonas	<i>Pseudomonas sp.</i>	(Lovley, 2013)
Archaea	Crenarchaeota	Thermoprotei	Thermoproteales	Thermoproteaceae	Pyrobaculum	<i>Pyrobaculum aerophilum</i>	(Lovley, 2013)
Archaea	Crenarchaeota	Thermoprotei	Thermoproteales	Thermoproteaceae	Pyrobaculum	<i>Pyrobaculum islandicum</i>	(Lovley, 2013)
Archaea	Euryarchaeota	Thermococci	Thermococcales	Thermococcaceae	Pyrococcus	<i>Pyrococcus furiosus</i>	(Lovley, 2013)
Archaea	Crenarchaeota	Thermoprotei	Desulfurococcales	Pyrodictiaceae	Pyrodictium	<i>Pyrodictium abyssi</i>	(Lovley, 2013)

Archaea	Crenarchaeota	Thermoprotei	Desulfurococcales	Pyrodictiaceae	Pyrodictium	<i>Pyrodictium occultum</i>	(Weber et al., 2006)
Bacteria	Proteobacteria	Alphaproteobacteria	Rhodobacterales	Rhodobacteraceae	Rhodobacter	<i>Rhodobacter capsulatus</i>	(Lovley, 2013)
Bacteria	Proteobacteria	Beta Proteobacteria	Burkholderiales	Comamonadaceae	Rhodoferax	<i>Rhodoferax ferrireducens</i>	(Weber et al., 2006)
Bacteria	Proteobacteria	Gamma proteobacteria	Enterobacteriales	Enterobacteriaceae	Serratia	<i>Serratia marcescans</i>	(Lovley, 2013)
Bacteria	Proteobacteria	Gamma Proteobacteria	Alteromonadales	Shewanellaceae	Shewanella	<i>Shewanella algae</i>	(Lovley, 2013)
Bacteria	Proteobacteria	Gamma Proteobacteria	Alteromonadales	Shewanellaceae	Shewanella	<i>Shewanella amazonensis</i>	(Lovley et al., 2004)
Bacteria	Proteobacteria	Gamma Proteobacteria	Alteromonadales	Shewanellaceae	Shewanella	<i>Shewanella frigidimarina</i>	(Lovley et al., 2004)
Bacteria	Proteobacteria	Gamma Proteobacteria	Alteromonadales	Shewanellaceae	Shewanella	<i>Shewanella gelidimarina</i>	(Lovley et al., 2004)
Bacteria	Proteobacteria	Gamma Proteobacteria	Alteromonadales	Shewanellaceae	Shewanella	<i>Shewanella olleyana</i>	(Lovley et al., 2004)
Bacteria	Proteobacteria	Gamma Proteobacteria	Alteromonadales	Shewanellaceae	Shewanella	<i>Shewanella oneidensis</i>	(Weber et al., 2006)
Bacteria	Proteobacteria	Gamma Proteobacteria	Alteromonadales	Shewanellaceae	Shewanella	<i>Shewanella paeleana</i>	(Lovley et al., 2004)
Bacteria	Proteobacteria	Gamma Proteobacteria	Alteromonadales	Shewanellaceae	Shewanella	<i>Shewanella putrefaciens</i>	(Lovley, 2013)
Bacteria	Proteobacteria	Gamma Proteobacteria	Alteromonadales	Shewanellaceae	Shewanella	<i>Shewanella saccharophila</i>	(Lovley, 2013)
Bacteria	Proteobacteria	Gamma Proteobacteria	Alteromonadales	Shewanellaceae	Shewanella	<i>Shewanella saccharophilus</i>	(Lovley et al., 2004)
Bacteria	Firmicutes	Bacilli	Bacillales	Alicyclobacillaceae	Sulfobacillus	<i>Sulfobacillus acidophilus</i>	(Lovley et al., 2004)
Bacteria	Firmicutes	Bacilli	Bacillales	Alicyclobacillaceae	Sulfobacillus	<i>Sulfobacillus sp.</i>	(Lovley et al., 2004)
Bacteria	Firmicutes	Bacilli	Bacillales	Alicyclobacillaceae	Sulfobacillus	<i>Sulfobacillus thermosulfidooxidans</i>	(Weber et al., 2006)

Bacteria	Firmicutes	Bacilli	Bacillales	Alicyclobacillaceae	Sulfobacillus	<i>Sulfobacillus thermosulfidoxidans</i>	(Lovley et al., 2004)
Archaea	Crenarchaeota	Thermoprotei	Sulfolobales	Sulfolobaceae	Sulfolobus	<i>Sulfolobus acidocaldarius</i>	(Lovley, 2013)
Bacteria	Proteobacteria	Epsilonproteobacteria	Campylobacterales	Campylobacteraceae	Sulfurospirillum	<i>Sulfurospirillum barnesii</i>	(Lovley, 2013)
Bacteria	Firmicutes	Clostridia	Thermoanaerobacterales	Thermoanaerobacteraceae	Thermoanaerobacter	<i>Thermoanaerobacter acetioethylicus</i>	(Lovley, 2013)
Bacteria	Firmicutes	Clostridia	Thermoanaerobacterales	Thermoanaerobacteraceae	Thermoanaerobacter	<i>Thermoanaerobacter brockii</i>	(Lovley et al., 2004)
Bacteria	Firmicutes	Clostridia	Thermoanaerobacterales	Thermoanaerobacteraceae	Thermoanaerobacter	<i>Thermoanaerobacter siderophilus</i>	(Lovley et al., 2004)
Bacteria	Firmicutes	Clostridia	Thermoanaerobacterales	Thermoanaerobacteraceae	Thermoanaerobacter	<i>Thermoanaerobacter sp.</i>	(Lovley et al., 2004)
Bacteria	Firmicutes	Clostridia	Thermoanaerobacterales	Thermoanaerobacteraceae	Thermoanaerobacter	<i>Thermoanaerobacter wiegeli</i>	(Lovley, 2013)
Archaea	Euryarchaeota	Thermococci	Thermococcales	Thermococcaceae	Thermococcus	<i>Thermococcus sp.</i>	(Weber et al., 2006)
Bacteria	Thermodesulfobacteria	Thermodesulfobacteria	Thermodesulfobacteriales	Thermodesulfobacteriaceae	Thermodesulfobacterium	<i>Thermodesulfobacterium commune</i>	(Weber et al., 2006)
Bacteria	Firmicutes	Clostridia	Thermoanaerobacterales	Thermoanaerobacteraceae	Thermoterrabacterium	<i>Thermoterrabacterium ferrireducens</i>	(Lovley, 2013)
Bacteria	Thermotogae	Thermotogales	Thermotogales	Thermotogaceae	Thermotoga	<i>Thermotoga maritima</i>	(Lovley, 2013)
Bacteria	Thermotogae	Thermotogales	Thermotogales	Thermotogaceae	Thermotoga	<i>Thermotoga subterranea</i>	(Lovley et al., 2004)
Bacteria	Firmicutes	Clostridia	Thermoanaerobacterales	Thermoanaerobacterales Family III. Incertae Sedis	Thermovenabulum	<i>Thermovenabulum ferriorganovorum</i>	(Weber et al., 2006)

Bacteria	Deinococcus-Thermus	Deinococci	Thermales	Thermaceae	Thermus	<i>Thermus scotoductus</i>	(Lovley et al., 2004)
Bacteria	Deinococcus-Thermus	Deinococci	Thermales	Thermaceae	Thermus	<i>Thermus sp.</i>	(Lovley, 2013)
Eubacteria	Proteobacteria	Acidithiobacillia	Acidithiobacillales	Acidithiobacillaceae	Acidithiobacillus	<i>Thiobacillus ferrooxidans</i>	(Pronk et al., 1992)
Eubacteria	Proteobacteria	Acidithiobacillia	Acidithiobacillales	Acidithiobacillaceae	Acidithiobacillus	<i>Thiobacillus thiooxidans</i>	(Lovley, 2013)
Bacteria	Proteobacteria	Deltaproteobacteria	Desulfuromonadales	Geobacteraceae	Geobacter	<i>Trichlorobacter thiogenes</i>	(Lovley et al., 2004)
Bacteria	Proteobacteria	Gammaproteobacteria	Vibrionales	Vibrionaceae	Vibrio	<i>Vibrio sp.</i>	(Lovley, 2013)
Bacteria	Proteobacteria	Epsilonproteobacteria	Campylobacteriales	Helicobacteraceae	Wolinella	<i>Wolinella succinogenes</i>	(Lovley, 2013)

Table S5.3 Assembled sulfate-reducing bacteria

king	phylum	class	order	family	genus	strain	
Bacteria	Proteobacteria	Deltaproteobacteria	Desulfobacterales	Desulfobacteraceae	Algorimarina	<i>Algorimarina butyrica</i>	(Muyzer & Stams, 2008)
Archaea	Euryarchaeota	Archaeoglobi	Archaeoglobales	Archaeoglobaceae	Archaeoglobus	<i>Archaeoglobus lithotrophicus</i>	(Muyzer & Stams, 2008)
Archaea	Euryarchaeota	Archaeoglobi	Archaeoglobales	Archaeoglobaceae	Archaeoglobus	<i>Archaeoglobus profundus</i>	(Muyzer & Stams, 2008)
Archaea	Euryarchaeota	Archaeoglobi	Archaeoglobales	Archaeoglobaceae	Archaeoglobus	<i>Archaeoglobus veneficus</i>	(Muyzer & Stams, 2008)
Archaea	Crenarchaeota	Thermoprotei	Thermoproteales	Thermoproteaceae	Caldivirga	<i>Caldivirga maquilgensis</i>	(Muyzer & Stams, 2008)
Bacteria	Proteobacteria	Deltaproteobacteria	Desulfobacterales	Desulfobacteraceae	Candidatus Magnetanas	<i>Candidatus Magnetanas rongchenensis</i>	(Muyzer & Stams, 2008)
Bacteria	Proteobacteria	Deltaproteobacteria	Desulfobacterales	Desulfobacteraceae	Candidatus Magnetanas	<i>Candidatus Magnetanas tsingtaoensis</i>	(Muyzer & Stams, 2008)
Bacteria	Proteobacteria	Deltaproteobacteria	Desulfobacterales	Desulfobacteraceae	Candidatus Magnetoglobus	<i>Candidatus Magnetoglobus multicellularis</i>	(Muyzer & Stams, 2008)
Bacteria	Proteobacteria	Deltaproteobacteria	Desulfobacterales	Desulfobacteraceae	Candidatus Magnetomorum	<i>Candidatus Magnetomorum litorale</i>	(Muyzer & Stams, 2008)
Bacteria	Proteobacteria	Deltaproteobacteria	Desulfobacterales	Desulfobacteraceae	Candidatus Magnetomorum	<i>Candidatus Magnetomorum sp.</i>	(Muyzer & Stams, 2008)
Bacteria	Proteobacteria	Deltaproteobacteria	Syntrophobacterales	Syntrophobacteraceae	Desulfacinum	<i>Desulfacinum hydrothermale</i>	(Muyzer & Stams, 2008)
Bacteria	Proteobacteria	Deltaproteobacteria	Syntrophobacterales	Syntrophobacteraceae	Desulfacinum	<i>Desulfacinum infernum</i>	(Muyzer & Stams, 2008)
Bacteria	Proteobacteria	Deltaproteobacteria	Syntrophobacterales	Syntrophobacteraceae	Desulfacinum	<i>Desulfacinum sp.</i>	(Muyzer & Stams, 2008)
Bacteria	Proteobacteria	Deltaproteobacteria	Syntrophobacterales	Syntrophobacteraceae	Desulfacinum	<i>Desulfacinum subterraneum</i>	(Muyzer & Stams, 2008)
Bacteria	Proteobacteria	Deltaproteobacteria	Desulfarculales	Desulfarculaceae	Desulfarculus	<i>Desulfarculus baarsii</i>	(Muyzer & Stams, 2008)

Bacteria	Proteobacteria	Deltaproteobacteria	Desulfobacterales	Desulfobacteraceae	Desulfatibacillum	<i>Desulfatibacillum aliphaticivorans</i>	(Muyzer & Stams, 2008)
Bacteria	Proteobacteria	Deltaproteobacteria	Desulfobacterales	Desulfobacteraceae	Desulfatibacillum	<i>Desulfatibacillum alkenivorans</i>	(Muyzer & Stams, 2008)
Bacteria	Proteobacteria	Deltaproteobacteria	Desulfobacterales	Desulfobacteraceae	Desulfatibacillum	<i>Desulfatibacillum sp.</i>	(Muyzer & Stams, 2008)
Bacteria	Proteobacteria	Deltaproteobacteria	Desulfobacterales	Desulfobacteraceae	Desulfatiferula	<i>Desulfatiferula olefinivorans</i>	(Muyzer & Stams, 2008)
Bacteria	Proteobacteria	Deltaproteobacteria	Desulfobacterales	Desulfobacteraceae	Desulfatiferula	<i>Desulfatiferula sp.</i>	(Muyzer & Stams, 2008)
Bacteria	Proteobacteria	Deltaproteobacteria	Desulfobacterales	Desulfobacteraceae	Desulfatiglans	<i>Desulfatiglans anilini</i>	(Muyzer & Stams, 2008)
Bacteria	Proteobacteria	Deltaproteobacteria	Desulfobacterales	Desulfobacteraceae	Desulfatiglans	<i>Desulfatiglans parachlorophenolica</i>	(Muyzer & Stams, 2008)
Bacteria	Proteobacteria	Deltaproteobacteria	Syntrophobacterales	Syntrophobacteraceae	Desulfatimicrobium	<i>Desulfatimicrobium mahresensis</i>	(Muyzer & Stams, 2008)
Bacteria	Proteobacteria	Deltaproteobacteria	Desulfobacterales	Desulfobacteraceae	Desulfatirhabdium	<i>Desulfatirhabdium butyrativorans</i>	(Muyzer & Stams, 2008)
Bacteria	Proteobacteria	Deltaproteobacteria	Desulfobacterales	Desulfobacteraceae	Desulfatitalea	<i>Desulfatitalea sp.</i>	(Muyzer & Stams, 2008)
Bacteria	Proteobacteria	Deltaproteobacteria	Desulfobacterales	Desulfobacteraceae	Desulfatitalea	<i>Desulfatitalea tepidiphila</i>	(Muyzer & Stams, 2008)
Bacteria	Proteobacteria	Deltaproteobacteria	Desulfobacterales	Desulfobacteraceae	Desulfobacter	<i>Desulfobacter curvatus</i>	(Muyzer & Stams, 2008)
Bacteria	Proteobacteria	Deltaproteobacteria	Desulfobacterales	Desulfobacteraceae	Desulfobacter	<i>Desulfobacter halotolerans</i>	(Muyzer & Stams, 2008)
Bacteria	Proteobacteria	Deltaproteobacteria	Desulfobacterales	Desulfobacteraceae	Desulfobacter	<i>Desulfobacter hydrogenophilus</i>	(Muyzer & Stams, 2008)
Bacteria	Proteobacteria	Deltaproteobacteria	Desulfobacterales	Desulfobacteraceae	Desulfobacter	<i>Desulfobacter latus</i>	(Muyzer & Stams, 2008)
Bacteria	Proteobacteria	Deltaproteobacteria	Desulfobacterales	Desulfobacteraceae	Desulfobacter	<i>Desulfobacter postgatei</i>	(Muyzer & Stams, 2008)
Bacteria	Proteobacteria	Deltaproteobacteria	Desulfobacterales	Desulfobacteraceae	Desulfobacter	<i>Desulfobacter psychrotolerans</i>	(Muyzer & Stams, 2008)

Bacteria	Proteobacteria	Deltaproteobacteria	Desulfobacterales	Desulfobacteraceae	Desulfobacter	<i>Desulfobacter sp.</i>	(Muyzer & Stams, 2008)
Bacteria	Proteobacteria	Deltaproteobacteria	Desulfobacterales	Desulfobacteraceae	Desulfobacter	<i>Desulfobacter vibrioformis</i>	(Muyzer & Stams, 2008)
Bacteria	Proteobacteria	Deltaproteobacteria	Desulfobacterales	Desulfobacteraceae	Desulfatiglans	<i>Desulfobacterium anilini</i>	(Muyzer & Stams, 2008)
Bacteria	Proteobacteria	Deltaproteobacteria	Desulfobacterales	Desulfobacteraceae	Desulfobacterium	<i>Desulfobacterium autotrophicum</i>	(Muyzer & Stams, 2008)
Bacteria	Proteobacteria	Deltaproteobacteria	Desulfobacterales	Desulfobacteraceae	Desulfobacterium	<i>Desulfobacterium corrodens</i>	(Muyzer & Stams, 2008)
Bacteria	Proteobacteria	Deltaproteobacteria	Desulfobacterales	Desulfobacteraceae	Desulfobacterium	<i>Desulfobacterium indolicum</i>	(Muyzer & Stams, 2008)
Bacteria	Proteobacteria	Deltaproteobacteria	Desulfobacterales	Desulfobacteraceae	Desulfobacterium	<i>Desulfobacterium sp.</i>	(Muyzer & Stams, 2008)
Bacteria	Proteobacteria	Deltaproteobacteria	Desulfobacterales	Desulfobacteraceae	Desulfobacterium	<i>Desulfobacterium vacuolatum</i>	(Muyzer & Stams, 2008)
Bacteria	Proteobacteria	Deltaproteobacteria	Desulfobacterales	Desulfobacteraceae	Desulfobacterium	<i>Desulfobacterium zeppelinii</i>	(Muyzer & Stams, 2008)
Bacteria	Proteobacteria	Deltaproteobacteria	Desulfobacterales	Desulfobacteraceae	Desulfobacula	<i>Desulfobacula phenolica</i>	(Muyzer & Stams, 2008)
Bacteria	Proteobacteria	Deltaproteobacteria	Desulfobacterales	Desulfobacteraceae	Desulfobacula	<i>Desulfobacula sp.</i>	(Muyzer & Stams, 2008)
Bacteria	Proteobacteria	Deltaproteobacteria	Desulfobacterales	Desulfobacteraceae	Desulfobacula	<i>Desulfobacula toluolica</i>	(Muyzer & Stams, 2008)
Bacteria	Proteobacteria	Deltaproteobacteria	Desulfobacterales	Desulfobacteraceae	Desulfobotulus	<i>Desulfobotulus alkaliphilus</i>	(Muyzer & Stams, 2008)
Bacteria	Proteobacteria	Deltaproteobacteria	Desulfobacterales	Desulfobacteraceae	Desulfobotulus	<i>Desulfobotulus sapovorans</i>	(Muyzer & Stams, 2008)
Bacteria	Proteobacteria	Deltaproteobacteria	Desulfobacterales	Desulfobacteraceae	Desulfobotulus	<i>Desulfobotulus sp.</i>	(Muyzer & Stams, 2008)
Bacteria	Proteobacteria	Deltaproteobacteria	Desulfobacterales	Desulfobulbaceae	Desulfobulbus	<i>Desulfobulbus alkaliphilus</i>	(Muyzer & Stams, 2008)
Bacteria	Proteobacteria	Deltaproteobacteria	Desulfobacterales	Desulfobulbaceae	Desulfobulbus	<i>Desulfobulbus elongatus</i>	(Muyzer & Stams, 2008)
Bacteria	Proteobacteria	Deltaproteobacteria	Desulfobacterales	Desulfobulbaceae	Desulfobulbus	<i>Desulfobulbus japonicus</i>	(Muyzer & Stams, 2008)

Bacteria	Proteobacteria	Deltaproteobacteria	Desulfobacterales	Desulfobulbaceae	Desulfobulbus	<i>Desulfobulbus marinus</i>	(Muyzer & Stams, 2008)
Bacteria	Proteobacteria	Deltaproteobacteria	Desulfobacterales	Desulfobulbaceae	Desulfobulbus	<i>Desulfobulbus mediterraneus</i>	(Muyzer & Stams, 2008)
Bacteria	Proteobacteria	Deltaproteobacteria	Desulfobacterales	Desulfobulbaceae	Desulfobulbus	<i>Desulfobulbus propionicus</i>	(Muyzer & Stams, 2008)
Bacteria	Proteobacteria	Deltaproteobacteria	Desulfobacterales	Desulfobulbaceae	Desulfobulbus	<i>Desulfobulbus rhabdiformis</i>	(Muyzer & Stams, 2008)
Bacteria	Proteobacteria	Deltaproteobacteria	Desulfobacterales	Desulfobulbaceae	Desulfobulbus	<i>Desulfobulbus sp.</i>	(Muyzer & Stams, 2008)
Bacteria	Proteobacteria	deltaproteobacteria	deltaproteobacteria	deltaproteobacteria	Desulfocaldus	<i>Desulfocaldus terraneus</i>	(Muyzer & Stams, 2008)
Bacteria	Proteobacteria	Deltaproteobacteria	Desulfobacterales	Desulfobulbaceae	Desulfocapsa	<i>Desulfocapsa sp.</i>	(Muyzer & Stams, 2008)
Bacteria	Proteobacteria	Deltaproteobacteria	Desulfobacterales	Desulfobulbaceae	Desulfocapsa	<i>Desulfocapsa sulfexigens</i>	(Muyzer & Stams, 2008)
Bacteria	Proteobacteria	Deltaproteobacteria	Desulfobacterales	Desulfobulbaceae	Desulfocapsa	<i>Desulfocapsa thiozymogenes</i>	(Muyzer & Stams, 2008)
Bacteria	Proteobacteria	Deltaproteobacteria	Desulfobacterales	Desulfobacteraceae	Desulfocella	<i>Desulfocella halophila</i>	(Muyzer & Stams, 2008)
Bacteria	Proteobacteria	Deltaproteobacteria	Desulfobacterales	Desulfobacteraceae	Desulfocella	<i>Desulfocella sp.</i>	(Muyzer & Stams, 2008)
Bacteria	Proteobacteria	Deltaproteobacteria	Desulfobacterales	Desulfobacteraceae	Desulfococcus	<i>Desulfococcus biacutus</i>	(Muyzer & Stams, 2008)
Bacteria	Proteobacteria	Deltaproteobacteria	Desulfobacterales	Desulfobacteraceae	Desulfococcus	<i>Desulfococcus multivorans</i>	(Muyzer & Stams, 2008)
Bacteria	Proteobacteria	Deltaproteobacteria	Desulfobacterales	Desulfobacteraceae	Desulfobacterium	<i>Desulfococcus niacini</i>	(Muyzer & Stams, 2008)
Bacteria	Proteobacteria	Deltaproteobacteria	Desulfobacterales	Desulfobacteraceae	Desulfococcus	<i>Desulfococcus oleovorans</i>	(Muyzer & Stams, 2008)
Bacteria	Proteobacteria	Deltaproteobacteria	Desulfobacterales	Desulfobacteraceae	Desulfococcus	<i>Desulfococcus sp.</i>	(Muyzer & Stams, 2008)
Bacteria	Proteobacteria	Deltaproteobacteria	Desulfobacterales	Desulfobacteraceae	Desulfofaba	<i>Desulfofaba fastidiosa</i>	(Muyzer & Stams, 2008)
Bacteria	Proteobacteria	Deltaproteobacteria	Desulfobacterales	Desulfobacteraceae	Desulfofaba	<i>Desulfofaba gelida</i>	(Muyzer & Stams, 2008)

Bacteria	Proteobacteria	Deltaproteobacteria	Desulfobacterales	Desulfobacteraceae	Desulfofaba	<i>Desulfofaba hansenii</i>	(Muyzer & Stams, 2008)
Bacteria	Proteobacteria	Deltaproteobacteria	Desulfobacterales	Desulfobacteraceae	Desulfofrigus	<i>Desulfofrigus fragile</i>	(Muyzer & Stams, 2008)
Bacteria	Proteobacteria	Deltaproteobacteria	Desulfobacterales	Desulfobacteraceae	Desulfofrigus	<i>Desulfofrigus oceanense</i>	(Muyzer & Stams, 2008)
Bacteria	Proteobacteria	Deltaproteobacteria	Desulfobacterales	Desulfobacteraceae	Desulfofrigus	<i>Desulfofrigus sp.</i>	(Muyzer & Stams, 2008)
Bacteria	Proteobacteria	Deltaproteobacteria	Desulfobacterales	Desulfobulbaceae	Desulfofustis	<i>Desulfofustis glycolicus</i>	(Muyzer & Stams, 2008)
Bacteria	Proteobacteria	Deltaproteobacteria	Desulfobacterales	Desulfobulbaceae	Desulfofustis	<i>Desulfofustis sp.</i>	(Muyzer & Stams, 2008)
Bacteria	Proteobacteria	Deltaproteobacteria	Syntrophobacterales	Syntrophobacteraceae	Desulfoglaeba	<i>Desulfoglaeba alkanexedens</i>	(Muyzer & Stams, 2008)
Bacteria	Proteobacteria	Deltaproteobacteria	Syntrophobacterales	Syntrophobacteraceae	Desulfoglaeba	<i>Desulfoglaeba sp.</i>	(Muyzer & Stams, 2008)
Bacteria	Proteobacteria	Deltaproteobacteria	Desulfovibrionales	Desulfohalobiaceae	Desulfohalobium	<i>Desulfohalobium retbaense</i>	(Muyzer & Stams, 2008)
Bacteria	Proteobacteria	Deltaproteobacteria	Desulfovibrionales	Desulfohalobiaceae	Desulfohalobium	<i>Desulfohalobium sp.</i>	(Muyzer & Stams, 2008)
Bacteria	Proteobacteria	Deltaproteobacteria	Desulfovibrionales	Desulfohalobiaceae	Desulfohalobium	<i>Desulfohalobium utahense</i>	(Muyzer & Stams, 2008)
Bacteria	Proteobacteria	Deltaproteobacteria	Desulfobacterales	Desulfobacteraceae	Desulfoluna	<i>Desulfoluna butyratoxydans</i>	(Muyzer & Stams, 2008)
Bacteria	Proteobacteria	Deltaproteobacteria	Desulfobacterales	Desulfobacteraceae	Desulfoluna	<i>Desulfoluna sp.</i>	(Muyzer & Stams, 2008)
Bacteria	Proteobacteria	Deltaproteobacteria	Desulfobacterales	Desulfobacteraceae	Desulfoluna	<i>Desulfoluna spongiiphila</i>	(Muyzer & Stams, 2008)
Bacteria	Proteobacteria	Deltaproteobacteria	Desulfovibrionales	Desulfomicrobiaceae	Desulfomicrobium	<i>Desulfomicrobium apsheronum</i>	(Muyzer & Stams, 2008)
Bacteria	Proteobacteria	Deltaproteobacteria	Desulfovibrionales	Desulfomicrobiaceae	Desulfomicrobium	<i>Desulfomicrobium baculatum</i>	(Muyzer & Stams, 2008)
Bacteria	Proteobacteria	Deltaproteobacteria	Desulfovibrionales	Desulfomicrobiaceae	Desulfomicrobium	<i>Desulfomicrobium escambiense</i>	(Muyzer & Stams, 2008)
Bacteria	Proteobacteria	Deltaproteobacteria	Desulfovibrionales	Desulfomicrobiaceae	Desulfomicrobium	<i>Desulfomicrobium hypogeium</i>	(Muyzer & Stams, 2008)

Bacteria	Proteobacteria	Deltaproteobacteria	Desulfovibrionales	Desulfomicrobiaceae	Desulfomicrobi- um	<i>Desulfomicrobium macestii</i>	(Muyzer & Stams, 2008)
Bacteria	Proteobacteria	Deltaproteobacteria	Desulfovibrionales	Desulfomicrobiaceae	Desulfomicrobi- um	<i>Desulfomicrobium norvegicum</i>	(Muyzer & Stams, 2008)
Bacteria	Proteobacteria	Deltaproteobacteria	Desulfovibrionales	Desulfomicrobiaceae	Desulfomicrobi- um	<i>Desulfomicrobium orale</i>	(Muyzer & Stams, 2008)
Bacteria	Proteobacteria	Deltaproteobacteria	Desulfovibrionales	Desulfomicrobiaceae	Desulfomicrobi- um	<i>Desulfomicrobium sp.</i>	(Muyzer & Stams, 2008)
Bacteria	Proteobacteria	Deltaproteobacteria	Desulfovibrionales	Desulfomicrobiaceae	Desulfomicrobi- um	<i>Desulfomicrobium thermophilum</i>	(Muyzer & Stams, 2008)
Bacteria	Proteobacteria	Deltaproteobacteria	Syntrophobacterales	Syntrophaceae	Desulfomonile	<i>Desulfomonile limimaris</i>	(Muyzer & Stams, 2008)
Bacteria	Proteobacteria	Deltaproteobacteria	Syntrophobacterales	Syntrophaceae	Desulfomonile	<i>Desulfomonile tiedjei</i>	(Muyzer & Stams, 2008)
Bacteria	Proteobacteria	Deltaproteobacteria	Desulfobacterales	Desulfobacteraceae	Desulfonatrono- bacter	<i>Desulfonatronobact- er acidivorans</i>	(Muyzer & Stams, 2008)
Bacteria	Proteobacteria	Deltaproteobacteria	Desulfobacterales	Desulfobacteraceae	Desulfonatrono- bacter	<i>Desulfonatronobact- er sp.</i>	(Muyzer & Stams, 2008)
Bacteria	Proteobacteria	Deltaproteobacteria	Desulfovibrionales	Desulfohalobiaceae	Desulfonatrono- vibrio	<i>Desulfonatronovibri- o hydrogenovorans</i>	(Muyzer & Stams, 2008)
Bacteria	Proteobacteria	Deltaproteobacteria	Desulfovibrionales	Desulfonatronumaceae	Desulfonatronu- m	<i>Desulfonatronum cooperativum</i>	(Muyzer & Stams, 2008)
Bacteria	Proteobacteria	Deltaproteobacteria	Desulfovibrionales	Desulfonatronumaceae	Desulfonatronu- m	<i>Desulfonatronum lacustre</i>	(Muyzer & Stams, 2008)
Bacteria	Proteobacteria	Deltaproteobacteria	Desulfovibrionales	Desulfonatronumaceae	Desulfonatronu- m	<i>Desulfonatronum thiodismutans</i>	(Muyzer & Stams, 2008)
Bacteria	Proteobacteria	Deltaproteobacteria	Desulfobacterales	Desulfobacteraceae	Desulfonema	<i>Desulfonema ishimotonii</i>	(Muyzer & Stams, 2008)
Bacteria	Proteobacteria	Deltaproteobacteria	Desulfobacterales	Desulfobacteraceae	Desulfonema	<i>Desulfonema limicola</i>	(Muyzer & Stams, 2008)
Bacteria	Proteobacteria	Deltaproteobacteria	Desulfobacterales	Desulfobacteraceae	Desulfonema	<i>Desulfonema magnum</i>	(Muyzer & Stams, 2008)
Bacteria	Proteobacteria	Deltaproteobacteria	Desulfobacterales	Desulfobacteraceae	Desulfonema	<i>Desulfonema sp.</i>	(Muyzer & Stams, 2008)
Bacteria	Proteobacteria	Deltaproteobacteria	Desulfobacterales	Desulfobulbaceae	Desulfopila	<i>Desulfopila aestuarii</i>	(Muyzer & Stams, 2008)

Bacteria	Proteobacteria	Deltaproteobacteria	Desulfobacterales	Desulfobulbaceae	Desulfopila	<i>Desulfopila inferna</i>	(Muyzer & Stams, 2008)
Bacteria	Proteobacteria	Deltaproteobacteria	Desulfobacterales	Desulfobulbaceae	Desulfopila	<i>Desulfopila sp.</i>	(Muyzer & Stams, 2008)
Bacteria	Proteobacteria	Deltaproteobacteria	Desulfobacterales	Desulfobacteraceae	Desulforegula	<i>Desulforegula conservatrix</i>	(Muyzer & Stams, 2008)
Bacteria	Proteobacteria	Deltaproteobacteria	Desulfobacterales	Desulfobacteraceae	Desulforegula	<i>Desulforegula sp.</i>	(Muyzer & Stams, 2008)
Bacteria	Proteobacteria	Deltaproteobacteria	Syntrophobacterales	Syntrophobacteraceae	Desulforhabdus	<i>Desulforhabdus ammigena</i>	(Muyzer & Stams, 2008)
Bacteria	Proteobacteria	Deltaproteobacteria	Syntrophobacterales	Syntrophobacteraceae	Desulforhabdus	<i>Desulforhabdus sp.</i>	(Muyzer & Stams, 2008)
Bacteria	Proteobacteria	Deltaproteobacteria	Desulfobacterales	Desulfobulbaceae	Desulforhopalus	<i>Desulforhopalus singaporensis</i>	(Muyzer & Stams, 2008)
Bacteria	Proteobacteria	Deltaproteobacteria	Desulfobacterales	Desulfobulbaceae	Desulforhopalus	<i>Desulforhopalus sp.</i>	(Muyzer & Stams, 2008)
Bacteria	Proteobacteria	Deltaproteobacteria	Desulfobacterales	Desulfobulbaceae	Desulforhopalus	<i>Desulforhopalus vacuolatus</i>	(Muyzer & Stams, 2008)
Bacteria	Proteobacteria	Deltaproteobacteria	Desulfobacterales	Desulfobacteraceae	Desulfosalsimonas	<i>Desulfosalsimonas propionicica</i>	(Muyzer & Stams, 2008)
Bacteria	Proteobacteria	Deltaproteobacteria	Desulfobacterales	Desulfobacteraceae	Desulfosalsimonas	<i>Desulfosalsimonas sp.</i>	(Muyzer & Stams, 2008)
Bacteria	Proteobacteria	Deltaproteobacteria	Desulfobacterales	Desulfobacteraceae	Desulfosarcina	<i>Desulfosarcina cetonica</i>	(Muyzer & Stams, 2008)
Bacteria	Proteobacteria	Deltaproteobacteria	Desulfobacterales	Desulfobacteraceae	Desulfosarcina	<i>Desulfosarcina ovata</i>	(Muyzer & Stams, 2008)
Bacteria	Proteobacteria	Deltaproteobacteria	Desulfobacterales	Desulfobacteraceae	Desulfosarcina	<i>Desulfosarcina sp.</i>	(Muyzer & Stams, 2008)
Bacteria	Proteobacteria	Deltaproteobacteria	Desulfobacterales	Desulfobacteraceae	Desulfosarcina	<i>Desulfosarcina variabilis</i>	(Muyzer & Stams, 2008)
Bacteria	Proteobacteria	Deltaproteobacteria	Syntrophobacterales	Syntrophobacteraceae	Desulfosoma	<i>Desulfosoma caldarium</i>	(Muyzer & Stams, 2008)
Bacteria	Proteobacteria	Deltaproteobacteria	Syntrophobacterales	Syntrophobacteraceae	Desulfosoma	<i>Desulfosoma profundum</i>	(Muyzer & Stams, 2008)
Bacteria	Proteobacteria	Deltaproteobacteria	Desulfobacterales	Desulfobacteraceae	Desulfospira	<i>Desulfospira joergensenii</i>	(Muyzer & Stams, 2008)

Bacteria	Proteobacteria	Deltaproteobacteria	Desulfobacterales	Desulfobacteraceae	Desulfospira	<i>Desulfospira sp.</i>	(Muyzer & Stams, 2008)
Bacteria	Firmicutes	Negativicutes	Selenomonadales	Veillonellaceae	Desulfosporomusa	<i>Desulfosporomusa polytropha</i>	(Muyzer & Stams, 2008)
Bacteria	Firmicutes	Clostridia	Clostridiales	Peptococcaceae	Desulfosporosinus	<i>Desulfosporosinus meridiei</i>	(Muyzer & Stams, 2008)
Bacteria	Firmicutes	Clostridia	Clostridiales	Peptococcaceae	Desulfosporosinus	<i>Desulfosporosinus orientis</i>	(Muyzer & Stams, 2008)
Bacteria	Firmicutes	Clostridia	Clostridiales	Peptococcaceae	Desulfosporosinus	<i>Desulfosporosinus youngii</i>	(Muyzer & Stams, 2008)
Bacteria	Proteobacteria	Deltaproteobacteria	Desulfobacterales	Desulfobulbaceae	Desulfotalea	<i>Desulfotalea arctica</i>	(Muyzer & Stams, 2008)
Bacteria	Proteobacteria	Deltaproteobacteria	Desulfobacterales	Desulfobulbaceae	Desulfotalea	<i>Desulfotalea psychrophila</i>	(Muyzer & Stams, 2008)
Bacteria	Proteobacteria	Deltaproteobacteria	Desulfobacterales	Desulfobulbaceae	Desulfotalea	<i>Desulfotalea sp.</i>	(Muyzer & Stams, 2008)
Bacteria	Proteobacteria	Deltaproteobacteria	Desulfobacterales	Desulfobacteraceae	Desulfotignum	<i>Desulfotignum balticum</i>	(Muyzer & Stams, 2008)
Bacteria	Proteobacteria	Deltaproteobacteria	Desulfobacterales	Desulfobacteraceae	Desulfotignum	<i>Desulfotignum phosphitoxidans</i>	(Muyzer & Stams, 2008)
Bacteria	Proteobacteria	Deltaproteobacteria	Desulfobacterales	Desulfobacteraceae	Desulfotignum	<i>Desulfotignum sp.</i>	(Muyzer & Stams, 2008)
Bacteria	Proteobacteria	Deltaproteobacteria	Desulfobacterales	Desulfobacteraceae	Desulfotignum	<i>Desulfotignum toluenicum</i>	(Muyzer & Stams, 2008)
Bacteria	Firmicutes	Clostridia	Clostridiales	Peptococcaceae	Desulfotomaculum	<i>Desulfotomaculum acetoxidans</i>	(Muyzer & Stams, 2008)
Bacteria	Firmicutes	Clostridia	Clostridiales	Peptococcaceae	Desulfotomaculum	<i>Desulfotomaculum aeronauticum</i>	(Muyzer & Stams, 2008)
Bacteria	Firmicutes	Clostridia	Clostridiales	Peptococcaceae	Desulfotomaculum	<i>Desulfotomaculum alcoholivorax</i>	(Muyzer & Stams, 2008)
Bacteria	Firmicutes	Clostridia	Clostridiales	Peptococcaceae	Desulfotomaculum	<i>Desulfotomaculum alkaliphilum</i>	(Muyzer & Stams, 2008)
Bacteria	Firmicutes	Clostridia	Clostridiales	Peptococcaceae	Desulfotomaculum	<i>Desulfotomaculum arcticum</i>	(Muyzer & Stams, 2008)
Bacteria	Firmicutes	Clostridia	Clostridiales	Peptococcaceae	Desulfotomaculum	<i>Desulfotomaculum australicum</i>	(Muyzer & Stams, 2008)

Bacteria	Firmicutes	Clostridia	Clostridiales	Peptococcaceae	Desulfotomaculum	<i>Desulfotomaculum carboxydivorans</i>	(Muyzer & Stams, 2008)
Bacteria	Firmicutes	Clostridia	Clostridiales	Peptococcaceae	Desulfotomaculum	<i>Desulfotomaculum geothermicum</i>	(Muyzer & Stams, 2008)
Bacteria	Firmicutes	Clostridia	Clostridiales	Peptococcaceae	Desulfotomaculum	<i>Desulfotomaculum gibsoniae</i>	(Muyzer & Stams, 2008)
Bacteria	Firmicutes	Clostridia	Clostridiales	Peptococcaceae	Desulfotomaculum	<i>Desulfotomaculum halophilum</i>	(Muyzer & Stams, 2008)
Bacteria	Firmicutes	Clostridia	Clostridiales	Peptococcaceae	Desulfotomaculum	<i>Desulfotomaculum hydrothermale</i>	(Muyzer & Stams, 2008)
Bacteria	Firmicutes	Clostridia	Clostridiales	Peptococcaceae	Desulfotomaculum	<i>Desulfotomaculum indicum</i>	(Muyzer & Stams, 2008)
Bacteria	Firmicutes	Clostridia	Clostridiales	Peptococcaceae	Desulfotomaculum	<i>Desulfotomaculum intricatum</i>	(Muyzer & Stams, 2008)
Bacteria	Firmicutes	Clostridia	Clostridiales	Peptococcaceae	Desulfotomaculum	<i>Desulfotomaculum kuznetsovii</i>	(Muyzer & Stams, 2008)
Bacteria	Firmicutes	Clostridia	Clostridiales	Peptococcaceae	Desulfotomaculum	<i>Desulfotomaculum luciae</i>	(Muyzer & Stams, 2008)
Bacteria	Firmicutes	Clostridia	Clostridiales	Peptococcaceae	Desulfotomaculum	<i>Desulfotomaculum nigrificans</i>	(Muyzer & Stams, 2008)
Bacteria	Firmicutes	Clostridia	Clostridiales	Peptococcaceae	Desulfotomaculum	<i>Desulfotomaculum peckii</i>	(Muyzer & Stams, 2008)
Bacteria	Firmicutes	Clostridia	Clostridiales	Peptococcaceae	Desulfotomaculum	<i>Desulfotomaculum putei</i>	(Muyzer & Stams, 2008)
Bacteria	Firmicutes	Clostridia	Clostridiales	Peptococcaceae	Desulfotomaculum	<i>Desulfotomaculum reducens</i>	(Junier et al., 2010)
Bacteria	Firmicutes	Clostridia	Clostridiales	Peptococcaceae	Desulfotomaculum	<i>Desulfotomaculum ruminis</i>	(Muyzer & Stams, 2008)
Bacteria	Firmicutes	Clostridia	Clostridiales	Peptococcaceae	Desulfotomaculum	<i>Desulfotomaculum salinum</i>	(Muyzer & Stams, 2008)
Bacteria	Firmicutes	Clostridia	Clostridiales	Peptococcaceae	Desulfotomaculum	<i>Desulfotomaculum sapomandens</i>	(Muyzer & Stams, 2008)
Bacteria	Firmicutes	Clostridia	Clostridiales	Peptococcaceae	Desulfotomaculum	<i>Desulfotomaculum solfataricum</i>	(Muyzer & Stams, 2008)
Bacteria	Firmicutes	Clostridia	Clostridiales	Peptococcaceae	Desulfotomaculum	<i>Desulfotomaculum sp.</i>	(Muyzer & Stams, 2008)

Bacteria	Firmicutes	Clostridia	Clostridiales	Peptococcaceae	Desulfotomaculum	<i>Desulfotomaculum thermoacetoxidans</i>	(Muyzer & Stams, 2008)
Bacteria	Firmicutes	Clostridia	Clostridiales	Peptococcaceae	Desulfotomaculum	<i>Desulfotomaculum thermobenzoicum</i>	(Muyzer & Stams, 2008)
Bacteria	Firmicutes	Clostridia	Clostridiales	Peptococcaceae	Desulfotomaculum	<i>Desulfotomaculum thermocisternum</i>	(Muyzer & Stams, 2008)
Bacteria	Firmicutes	Clostridia	Clostridiales	Peptococcaceae	Desulfotomaculum	<i>Desulfotomaculum thermosapovorans</i>	(Muyzer & Stams, 2008)
Bacteria	Firmicutes	Clostridia	Clostridiales	Peptococcaceae	Desulfotomaculum	<i>Desulfotomaculum thermosubterraneum</i>	(Muyzer & Stams, 2008)
Bacteria	Firmicutes	Clostridia	Clostridiales	Peptococcaceae	Desulfotomaculum	<i>Desulfotomaculum varum</i>	(Muyzer & Stams, 2008)
Bacteria	Proteobacteria	Deltaproteobacteria	Desulfovibrionales	Desulfovibrionaceae	Desulfovibrio	<i>Desulfovibrio acrylicus</i>	(Wikipedia, 2015)
Bacteria	Proteobacteria	Deltaproteobacteria	Desulfovibrionales	Desulfovibrionaceae	Desulfovibrio	<i>Desulfovibrio aerotolerans</i>	(Wikipedia, 2015)
Bacteria	Proteobacteria	Deltaproteobacteria	Desulfovibrionales	Desulfovibrionaceae	Desulfovibrio	<i>Desulfovibrio aespoeensis</i>	(Wikipedia, 2015)
Bacteria	Proteobacteria	Deltaproteobacteria	Desulfovibrionales	Desulfovibrionaceae	Desulfovibrio	<i>Desulfovibrio africanus</i>	(Wikipedia, 2015)
Bacteria	Proteobacteria	Deltaproteobacteria	Desulfovibrionales	Desulfovibrionaceae	Desulfovibrio	<i>Desulfovibrio alaskensis</i>	(Wikipedia, 2015)
Bacteria	Proteobacteria	Deltaproteobacteria	Desulfovibrionales	Desulfovibrionaceae	Desulfovibrio	<i>Desulfovibrio alcoholivorans</i>	(Wikipedia, 2015)
Bacteria	Proteobacteria	Deltaproteobacteria	Desulfovibrionales	Desulfovibrionaceae	Desulfovibrio	<i>Desulfovibrio alitoralis</i>	(Wikipedia, 2015)
Bacteria	Proteobacteria	Deltaproteobacteria	Desulfovibrionales	Desulfovibrionaceae	Desulfovibrio	<i>Desulfovibrio alkalitolerans</i>	(Wikipedia, 2015)
Bacteria	Proteobacteria	Deltaproteobacteria	Desulfovibrionales	Desulfovibrionaceae	Desulfovibrio	<i>Desulfovibrio aminophilus</i>	(Wikipedia, 2015)
Bacteria	Proteobacteria	Deltaproteobacteria	Desulfovibrionales	Desulfovibrionaceae	Desulfovibrio	<i>Desulfovibrio arcticus</i>	(Wikipedia, 2015)
Bacteria	Proteobacteria	Deltaproteobacteria	Desulfovibrionales	Desulfovibrionaceae	Desulfovibrio	<i>Desulfovibrio baarsii</i>	(Wikipedia, 2015)

Bacteria	Proteobacteria	Deltaproteobacteria	Desulfovibrionales	Desulfovibrionaceae	Desulfovibrio	<i>Desulfovibrio baculatus</i>	(Wikipedia, 2015)
Bacteria	Proteobacteria	Deltaproteobacteria	Desulfovibrionales	Desulfovibrionaceae	Desulfovibrio	<i>Desulfovibrio bastinii</i>	(Wikipedia, 2015)
Bacteria	Proteobacteria	Deltaproteobacteria	Desulfovibrionales	Desulfovibrionaceae	Desulfovibrio	<i>Desulfovibrio bizertensis</i>	(Wikipedia, 2015)
Bacteria	Proteobacteria	Deltaproteobacteria	Desulfovibrionales	Desulfovibrionaceae	Desulfovibrio	<i>Desulfovibrio burkinensis</i>	(Wikipedia, 2015)
Bacteria	Proteobacteria	Deltaproteobacteria	Desulfovibrionales	Desulfovibrionaceae	Desulfovibrio	<i>Desulfovibrio butyratiphilus</i>	(Wikipedia, 2015)
Bacteria	Proteobacteria	Deltaproteobacteria	Desulfovibrionales	Desulfovibrionaceae	Desulfovibrio	<i>Desulfovibrio capillatus</i>	(Wikipedia, 2015)
Bacteria	Proteobacteria	Deltaproteobacteria	Desulfovibrionales	Desulfovibrionaceae	Desulfovibrio	<i>Desulfovibrio carbinolicus</i>	(Wikipedia, 2015)
Bacteria	Proteobacteria	Deltaproteobacteria	Desulfovibrionales	Desulfovibrionaceae	Desulfovibrio	<i>Desulfovibrio carbinoliphilus</i>	(Wikipedia, 2015)
Bacteria	Proteobacteria	Deltaproteobacteria	Desulfovibrionales	Desulfovibrionaceae	Desulfovibrio	<i>Desulfovibrio cuneatus</i>	(Wikipedia, 2015)
Bacteria	Proteobacteria	Deltaproteobacteria	Desulfovibrionales	Desulfovibrionaceae	Desulfovibrio	<i>Desulfovibrio dechloracetivorans</i>	(Wikipedia, 2015)
Bacteria	Proteobacteria	Deltaproteobacteria	Desulfovibrionales	Desulfovibrionaceae	Desulfovibrio	<i>Desulfovibrio desulfuricans</i>	(Wikipedia, 2015)
Bacteria	Proteobacteria	Deltaproteobacteria	Desulfovibrionales	Desulfovibrionaceae	Desulfovibrio	<i>Desulfovibrio ferrireducens</i>	(Wikipedia, 2015)
Bacteria	Proteobacteria	Deltaproteobacteria	Desulfovibrionales	Desulfovibrionaceae	Desulfovibrio	<i>Desulfovibrio frigidus</i>	(Wikipedia, 2015)
Bacteria	Proteobacteria	Deltaproteobacteria	Desulfovibrionales	Desulfovibrionaceae	Desulfovibrio	<i>Desulfovibrio fructosivorans</i>	(Wikipedia, 2015)
Bacteria	Proteobacteria	Deltaproteobacteria	Desulfovibrionales	Desulfovibrionaceae	Desulfovibrio	<i>Desulfovibrio furfuralis</i>	(Wikipedia, 2015)
Bacteria	Proteobacteria	Deltaproteobacteria	Desulfovibrionales	Desulfovibrionaceae	Desulfovibrio	<i>Desulfovibrio gabonensis</i>	(Wikipedia, 2015)
Bacteria	Proteobacteria	Deltaproteobacteria	Desulfovibrionales	Desulfovibrionaceae	Desulfovibrio	<i>Desulfovibrio giganteus</i>	(Wikipedia, 2015)
Bacteria	Proteobacteria	Deltaproteobacteria	Desulfovibrionales	Desulfovibrionaceae	Desulfovibrio	<i>Desulfovibrio gigas</i>	(Wikipedia, 2015)

Bacteria	Proteobacteria	Deltaproteobacteria	Desulfovibrionales	Desulfovibrionaceae	Desulfovibrio	<i>Desulfovibrio gracilis</i>	(Wikipedia, 2015)
Bacteria	Proteobacteria	Deltaproteobacteria	Desulfovibrionales	Desulfovibrionaceae	Desulfovibrio	<i>Desulfovibrio halophilus</i>	(Wikipedia, 2015)
Bacteria	Proteobacteria	Deltaproteobacteria	Desulfovibrionales	Desulfovibrionaceae	Desulfovibrio	<i>Desulfovibrio hydrothermalis</i>	(Wikipedia, 2015)
Bacteria	Proteobacteria	Deltaproteobacteria	Desulfovibrionales	Desulfovibrionaceae	Desulfovibrio	<i>Desulfovibrio idahonensis</i>	(Wikipedia, 2015)
Bacteria	Proteobacteria	Deltaproteobacteria	Desulfovibrionales	Desulfovibrionaceae	Desulfovibrio	<i>Desulfovibrio indonesiensis</i>	(Wikipedia, 2015)
Bacteria	Proteobacteria	Deltaproteobacteria	Desulfovibrionales	Desulfovibrionaceae	Desulfovibrio	<i>Desulfovibrio inopinatus</i>	(Wikipedia, 2015)
Bacteria	Proteobacteria	Deltaproteobacteria	Desulfovibrionales	Desulfovibrionaceae	Desulfovibrio	<i>Desulfovibrio intestinalis</i>	(Wikipedia, 2015)
Bacteria	Proteobacteria	Deltaproteobacteria	Desulfovibrionales	Desulfovibrionaceae	Desulfovibrio	<i>Desulfovibrio legallii</i>	(Wikipedia, 2015)
Bacteria	Proteobacteria	Deltaproteobacteria	Desulfovibrionales	Desulfovibrionaceae	Desulfovibrio	<i>Desulfovibrio longreachensis</i>	(Wikipedia, 2015)
Bacteria	Proteobacteria	Deltaproteobacteria	Desulfovibrionales	Desulfovibrionaceae	Desulfovibrio	<i>Desulfovibrio longus</i>	(Wikipedia, 2015)
Bacteria	Proteobacteria	Deltaproteobacteria	Desulfovibrionales	Desulfovibrionaceae	Desulfovibrio	<i>Desulfovibrio magneticus</i>	(Wikipedia, 2015)
Bacteria	Proteobacteria	Deltaproteobacteria	Desulfovibrionales	Desulfovibrionaceae	Desulfovibrio	<i>Desulfovibrio marinisediminis</i>	(Wikipedia, 2015)
Bacteria	Proteobacteria	Deltaproteobacteria	Desulfovibrionales	Desulfovibrionaceae	Desulfovibrio	<i>Desulfovibrio marinus</i>	(Wikipedia, 2015)
Bacteria	Proteobacteria	Deltaproteobacteria	Desulfovibrionales	Desulfovibrionaceae	Desulfovibrio	<i>Desulfovibrio marrakechensis</i>	(Wikipedia, 2015)
Bacteria	Proteobacteria	Deltaproteobacteria	Desulfovibrionales	Desulfovibrionaceae	Desulfovibrio	<i>Desulfovibrio mexicanus</i>	(Wikipedia, 2015)
Bacteria	Proteobacteria	Deltaproteobacteria	Desulfovibrionales	Desulfovibrionaceae	Desulfovibrio	<i>Desulfovibrio multispirans</i>	(Wikipedia, 2015)
Bacteria	Proteobacteria	Deltaproteobacteria	Desulfovibrionales	Desulfovibrionaceae	Desulfovibrio	<i>Desulfovibrio oceani</i>	(Wikipedia, 2015)
Bacteria	Proteobacteria	Deltaproteobacteria	Desulfovibrionales	Desulfovibrionaceae	Desulfovibrio	<i>Desulfovibrio oxamicus</i>	(Wikipedia, 2015)

Bacteria	Proteobacteria	Deltaproteobacteria	Desulfovibrionales	Desulfovibrionaceae	Desulfovibrio	<i>Desulfovibrio oxyclinae</i>	(Wikipedia, 2015)
Bacteria	Proteobacteria	Deltaproteobacteria	Desulfovibrionales	Desulfovibrionaceae	Desulfovibrio	<i>Desulfovibrio paquesii</i>	(Wikipedia, 2015)
Bacteria	Proteobacteria	Deltaproteobacteria	Desulfovibrionales	Desulfovibrionaceae	Desulfovibrio	<i>Desulfovibrio piezophilus</i>	(Wikipedia, 2015)
Bacteria	Proteobacteria	Deltaproteobacteria	Desulfovibrionales	Desulfovibrionaceae	Desulfovibrio	<i>Desulfovibrio pigra</i>	(Wikipedia, 2015)
Bacteria	Proteobacteria	Deltaproteobacteria	Desulfovibrionales	Desulfovibrionaceae	Desulfovibrio	<i>Desulfovibrio portus</i>	(Wikipedia, 2015)
Bacteria	Proteobacteria	Deltaproteobacteria	Desulfovibrionales	Desulfovibrionaceae	Desulfovibrio	<i>Desulfovibrio profundus</i>	(Wikipedia, 2015)
Bacteria	Proteobacteria	Deltaproteobacteria	Desulfovibrionales	Desulfovibrionaceae	Desulfovibrio	<i>Desulfovibrio psychrotolerans</i>	(Wikipedia, 2015)
Bacteria	Proteobacteria	Deltaproteobacteria	Desulfovibrionales	Desulfovibrionaceae	Desulfovibrio	<i>Desulfovibrio putealis</i>	(Wikipedia, 2015)
Bacteria	Proteobacteria	Deltaproteobacteria	Desulfovibrionales	Desulfovibrionaceae	Desulfovibrio	<i>Desulfovibrio salixigens</i>	(Wikipedia, 2015)
Bacteria	Proteobacteria	Deltaproteobacteria	Desulfovibrionales	Desulfovibrionaceae	Desulfovibrio	<i>Desulfovibrio sapovorans</i>	(Wikipedia, 2015)
Bacteria	Proteobacteria	Deltaproteobacteria	Desulfovibrionales	Desulfovibrionaceae	Desulfovibrio	<i>Desulfovibrio senezii</i>	(Wikipedia, 2015)
Bacteria	Proteobacteria	Deltaproteobacteria	Desulfovibrionales	Desulfovibrionaceae	Desulfovibrio	<i>Desulfovibrio simplex</i>	(Wikipedia, 2015)
Bacteria	Proteobacteria	Deltaproteobacteria	Desulfovibrionales	Desulfovibrionaceae	Desulfovibrio	<i>Desulfovibrio sulfodismutans</i>	(Wikipedia, 2015)
Bacteria	Proteobacteria	Deltaproteobacteria	Desulfovibrionales	Desulfovibrionaceae	Desulfovibrio	<i>Desulfovibrio termitidis</i>	(Wikipedia, 2015)
Bacteria	Proteobacteria	Deltaproteobacteria	Desulfovibrionales	Desulfovibrionaceae	Desulfovibrio	<i>Desulfovibrio thermophilus</i>	(Wikipedia, 2015)
Bacteria	Proteobacteria	Deltaproteobacteria	Desulfovibrionales	Desulfovibrionaceae	Desulfovibrio	<i>Desulfovibrio tunisiensis</i>	(Wikipedia, 2015)
Bacteria	Proteobacteria	Deltaproteobacteria	Desulfovibrionales	Desulfovibrionaceae	Desulfovibrio	<i>Desulfovibrio vietnamensis</i>	(Wikipedia, 2015)
Bacteria	Proteobacteria	Deltaproteobacteria	Desulfovibrionales	Desulfovibrionaceae	Desulfovibrio	<i>Desulfovibrio vulgaris</i>	(Wikipedia, 2015)

Bacteria	Proteobacteria	Deltaproteobacteria	Desulfovibrionales	Desulfovibrionaceae	Desulfovibrio	<i>Desulfovibrio zosteriae</i>	(Wikipedia, 2015)
Bacteria	Proteobacteria	Deltaproteobacteria	Syntrophobacterales	Syntrophobacteraceae	Desulfovirga	<i>Desulfovirga adipica</i>	(Muyzer & Stams, 2008)
Bacteria	Proteobacteria	Deltaproteobacteria	Syntrophobacterales	Syntrophobacteraceae	Desulfovirga	<i>Desulfovirga sp.</i>	(Muyzer & Stams, 2008)
Bacteria	Proteobacteria	Deltaproteobacteria	Desulfobacterales	Desulfobulbaceae	Desulfurivibrio	<i>Desulfurivibrio alkaliphilus</i>	(Muyzer & Stams, 2008)
Bacteria	Proteobacteria	Deltaproteobacteria	Desulfobacterales	Desulfobulbaceae	Desulfurivibrio	<i>Desulfurivibrio sp.</i>	(Muyzer & Stams, 2008)
Bacteria	Proteobacteria	Deltaproteobacteria	Syntrophobacterales	Syntrophobacteraceae	Syntrophobacter	<i>Syntrophobacter fumaroxidans</i>	(Muyzer & Stams, 2008)
Bacteria	Proteobacteria	Deltaproteobacteria	Syntrophobacterales	Syntrophobacteraceae	Syntrophobacter	<i>Syntrophobacter pfennigii</i>	(Muyzer & Stams, 2008)
Bacteria	Proteobacteria	Deltaproteobacteria	Syntrophobacterales	Syntrophobacteraceae	Syntrophobacter	<i>Syntrophobacter sp.</i>	(Muyzer & Stams, 2008)
Bacteria	Proteobacteria	Deltaproteobacteria	Syntrophobacterales	Syntrophobacteraceae	Syntrophobacter	<i>Syntrophobacter sulfatireducens</i>	(Muyzer & Stams, 2008)
Bacteria	Proteobacteria	Deltaproteobacteria	Syntrophobacterales	Syntrophobacteraceae	Syntrophobacter	<i>Syntrophobacter wolinii</i>	(Muyzer & Stams, 2008)
Archaea	Crenarchaeota	Thermoprotei	Thermoproteales	Thermoproteaceae	Thermocladium	<i>Thermocladium modestius</i>	(Muyzer & Stams, 2008)
Bacteria	Thermodesulfobacteria	Thermodesulfobacteria	Thermodesulfobacterales	Thermodesulfobacteriaceae	Thermodesulfator	<i>Thermodesulfator indicus</i>	(Muyzer & Stams, 2008)
Bacteria	Thermodesulfobacteria	Thermodesulfobacteria	Thermodesulfobacterales	Thermodesulfobacteriaceae	Thermodesulfobacterium	<i>Thermodesulfobacterium commune</i>	(Muyzer & Stams, 2008)
Bacteria	Thermodesulfobacteria	Thermodesulfobacteria	Thermodesulfobacterales	Thermodesulfobacteriaceae	Thermodesulfobacterium	<i>Thermodesulfobacterium hveragerdense</i>	(Muyzer & Stams, 2008)
Bacteria	Thermodesulfobacteria	Thermodesulfobacteria	Thermodesulfobacterales	Thermodesulfobacteriaceae	Thermodesulfobacterium	<i>Thermodesulfobacterium hydrogeniphilum</i>	(Muyzer & Stams, 2008)
Bacteria	Thermodesulfobacteria	Thermodesulfobacteria	Thermodesulfobacterales	Thermodesulfobacteriaceae	Thermodesulfobacterium	<i>Thermodesulfobacterium thermophilum</i>	(Muyzer & Stams, 2008)
Bacteria	Firmicutes	Clostridia	Thermoanaerobacterales	Thermodesulfobiaceae	Thermodesulfobium	<i>Thermodesulfobium narugense</i>	(Muyzer & Stams, 2008)

Bacteria	Proteobacteria	Deltaproteobacteria	Syntrophobacterales	Syntrophobacteraceae	Thermodesulforhabdus	<i>Thermodesulforhabdus norvegica</i>	(Muyzer & Stams, 2008)
Bacteria	Proteobacteria	Deltaproteobacteria	Syntrophobacterales	Syntrophobacteraceae	Thermodesulforhabdus	<i>Thermodesulforhabdus sp.</i>	(Muyzer & Stams, 2008)
Bacteria	Nitrospirae	Nitrospira	Nitrospirales	Nitrospiraceae	Thermodesulfovibrio	<i>Thermodesulfovibrio islandicus</i>	(Muyzer & Stams, 2008)
Bacteria	Nitrospirae	Nitrospira	Nitrospirales	Nitrospiraceae	Thermodesulfovibrio	<i>Thermodesulfovibrio yellowstonii</i>	(Muyzer & Stams, 2008)

Table S5.4 Assembled methanogens from Department of Biotechnology University of Wrocław (2015)

King	Phylum	Class	Order	Family	Genus	Strain
Archaea	Euryarchaeota	Methanobacteria	Methanobacteriales	Methanobacteriaceae	Methanobacterium	<i>Methanobacterium aarhusense</i>
Archaea	Euryarchaeota	Methanobacteria	Methanobacteriales	Methanobacteriaceae	Methanobacterium	<i>Methanobacterium alcaliphilum</i>
Archaea	Euryarchaeota	Methanobacteria	Methanobacteriales	Methanobacteriaceae	Methanobacterium	<i>Methanobacterium arcticum</i>
Archaea	Euryarchaeota	Methanobacteria	Methanobacteriales	Methanobacteriaceae	Methanobacterium	<i>Methanobacterium beijingense</i>
Archaea	Euryarchaeota	Methanobacteria	Methanobacteriales	Methanobacteriaceae	Methanobacterium	<i>Methanobacterium bryantii</i>
Archaea	Euryarchaeota	Methanobacteria	Methanobacteriales	Methanobacteriaceae	Methanobacterium	<i>Methanobacterium congolense</i>
Archaea	Euryarchaeota	Methanobacteria	Methanobacteriales	Methanobacteriaceae	Methanobacterium	<i>Methanobacterium espanolae</i>
Archaea	Euryarchaeota	Methanobacteria	Methanobacteriales	Methanobacteriaceae	Methanobacterium	<i>Methanobacterium ferruginis</i>
Archaea	Euryarchaeota	Methanobacteria	Methanobacteriales	Methanobacteriaceae	Methanobacterium	<i>Methanobacterium flexile</i>
Archaea	Euryarchaeota	Methanobacteria	Methanobacteriales	Methanobacteriaceae	Methanobacterium	<i>Methanobacterium formicicum</i>
Archaea	Euryarchaeota	Methanobacteria	Methanobacteriales	Methanobacteriaceae	Methanobacterium	<i>Methanobacterium ivanovii</i>
Archaea	Euryarchaeota	Methanobacteria	Methanobacteriales	Methanobacteriaceae	Methanobacterium	<i>Methanobacterium kanagiense</i>
Archaea	Euryarchaeota	Methanobacteria	Methanobacteriales	Methanobacteriaceae	Methanobacterium	<i>Methanobacterium lacus</i>
Archaea	Euryarchaeota	Methanobacteria	Methanobacteriales	Methanobacteriaceae	Methanobacterium	<i>Methanobacterium movens</i>
Archaea	Euryarchaeota	Methanobacteria	Methanobacteriales	Methanobacteriaceae	Methanobacterium	<i>Methanobacterium movilense</i>
Archaea	Euryarchaeota	Methanobacteria	Methanobacteriales	Methanobacteriaceae	Methanobacterium	<i>Methanobacterium oryzae</i>
Archaea	Euryarchaeota	Methanobacteria	Methanobacteriales	Methanobacteriaceae	Methanobacterium	<i>Methanobacterium palustre</i>
Archaea	Euryarchaeota	Methanobacteria	Methanobacteriales	Methanobacteriaceae	Methanobacterium	<i>Methanobacterium petrolearium</i>
Archaea	Euryarchaeota	Methanobacteria	Methanobacteriales	Methanobacteriaceae	Methanobacterium	<i>Methanobacterium subterraneum</i>
Archaea	Euryarchaeota	Methanobacteria	Methanobacteriales	Methanobacteriaceae	Methanobacterium	<i>Methanobacterium thermaggrens</i>
Archaea	Euryarchaeota	Methanobacteria	Methanobacteriales	Methanobacteriaceae	Methanobacterium	<i>Methanobacterium uliginosum</i>
Archaea	Euryarchaeota	Methanobacteria	Methanobacteriales	Methanobacteriaceae	Methanobacterium	<i>Methanobacterium veterum</i>
Archaea	Euryarchaeota	Methanobacteria	Methanobacteriales	Methanobacteriaceae	Methanobrevibacter	<i>Methanobrevibacter acididurans</i>
Archaea	Euryarchaeota	Methanobacteria	Methanobacteriales	Methanobacteriaceae	Methanobrevibacter	<i>Methanobrevibacter arboriphilus</i>
Archaea	Euryarchaeota	Methanobacteria	Methanobacteriales	Methanobacteriaceae	Methanobrevibacter	<i>Methanobrevibacter boviskoreani</i>

Archaea	Euryarchaeota	Methanobacteria	Methanobacteriales	Methanobacteriaceae	Methanobrevibacter	<i>Methanobrevibacter curvatus</i>
Archaea	Euryarchaeota	Methanobacteria	Methanobacteriales	Methanobacteriaceae	Methanobrevibacter	<i>Methanobrevibacter cuticularis</i>
Archaea	Euryarchaeota	Methanobacteria	Methanobacteriales	Methanobacteriaceae	Methanobrevibacter	<i>Methanobrevibacter filiformis</i>
Archaea	Euryarchaeota	Methanobacteria	Methanobacteriales	Methanobacteriaceae	Methanobrevibacter	<i>Methanobrevibacter gottschalkii</i>
Archaea	Euryarchaeota	Methanobacteria	Methanobacteriales	Methanobacteriaceae	Methanobrevibacter	<i>Methanobrevibacter millerae</i>
Archaea	Euryarchaeota	Methanobacteria	Methanobacteriales	Methanobacteriaceae	Methanobrevibacter	<i>Methanobrevibacter olleyae</i>
Archaea	Euryarchaeota	Methanobacteria	Methanobacteriales	Methanobacteriaceae	Methanobrevibacter	<i>Methanobrevibacter oralis</i>
Archaea	Euryarchaeota	Methanobacteria	Methanobacteriales	Methanobacteriaceae	Methanobrevibacter	<i>Methanobrevibacter ruminantium</i>
Archaea	Euryarchaeota	Methanobacteria	Methanobacteriales	Methanobacteriaceae	Methanobrevibacter	<i>Methanobrevibacter smithii</i>
Archaea	Euryarchaeota	Methanobacteria	Methanobacteriales	Methanobacteriaceae	Methanobrevibacter	<i>Methanobrevibacter thaueri</i>
Archaea	Euryarchaeota	Methanobacteria	Methanobacteriales	Methanobacteriaceae	Methanobrevibacter	<i>Methanobrevibacter woesei</i>
Archaea	Euryarchaeota	Methanobacteria	Methanobacteriales	Methanobacteriaceae	Methanobrevibacter	<i>Methanobrevibacter wolinii</i>
Archaea	Euryarchaeota	Methanomicrobia	Methanomicrobiales	Methanocalculaceae	Methanocalculus	<i>Methanocalculus chunghsingensis</i>
Archaea	Euryarchaeota	Methanomicrobia	Methanomicrobiales	Methanocalculaceae	Methanocalculus	<i>Methanocalculus halotolerans</i>
Archaea	Euryarchaeota	Methanomicrobia	Methanomicrobiales	Methanocalculaceae	Methanocalculus	<i>Methanocalculus natronophilus</i>
Archaea	Euryarchaeota	Methanomicrobia	Methanomicrobiales	Methanocalculaceae	Methanocalculus	<i>Methanocalculus pumilus</i>
Archaea	Euryarchaeota	Methanomicrobia	Methanomicrobiales	Methanocalculaceae	Methanocalculus	<i>Methanocalculus taiwanensis</i>
Archaea	Euryarchaeota	Methanococci	Methanococcales	Methanocaldococcaceae	Methanocaldococcus	<i>Methanocaldococcus fervens</i>
Archaea	Euryarchaeota	Methanococci	Methanococcales	Methanocaldococcaceae	Methanocaldococcus	<i>Methanocaldococcus indicus</i>
Archaea	Euryarchaeota	Methanococci	Methanococcales	Methanocaldococcaceae	Methanocaldococcus	<i>Methanocaldococcus infernus</i>
Archaea	Euryarchaeota	Methanococci	Methanococcales	Methanocaldococcaceae	Methanocaldococcus	<i>Methanocaldococcus jannaschii</i>
Archaea	Euryarchaeota	Methanococci	Methanococcales	Methanocaldococcaceae	Methanocaldococcus	<i>Methanocaldococcus villosus</i>
Archaea	Euryarchaeota	Methanococci	Methanococcales	Methanocaldococcaceae	Methanocaldococcus	<i>Methanocaldococcus vulcanius</i>
Archaea	Euryarchaeota	Methanomicrobia	Methanocellales	Methanocellaceae	Methanocella	<i>Methanocella arvoryzae</i>
Archaea	Euryarchaeota	Methanomicrobia	Methanocellales	Methanocellaceae	Methanocella	<i>Methanocella conradii</i>

Archaea	Euryarchaeota	Methanomicrobia	Methanocellales	Methanocellaceae	Methanocella	<i>Methanocella paludicola</i>
Archaea	Euryarchaeota	Methanomicrobia	Methanosarcinales	Methanosarcinaceae	Methanococcoides	<i>Methanococcoides alaskense</i>
Archaea	Euryarchaeota	Methanomicrobia	Methanosarcinales	Methanosarcinaceae	Methanococcoides	<i>Methanococcoides burtonii</i>
Archaea	Euryarchaeota	Methanomicrobia	Methanosarcinales	Methanosarcinaceae	Methanococcoides	<i>Methanococcoides methylutens</i>
Archaea	Euryarchaeota	Methanomicrobia	Methanosarcinales	Methanosarcinaceae	Methanococcoides	<i>Methanococcoides vulcani</i>
Archaea	Euryarchaeota	Methanococci	Methanococcales	Methanococcaceae	Methanococcus	<i>Methanococcus aeolicus</i>
Archaea	Euryarchaeota	Methanococci	Methanococcales	Methanococcaceae	Methanococcus	<i>Methanococcus maripaludis</i>
Archaea	Euryarchaeota	Methanococci	Methanococcales	Methanococcaceae	Methanococcus	<i>Methanococcus vannielii</i>
Archaea	Euryarchaeota	Methanococci	Methanococcales	Methanococcaceae	Methanococcus	<i>Methanococcus voltae</i>
Archaea	Euryarchaeota	Methanomicrobia	Methanomicrobiales	Methanocorpusculaceae	Methanocorpusculum	<i>Methanocorpusculum aggregans</i>
Archaea	Euryarchaeota	Methanomicrobia	Methanomicrobiales	Methanocorpusculaceae	Methanocorpusculum	<i>Methanocorpusculum bavaricum</i>
Archaea	Euryarchaeota	Methanomicrobia	Methanomicrobiales	Methanocorpusculaceae	Methanocorpusculum	<i>Methanocorpusculum labreanum</i>
Archaea	Euryarchaeota	Methanomicrobia	Methanomicrobiales	Methanocorpusculaceae	Methanocorpusculum	<i>Methanocorpusculum parvum</i>
Archaea	Euryarchaeota	Methanomicrobia	Methanomicrobiales	Methanocorpusculaceae	Methanocorpusculum	<i>Methanocorpusculum sinense</i>
Archaea	Euryarchaeota	Methanomicrobia	Methanomicrobiales	Methanomicrobiaceae	Methanoculleus	<i>Methanoculleus bourgensis</i>
Archaea	Euryarchaeota	Methanomicrobia	Methanomicrobiales	Methanomicrobiaceae	Methanoculleus	<i>Methanoculleus chikugoensis</i>
Archaea	Euryarchaeota	Methanomicrobia	Methanomicrobiales	Methanomicrobiaceae	Methanoculleus	<i>Methanoculleus horonobensis</i>
Archaea	Euryarchaeota	Methanomicrobia	Methanomicrobiales	Methanomicrobiaceae	Methanoculleus	<i>Methanoculleus hydrogenitrophicus</i>
Archaea	Euryarchaeota	Methanomicrobia	Methanomicrobiales	Methanomicrobiaceae	Methanoculleus	<i>Methanoculleus marisnigri</i>
Archaea	Euryarchaeota	Methanomicrobia	Methanomicrobiales	Methanomicrobiaceae	Methanoculleus	<i>Methanoculleus palmolei</i>
Archaea	Euryarchaeota	Methanomicrobia	Methanomicrobiales	Methanomicrobiaceae	Methanoculleus	<i>Methanoculleus receptaculi</i>
Archaea	Euryarchaeota	Methanomicrobia	Methanomicrobiales	Methanomicrobiaceae	Methanoculleus	<i>Methanoculleus submarinus</i>
Archaea	Euryarchaeota	Methanomicrobia	Methanomicrobiales	Methanomicrobiaceae	Methanoculleus	<i>Methanoculleus thermophilus</i>
Archaea	Euryarchaeota	Methanomicrobia	Methanomicrobiales	Methanomicrobiaceae	Methanofollis	<i>Methanofollis aquaemaris</i>
Archaea	Euryarchaeota	Methanomicrobia	Methanomicrobiales	Methanomicrobiaceae	Methanofollis	<i>Methanofollis ethanolicus</i>
Archaea	Euryarchaeota	Methanomicrobia	Methanomicrobiales	Methanomicrobiaceae	Methanofollis	<i>Methanofollis formosanus</i>
Archaea	Euryarchaeota	Methanomicrobia	Methanomicrobiales	Methanomicrobiaceae	Methanofollis	<i>Methanofollis liminatans</i>
Archaea	Euryarchaeota	Methanomicrobia	Methanomicrobiales	Methanomicrobiaceae	Methanofollis	<i>Methanofollis tationis</i>
Archaea	Euryarchaeota	Methanomicrobia	Methanomicrobiales	Methanomicrobiaceae	Methanogenium	<i>Methanogenium boonei</i>

Archaea	Euryarchaeota	Methanomicrobia	Methanomicrobiales	Methanomicrobiaceae	Methanogenium	<i>Methanogenium cariaci</i>
Archaea	Euryarchaeota	Methanomicrobia	Methanomicrobiales	Methanomicrobiaceae	Methanogenium	<i>Methanogenium frigidum</i>
Archaea	Euryarchaeota	Methanomicrobia	Methanomicrobiales	Methanomicrobiaceae	Methanogenium	<i>Methanogenium marinum</i>
Archaea	Euryarchaeota	Methanomicrobia	Methanomicrobiales	Methanomicrobiaceae	Methanogenium	<i>Methanogenium organophilum</i>
Archaea	Euryarchaeota	Methanomicrobia	Methanosarcinales	Methanosarcinaceae	Methanohalobium	<i>Methanohalobium evestigatum</i>
Archaea	Euryarchaeota	Methanomicrobia	Methanosarcinales	Methanosarcinaceae	Methanohalophilus	<i>Methanohalophilus euhalobius</i>
Archaea	Euryarchaeota	Methanomicrobia	Methanosarcinales	Methanosarcinaceae	Methanohalophilus	<i>Methanohalophilus halophilus</i>
Archaea	Euryarchaeota	Methanomicrobia	Methanosarcinales	Methanosarcinaceae	Methanohalophilus	<i>Methanohalophilus levihalophilus</i>
Archaea	Euryarchaeota	Methanomicrobia	Methanosarcinales	Methanosarcinaceae	Methanohalophilus	<i>Methanohalophilus mahii</i>
Archaea	Euryarchaeota	Methanomicrobia	Methanosarcinales	Methanosarcinaceae	Methanohalophilus	<i>Methanohalophilus portucalensis</i>
Archaea	Euryarchaeota	Methanomicrobia	Methanomicrobiales	Methanomicrobiaceae	Methanolacinia	<i>Methanolacinia paynteri</i>
Archaea	Euryarchaeota	Methanomicrobia	Methanomicrobiales	Methanoregulaceae	Methanolinea	<i>Methanolinea mesophila</i>
Archaea	Euryarchaeota	Methanomicrobia	Methanomicrobiales	Methanoregulaceae	Methanolinea	<i>Methanolinea tarda</i>
Archaea	Euryarchaeota	Methanomicrobia	Methanosarcinales	Methanosarcinaceae	Methanolobus	<i>Methanolobus bombayensis</i>
Archaea	Euryarchaeota	Methanomicrobia	Methanosarcinales	Methanosarcinaceae	Methanolobus	<i>Methanolobus oregonensis</i>
Archaea	Euryarchaeota	Methanomicrobia	Methanosarcinales	Methanosarcinaceae	Methanolobus	<i>Methanolobus profundus</i>
Archaea	Euryarchaeota	Methanomicrobia	Methanosarcinales	Methanosarcinaceae	Methanolobus	<i>Methanolobus psychrophilus</i>
Archaea	Euryarchaeota	Methanomicrobia	Methanosarcinales	Methanosarcinaceae	Methanolobus	<i>Methanolobus taylorii</i>
Archaea	Euryarchaeota	Methanomicrobia	Methanosarcinales	Methanosarcinaceae	Methanolobus	<i>Methanolobus tindarius</i>
Archaea	Euryarchaeota	Methanomicrobia	Methanosarcinales	Methanosarcinaceae	Methanolobus	<i>Methanolobus vulcani</i>
Archaea	Euryarchaeota	Methanomicrobia	Methanosarcinales	Methanosarcinaceae	Methanolobus	<i>Methanolobus zinderi</i>
Archaea	Euryarchaeota	Methanomicrobia	Methanomassiliicoccus	Methanomassiliicoccaceae	Methanomassiliicoccus	<i>Methanomassiliicoccus luminyensis</i>
Archaea	Euryarchaeota	Methanomicrobia	Methanosarcinales	Methanosarcinaceae	Methanomethylovorans	<i>Methanomethylovorans hollandica</i>
Archaea	Euryarchaeota	Methanomicrobia	Methanosarcinales	Methanosarcinaceae	Methanomethylovorans	<i>Methanomethylovorans thermophila</i>
Archaea	Euryarchaeota	Methanomicrobia	Methanosarcinales	Methanosarcinaceae	Methanomethylovorans	<i>Methanomethylovorans uponensis</i>
Archaea	Euryarchaeota	Methanomicrobia	Methanomicrobiales	Methanomicrobiaceae	Methanomicrobium	<i>Methanomicrobium mobile</i>
Archaea	Euryarchaeota	Methanomicrobia	Methanosarcinales	Methanosarcinaceae	Methanomicrococcus	<i>Methanomicrococcus blatticola</i>

Archaea	Euryarchaeota	Methanomicrobia	Methanomicrobiales	Methanomicrobiaceae	Methanoplanus	<i>Methanoplanus endosymbiosus</i>
Archaea	Euryarchaeota	Methanomicrobia	Methanomicrobiales	Methanomicrobiaceae	Methanoplanus	<i>Methanoplanus limicola</i>
Archaea	Euryarchaeota	Methanomicrobia	Methanomicrobiales	Methanomicrobiaceae	Methanoplanus	<i>Methanoplanus petrolearius</i>
Archaea	Euryarchaeota	Methanopyri	Methanopyrales	Methanopyraceae	Methanopyrus	<i>Methanopyrus kandleri</i>
Archaea	Euryarchaeota	Methanomicrobia	Methanomicrobiales	Methanoregulaceae	Methanoregula	<i>Methanoregula boonei</i>
Archaea	Euryarchaeota	Methanomicrobia	Methanomicrobiales	Methanoregulaceae	Methanoregula	<i>Methanoregula formicica</i>
Archaea	Euryarchaeota	Methanomicrobia	Methanosarcinales	Methanosaetaceae	Methanosaeta	<i>Methanosaeta concilii</i>
Archaea	Euryarchaeota	Methanomicrobia	Methanosarcinales	Methanosaetaceae	Methanosaeta	<i>Methanosaeta harundinacea</i>
Archaea	Euryarchaeota	Methanomicrobia	Methanosarcinales	Methanosaetaceae	Methanosaeta	<i>Methanosaeta pelagica</i>
Archaea	Euryarchaeota	Methanomicrobia	Methanosarcinales	Methanosaetaceae	Methanosaeta	<i>Methanosaeta thermophila</i>
Archaea	Euryarchaeota	Methanomicrobia	Methanosarcinales	Methanosarcinaceae	Methanosalsum	<i>Methanosalsum zhilinae</i>
Archaea	Euryarchaeota	Methanomicrobia	Methanosarcinales	Methanosarcinaceae	Methanosarcina	<i>Methanosarcina acetivorans</i>
Archaea	Euryarchaeota	Methanomicrobia	Methanosarcinales	Methanosarcinaceae	Methanosarcina	<i>Methanosarcina baltica</i>
Archaea	Euryarchaeota	Methanomicrobia	Methanosarcinales	Methanosarcinaceae	Methanosarcina	<i>Methanosarcina barkeri</i>
Archaea	Euryarchaeota	Methanomicrobia	Methanosarcinales	Methanosarcinaceae	Methanosarcina	<i>Methanosarcina horonobensis</i>
Archaea	Euryarchaeota	Methanomicrobia	Methanosarcinales	Methanosarcinaceae	Methanosarcina	<i>Methanosarcina lacustris</i>
Archaea	Euryarchaeota	Methanomicrobia	Methanosarcinales	Methanosarcinaceae	Methanosarcina	<i>Methanosarcina mazei</i>
Archaea	Euryarchaeota	Methanomicrobia	Methanosarcinales	Methanosarcinaceae	Methanosarcina	<i>Methanosarcina semesiae</i>
Archaea	Euryarchaeota	Methanomicrobia	Methanosarcinales	Methanosarcinaceae	Methanosarcina	<i>Methanosarcina siciliae</i>
Archaea	Euryarchaeota	Methanomicrobia	Methanosarcinales	Methanosarcinaceae	Methanosarcina	<i>Methanosarcina soligelidi</i>
Archaea	Euryarchaeota	Methanomicrobia	Methanosarcinales	Methanosarcinaceae	Methanosarcina	<i>Methanosarcina thermophila</i>
Archaea	Euryarchaeota	Methanomicrobia	Methanosarcinales	Methanosarcinaceae	Methanosarcina	<i>Methanosarcina vacuolata</i>
Archaea	Euryarchaeota	Methanobacteria	Methanobacteriales	Methanobacteriaceae	Methanosphaera	<i>Methanosphaera cuniculi</i>
Archaea	Euryarchaeota	Methanobacteria	Methanobacteriales	Methanobacteriaceae	Methanosphaera	<i>Methanosphaera stadtmanae</i>
Archaea	Euryarchaeota	Methanomicrobia	Methanomicrobiales	Methanoregulaceae	Methanosphaerula	<i>Methanosphaerula palustris</i>
Archaea	Euryarchaeota	Methanomicrobia	Methanomicrobiales	Methanospirillaceae	Methanospirillum	<i>Methanospirillum hungatei</i>
Archaea	Euryarchaeota	Methanomicrobia	Methanomicrobiales	Methanospirillaceae	Methanospirillum	<i>Methanospirillum lacunae</i>
Archaea	Euryarchaeota	Methanomicrobia	Methanomicrobiales	Methanospirillaceae	Methanospirillum	<i>Methanospirillum psychrodurum</i>
Archaea	Euryarchaeota	Methanomicrobia	Methanomicrobiales	Methanospirillaceae	Methanospirillum	<i>Methanospirillum stamsii</i>
Archaea	Euryarchaeota	Methanobacteria	Methanobacteriales	Methanobacteriaceae	Methanothermobacter	<i>Methanothermobacter crinale</i>
Archaea	Euryarchaeota	Methanobacteria	Methanobacteriales	Methanobacteriaceae	Methanothermobacter	<i>Methanothermobacter defluvii</i>

Archaea	Euryarchaeota	Methanobacteria	Methanobacteriales	Methanobacteriaceae	Methanothermobacter	<i>Methanothermobacter marburgensis</i>
Archaea	Euryarchaeota	Methanobacteria	Methanobacteriales	Methanobacteriaceae	Methanothermobacter	<i>Methanothermobacter tenebrarum</i>
Archaea	Euryarchaeota	Methanobacteria	Methanobacteriales	Methanobacteriaceae	Methanothermobacter	<i>Methanothermobacter thermautotrophicus</i>
Archaea	Euryarchaeota	Methanobacteria	Methanobacteriales	Methanobacteriaceae	Methanothermobacter	<i>Methanothermobacter thermoflexus</i>
Archaea	Euryarchaeota	Methanobacteria	Methanobacteriales	Methanobacteriaceae	Methanothermobacter	<i>Methanothermobacter thermophilus</i>
Archaea	Euryarchaeota	Methanobacteria	Methanobacteriales	Methanobacteriaceae	Methanothermobacter	<i>Methanothermobacter wolfeii</i>
Archaea	Euryarchaeota	Methanococci	Methanococcales	Methanococcaceae	Methanothermococcus	<i>Methanothermococcus okinawensis</i>
Archaea	Euryarchaeota	Methanococci	Methanococcales	Methanococcaceae	Methanothermococcus	<i>Methanothermococcus thermolithotrophicus</i>
Archaea	Euryarchaeota	Methanobacteria	Methanobacteriales	Methanobacteriaceae	Methanothermus	<i>Methanothermus fervidus</i>
Archaea	Euryarchaeota	Methanobacteria	Methanobacteriales	Methanobacteriaceae	Methanothermus	<i>Methanothermus sociabilis</i>
Archaea	Euryarchaeota	Methanococci	Methanococcales	Methanocaldococcaceae	Methanotorris	<i>Methanotorris formicicus</i>
Archaea	Euryarchaeota	Methanococci	Methanococcales	Methanocaldococcaceae	Methanotorris	<i>Methanotorris igneus</i>
Archaea	Euryarchaeota	Methanomicrobia	Methanosarcinales	Methermicoccaceae	Methermicoccus	<i>Methermicoccus shengliensis</i>

Table S5.5 Elemental composition of activated carbon (AC), OAK700, low-T (GRASS300) and high-T (GRASS600) switchgrass, and high-T poultry manure (MANURE600) biochars

Element	AC	OAK700	GRASS300 ^a	GRASS600 ^a	MANURE600
C, %	98.0±0.8	99.9±0.6	70.2±1.7	94.5±1.4	18.5±1.4
S, %	0.18±0.01	<0.01	0.10±0.01	0.55±0.02	0.48±0.02
Ag, µg g ⁻¹	< 0.01	< 0.01	0.06	0.87	0.16
Al, µg g ⁻¹	1400	45	160	240	14000
Ar, µg g ⁻¹	< 0.5	< 0.5	< 0.5	< 0.5	1.9
Ba, µg g ⁻¹	59	67	22	37	200
Be, µg g ⁻¹	0.09	0.02	< 0.02	< 0.02	0.60
Bi, µg g ⁻¹	< 0.09	< 0.09	< 0.09	< 0.09	< 0.09
Ca, µg g ⁻¹	7200	2900	9200	14000	44000
Cd, µg g ⁻¹	< 0.02	< 0.02	0.03	< 0.02	1.2
Co, µg g ⁻¹	0.51	0.63	0.16	0.21	3.5
Cr, µg g ⁻¹	4.3	1.2	3.4	5.4	27
Cu, µg g ⁻¹	9.1	4.5	7.2	12	34
Fe, µg g ⁻¹	1700	13	2100	1700	10000
K, µg g ⁻¹	910	2600	9300	11000	28000
Li, µg g ⁻¹	< 2	< 2	< 2	< 2	9
Mg, µg g ⁻¹	4200	690	2100	3500	7700
Mn, µg g ⁻¹	110	120	210	260	250
Mo, µg g ⁻¹	0.4	< 0.1	0.2	0.4	7.1
Na, µg g ⁻¹	910	5.2	18	29	17000
Ni, µg g ⁻¹	1.7	2.7	0.6	1.2	8.4
P, µg g ⁻¹	890	110	930	1600	14000
Pb, µg g ⁻¹	0.08	1.2	0.47	1.2	140
Sb, µg g ⁻¹	< 0.8	< 0.8	< 0.8	< 0.8	< 0.8
Se, µg g ⁻¹	1.4	< 0.7	< 0.7	< 0.7	1.7
Sn, µg g ⁻¹	0.6	< 0.5	7.0	130	4.5
Sr, µg g ⁻¹	60	17	18	30	180
Ti, µg g ⁻¹	98	1.5	11	27	1800
Tl, µg g ⁻¹	< 0.02	< 0.02	< 0.02	< 0.02	0.12
U, µg g ⁻¹	0.19	0.006	0.008	0.012	1.2
V, µg g ⁻¹	10	< 1	< 1	< 1	21
Y, µg g ⁻¹	0.69	0.39	0.38	0.39	7.6
Zn, µg g ⁻¹	1.8	7.8	23	35	330

^a indicates the data from Chapter 4.

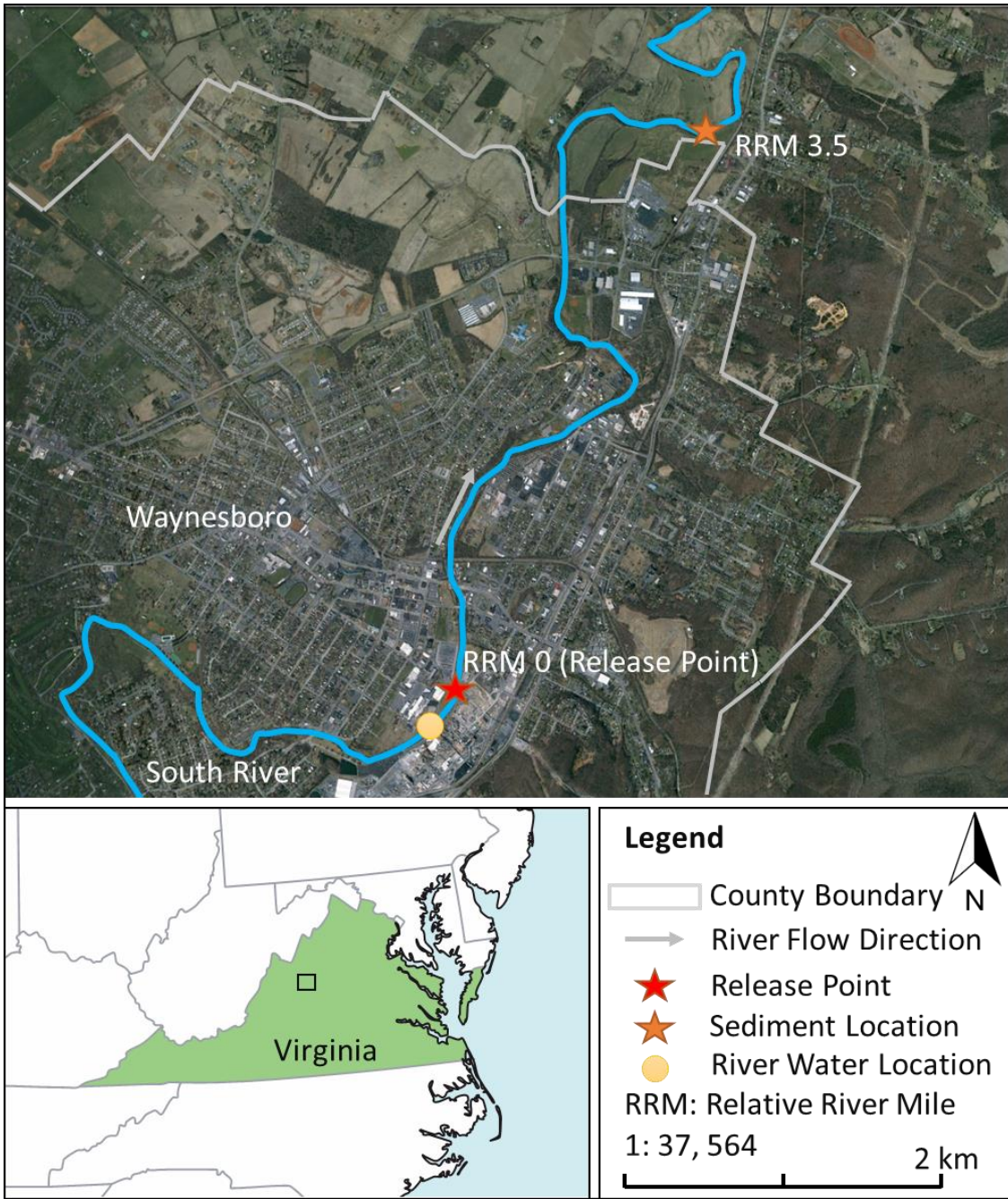


Figure S5.1. Sampling locations of sediment and river water used in this study.

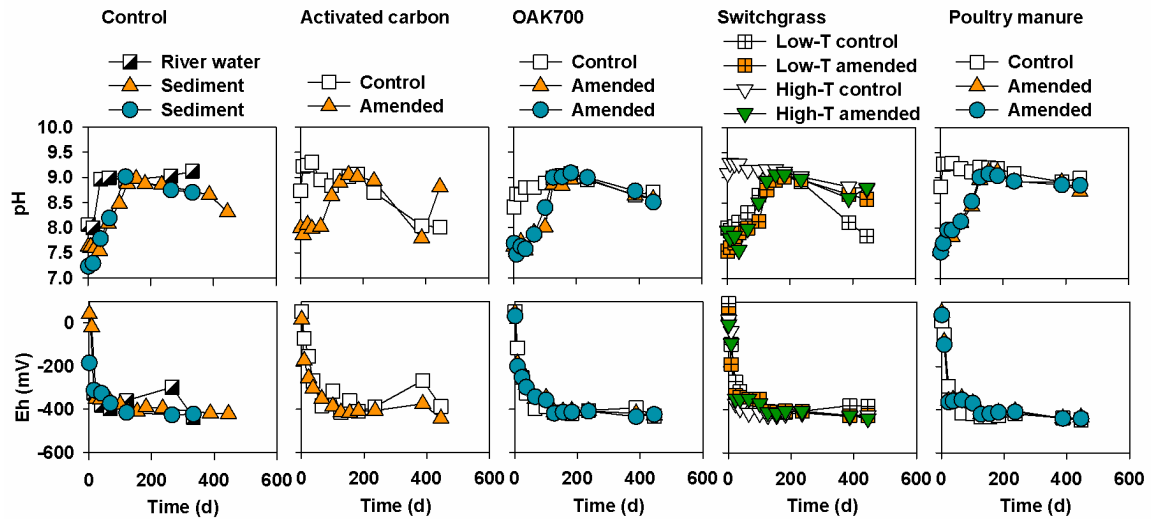


Figure S5.2. pH and Eh of controls and amended systems against time. The values of pH and Eh sediment control and low-T and high-T switchgrass biochar are from Chapter 4.

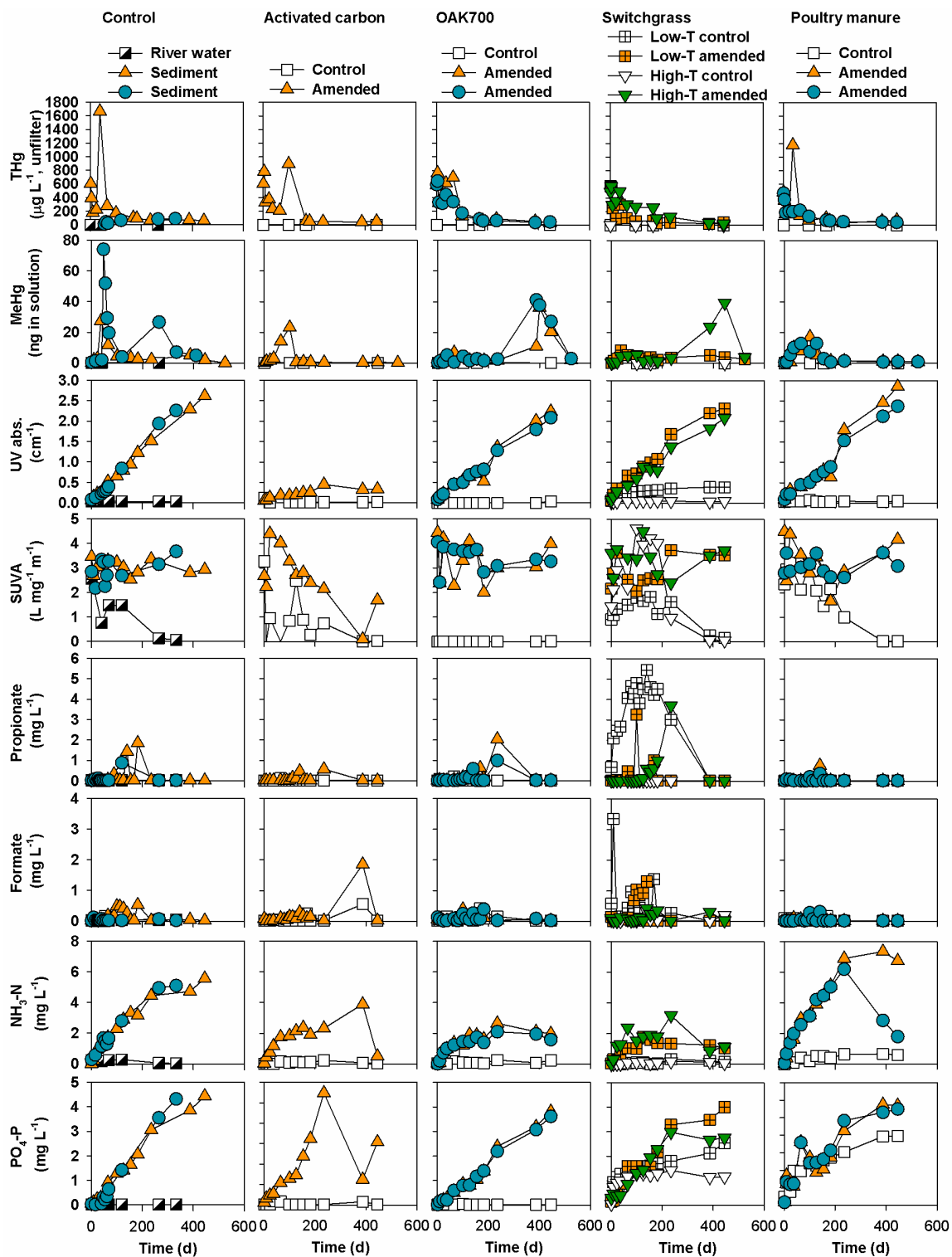


Figure S5.3. Concentrations of unfiltered THg, mass of MeHg in solution, UV absorbance at 254 nm⁻¹, specific UV absorbance (SUVA), and concentrations of propionate, formate, NH₃-N, and PO₄-P of controls and amended systems against time.

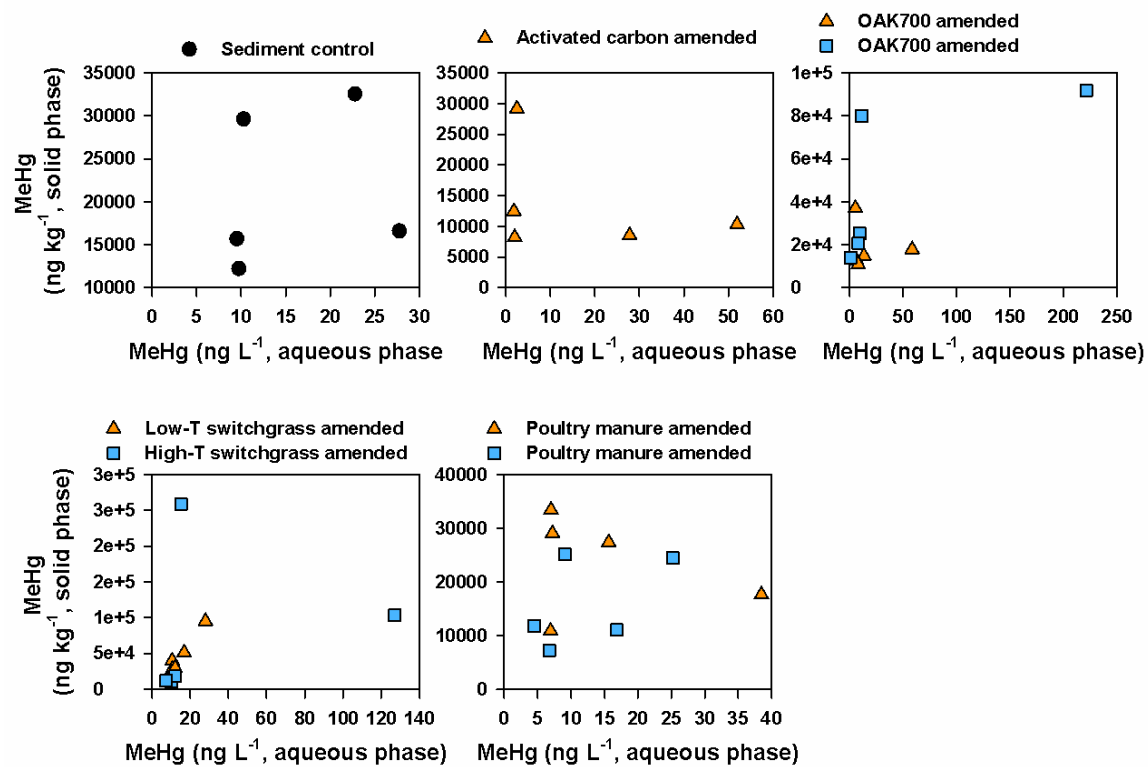


Figure S5.4. MeHg concentrations in aqueous phase against MeHg contents in solid phase of sediment control and amended systems.

Appendix E: *Summary of Data and
Supplementary Information Presented in
Chapter 6*

Table S6.1. EXAFS fitting results of Hg and Cu enriched areas from the corresponding μ -XRF maps^a

Spot	Model	path	CN	R (Å)	S ₀ ²	σ^2 (Å ²)	R-factor
Cu							
Fresh SRD_M6	CuO	Cu-O	2.34±0.27	1.94±0.02	0.792 ^a	0.003 ^a	0.08
AC-387_M1	Cu ₂ S	Cu-S	2.98±0.47	2.28±0.05	0.724 ^a	0.006 ^a	0.04
		Cu-Cu	1.68±0.66	2.33±0.09	0.724 ^a	0.009 ^a	0.04
CL2-235_M3	Cu ₂ S	Cu-S	4.86±1.64	2.26±0.06	0.724 ^a	0.006 ^a	0.09
		Cu-Cu	3.57±2.73	2.37±0.06	0.724 ^a	0.009 ^a	0.09
CL2-387_M1	Cu foil	Cu-Cu	3.18±1.70	2.64±0.13	0.902 ^a	0.009 ^a	0.10
CL2-387_M3	Cu ₂ S	Cu-S	4.96±1.89	2.23±0.06	0.724 ^a	0.006 ^a	0.08
		Cu-Cu	5.42±3.31	2.30±0.02	0.724 ^a	0.009 ^a	0.08
Hg							
CL2-235_M3	α -HgS	Hg-S	2.71±0.34	2.34±0.02	0.841 ^a	0.005 ^a	0.13
CL2-387_M3	α -HgS	Hg-S	1.76±0.87	2.38±0.11	0.841 ^a	0.005 ^a	0.06
CL2-387_M5	α -HgS	Hg-S	1.27±0.16	2.34±0.02	0.841 ^a	0.005 ^a	0.02
CL2-387_M6	α -HgS	Hg-S	2.72±0.47	2.35±0.04	0.841 ^a	0.005 ^a	0.02
CL2-387_M7	α -HgS	Hg-S	0.78±0.19	2.26±0.04	0.841 ^a	0.005 ^a	0.19

^a CN = coordination number, R = bond length, and R-factor = fitting statistic.

Table S6.2. EXAFS fitting results of Hg and Cu reference materials^a

Reference material	path	CN	R (Å)	S_0^2	σ^2 (Å ²)	R-factor
Cu ₂ S	Cu-S	3	2.16	0.724±0.18	0.006 (±0.003)	0.02
	Cu-Cu					
CuS	Cu-S	3	2.26	0.951±0.099	0.009±0.001	0.02
CuO	Cu-O	4	1.95	0.792±0.116	0.003±0.001	0.03
Cu foil	Cu-Cu	12	2.54	0.902±0.151	0.008±0.001	0.022
Cinnabar	Hg-S	2	2.37	0.841±0.123	0.005±0.001	0.015
HgO	Hg-O	2	2.05	0.962±0.126	0.004±0.001	0.009
Metacinnabar	Hg-S	4	2.52	0.718±0.035	0.009±0.001	0.0008

^a CN = coordination number, R = bond length, and R-factor = fitting statistic.

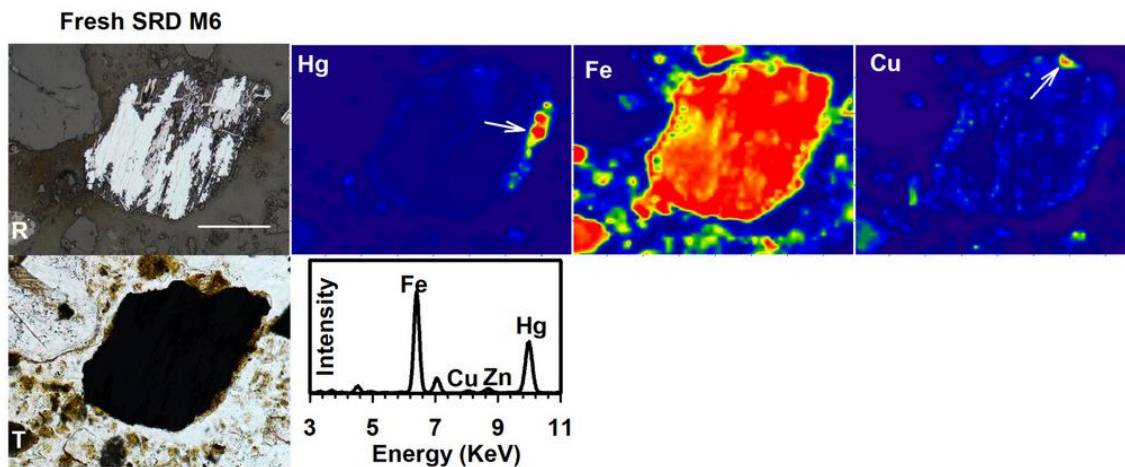


Figure S6.1. Micro-XRF Hg L_{α} , Fe K_{α} , and Cu K_{α} maps of grains from fresh sediment. R and T represent pictures taken in reflection and transmission mode. The white bar represents 100 μm . The arrow in Hg map indicates the position for collecting the XRF spectra (bottom right) and Hg EXAFS spectra. The arrow in Cu map indicates the position for collecting Cu EXAFS spectra. The maps were collected at Sector 13 ID-E at the Advanced Photon Source, Argonne National Laboratory.

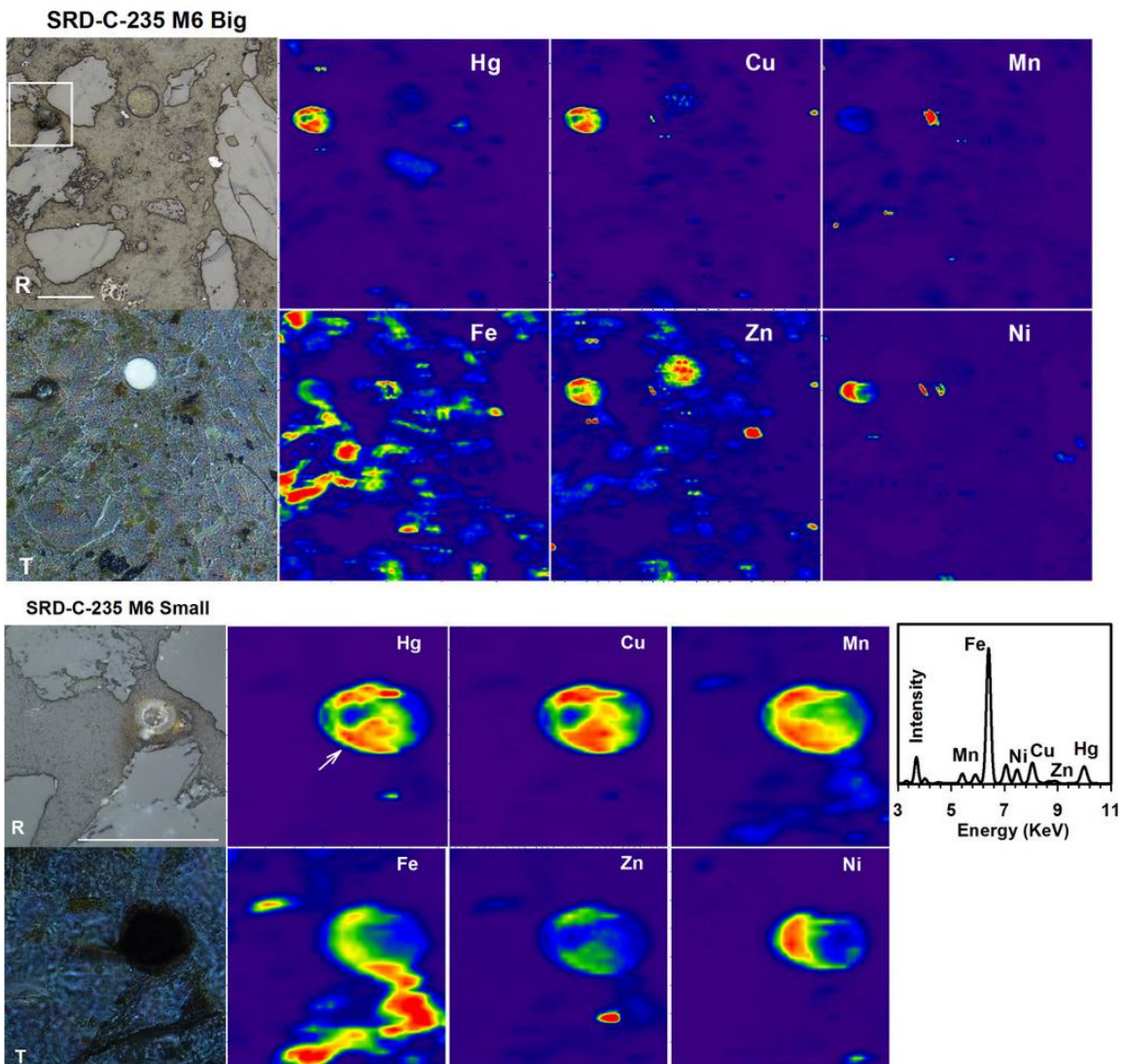


Figure S6.2. Micro-XRF Hg L_{α} , Fe K_{α} , Cu K_{α} , Zn K_{α} , Mn K_{α} , and Ni K_{α} maps of grains from sediment control on day 235. R and T represent pictures taken in reflection and transmission mode. The white bar represents 100 μm . The area of the lower $\mu\text{-XRF}$ maps is indicated by the white box in the upper $\mu\text{-XRF}$ maps. The arrow in Hg map indicates the position for collecting the XRF spectra (top right at SRD-235 M6 Small) and Hg EXAFS spectra. The maps were collected at Sector 13 ID-E at the Advanced Photon Source, Argonne National Laboratory.

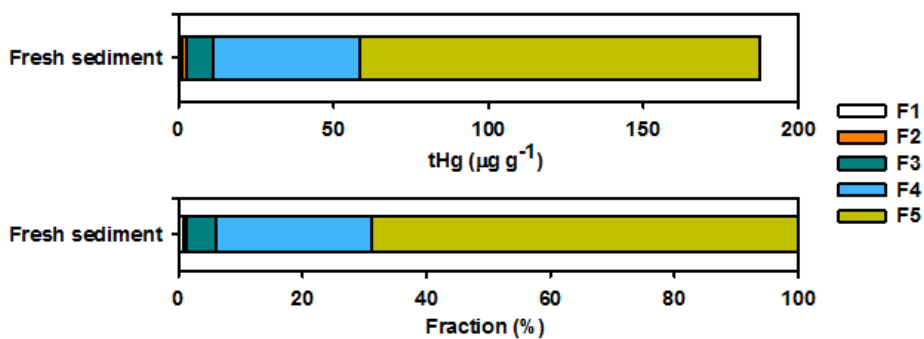


Figure S6.3. Hg sequential extraction results of fresh sediment. F1 (white) represents water soluble Hg, including HgCl_2 and HgSO_4 ; F2 (orange red) represents weak acid extractable Hg, including HgO ; F3 (dark spring green) represents organo complexed Hg, including Hg-humics, Hg_2Cl_2 ; F4 (turquoise) represents strong complexed Hg, including Hg in mineral lattice, Hg_2Cl_2 , Hg^0 ; F5 (old gold) represents residue, including cinnabar, metacinnabar, HgSe , and HgAu .

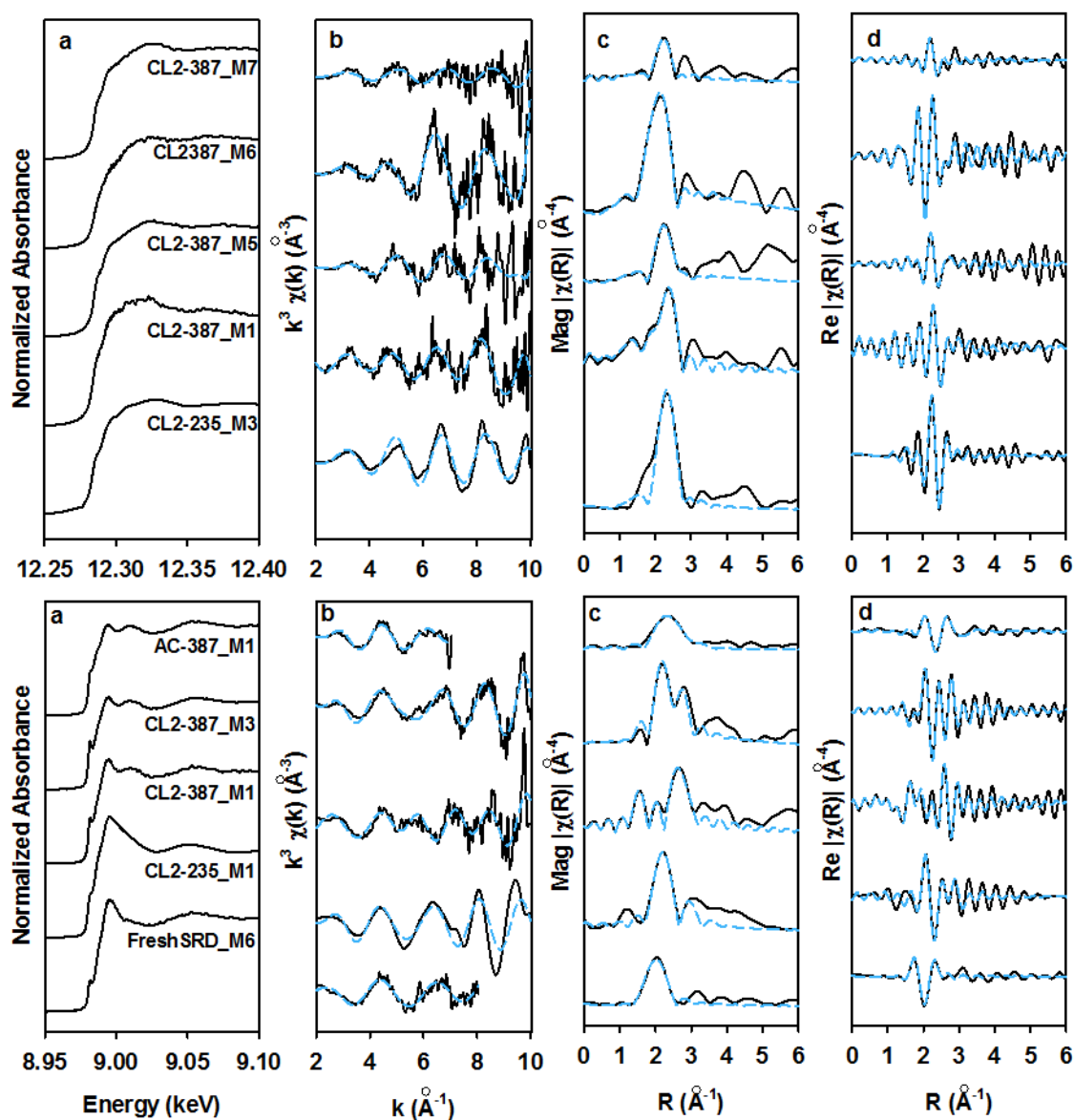
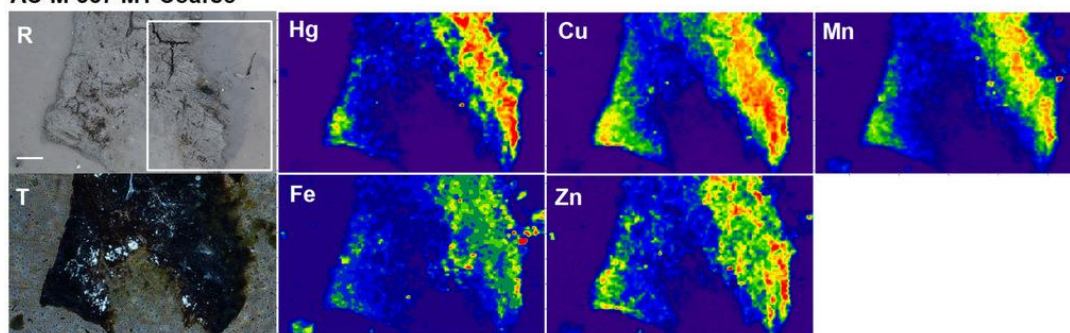
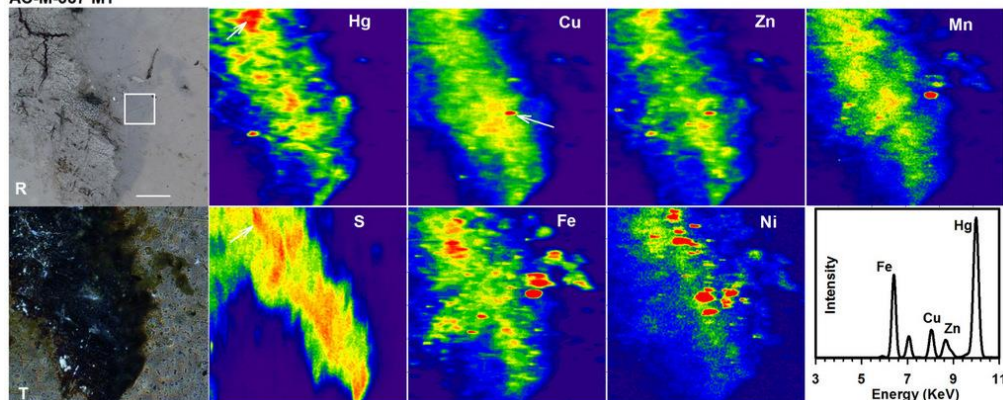


Figure S6.4 ^a Edge-step normalized Cu K-edge (lower) and Hg L_{III}-edge (upper) XANES spectra of the spots indicated in the μ -XRF maps. ^b k^3 -weighted chi spectra (black solid line) and the best fit data (light blue dash line). ^c Fourier-transform magnitude spectra and the best fit data. Fourier transform data are corrected for phase shift. ^d Fourier-transform real part and the best fit data. The Hg EXAFS results were all from extra Hg-enriched area of oak biochar (CL2) amended systems.

AC-M-387 M1 Coarse



AC-M-387 M1



AC-M-387 M1 Fine

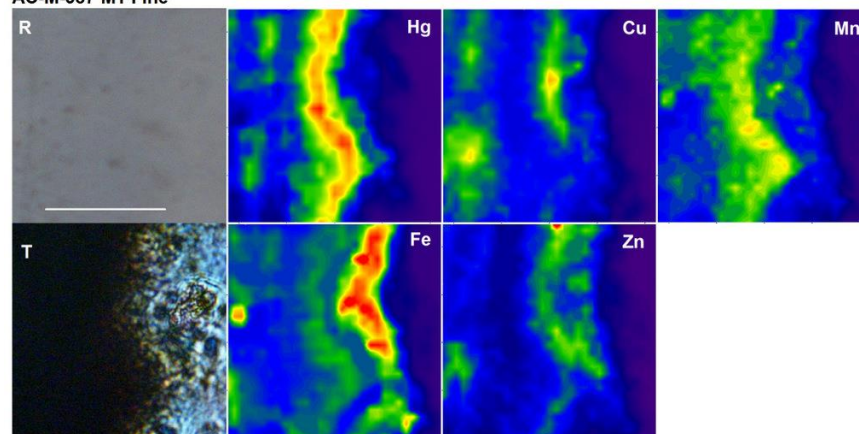


Figure S6.5. Micro-XRF Hg L_{α} , Fe K_{α} , Cu K_{α} , Zn K_{α} , Mn K_{α} , and Ni K_{α} maps of grains from activated carbon amended system on day 387. R and T represent pictures taken in reflection and transmission mode. The white bar represents 100 μm . The area of the lower $\mu\text{-XRF}$ maps is indicated by the white box in the upper $\mu\text{-XRF}$ maps. The arrow in Hg map indicates the position for collecting the XRF spectra and Hg EXAFS spectra. The arrow in Cu map indicates the position for collecting Cu EXAFS spectra. The coarse and fine maps was collected at Sector 20 ID-B at Advance Photon Source. The step size of the coarse map was 25*25 μm . The middle one was collected at Sector 13 ID-E at the Advanced Photon Source, Argonne National Laboratory.

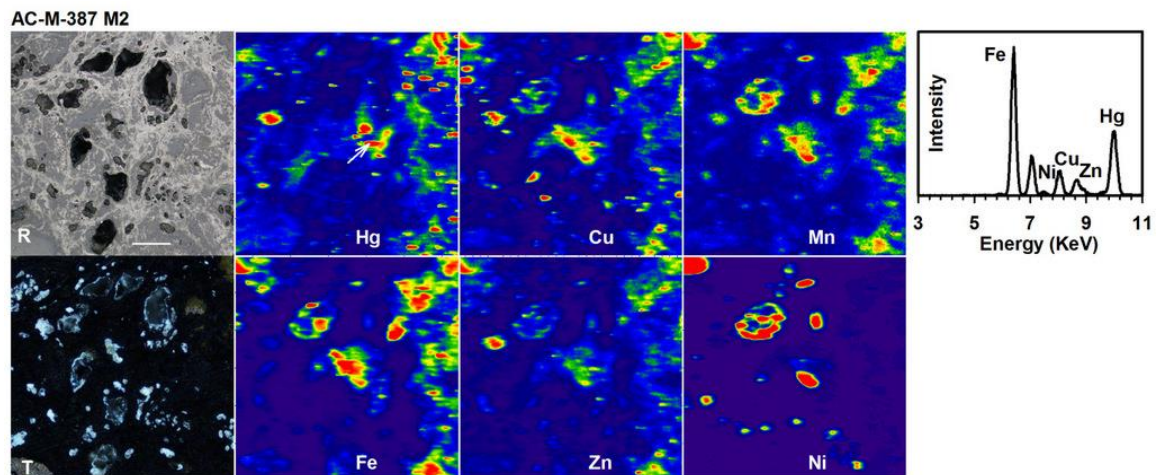


Figure S6.6. Micro-XRF Hg L_{α} , Fe K_{α} , Cu K_{α} , Zn K_{α} , Mn K_{α} , and Ni K_{α} maps of grains from activated carbon amended system on day 387. R and T represent pictures taken in reflection and transmission mode. The white bar represents 100 μm . The arrow in Hg map indicates the position for collecting the XRF spectra on the left side. The maps were collected at Sector 13 ID-E at the Advanced Photon Source, Argonne National Laboratory.

CL2-M-235 M3

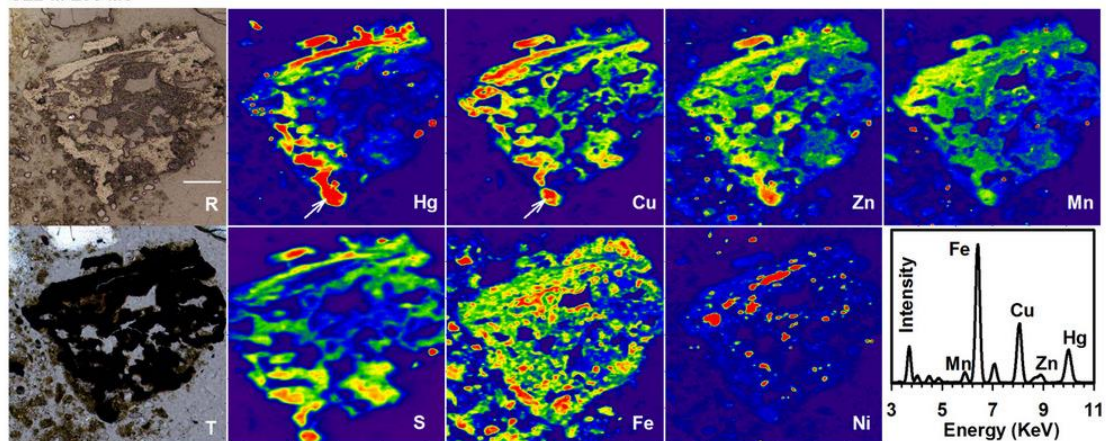
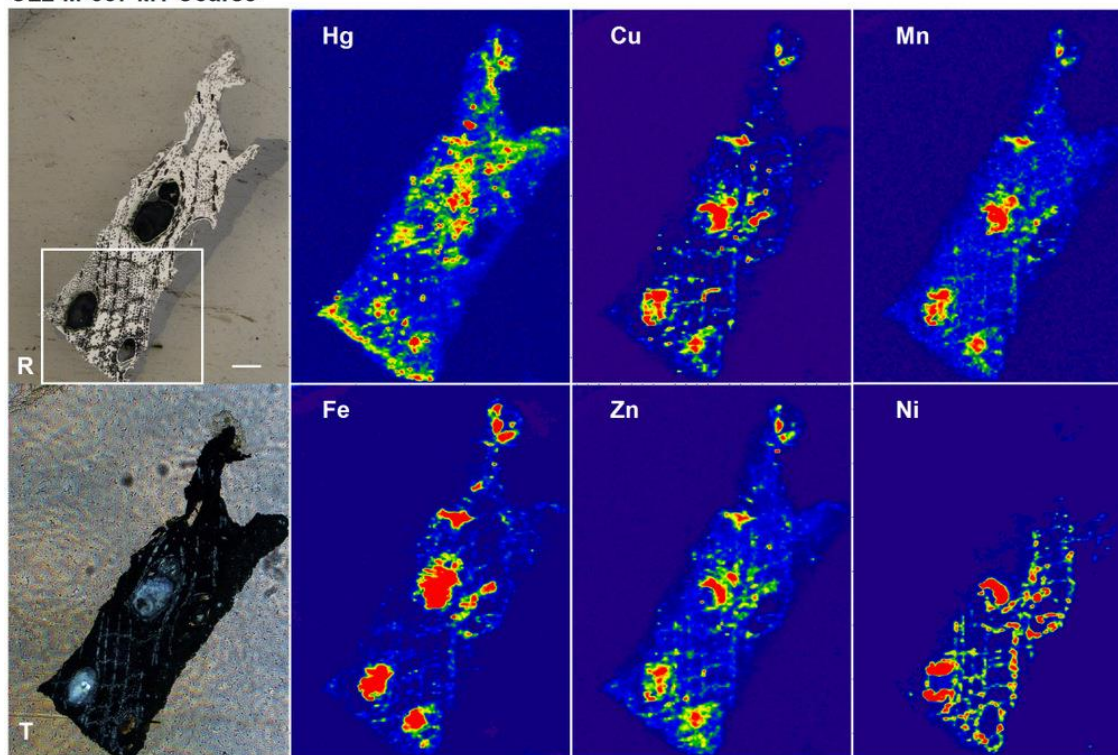


Figure S6.7. Micro-XRF Hg L_{α} , S K_{α} , Fe K_{α} , Cu K_{α} , Zn K_{α} , Mn K_{α} , and Ni K_{α} maps of grains from hardwood amended system on day 235. R and T represent pictures taken in reflection and transmission mode. The white bar represents 100 μm . The arrow in Hg map indicates the position for collecting the XRF spectra and Hg EXAFS. The arrow in Cu map indicates the position for collecting Cu EXAFS. The maps were collected at Sector 13 ID-E at the Advanced Photon Source, Argonne National Laboratory.

CL2-M-387 M1 Coarse



CL2-M-387 M1

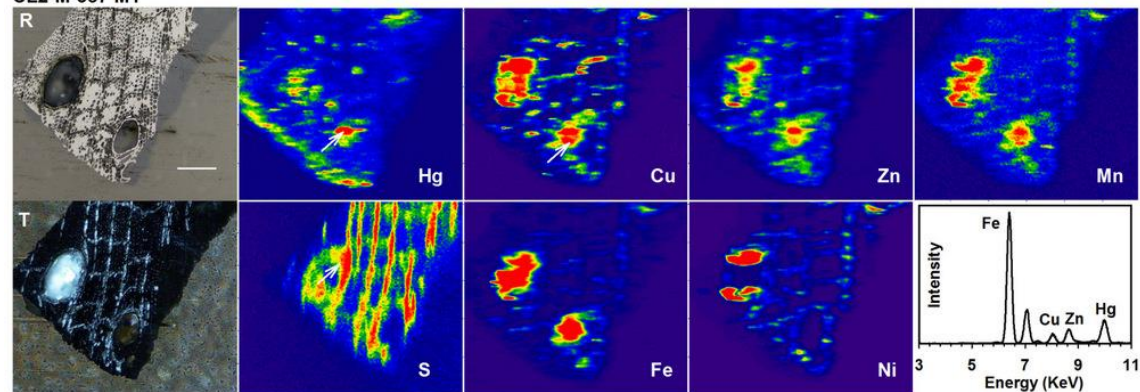


Figure S6.8. Micro-XRF Hg L_{α} , S K_{α} , Fe K_{α} , Cu K_{α} , Zn K_{α} , Mn K_{α} , and Ni K_{α} maps of grains from hardwood amended system on day 235. R and T represent pictures taken in reflection and transmission mode. The white bar represents 100 μm . The area of the lower $\mu\text{-XRF}$ maps is indicated by the white box in the upper $\mu\text{-XRF}$ maps. The arrow in Hg map indicates the position for collecting the XRF spectra and Hg EXAFS. The arrow in Cu map indicates the position for collecting Cu EXAFS. The maps were collected at Sector 13 ID-E at the Advanced Photon Source, Argonne National Laboratory.

CL2-M-387 M2

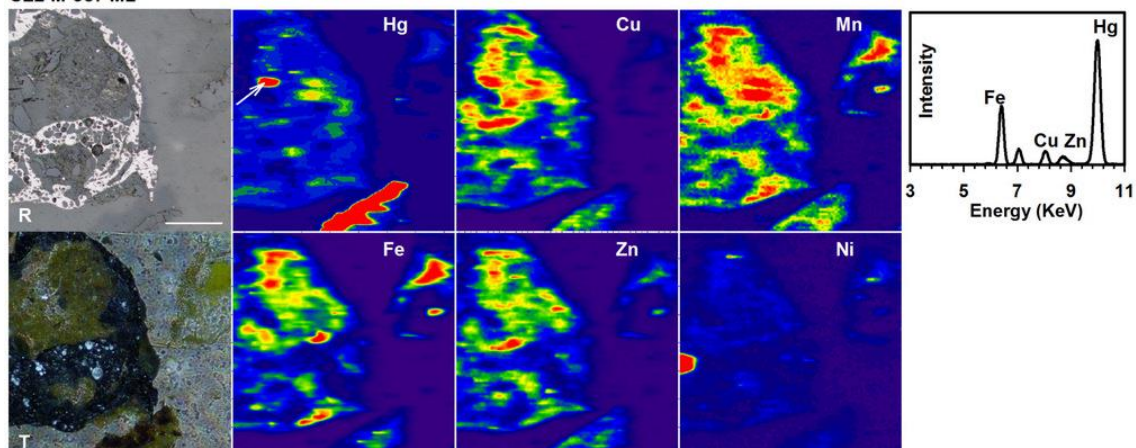


Figure S6.9. Micro-XRF Hg L_{α} , Fe K_{α} , Cu K_{α} , Zn K_{α} , Mn K_{α} , and Ni K_{α} maps of grains from hardwood amended system on day 387. R and T represent pictures taken in reflection and transmission mode. The white bar represents 100 μm . The arrow in Hg map indicates the position for collecting the XRF spectra and Hg EXAFS. The maps were collected at Sector 13 ID-E at the Advanced Photon Source, Argonne National Laboratory.

CL2-M-387 M3

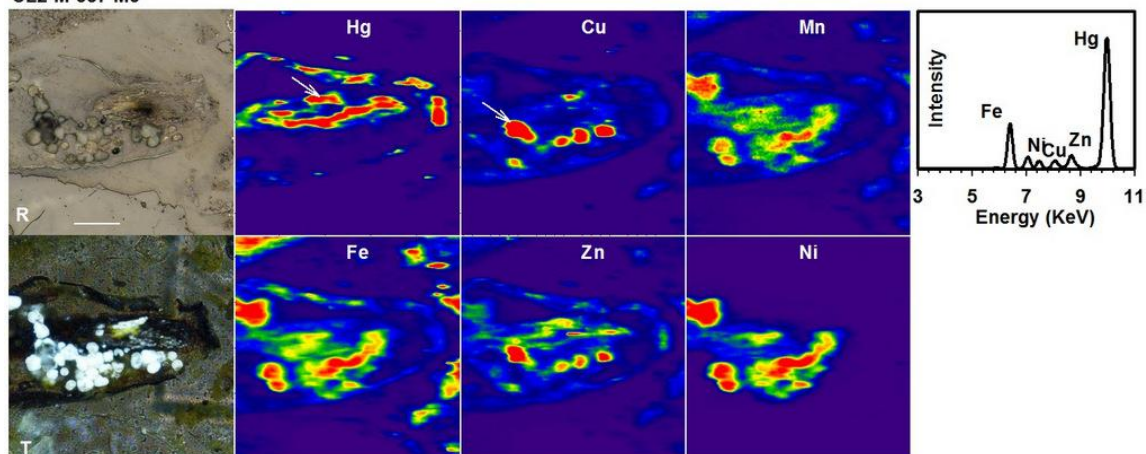


Figure S6.10. Micro-XRF Hg L_{α} , Fe K_{α} , Cu K_{α} , Zn K_{α} , Mn K_{α} , and Ni K_{α} maps of grains from hardwood amended system on day 387. R and T represent pictures taken in reflection and transmission mode. The white bar represents 100 μm . The arrow in Hg map indicates the position for collecting the XRF spectra and Hg EXAFS. The arrow in Cu map indicates the position for collecting Cu EXAFS spectra. The maps were collected at Sector 13 ID-E at the Advanced Photon Source, Argonne National Laboratory.

CL2-M-387 M4

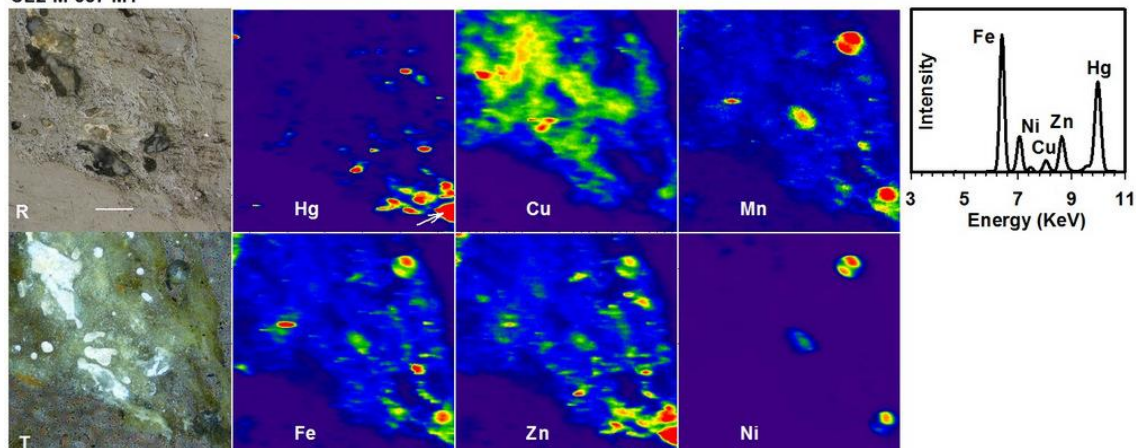
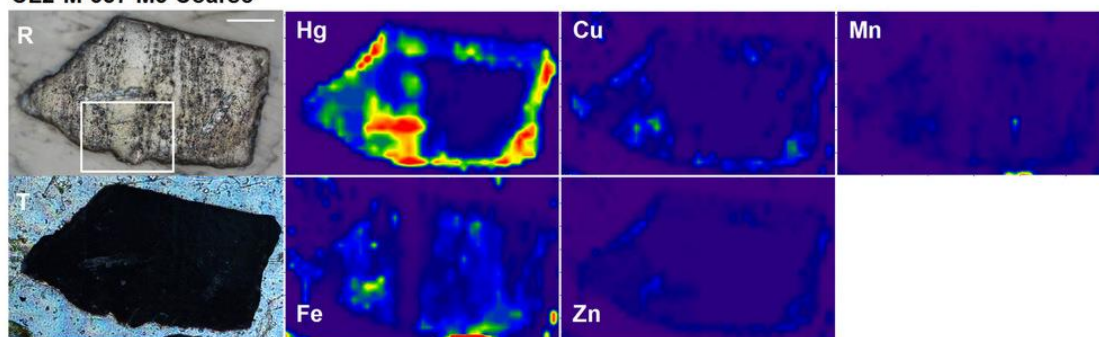


Figure S6.11. Micro-XRF Hg L_{α} , Fe K_{α} , Cu K_{α} , Zn K_{α} , Mn K_{α} , and Ni K_{α} maps of grains from hardwood amended system on day 387. R and T represent pictures taken in reflection and transmission mode. The white bar represents 100 μm . The arrow in Hg map indicates the position for collecting the XRF spectra and Hg EXAFS. The maps were collected at Sector 13 ID-E at the Advanced Photon Source, Argonne National Laboratory.

CL2-M-387 M5 Coarse



CL2-M-387 M5 Fine

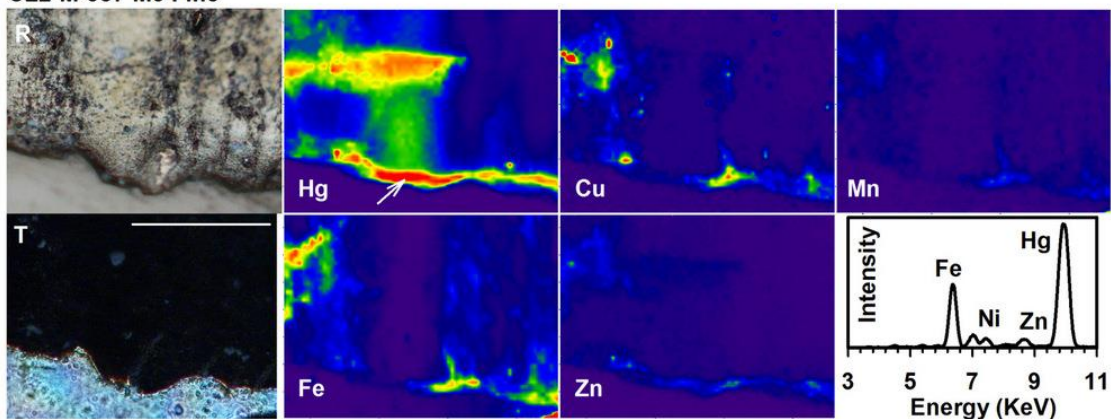


Figure S6.12. Micro-XRF Hg L_{α} , Fe K_{α} , Cu K_{α} , Zn K_{α} , and Mn K_{α} maps of grains from hardwood amended system on day 387. R and T represent pictures taken in reflection and transmission mode. The white bar represents 100 μm . The area of the lower $\mu\text{-XRF}$ maps is indicated by the white box in the upper $\mu\text{-XRF}$ maps. The arrow in Hg map indicates the position for collecting the XRF spectra and Hg EXAFS. The maps were collected at Sector 20 ID-B at the Advanced Photon Source, Argonne National Laboratory.

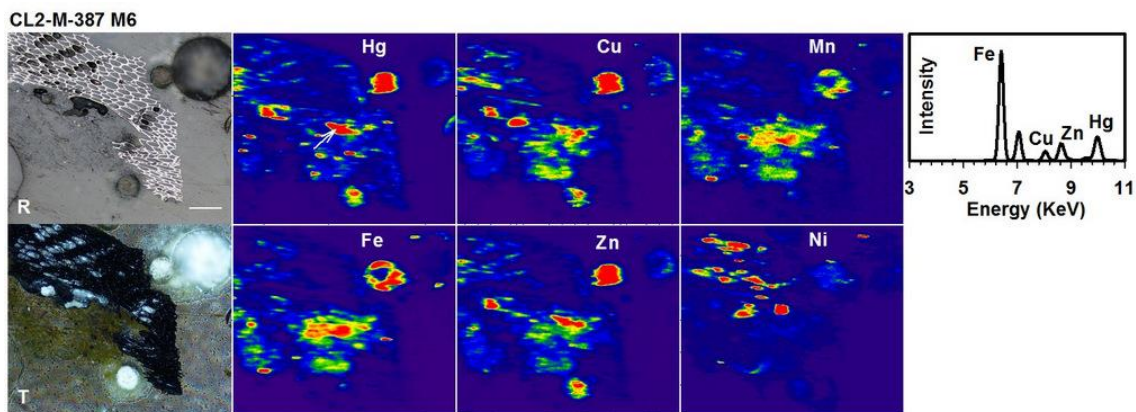
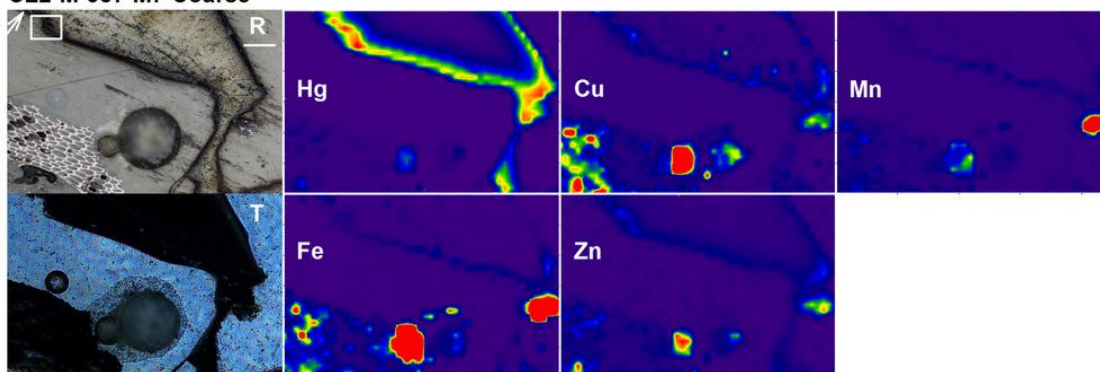
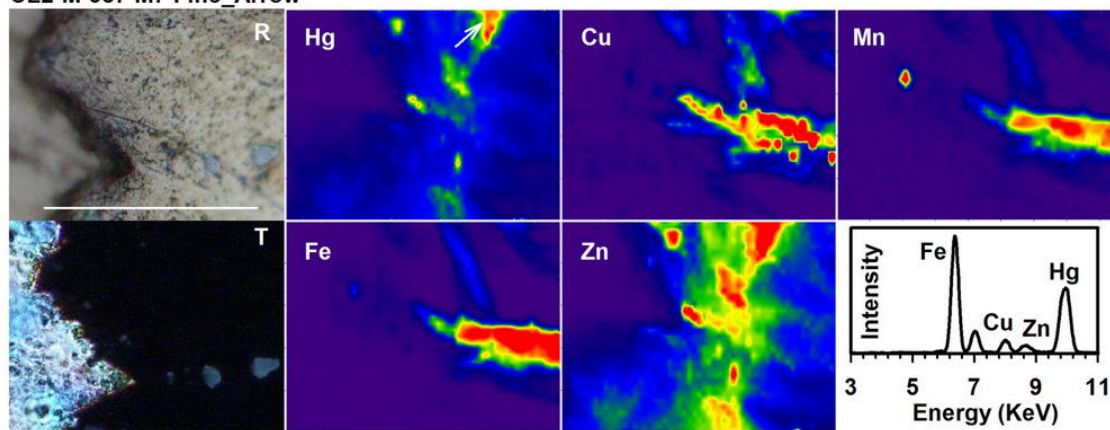


Figure S6.13. Micro-XRF Hg L_α, Fe K_α, Cu K_α, Zn K_α, Mn K_α, and Ni K_α maps of grains from hardwood amended system on day 387. R and T represent pictures taken in reflection and transmission mode. The white bar represents 100 μm. The arrow in Hg map indicates the position for collecting the XRF spectra and Hg EXAFS. The maps were collected at Sector 13 ID-E at the Advanced Photon Source, Argonne National Laboratory.

CL2-M-387 M7 Coarse



CL2-M-387 M7 Fine_Arrow



CL2-M-387 M7 Fine_box

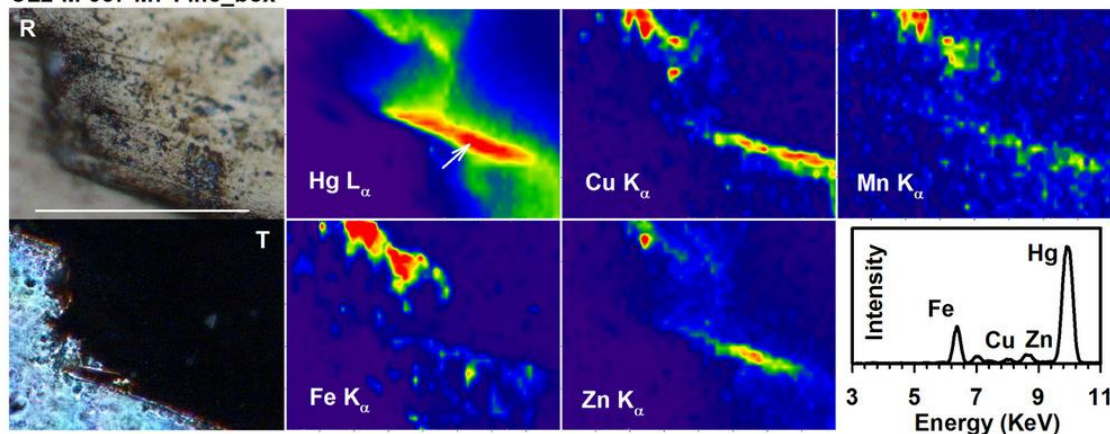


Figure S6.14. Micro-XRF Hg L α , Fe K α , Cu K α , Zn K α , and Mn K α maps of grains from hardwood amended system on day 387. R and T represent pictures taken in reflection and transmission mode. The white bar represents 100 μ m. The area of the lower μ -XRF maps is indicated by the white box and arrow in microscope picture of the upper μ -XRF maps. The arrow in Hg map indicates the position for collecting the XRF spectra and Hg EXAFS. The maps were collected at Sector 20 ID-B at the Advanced Photon Source, Argonne National Laboratory.

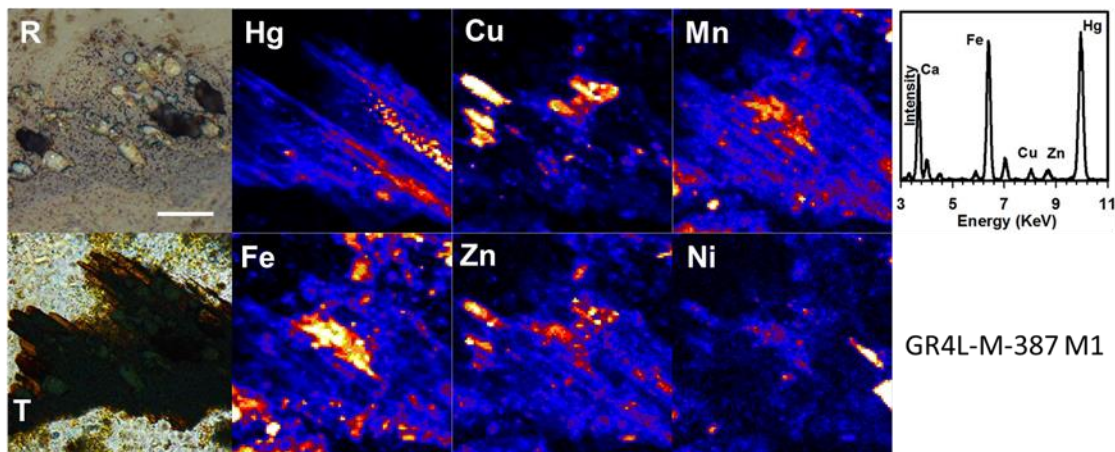


Figure S6.15. Micro-XRF Hg L α , Fe K α , Cu K α , Zn K α , Mn K α , and Ni K α maps of grains from low-T switchgrass biochar amended system on day 387. R and T represent pictures taken in reflection and transmission mode. The white bar represents 100 μ m. The arrow in Hg map indicates the position for collecting the XRF spectra. The maps were collected at Sector 13 ID-E at the Advanced Photon Source, Argonne National Laboratory.

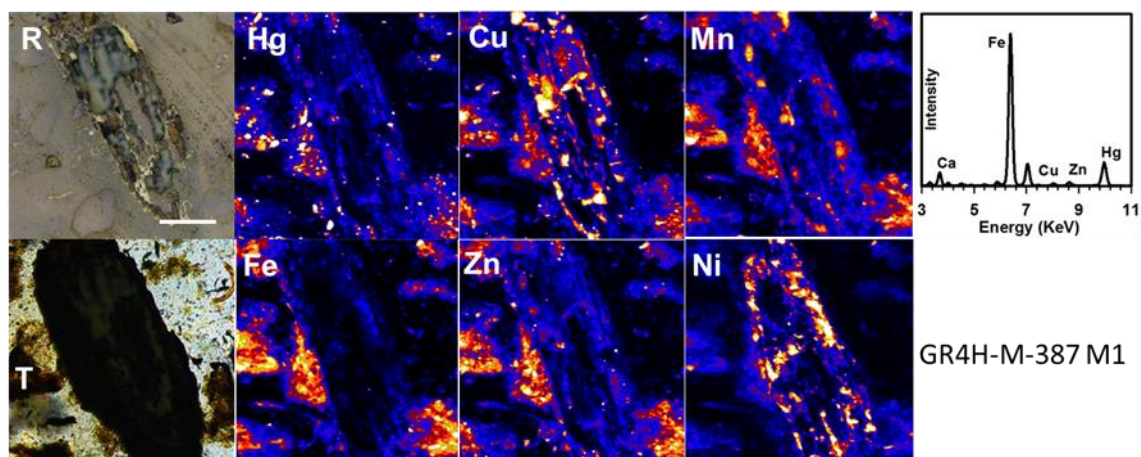


Figure S6.16. Micro-XRF Hg L_{α} , Fe K_{α} , Cu K_{α} , Zn K_{α} , Mn K_{α} , and Ni K_{α} maps of grains from high-T switchgrass biochar amended system on day 387. R and T represent pictures taken in reflection and transmission mode. The white bar represents 100 μm . The arrow in Hg map indicates the position for collecting the XRF spectra and Hg EXAFS. The maps were collected at Sector 13 ID-E at the Advanced Photon Source, Argonne National Laboratory.

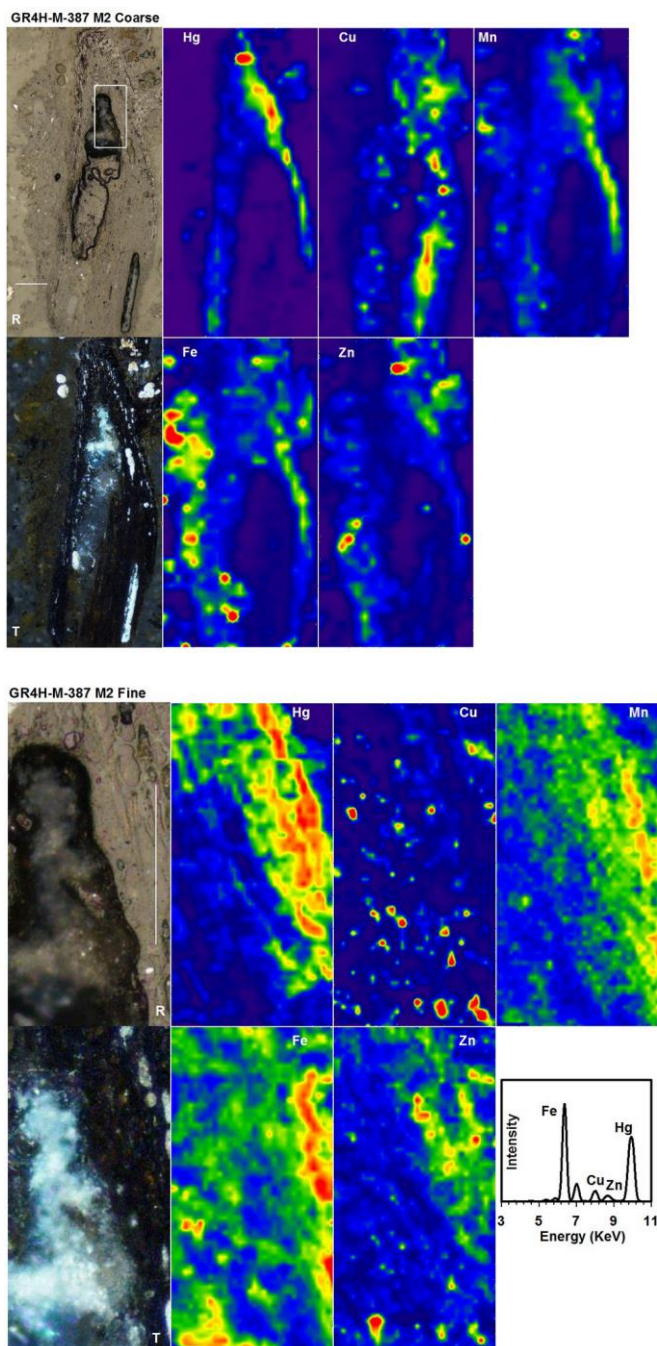


Figure S6.17. Micro-XRF Hg L_{α} , Fe K_{α} , Cu K_{α} , Zn K_{α} , and Mn K_{α} maps of grains from high-T switchgrass biochar amended system on day 387. R and T represent pictures taken in reflection and transmission mode. The white bar represents 100 μm . The area of the lower $\mu\text{-XRF}$ maps is indicated by the white box in the microscope picture of the upper $\mu\text{-XRF}$ maps. The arrow in Hg map indicates the position for collecting the XRF spectra. The maps were collected at Sector 20 ID-B at the Advanced Photon Source, Argonne National Laboratory.

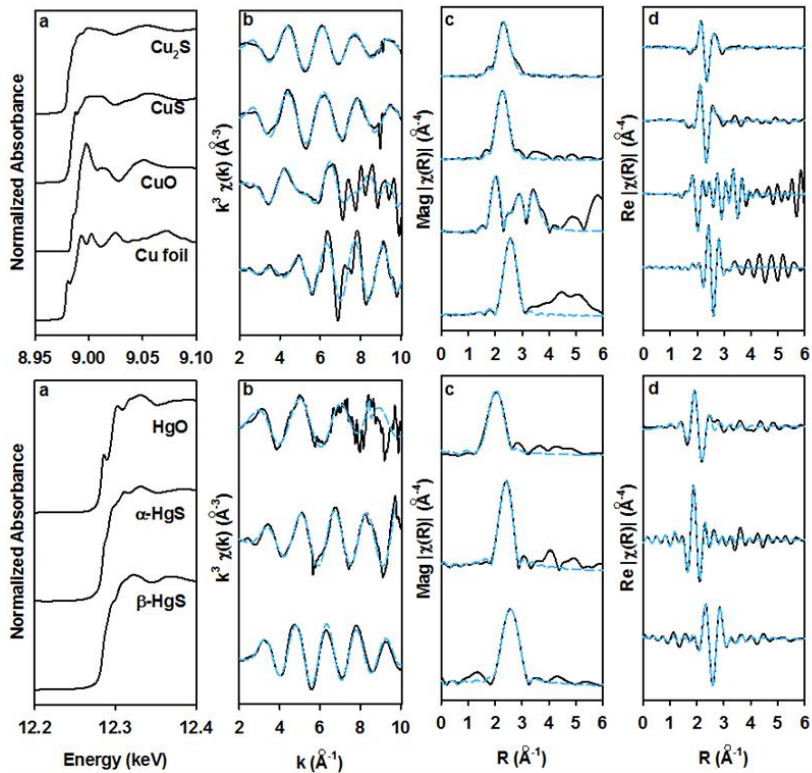


Figure S6.18. ^a Edge-step normalized Hg L_{III}-edge XANES spectra of Cu and Hg reference materials. ^b k^3 -weighted chi spectra (black solid line) and the best fit data (light-blue dash line). ^c Fourier-transform magnitude spectra and the best fit data. Fourier transform data are corrected for phase shift. ^d Fourier-transform real part and the best fit data.

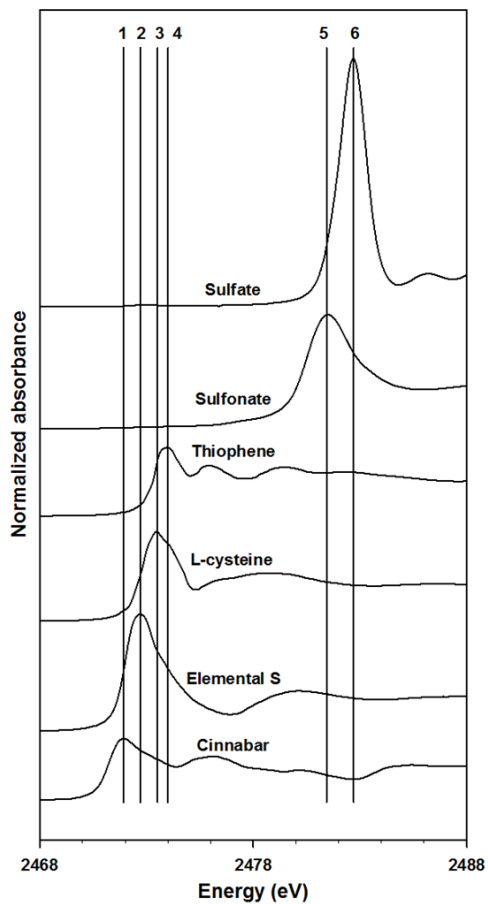


Figure S6.19. S XANES spectra of reference material. From bottom to top (line 1-6): cinnabar, elemental S, L-cysteine, dibenzo thiophene, Na methane sulfonate, and K_2SO_4 .

Appendix F: *Supplementary Information in Chapter 7*

Table S7.1. Elemental composition used for X-ray fluorescence attenuation correction of CL2, dimercapto-modified CL2 (CL2-DMC), and polysulfide-modified CL2 (CL2-CPS).

Element	CL2	CL2-DMC ^d	CL2-CPS ^d
Particle density, g cm ⁻³	1.34 ^a	1.34	1.34
H, %	1.1 ^a	1.1	1.1
C, %	92.4 ^a	91.8	91.8
N, %	0.01 ^a	0.01	0.01
O, %	4.5 ^a	4.4	4.4
F, μg g ⁻¹	16 ^a	16	16
Na, μg g ⁻¹	5.2 ^b	5.2	5.2
Mg, μg g ⁻¹	690 ^b	690	690
Al, μg g ⁻¹	45 ^b	45	45
Si, %	1 ^a	1	1
P, μg g ⁻¹	110 ^b	110	110
S, %	0.001 ^a	0.85	0.85
Cl, %	0.01 ^a	0.01	0.01
K, μg g ⁻¹	2600 ^b	2600	2600
Ca, μg g ⁻¹	2900 ^b	3500	2900
Ti, μg g ⁻¹	1.5 ^b	1.5	1.5
V, μg g ⁻¹	0.01 ^b	0.01	0.01
Cr, μg g ⁻¹	1.2 ^b	1.2	1.2
Mn, μg g ⁻¹	120 ^b	120	120
Fe, μg g ⁻¹	13 ^b	13	13
Co, μg g ⁻¹	0.63 ^b	0.63	0.63
Ni, μg g ⁻¹	2.7 ^b	2.7	2.7
Cu, μg g ⁻¹	4.5 ^b	4.5	4.5
Zn, μg g ⁻¹	7.8 ^b	7.8	7.8
As, μg g ⁻¹	0.01 ^b	0.01	0.01
Se, μg g ⁻¹	0.01 ^b	0.01	0.01
Br, μg g ⁻¹	2 ^b	2	2
Ag, μg g ⁻¹	0.01 ^b	0.01	0.01
Cd, μg g ⁻¹	0.01 ^b	0.01	0.01
Sn, μg g ⁻¹	0.01 ^b	0.01	0.01
Ba, μg g ⁻¹	67 ^b	67	67
W, μg g ⁻¹	0.01 ^b	0.01	0.01
Hg, μg g ⁻¹	900 ^c	950 ^c	950 ^c
Pb, μg g ⁻¹	1.2 ^b	1.2	1.2

^a value estimated from previous studies (Brewer et al., 2014; Dong et al., 2011; Lin et al., 2012; Xie et al., 2016).

^b values obtained by digestion following EPA Method 3052 (multi-acid digest with microwave assist) (US-EPA, 1996) and analyzed by inductively coupled plasma-optical emission spectrometry (ICP-OES) and inductively coupled plasma-mass spectrometry (ICP-MS).

^c Hg content calculated based on mass balance in the solid and aqueous phase.

^d of CL2-DMC and CL2-CPS estimated based on CL2.

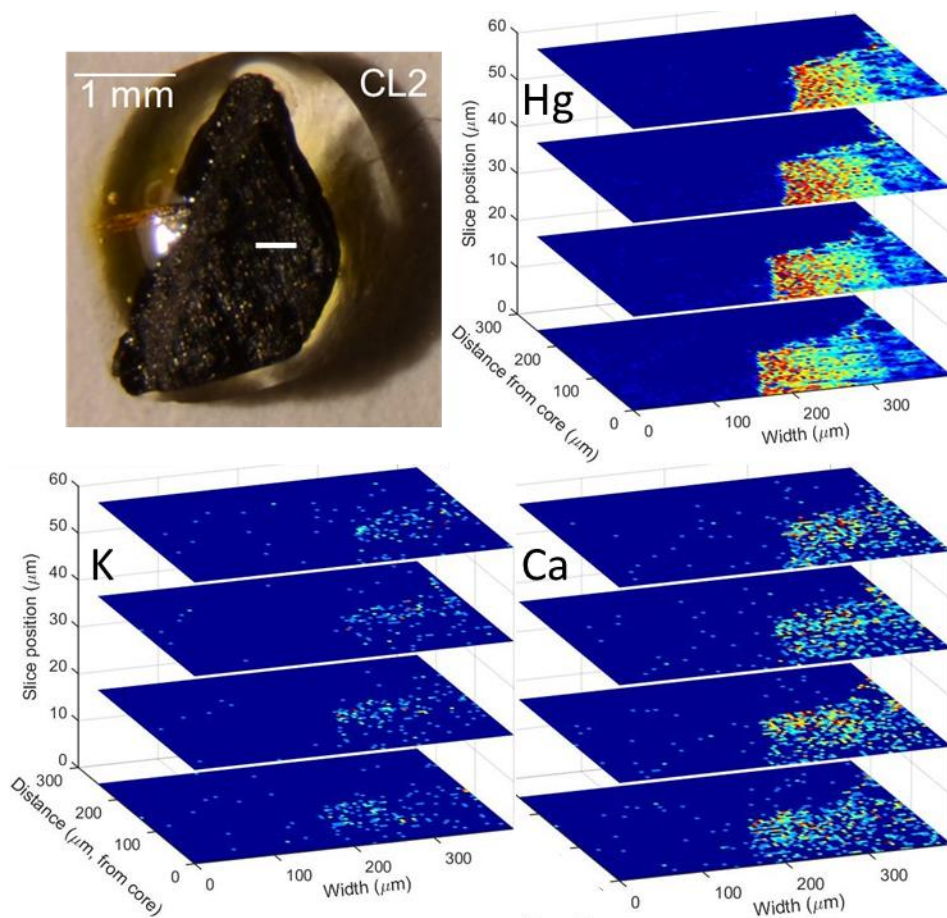


Figure S7.1. Confocal X-ray micro-fluorescence imaging showing the distribution of Hg, K, and Ca in an unmodified biochar particle with adsorbed Hg. S distribution is not provided because S is undistinguishable from the background.

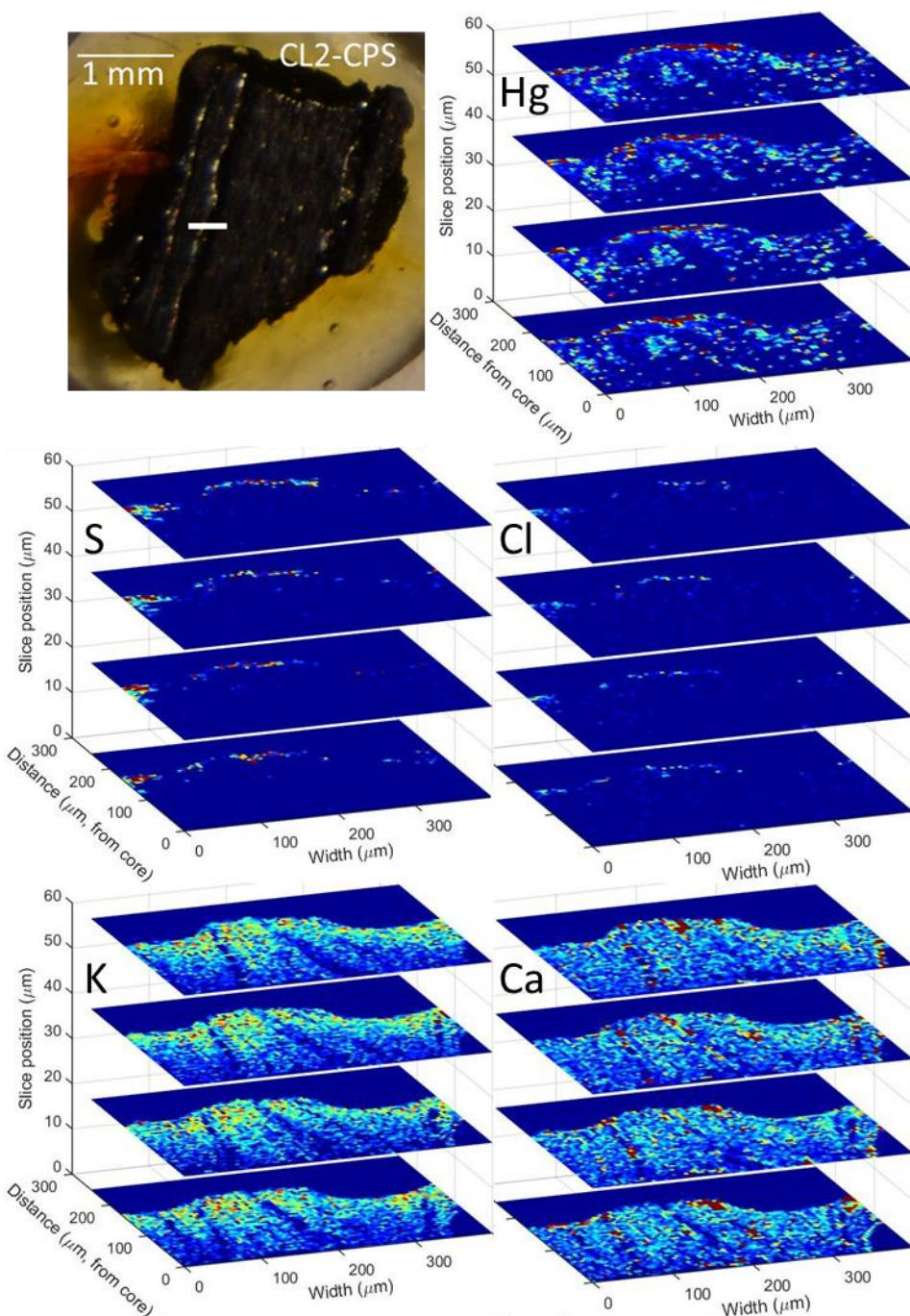


Figure S7.2. Confocal X-ray micro-fluorescence imaging showing the elemental distribution of Hg, S, Cl, K, and Ca in a polysulfide modified biochar particle with adsorbed Hg.

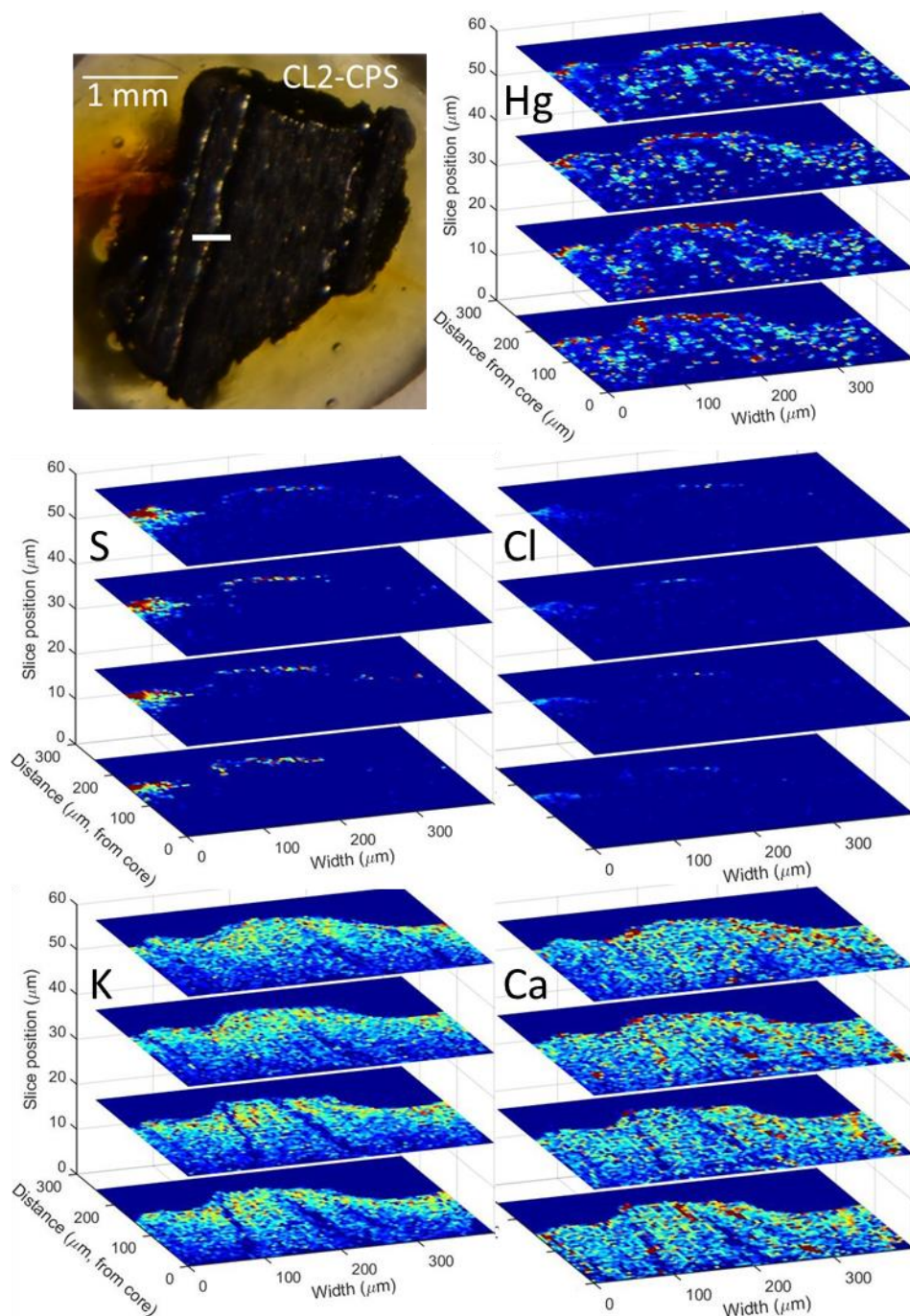


Figure S7.3. Confocal X-ray micro-fluorescence imaging showing the elemental distribution of Hg, S, Cl, K, and Ca in the 2nd polysulfide modified biochar particle with adsorbed Hg.

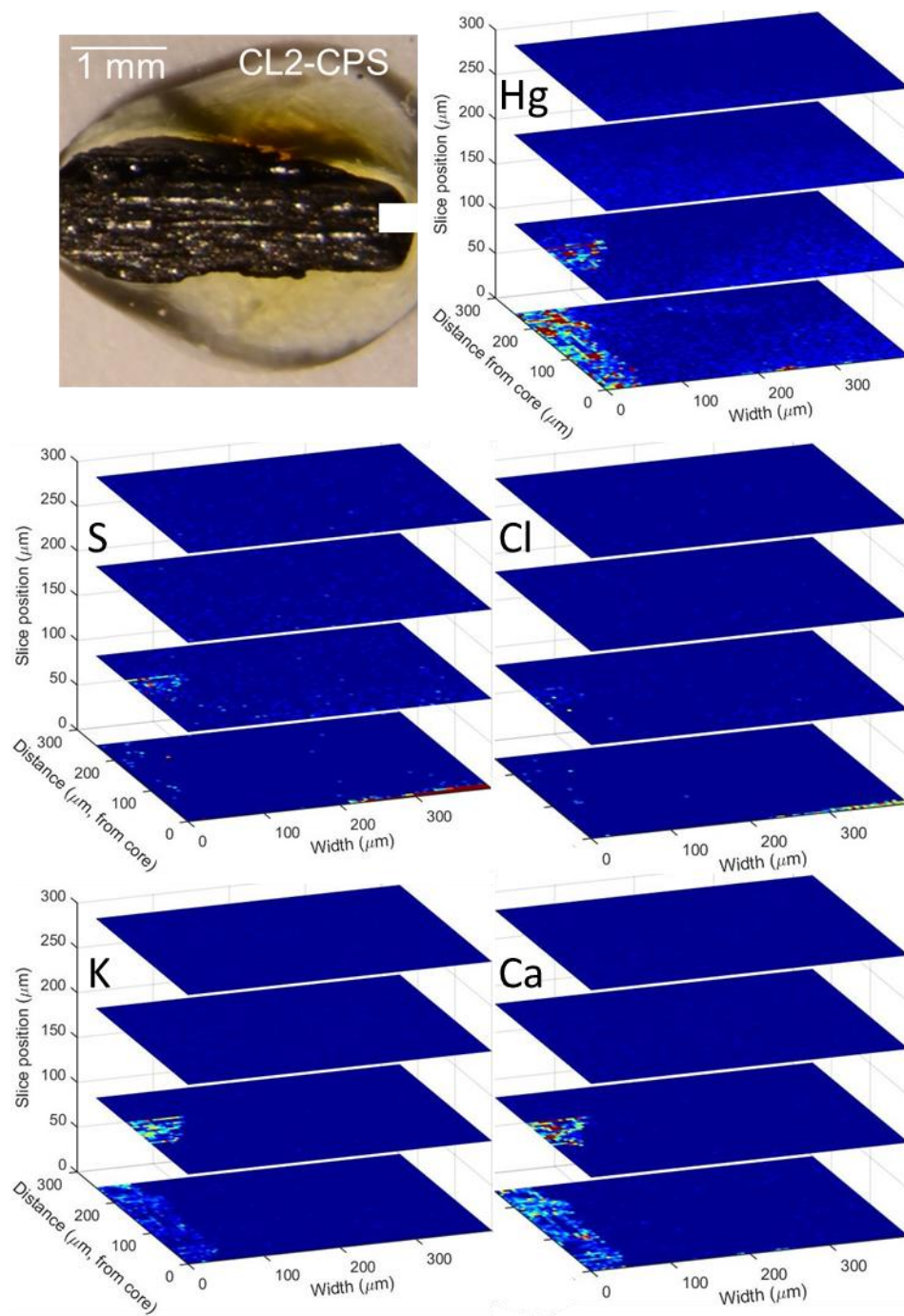


Figure S7.4. Confocal X-ray micro-fluorescence imaging showing the elemental distribution of Hg, S, Cl, K, and Ca in the 3rd polysulfide modified biochar particle with adsorbed Hg.

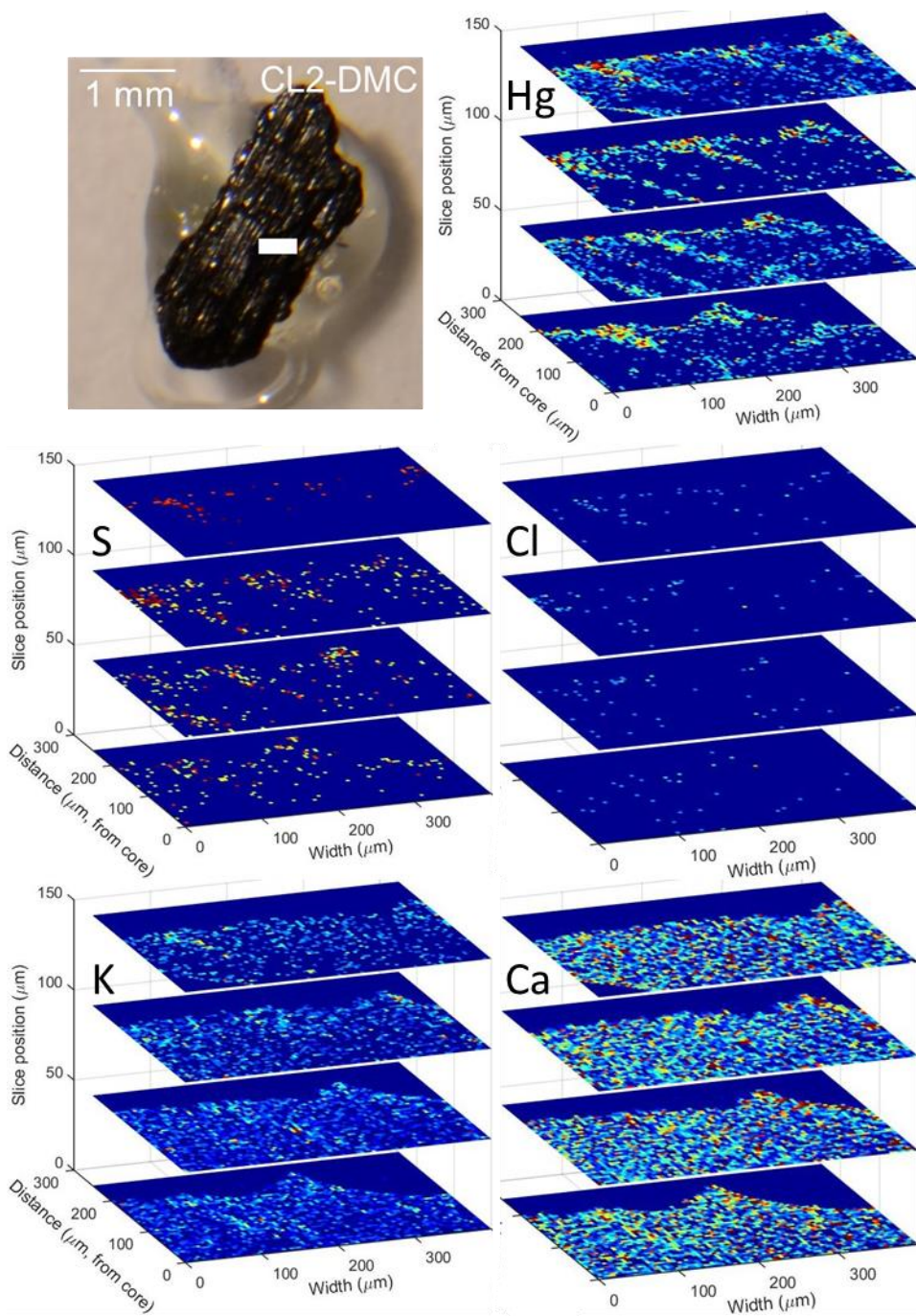


Figure S7.5. Confocal X-ray micro-fluorescence imaging showing the elemental distribution of Hg, S, Cl, K, and Ca in a dimercapto modified biochar particle with adsorbed Hg.

Appendix G: *Release of Nutrients and Trace Elements from Various Biochars and Implications for Mercury Remediation*

G.1 Executive Summary

Batch-style experiments were conducted to evaluate the removal of Hg and release of various components (dissolved organic carbon, anions, cations, trace elements, and nutrients) from 36 biochars prepared from distinct feedstocks and at different temperatures. The Hg was effectively removed from the solution. Elevated concentrations of other components were observed in the majority of the aqueous solutions mixed with biochars. No significant differences were observed for concentrations of NO_3^- , Cl^- , Na, Ca, Fe, Cu, $\text{PO}_4\text{-P}$, $\text{NH}_3\text{-N}$, and K between low-T and high-T biochars. The concentrations of Cl^- , Na, Mn, Ca, and K of agricultural residue-based biochar were significantly lower than those in manure-based biochars. The aqueous data was modeled using PHREEQC by considering thermodynamic constants between the Hg and dissolved organic matter (DOM). DOM was assumed to be composed of thiol, carboxylic, and phenolic functional groups. Modelling results suggest that the majority of Hg was likely complexed with the thiol group. The effective removal of Hg by biochar suggests biochar may be a viable alternative for Hg-contaminated water treatment. However, the DOM-Hg complexes may affect the Hg speciation, bioavailability, transport, and methylation processes. The elevated anions, cations, trace elements and nutrients may affect the geochemical properties of the receiving water body after the application of biochar. Long-term evaluation is required for the impact of biochar application on the surrounding environment.

G.2 Introduction

Biochar has been proposed as a reactive material for removing mercury (Hg) from aqueous solutions and as an additive to stabilize Hg in soils and sediments by co-blending (Gomez-Eyles et al., 2013; Liu et al., 2016a; Liu et al., 2016b). A number of studies have

documented moderate to high rates of Hg uptake by biochars (Boutsika et al., 2014; Bundschuh et al., 2015; Gomez-Eyles et al., 2013; Tang et al., 2015a). However, the primary concerns in application of biochar for Hg removal are the conversion of Hg to more toxic methyl Hg (MeHg) and facilitated Hg transport.

The process of producing biochars leads to stabilization of carbon and some elements, but also to the release of soluble constituents, including inorganic and organic carbon, anions (Cl , NO_3^- , SO_4^{2-}), major cations (Na, Mg, and Ca), major nutrients (N, P, K, and Si) and trace elements (Mn, Fe, Cu, As, etc.) (Hass et al., 2012; Jin et al., 2016; Liu et al., 2015; Xie et al., 2016; Yargicoglu et al., 2015; Zornoza et al., 2016). Further understanding of the variation in forms and concentrations of these constituents in relation to feedstock type and pyrolysis temperature is required to apply biochar as an effective reactive material for Hg and other contaminants.

Liu et al. (2015 & 2016) conducted previous studies on a series of biochars produced from a variety of feedstocks and at different pyrolysis temperatures. These studies focused on the effectiveness and mechanisms of Hg uptake by different groups of biochars, the forms of sulfur and other functional groups of the biochars, and the release of soluble carbon and S constituents from the biochars.

The released soluble C includes dissolved organic carbon (DOC; including labile organic carbon) and inorganic carbon (for example, alkalinity) (Liu et al., 2015; Mukherjee & Zimmerman, 2013; Qiu et al., 2015). These carbon forms can be utilized as electron donors by potential Hg methylators to convert Hg to MeHg. Inorganic S (*e.g.*, SO_4^{2-}) can also be released from various biochars (Liu et al., 2016b; Yao et al., 2010) and can be utilized by sulfate-reducing bacteria (SRB) for Hg methylation. Additionally,

dissolved organic matter (DOM) can be released from biochar and can facilitate Hg transport by forming complexes with Hg (Haitzer et al., 2002; Wallschläger et al., 1996).

Previous studies show DOC ranged from <0.1-3% of the total C in biochar. The DOM is widely known to form strong complexes with Hg²⁺ ions, and Hg species can be affected by the formation of complexes with DOM. DOM also can potentially enhance the transport of Hg in flood plain soil, fresh water and sediment pore water, by either limiting adsorption onto solid phases or by enhancing the solubility of Hg precipitates. DOM can also affect Hg methylation processes by decreasing or increasing the bioavailability of Hg and through stimulation of microbial activity. Therefore, improved understanding of the formation of Hg-DOM complexes can assist in understanding Hg complexation and bioavailability in aqueous solution.

This study adds to the previous work by evaluating the release of anions, cations, major nutrients and trace elements from the same set of biochars, and by modelling the potential formation of Hg-DOM complexes. The biochars were prepared from wood-, agricultural residue- and manure-based feedstocks at different pyrolysis temperatures. These new findings are integrated with the results of the previous studies by Liu et al. (2015 & 2016) with the overall goal of identifying biochar types that optimize Hg uptake but minimize release of constituents that promote methylation reactions.

G.3 Materials and Methods

G.3.1 Biochar Samples

Thirty-six biochar samples were evaluated for nutrient release in batch-style experiments. The feedstocks for biochar preparation included corn cobs (CC), corn stovers (CS), cocoa husk (CA), cotton seed husk (CT), wheat shaft (GR2), spent hop (GR3), switchgrass (GR4), pine mulch and bark (SW), poultry (MP) and cattle (MB) manures, and

mushroom soils (MU). The feedstocks were first air dried, cut into pieces, and then pyrolyzed in a pre-heated kiln at either 300°C (L, low-T) or 600°C (H, high-T) under limited oxygen supply. Details of the preparation method and feedstocks are described previously (Liu et al., 2015). Three commercial products pyrolyzed at ~700 °C were purchased from Wicked Good Charcoal Co., US (CL1), Cowboy Charcoal Co., US (CL2), and Biochar Engineering Corp., US (CL5). Two batches of activated carbon (AC1 and AC2) were used as benchmark materials (Sigma-Aldrich Corp., St. Louis, US). The biochars were categorized into three groups as wood-based (AC, CL, SW), agricultural residue-based (CC, CS, CA, CT, GR), and manure-based (MP, MB, MU) groups.

G.3.2 Batch-Experiment Set-up

The batch-style experiment was conducted by mixing 2 g of biochar with 150 mL of Hg-spiked river water collected from the South River near Waynesboro, VA, USA. The initial Hg concentration of the spiked water was ~10 µg L⁻¹ (10 000 ng L⁻¹). The mixture was shaken thoroughly, and then allowed to settle for equilibration at room temperature for 2 days. Ultrapure water and river water were used as controls to assess the potential Hg contamination during the laboratory procedures. Samples containing river water only and biochar mixed with unspiked river water were also used as controls. Details of the experiments are described previously (Liu et al., 2015; Liu et al., 2016b).

At the termination of the experiments, water samples were filtered using 0.45 µm cellulose acetate filters (Pall Corp., UK). The filtered first 5 mL sample was discarded and the rest was collected for major cation, trace element, anion, ammonia (NH₄-N), and phosphate (PO₄-P) analyses. Samples for major cation and trace element analysis were acidified to pH<2 using ultra-pure 15.8N HNO₃. Samples for NH₄-N and PO₄-P analyses

were acidified to pH<2 using ultra-pure H₂SO₄. All the samples were preserved at 4 °C before analysis.

G.3.3 Water Sample Analysis

NH₃-N concentrations were determined using the salicylate spectrophotometric method (Hach Test Method 8155). PO₄-P concentrations were measured using the ascorbic acid spectrophotometric method (Hach Test Method 8048). Samples for major cations were analyzed by inductively-coupled plasma atomic emission spectroscopy (Thermo Scientific iCAP 6000) and for trace elements by inductively-coupled plasma mass spectroscopy (Thermo Scientific XSeries II). Concentrations of anions were determined on unacidified samples using ion chromatography (DX-600, Dionex Corp.) with an IonPac AS11 4×250 mm column.

The THg, pH, alkalinity, organic acids (OAs), and DOC were also measured at the time of sample collection. The detailed sampling and analysis information was described previously (Liu et al., 2015; Liu et al., 2016b).

G.3.4 Specific Surface Area

The specific surface area (SSA) was determined with N_{2(g)} at 77 K using a Gemini VII 2390 Surface Area Analyzer (Micromeritics Co.). All samples were out-gassed at 105 °C under vacuum conditions for 24 h using a Gemini 2375 ValPrep 061 (Micromeritics Co.) before N_{2(g)} adsorption. The multipoint Brunauer-Emmett-Teller (BET) method was employed to calculate SSA (Brunauer et al., 1938).

G.3.5 Speciation Modeling

Speciation modeling was conducted to determine the complexation of Hg with inorganic species and thiol, carboxylic, and phenolic functional groups of dissolved organic matter

(DOM). The model calculations were executed with PHREEQCi (Parkhurst & Appelo, 1999) using the modified MINTEQA2 database (Allison et al., 1991). Thermodynamic reaction constants for Hg²⁺ and other metals with thiol, carboxylic, and phenolic ligands were added into the database (Table G.1). The pH, Eh, and concentrations of cations, anions, alkalinity, OAs, and DOC (Liu et al., 2015) were used as model inputs.

G.3.6 Statistical Analysis

Differences among the feedstock type and pyrolysis temperature were assessed by two-fractional analysis of variance (ANOVA). If significant differences were observed, the post hoc Tukey's HSD test was further performed at $P < 0.05$. The correlations between THg and SSA were evaluated by Pearson product-moment correlation coefficients (r). The statistical analysis was performed in Microsoft Excel.

G.4 Results and Discussion

G.4.1 Summary of Hg Removal and Release of SO₄²⁻, OAs, and DOC

The results of THg concentrations, Hg removal, and release of SO₄²⁻, DOC, and OA were presented previously by Liu et al. 2015 and 2016. The results indicate that compared with the THg concentration of the Hg-spiked river water control, Hg was effectively removed by the biochars (Table G.2). THg concentrations decreased from ~10 000 ng L⁻¹ to less than 50 ng L⁻¹ in solutions mixed with activated carbon (AC2), charcoal (CL5), and high-T corn stover (CS1), wheat straw (GR2), and mushroom soil (MU2) biochars. The Hg removal was greater than 95% for activated carbon (AC), all high-T wood-based biochars (CL5, CL2, CL1, SW1, and SW2), high-T corn stover (CS1 and CS2), corn cobs (CC1), switchgrass (GR4), wheat straw (GR2), poultry manure (MP1), and mushroom soil (MU2 and MU3) biochars, and low-T poultry manure (MP1) and mushroom soil (MU2 and MU1) biochars.

The SO_4^{2-} concentrations ranged from 6.0 to 1000 mg L^{-1} in solutions mixed with biochars (Table G.2). The SO_4^{2-} concentrations were elevated in the solution mixed with biochar compared with the river water control. The highest concentrations of SO_4^{2-} (72-1000 mg L^{-1} , half of concentrations $>400 \text{ mg L}^{-1}$) were observed in samples mixed with mushroom soil and poultry manure biochars compared with other two groups of biochar. The least elevated concentrations of SO_4^{2-} were observed in wood-based biochars. No significant differences of SO_4^{2-} concentrations were observed between low-T and high-T biochars.

The concentrations of OAs and DOC observed in the aqueous solutions mixed with the biochar samples decreased following the general order: DOC >acetate >formate >propionate >lactate (Table G.2). Concentrations of OAs and DOC varied as a function of pyrolysis temperature and raw materials. The highest concentrations of OAs and DOC were observed in the batch mixture containing high-T cocoa husk biochar. Relatively high concentrations of OAs and DOC were observed in the batch mixtures containing low-T agricultural-residue and manure biochars, while lower concentrations were observed in the samples containing wood-based biochars.

The released SO_4^{2-} and DOC (including OA) from biochar may be problematic for applications of biochar at Hg-contaminated site, especially under reducing conditions. The SO_4^{2-} and DOC can be utilized as electron donor and acceptor by SRB to methylate Hg (Gilmour et al., 1992; Hsu-Kim et al., 2013).

G.4.2 Specific Surface Area

The SSA of activated carbon was $\sim 575 \text{ m}^2 \text{ g}^{-1}$ and of charcoal was between 52.8 and 243 $\text{m}^2 \text{ g}^{-1}$ (Fig. G.1). The SSAs of the low-T biochars ranged from 1.06 to 11.3 $\text{m}^2 \text{ g}^{-1}$. The

SSAs of the high-T biochars varied considerably, from 1.93 to 229 m² g⁻¹. For any given feedstock, the ratio of the SSAs of high-T to low-T biochars ranged from 0.67 to 131 (with the majority >>10), which indicates that high temperature pyrolysis can greatly increase the SSA. It was not the case for all feedstocks, *e.g.* the SSAs of cotton seed husk, hop, poultry manure, and mushroom soil high-T biochars were similar to the corresponding low-T biochars.

The post hoc Tukey's HSD test determined that SSAs of high-T biochar was significantly greater than those of low-T biochars and SSAs of wood-based biochar was significantly greater than those of the other two groups ($P < 0.05$). The low SSAs of the low-T biochars indicate that either the biochars are not micro-porous or that the pores within these biochars are small and dead-ended, preventing access to the adsorbing gas (Liu et al., 2015). The trend is consistent with coconut coir (Shen et al., 2012) and cotton seed husk biochars (Uchimiya et al., 2011). Increased pyrolysis temperature typically results in the formation of more micro-pores and meso-pores, which increase the SSA.

The correlation analysis indicates that the Hg removal was not significantly correlated with the SSA. The lack of correlation indicates that other parameters or integration of parameters may control the Hg removal. The lack of correlation may also be due to the relatively low initial THg concentration.

G.4.3 Anions

Elevated concentrations of anions were observed in aqueous samples obtained from batch experiments for the majority of biochar samples compared with the river water control (Fig. G.2). The highest concentrations of NO₃⁻ and Cl⁻ (up to 350 mg L⁻¹) were observed

in the solutions mixed with the manure-based biochars, while lower concentrations were observed in solutions mixed with biochars prepared from wood.

The concentrations of NO_3^- decreased from 1.8 mg L^{-1} to as low as 0.6 mg L^{-1} in batch mixtures containing wood-based biochars and increased to as high as 3.2 mg L^{-1} in batch mixtures containing agricultural residue-based and manure-based biochars.

Elevated concentrations of Cl^- were observed in the majority of mixtures compared with the river water control, especially in the mixtures containing poultry manure and mushroom soil biochars (up to 350 mg L^{-1}). The statistical analysis indicates that no significant differences of NO_3^- and Cl^- concentrations were observed between the low-T and high-T biochars, whereas the Cl^- concentrations of agricultural residue-based biochars were significantly lower than manure-based biochars using post hoc Tukey's HSD test ($P < 0.05$).

The application of biochars with potential to release high concentration of Cl^- should may also be of concern, as Cl^- can affect the speciation of Hg in solution (Hsu-Kim et al., 2013) and the abiotic methylation of inorganic Hg is accelerated by the presence of elevated concentrations of Cl^- (Celo et al., 2006).

G.4.4 Major Cations

The concentrations of Na and Mg in the majority of the mixtures were greater than concentrations in the control (Fig. G.3). The Ca concentrations in most solutions mixed with high-T biochars were lower than the concentrations in control. The highest concentrations of Na, Mn, and Ca were observed in solutions mixed with low-T biochars; the concentrations were 115 mg L^{-1} (poultry manure (MP1)), 23.0 mg L^{-1} (mushroom soil (M1)), and 221 mg L^{-1} (mushroom soil (M1)), respectively.

The statistical analyses indicate the concentrations of Na and Ca in high-T and low-T systems were not significantly different, and Mg concentrations in low-T systems were significantly greater than those in high-T systems. The concentrations of Na, Mn, and Ca were significantly greater in solutions mixed with manure-based biochars than those in solutions mixed with agricultural residue-based biochars. The correlation analysis indicates the concentration of Na and Ca was positively correlated. The concentrations of Na, Mn, and Ca were not significantly correlated with THg concentrations.

The elements with elevated concentrations in the leaching solutions also were present in the solid-phase as indicated by analysis with scanning electron microscopy/energy-dispersive X-ray spectroscopy (SEM/EDX) (Liu et al., 2015). Elevated concentrations of Na, Mg, and Ca in wood-based biochars also were observed in a previous study (Yargicoglu et al., 2015). The ionic strength and Hg speciation in solution can be affected by the released cations.

G.4.5 Trace Elements

Elevated concentrations of Mn and As were observed in solutions mixed with biochars compared with the river water control (Fig. G.4). The concentrations of Fe and Cu in less than half of the solutions mixed with biochars were lower than concentrations in the control. The greatest concentrations of Mn ($283 \mu\text{g L}^{-1}$) were observed in solution mixed with low-T pine mulch biochar (SW1), Fe ($463 \mu\text{g L}^{-1}$) with high-T spent hop biochar (GR3), Cu ($211 \mu\text{g L}^{-1}$) with high-T poultry manure biochar (MP3), and As ($4.33 \mu\text{g L}^{-1}$) with low-T mushroom soil biochar (MS2). The concentrations of these elements (Fig. G.4) and Cr, Cd, B, Be, Sb, Ti, Ni, Ag, and Zn (data not shown; majority <method

detection limit) in most solutions were lower than National Recommended Water Quality Criteria of US EPA (EPA, 2009).

The statistical analyses indicate the concentrations of Mn and As in low-T systems were significantly lower than those in high-T systems, and no significant differences were observed in the concentrations of Fe and Cu between low-T and high-T systems. The concentrations of these elements were not significantly different among the three groups of biochar. The observation of elevated concentrations of Mn, Fe, Cu, and As in wood-based biochars differed from a previous study (Yargicoglu et al., 2015), which reported the concentrations of these elements were all below detection limits.

G.4.6 Nutrients

Elevated concentrations of PO₄-P, NH₃-N, K, and Si were observed in aqueous samples obtained from batch experiments for the majority of biochar samples compared with the river water control (Fig. G.5), except the concentrations of Si in solutions mixed with wood-based biochar were all less than the concentration in the control. Biochars prepared from agricultural residue leached elevated concentrations of PO₄-P (mean as 5.0 mg L⁻¹), K (mean as 250 mg L⁻¹), and Si (mean as 8.1 mg L⁻¹). The manure-based biochars leached 0.35 mg L⁻¹ of NH₃-N and 364 mg L⁻¹ of K. The biochars prepared from wood material had the lowest concentrations of leached PO₄-P (0.53 mg L⁻¹), NH₃-N (0.18 mg L⁻¹), K (16.5 mg L⁻¹), and Si (2.87 mg L⁻¹). The highest concentration of PO₄-P was released by cocoa husk biochars up to 28.1 mg L⁻¹. More NH₃-N was released by poultry manure biochars than others. Elevated concentrations of K were leached up to 707 mg L⁻¹ by cocoa husk, corn, and mushroom soil biochars. The highest concentrations of Si were 30.5 mg L⁻¹ in solutions mixed with high-T corn stover biochar (CS2). The elevated

concentrations of K and Si are consistent with high K content in the biochars made from corn stover (Cheah et al., 2014) and SEM/EDX results (Liu et al., 2015).

The statistical analysis indicates that no significant differences of PO₄-P, NH₃-N, and K concentrations were observed among high-T and low-T biochars. The Si concentrations in high-T systems were significantly greater than those in low-T systems. The K concentrations in batch mixtures with manure-based biochar were significantly greater than those with agricultural residue-based and wood-based biochars. The Si concentrations in solutions mixed with agricultural residue-based were significantly greater than those from wood-based biochars. The NH₃-N concentrations were significantly higher released by high-T agricultural residue-based biochars than the corresponding low-T biochars. These observations are consistent with a previous study, that higher concentrations of NH₃-N are leached by grass biochars produced at 250 °C than those produced at 650 °C (Mukherjee & Zimmerman, 2013). The feedstock plays a key role in the leaching of nutrients. For example, high percentages of nutrient are observed in raw manure and cocoa husk (Agyarko & Asiedu, 2012). If biochars with elevated concentrations of nutrient are used for Hg-contaminated site remediation, special attention should be paid. The leached nutrient can be utilized by plants and microbes (including Hg methylators).

G.4.7 Hg-DOM Complexes Modelled by PHREEQC

The following equations were used to estimate the concentrations of thiol (Equ. 1), carboxylic (Equ. 2), and phenolic (Equ. 3) ligands in DOM using DOC concentrations:

$$[DomsH]=[DOM]\times F_1\times F_2\times F_3/W_S \quad (1)$$

$$[DomcooH]=C_1\times [DOC]/1000 \quad (2)$$

$$[DomoH]=C_2\times [DOC]/1000 \quad (3)$$

Where $[DomsH]$, $[DomcooH]$, and $[DomoH]$ represent the concentrations of thiol, carboxylic, and phenolic ligands as mmol L^{-1} ; $[DOM]$ and $[DOC]$ represent the concentrations of DOM and DOC as mg L^{-1} . DOM concentrations are treated as two times DOC concentrations by mass (Dong et al., 2010). In Equ. 1, F_1 is the total sulfur content percentage in DOM by mass, F_2 is the percentage of reduced sulfur content (thiol ligand) in total sulfur, F_3 is the percentage of reactive thiol ligand in the reduced sulfur content, and W_S = atomic weight of sulfur. In Equ. 2 and 3, C_1 and C_2 is the conversion factor for carboxylic and phenolic ligands from DOM. F_1 , F_2 and F_3 are selected as 0.86% (Benoit et al., 2001b; Dong et al., 2010; Haitzer et al., 2003), 50% (Haitzer et al., 2003; Skyllberg et al., 2006), and 2% (Skyllberg et al., 2006), respectively. C_1 and C_2 are used as 9.5 and 4.1 mmol g^{-1} DOC (Lu & Allen, 2002). F_1 , F_2 , F_3 , C_1 , and C_2 were conservative estimates. For samples with concentrations below detection limits (DL), a value of half DL was entered for modelling purpose (Ettler et al., 2007).

The modelling results indicate that most of the Hg in the solution was bound to thiol functional groups ($Doms^-$ and $DomcooDoms^{2-}$, >95%) of DOM (Fig. G.6). The modelled concentrations of Hg-DOM complexes were greater for low-T biochar than for high-T biochar. The concentrations of Hg-DOM complexes were lower in charcoal and activated carbon than those of other biochars, as a result of low concentrations of DOC in charcoal and activated carbon (Liu et al., 2015) and Hg (Table G.2). The only samples with $Hg(OH)_2$ (aq) as a major species were the control (river water), and high-T poultry manure and mushroom soil biochars, which is likely due to low concentrations of DOC and high pH (Liu et al., 2015).

The high percentages of Hg-DOM complexes were likely due to the low Hg concentrations (Table G.2) and relatively abundant thiol functional groups. The greater concentrations of Hg-DOM complexes in solutions mixed with low-T biochars than those mixed with high-T biochars are likely due to the much greater DOC concentrations leached by low-T biochars (Liu et al., 2015). The relatively high percentages of Hg(OH)₂ (aq) species in high-T biochar may be due to the high pH values in solutions mixed with high-T biochars and low DOC concentrations.

The Hg-DOM complexes may affect the speciation, transformation, and bioavailability of Hg. Complexation between Hg and DOM may inhibit Hg²⁺ sorption on the surface of minerals and facilitate the transport of Hg from polluted soils and sediments to rivers, lake, and groundwater (Haitzer et al., 2002; Hsu-Kim et al., 2013; Liang et al., 2013; Wallschläger et al., 1996). For example, a study on Hg at Matagami Lake, Québec (Canada), shows an increase of THg content correlated well with the increase of organic matter in the sediment cores (Moingt et al., 2014). For the biogeochemical role of DOM in Hg methylation, early findings are that the bioaccumulation of Hg in food webs may be decreased by lowering the bioavailability of Hg (II) for methylation (Benoit et al., 2001b), because the DOM molecules are generally too large for microbes uptake (Gilmour & Henry, 1991). Recent findings consider Hg-DOM complexes play a positive role in Hg methylation by increasing the solubility of Hg compounds (Hsu-Kim et al., 2013) and providing carbon sources for Hg methylators (Chiasson-Gould et al., 2014).

G.5 Conclusion

The results of this study show biochars have the potential to be effective materials for removing Hg at environmental-level concentrations from aqueous solution. The THg

concentrations in aqueous phase in contact with biochars decreased for the majority of biochar materials evaluated, with removal percentages >90% for high-T biochars. The SSAs of the tested biochars varied greatly from 1.06 to 575 m² g⁻¹. Elevated concentrations of anions, cations, trace elements, and nutrient were observed in the solutions mixed with the majority of the biochars. The geochemistry modelling results indicate >95% of Hg was complexed with DOM in the solutions mixed with biochars. The pyrolysis temperature and feedstock type play an important role in the Hg removal and the release of these components.

Despite the high Hg removal by the biochars, attention should also be paid to the alteration of the solution and the leached component from biochars (nutrient, DOC, SO₄²⁻, etc.). These components can affect the Hg species in solution, bioavailability, transport, and methylation process. The longevity of Hg stabilization is also unknown. Long-term experiments are required to test these unknowns.

Table G.1. Selected thermodynamic reaction constants for Hg^{2+} and other metals with thiol, carboxylic, and phenolic ligands at temperature = 25 °C, ionic strength =0, and pressure 10^5 Pa

Reactions	log K	Reference
^a $\text{DomsH} = \text{Doms}^- + \text{H}^+$	-10	(Martell & Smith, 2004)
^c $\text{DomcooH} = \text{Domcoo}^- + \text{H}^+$	-5.12	(Temminghoff et al., 2000)
^e $\text{DomoH} = \text{Domo}^- + \text{H}^+$	-9.78	(Temminghoff et al., 2000)
$\text{Hg}^{+2} + \text{Doms}^- = \text{HgDoms}^-$	28.0	(Dong et al., 2010)
$\text{Hg}^{+2} + 2\text{Doms}^- = \text{Hg}(\text{Doms})_2$	34.0	(Dong et al., 2010)
$\text{Hg}^{+2} + \text{Domcoo}^- = \text{HgDomcoo}^+$	10.0	(Dong et al., 2010; Gismera et al., 2007)
$\text{Hg}^{+2} + \text{Domo}^- = \text{HgDomo}^+$	8.78	(Gismera et al., 2007)
$\text{Hg}^{+2} + \text{Domcoo}^- + \text{Doms}^- = \text{HgDomcooDoms}$	31.6	(Dong et al., 2010)
$\text{Doms}^- + \text{Ca}^{+2} = \text{CaDoms}^+$	2.5	(Martell & Smith, 2004)
$\text{Doms}^- + \text{Mn}^{+2} = \text{MnDoms}^+$	4.75	(Martell & Smith, 2004)
$\text{Doms}^- + \text{Fe}^{+2} = \text{FeDoms}^+$	6.60	(Martell & Smith, 2004)
$\text{Doms}^- + \text{Co}^{+2} = \text{CoDoms}^+$	8.14	(Martell & Smith, 2004)
$\text{Doms}^- + \text{Ni}^{+2} = \text{NiDoms}^+$	9.79	(Martell & Smith, 2004)
$\text{Doms}^- + \text{Zn}^{+2} = \text{ZnDoms}^+$	9.11	(Martell & Smith, 2004)
$\text{Doms}^- + \text{Cd}^{+2} = \text{CdDoms}^+$	10.1	(Martell & Smith, 2004)
$\text{Doms}^- + \text{Cu}^{+2} = \text{CuDoms}^+$	14.1	(Laglera & van den Berg, 2003)
$\text{Doms}^- + \text{Mg}^{+2} = \text{MgDoms}^+$	2.75	(Martell & Smith, 2004)
$\text{Doms}^- + \text{Pb}^{+2} = \text{PbDoms}^+$	12.2	(Martell & Smith, 2004)
$\text{Fe}^{+3} + \text{Doms}^- = \text{FeDoms}^{+2}$	12.3	(Berthon, 1995)
$\text{Mg}^{+2} + \text{Domcoo}^- = \text{MgDomcoo}^+$	1.1	(Bryan et al., 2002)
$\text{Al}^{+3} + \text{Domcoo}^- = \text{AlDomcoo}^{+2}$	2.5	(Bryan et al., 2002)
$\text{Ca}^{+2} + \text{Domcoo}^- = \text{CaDomcoo}^+$	3.57	(Temminghoff et al., 2000)
$\text{Cu}^{+2} + \text{Domcoo}^- = \text{CuDomcoo}^+$	5.4	(Temminghoff et al., 2000)
$\text{Fe}^{+2} + \text{Domcoo}^- = \text{FeDomcoo}^+$	1.6	(Bryan et al., 2002)
$\text{Fe}^{+3} + \text{Domcoo}^- = \text{FeDomcoo}^{+2}$	2.4	(Bryan et al., 2002)
$\text{Zn}^{+2} + \text{Domcoo}^- = \text{ZnDomcoo}^+$	1.6	(Bryan et al., 2002)
$\text{Mg}^{+2} + \text{Domo}^- = \text{MgDomo}^+$	2.58	(Bryan et al., 2002)
$\text{Al}^{+3} + \text{Domo}^- = \text{AlDomo}^{+2}$	7.33	(Bryan et al., 2002)
$\text{Fe}^{+2} + \text{Domo}^- = \text{FeDomo}^+$	4.27	(Bryan et al., 2002)
$\text{Fe}^{+3} + \text{Domo}^- = \text{FeDomo}^{+2}$	6.99	(Bryan et al., 2002)
$\text{Zn}^{+2} + \text{Domo}^- = \text{ZnDomo}^+$	4.27	(Bryan et al., 2002)
$\text{Ca}^{+2} + \text{Domo}^- = \text{CaDomo}^+$	5.05	(Temminghoff et al., 2000)
$\text{Cu}^{+2} + \text{Domo}^- = \text{CuDomo}^+$	10.5	(Temminghoff et al., 2000)

^a DomsH thiol functional group in DOM;

^b Doms^- deprotonated thiol functional group in DOM;

^c DomcooH carboxylic functional group in DOM;

^d Domcoo⁻ deprotonated carboxylic functional group in DOM;

^e DomoH phenolic functional group in DOM;

^f Domo⁻ deprotonated phenolic functional group in DOM.

Table G.2. Summary of data published by Liu et al. (2015) and Liu et al. (2016).

Group	Biochar	THg ^a (ng L ⁻¹)		Removal ^a (%)		SO ₄ ²⁻ ^a (mg L ⁻¹)		DOC ^b (mg L ⁻¹)		Acetate ^b (mg L ⁻¹)	
		Low	High	Low	High	Low	High	Low	High	Low	High
Wood	AC2**	-	4.38	-	99.9	-	16.5	-	<0.05	-	0.12
	AC1**	-	55.6	-	99.4	-	15.1	-	1.39	-	0.12
	CL5**	-	21	-	99.7	-	10.2	-	3.68	-	1.99
	CL2**	-	297	-	97.0	-	5.99	-	5.38	-	0.17
	CL1**	-	346	-	96.5	-	11.3	-	3.82	-	3.07
	SW1	1440	409	81.3	95.8	11	7.11	91.8	2.3	29.2	2.59
	SW2	5850	333	32.8	96.6	9.72	5.96	7.50	1.72	4.33	0.08
Agricu- ltural residue	CS1	521	21.2	94	99.7	19.1	17.6	148	2.81	31.3	0.18
	CS2	963	86.8	89.9	98.8	12.5	38.1	51.1	5.49	37.5	0.18
	CC2	1590	521	79.4	94.7	10.2	6	9.35	2.99	7.91	0.24
	GR4	1890	317	78.3	96.8	13.4	8.94	13.1	2.12	8.42	0.15
	GR2	2220	46.7	76.8	99.4	61.8	78	26.8	3.64	22.5	0.21
	GR3	1830	1500	76.3	84.6	9.54	5.91	2.14	1.5	<0.05	<0.05
	CC1	3100	234	64.4	96.8	10.3	7.54	13.5	3.33	13.4	0.12
	CT1	3800	1330	60.2	81.8	11	7.46	24.6	3.76	23.7	0.16
	CA1	4640	4910	39.9	32.7	50.6	42.7	147	139	84.2	115
Manure	MP1	194	72.7	98	99.2	101	96.4	59.8	<0.05	<0.05	0.30
	MU2	422	21.7	95.6	99.8	987	914	144	<0.05	33.04	0.28
	MU3**	-	225	-	97.1	-	72.1	-	3.94	-	0.55
	MP2*	484	-	94.9	-	131	-	79.71	-	15.51	-
	MP3**	-	859	-	88.9	-	415	-	<0.05	-	0.50
	MU1	292	1620	96.6	81.4	1000	709	124	<0.05	39.06	0.42
	MB1	1340	867	84.6	90.0	12	10.2	20.7	20.2	17.31	0.32
	Control	6940		29		5.96		1.81		<0.05	

Note: Control represents Hg-spiked river water with no biochar added. * Data not available for high-temperature (high-T) biochar. ** Data not available for low-temperature (low-T) biochar. ^a means data from Liu et al. (2016). ^b means data from Liu et al. (2015).

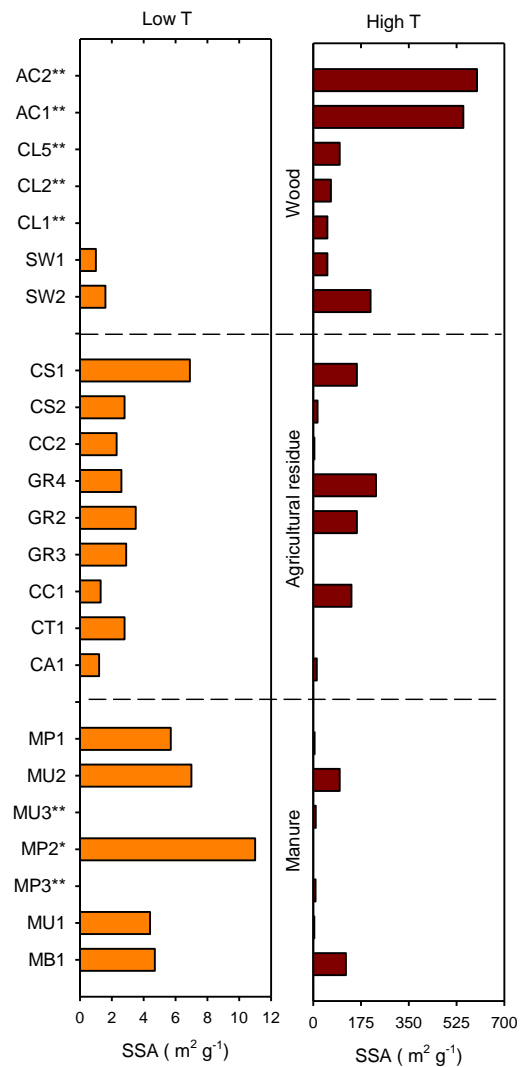


Figure G.1. Specific surface area (SSA) of low-T (left) and high-T biochar. * Data not available for high-temperature (high-T) biochar. ** Data not available for low-temperature (low-T) biochar.

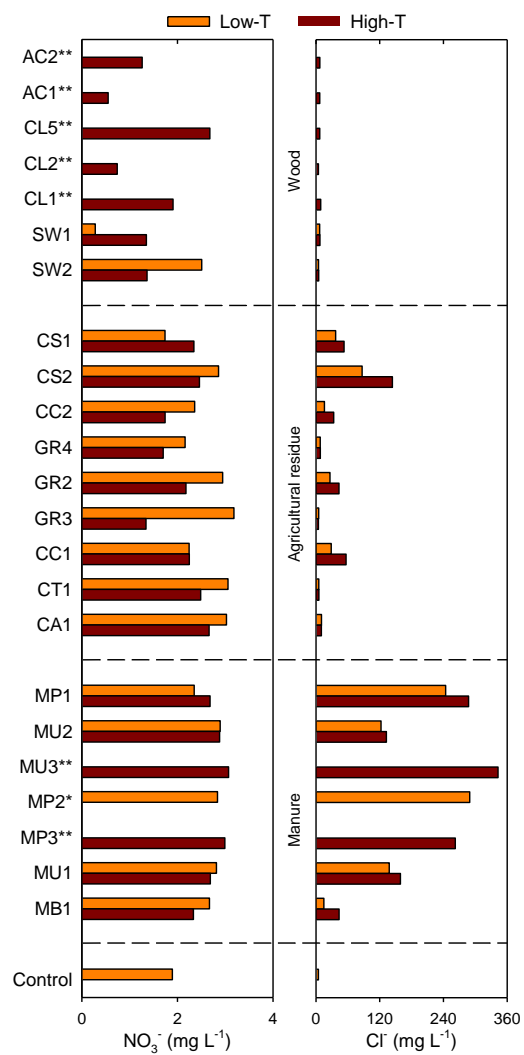


Figure G.2. Concentrations of NO₃⁻ and Cl⁻ in aqueous solution in batch tests containing biochar and river water spiked with Hg. Control represents Hg-spiked river water with no biochar added. * Data not available for high-temperature (high-T) biochar. ** Data not available for low-temperature (low-T) biochar.

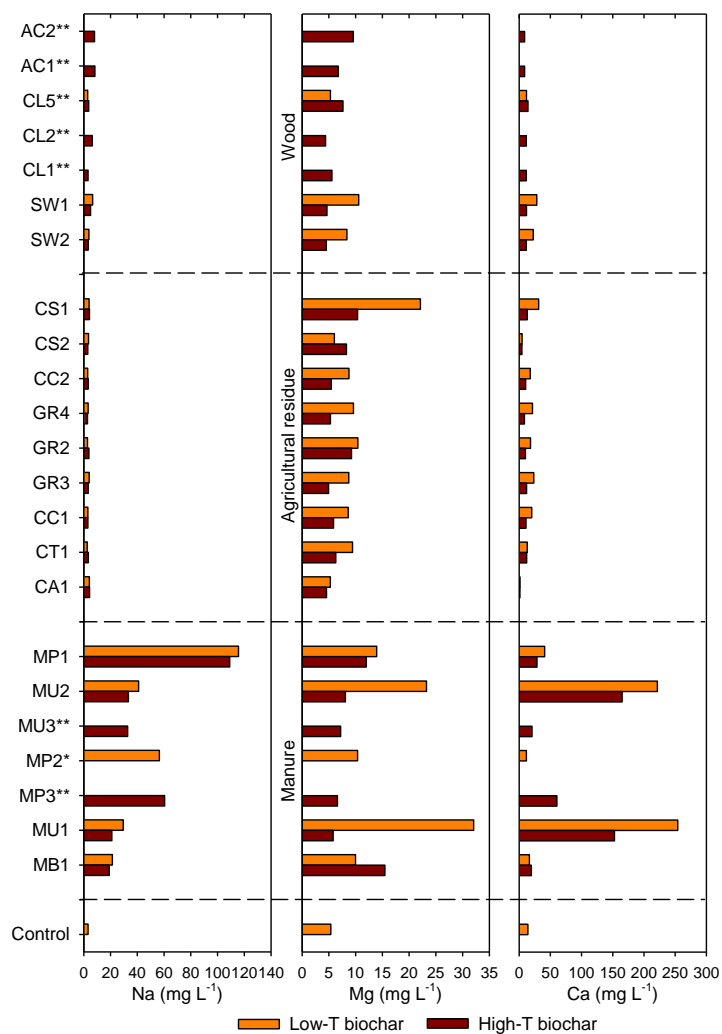


Figure G.3. Concentrations of major cations (Na, Mg, and Ca) in aqueous solution in batch tests containing biochar and river water spiked with Hg. Control represents Hg-spiked river water with no biochar added. * Data not available for high-temperature (high-T) biochar. ** Data not available for low-temperature (low-T) biochar.

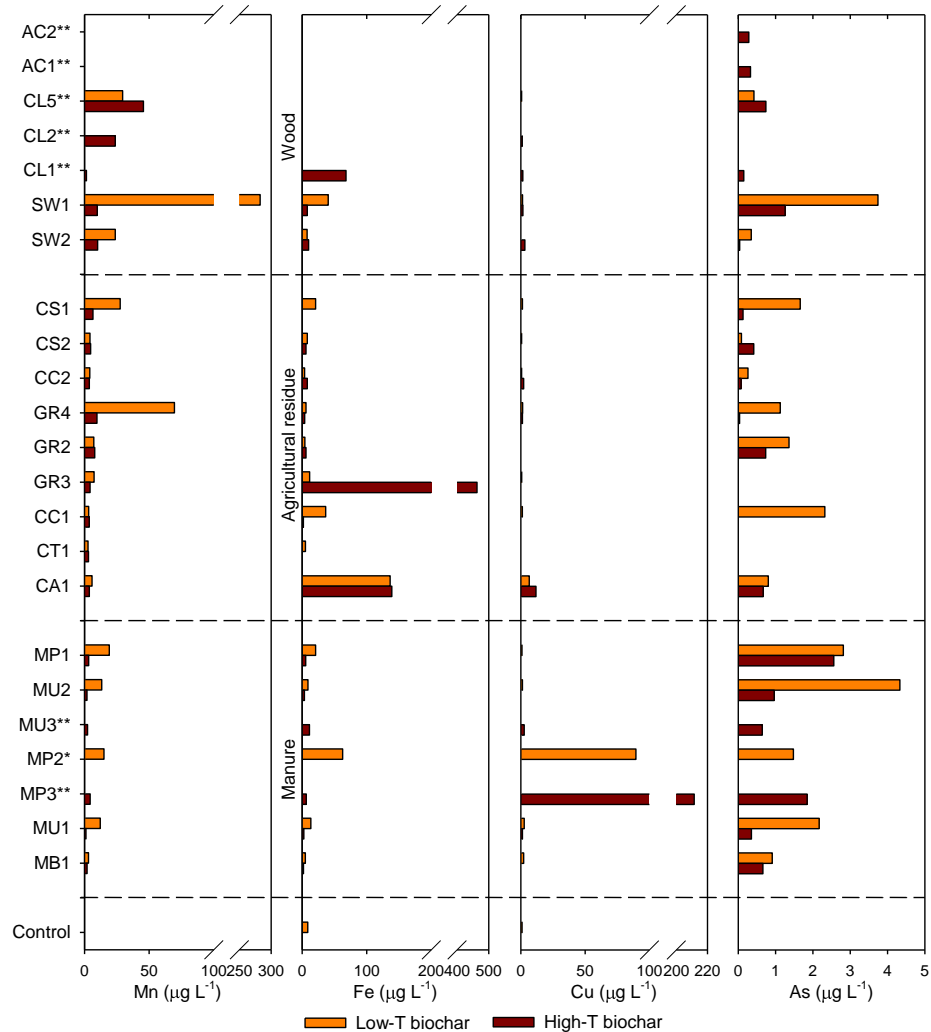


Figure G.4. Concentrations of trace elements (Mn, Fe, Cu, and As) in aqueous solution in batch tests containing biochar and river water spiked with Hg. Control represents Hg-spiked river water with no biochar added. * Data not available for high-temperature (high-T) biochar. ** Data not available for low-temperature (low-T) biochar.

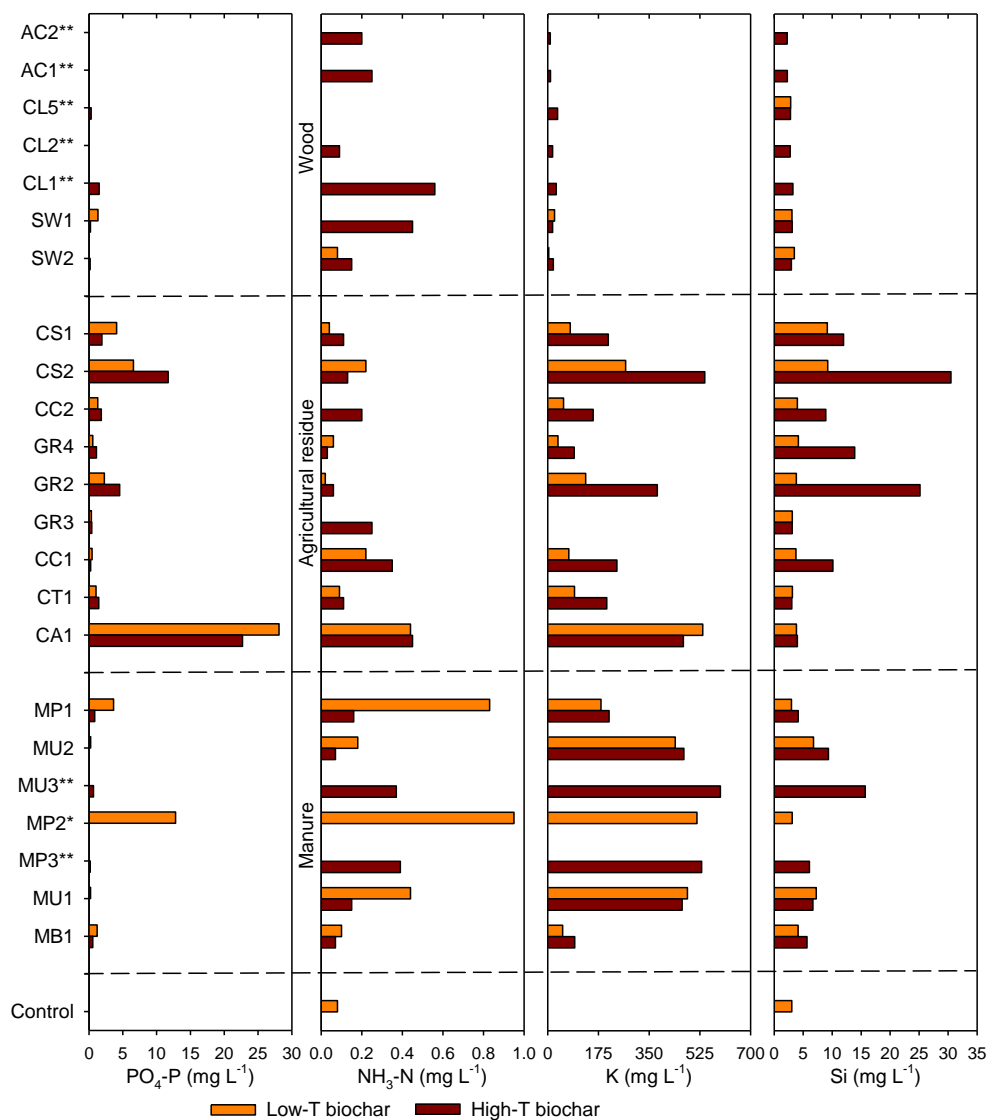


Figure G.5. Concentrations of nutrients (PO₄-P, NH₃-N, K and Si) in aqueous solution in batch tests containing biochar and river water spiked with Hg. Control represents Hg-spiked river water with no biochar added. * Data not available for high-temperature (high-T) biochar. ** Data not available for low-temperature (low-T) biochar.

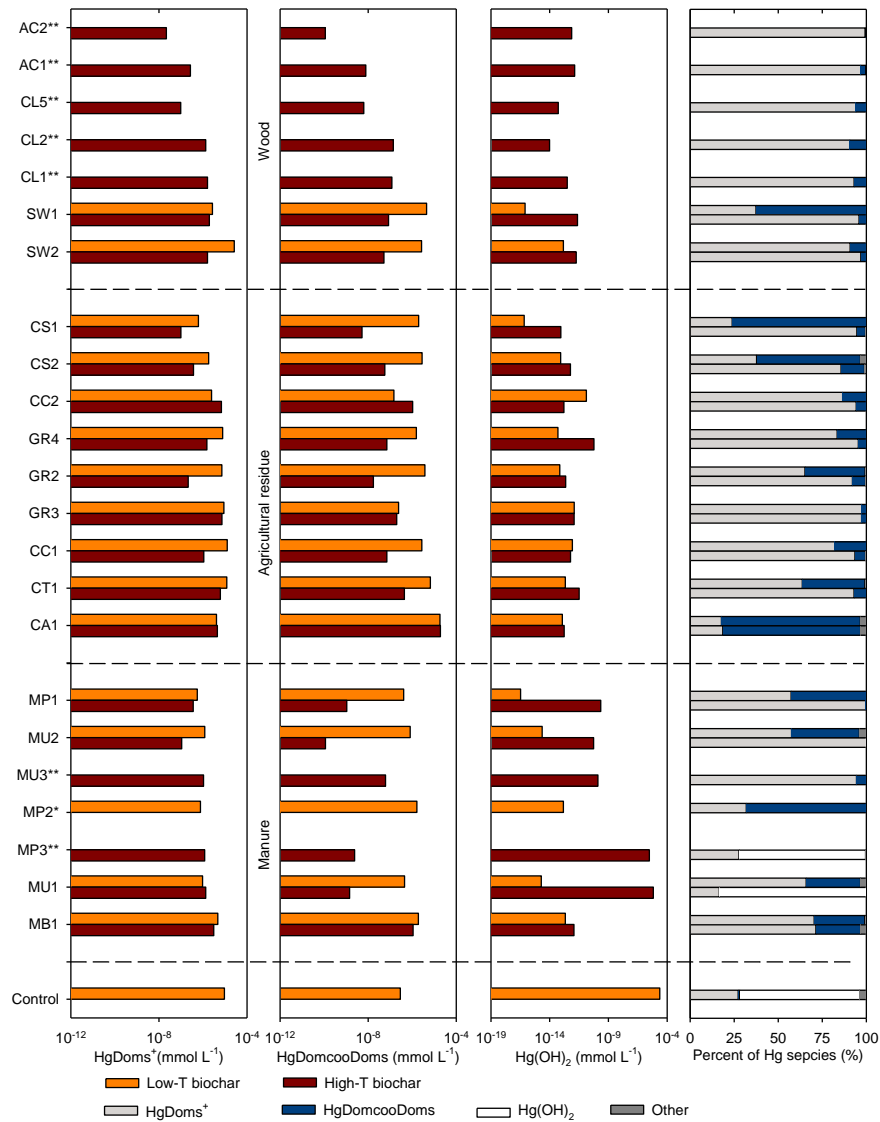


Figure G.6. PHREEQC modeling results of Hg and DOM complexes in aqueous solution in batch tests containing biochar and river water spiked with Hg. Control represents Hg-spiked river water with no biochar added. * Data not available for high-temperature (high-T) biochar. ** Data not available for low-temperature (low-T) biochar.